

**Autogenous shrinkage of alkali-activated slag and fly ash materials
From mechanism to mitigating strategies**

Li, Z.

DOI

[10.4233/uuid:cfb1c40b-464d-4cae-b0af-72ce29a53f96](https://doi.org/10.4233/uuid:cfb1c40b-464d-4cae-b0af-72ce29a53f96)

Publication date

2021

Document Version

Final published version

Citation (APA)

Li, Z. (2021). *Autogenous shrinkage of alkali-activated slag and fly ash materials: From mechanism to mitigating strategies*. [Dissertation (TU Delft), Delft University of Technology].
<https://doi.org/10.4233/uuid:cfb1c40b-464d-4cae-b0af-72ce29a53f96>

Important note

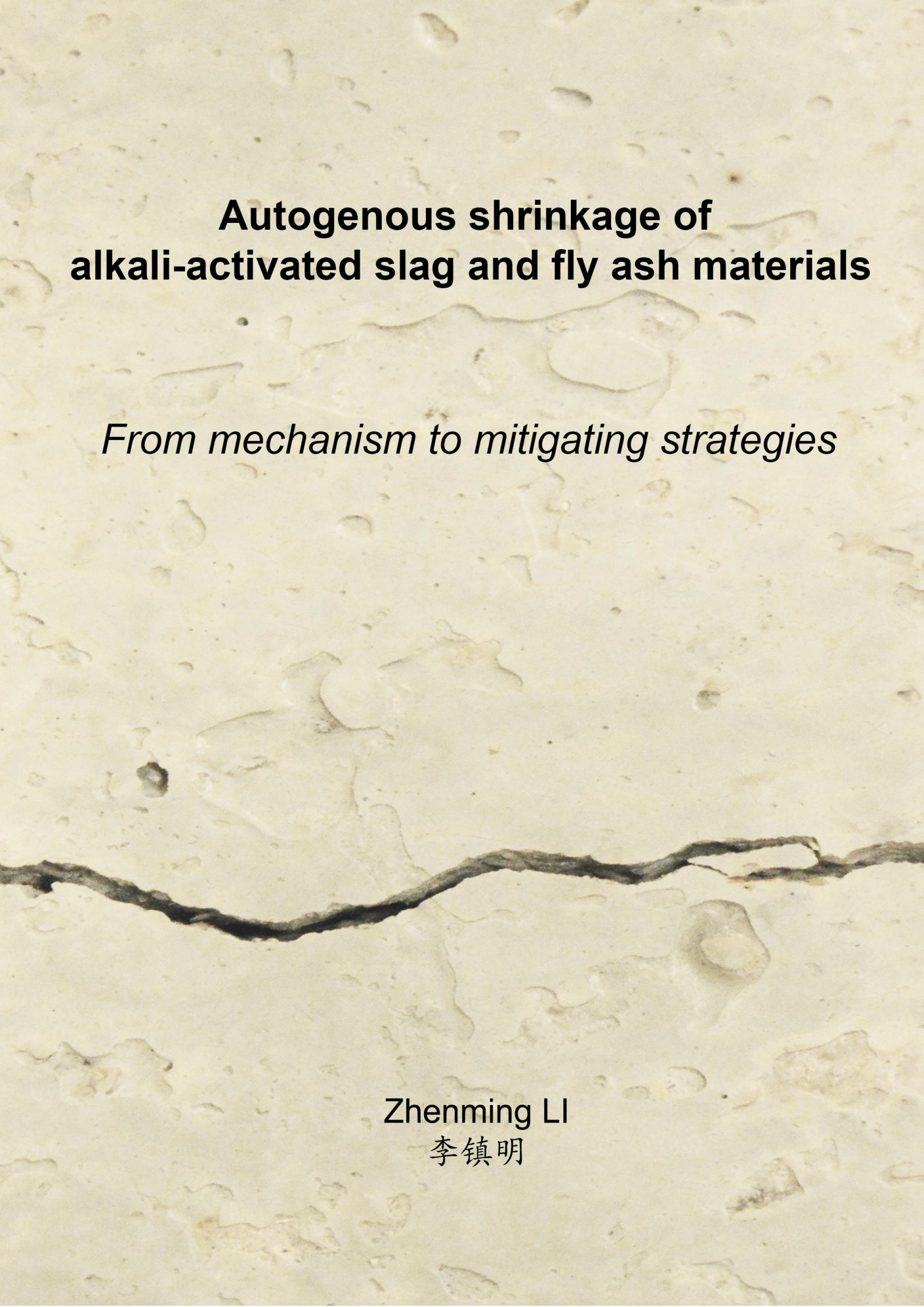
To cite this publication, please use the final published version (if applicable).
Please check the document version above.

Copyright

Other than for strictly personal use, it is not permitted to download, forward or distribute the text or part of it, without the consent of the author(s) and/or copyright holder(s), unless the work is under an open content license such as Creative Commons.

Takedown policy

Please contact us and provide details if you believe this document breaches copyrights.
We will remove access to the work immediately and investigate your claim.

The background of the cover is a microscopic image of a material surface. It shows a light-colored, textured surface with numerous small, irregular pores and a prominent, dark, jagged crack running horizontally across the lower half of the image. The overall appearance is that of a porous, possibly brittle material.

**Autogenous shrinkage of
alkali-activated slag and fly ash materials**

From mechanism to mitigating strategies

Zhenming LI

李镇明

Autogenous shrinkage of alkali-activated slag and fly ash materials: From mechanism to mitigating strategies

Dissertation

For the purpose of obtaining the degree of doctor
at Delft University of Technology
by the authority of the Rector Magnificus Prof.dr.ir. T.H.J.J. van der Hagen
chair of the Board for Doctorates
to be defended publicly on
Monday 15 March 2021 at 12:30 o'clock

By

Zhenming LI

Master of Engineering in Structural Engineering
Harbin Institute of Technology, P.R. China
Born in Hebei Province, P.R. China

This dissertation has been approved by the promotor

Promotor: Prof. K. van Breugel

Promotor: Dr. G. Ye

Composition of the doctoral committee:

Rector Magnificus,	chairperson
Prof. K. van Breugel	Delft University of Technology, promotor
Dr. G. Ye	Delft University of Technology, promotor

Independent Members:

Prof. dr. J. Ou	Harbin Institute of Technology
Prof. dr. O. M. Jensen	Technical University of Denmark
Prof. dr. F. Benboudjema	ENS Paris-Saclay
Prof. dr. ir. E. Schlangen	Delft University of Technology
Dr. O. Cizer	KU Leuven
Prof. dr. ir. S.M.J.G. Erkens	Delft University of Technology, reserve member

Keywords: Alkali-activated materials; autogenous shrinkage; slag; fly ash; metakaolin; internal curing; mechanism; cracking; mitigating strategies; microstructure; modeling

Printed by: Ipskamp Printing, The Netherlands

Thesis format by: Zhenming Li

Cover design: Zhenming Li & Yu Chen

Copyright © 2019 by Z. Li

All rights reserved. This copy of the thesis has been supplied on condition that anyone who consults it is understood to recognize that its copyright rests with its author and that no quotation from the thesis and no information derived from it may be published without the author's prior consent.

ISBN 978-94-6421-279-2

An electronic version of this dissertation is available at

<http://repository.tudelft.nl/>

Things in the world can be easy or difficult. If we do them, difficult things will become easy; if we don't, easy things will become difficult.

天下事有难易乎？为之，则难者亦易矣；不为，则易者亦难矣。

- *Duanshu Peng* 彭端淑 (1699 - 1779)

Table of Contents

List of Symbols.....	9
List of Abbreviations.....	11
Summary	13
Samenvatting.....	15
Chapter 1.....	17
Introduction.....	17
1.1 Research background	17
1.2 Research aim and strategy	19
1.3 Research scope	20
1.4 Outline of this research	20
Chapter 2.....	22
Literature survey on autogenous shrinkage of AAMs.....	22
2.1 Introduction	22
2.2 General introduction of AAMs	22
2.3 Autogenous shrinkage of AAMs	24
2.3.1 Autogenous shrinkage of AAS	24
2.3.2 Autogenous shrinkage of AAF	28
2.3.3 Autogenous shrinkage of AASF	29
2.4 Strategies to mitigate the autogenous shrinkage	31
2.4.1 SRA and other chemical admixtures	31
2.4.2 Expansive additive.....	32
2.4.3 Nano-particles	33
2.4.4 Internal curing	34
2.4.5 Elevated-temperature curing.....	35
2.5 Problem definition.....	35
2.6 Conclusions.....	36
Chapter 3.....	38
Mechanisms of autogenous shrinkage of AAMs.....	38
3.1 Introduction	38
3.2 Materials and experiments.....	38

3.2.1	Raw materials and mixture proportions	38
3.2.2	Experimental methods	40
3.3	Results and discussion	42
3.3.1	Autogenous shrinkage.....	42
3.3.2	Microstructure characterization	43
3.3.3	Chemical shrinkage	47
3.3.4	Internal RH and pore pressure	48
3.3.5	Shrinkage under saturated condition.	50
3.3.6	Elastic modulus evolution	53
3.3.7	Modelling of the autogenous shrinkage	54
3.4	Concluding remarks	59
Chapter 4	60
Mitigation strategies of autogenous shrinkage of AAMs Part 1: internal curing with SAPs ...		60
4.1	Introduction	60
4.2	Materials and methods	61
4.2.1	Raw materials	61
4.2.2	Determination of SAPs content.....	61
4.2.3	Mixtures	63
4.2.4	Experimental methods	64
4.3	Results.....	65
4.3.1	Absorption behaviours of SAPs	65
4.3.2	Reaction heat	66
4.3.3	Setting time	68
4.3.4	Internal RH.....	68
4.3.5	Autogenous shrinkage.....	69
4.3.6	CT scan.....	71
4.3.7	SEM analysis	73
4.3.8	Mechanical properties	75
4.4	Discussion	76
4.4.1	Absorbing and releasing behaviours of SAPs	76
4.4.2	Reaction kinetics and setting	77
4.4.3	Mitigating effect of internal curing on autogenous shrinkage	79

Table of Contents	VII
4.4.4 Mechanical properties	81
4.5 Concluding remarks	82
Chapter 5	83
Mitigation strategies of autogenous shrinkage of AAMs Part 2: incorporation of metakaolin	83
5.1 Introduction	83
5.2 Methodological approach	84
5.2.1 General framework of this chapter	84
5.2.2 Raw materials and mixture proportions	85
5.2.3 Experimental methods	86
5.3 Results and discussion	87
5.3.1 Autogenous shrinkage.....	87
5.3.2 Microstructure characterization	89
5.3.3 Autogenous shrinkage induced by steric-hydration force.....	99
5.3.4 Autogenous shrinkage induced by pore pressure	100
5.3.5 Compressive and flexural strength	104
5.4 Concluding remarks	106
Chapter 6	108
Cracking tendency of alkali-activated concrete subjected to restrained autogenous shrinkage	108
6.1 Introduction	108
6.2 Materials and methods	109
6.2.1 Raw materials and mixtures.....	109
6.2.2 Experimental methods	109
6.2.3 Prediction of the autogenous shrinkage-induced stress	114
6.3 Experimental results on cracking tendency of AAC.....	117
6.3.1 Mechanical properties	117
6.3.2 Autogenous shrinkage.....	119
6.3.3 Autogenous shrinkage-induced stress	120
6.4 Prediction of the autogenous shrinkage-induced stress in AAC	121
6.4.1 Calculated stress based on autogenous shrinkage	121
6.4.2 Calculated stress based on the elastic part of autogenous shrinkage.....	122
6.4.3 Calculated stress by taking into account creep and relaxation	123

6.5	Effectiveness of internal curing and incorporation of MK	124
6.5.1	Workability and strength	125
6.5.2	Autogenous shrinkage.....	127
6.5.3	Autogenous shrinkage-induced stress	127
6.6	Concluding remarks	128
Chapter 7	130
Retrospection, conclusions, contributions and future research.....		130
7.1	Retrospection	130
7.2	Conclusions.....	131
7.3	Contributions of this study	132
7.4	Future research	133
Appendix A	135
Ultimate total heat and overall reaction degree		135
References.....		137
Propositions.....		155
List of publications		156
Curriculum Vitae.....		159
Acknowledgements.....		160

List of Symbols

Roman lower case letters

r	Radius of menisci	[m]
f_c	Compressive strength	[MPa]
f_t	Splitting tensile strength	[MPa]
t	Time	[days]
t_{cr}	Cracking time	[days]
m	Mass	[g]
n	Fitting parameter	[-]
d	Fitting parameter	[-]

Roman capital case letters

RH	Relative humidity	[-]
RH_S	Relative humidity of pore solution	[-]
RH_K	Relative humidity related to gas-liquid menisci	[-]
V_w	Molar volume of pore solution	[m ³ /mol]
R	Universal gas constant	[J/(mol·K)]
T	Temperature expressed in the absolute scale	[K]
S	Saturation degree of paste	[-]
V_l	Liquid volume in paste	[ml]
V_p	Total pore volume in paste	[ml]
V_{il}	Initial liquid volume in paste	[ml]
V_{nl}	Non-evaporable liquid volume in paste	[ml]
V_{cs}	Volume reduction associated with chemical shrinkage	[ml]
K	Bulk modulus of the whole porous body	[GPa]
K_S	Bulk modulus of the solid material	[GPa]
E	Modulus of elasticity	[GPa]
Q	Reaction heat	[J]

Q_{max}	Ultimate reaction heat	[J]
CS	Chemical shrinkage	[ml/g]

Greek letters

γ	Surface tension of pore solution	[N/m]
σ	Pore pressure	[MPa]
ε_{lin}	Linear autogenous shrinkage	[m/m]
ν	Poisson's ratio	[-]
ε_{AS}	Autogenous shrinkage	[m/m]
ε_{pore}	Autogenous shrinkage related to pore pressure	[m/m]
ε_{ste}	Autogenous shrinkage related to steric-hydration force	[m/m]
ε_{elas}	Elastic deformation	[m/m]
ε_{creep}	Creep/time-dependent deformation	[m/m]
φ	Creep factor	[-]
τ	Time	[days]
ψ	Relaxation factor	[-]
α	Degree of reaction	[-]
α_{max}	Ultimate degree of reaction	[-]
ω	Water-binder ratio	[g/g]
ρ_a	Density of activator	[g/ml]
σ_{AS}	Stress due to restrain shrinkage	[MPa]
σ_{rel}	Stress when relaxation is considered	[MPa]
θ	Fitting parameter associated with time	[days]
β	Fitting parameter associated with shape of the exponential model	[-]

List of Abbreviations

AAMs	Alkali-activated materials
OPC	Ordinary Portland cement
AAC	Alkali-activated concrete
ASR	Alkali-silica reaction
AAS	Alkali-activated slag
AAF	Alkali-activated fly ash
AASF	Alkali-activated slag-fly ash blends
C-S-H	Calcium-silicate-hydrate
C-A-S-H	Calcium-aluminosilicate-hydrate
N-A-S-H	Sodium-aluminosilicate-hydrate
K-A-S-H	Potassium-aluminosilicate-hydrate
DLVO	Derjaguin-Landau-Verwey-Overbeek
RH	Relative humidity
SRA	Shrinkage reducing admixtures
w/b	Water to binder ratio
w/c	Water to cement ratio
w/s	Water to solid ratio
l/b	Liquid to binder ratio
SAPs	Superabsorbent polymers
LWA	Lightweight aggregates
XRF	X-ray fluorescence
XRD	X-ray diffraction
EN	European Standards
NEN	Netherlands Standardization Institute,
ASTM	American Society for Testing and Materials

FTIR	Fourier transform infrared spectroscopy
BJH	Barrett-Joyner-Halenda
EMM-ARM	Elasticity Modulus Monitoring through Ambient Response Method
SEM	Scanning electron microscopy
CT	Computed tomography
MK	Metakaolin
LVDTs	Linear variable differential transformers
ADTM	Autogenous Deformation Testing Machine
TSTM	Temperature Stress Testing Machine
Q ⁿ	Silicate units, where n represents the number of Si–O linkages
R-square	Coefficient of determination

Summary

Alkali-activated materials (AAMs), as eco-friendly alternatives to Ordinary Portland cement (OPC), have attracted increasing attention of researchers in the past decades. Unlike cement, which requires calcination of limestone, AAMs can be made from industrial by-products, or even wastes, with the use of alkali-activator. The production of AAMs consumes 40% less energy and emits 25-50% less CO₂ compared to the production of OPC.

Despite the eco-friendly nature of AAMs, doubts about these materials as an essential ingredient of concrete exist, regarding, for example, their volume stability. One possible volume change concerns autogenous shrinkage. Autogenous shrinkage is the reduction in volume caused by the material itself without substance or heat exchange with the environment. If the autogenous shrinkage of a binder material is too large, cracking might happen, which will seriously impair the durability of concrete. According to the literature, AAMs can show higher autogenous shrinkage than OPC-based materials. However, the mechanism behind the high autogenous shrinkage of AAMs is still unclear. Existing shrinkage-mitigating strategies for OPC are not necessarily applicable for AAMs. There is also a lack of new strategies particularly designed for AAMs. Moreover, the cracking sensitivity of AAMs-based concrete induced by restrained autogenous shrinkage has not been investigated yet.

The aim of this study is, therefore, set to understand and mitigate the autogenous shrinkage and the cracking tendency of AAMs.

At first, the autogenous shrinkage of AAMs is studied experimentally. It is found that AAMs made from slag and fly ash show much higher autogenous shrinkage than commonly used OPC mixtures do. The more slag is used in the precursor, the larger is the autogenous shrinkage of the paste. To clarify the mechanisms behind it, the reaction kinetics, nature of reaction products and microstructure of AAMs paste are comprehensively characterized. It is shown that self-desiccation is not the exclusive mechanism of autogenous shrinkage of AAMs. Other driving forces, such as the steric-hydration force between colloid associated with the change in ion concentrations in the pore solution, also play a role, especially in the very early age. Besides, AAMs show pronounced viscoelasticity, which means a large time-dependent deformation/creep. To estimate the time-dependent deformation in autogenous shrinkage of AAMs, a computational model is proposed. The correspondingly calculated autogenous shrinkage matches well with the measured result.

Based on the clarified mechanisms, two strategies are proposed aiming at mitigating the driving forces of autogenous shrinkage. One of the strategies is internal curing with superabsorbent polymers (SAPs). With micro-CT scan, the internal curing process in AAMs paste is monitored. The liquid is released gradually from the SAP particles to the surrounding paste and big voids are left. The internal relative humidity of the paste is, therefore, kept at a high level. At a suitable dosage, SAPs can greatly mitigate the autogenous shrinkage of AAMs, especially the part that is caused by self-desiccation. Partially due to the SAPs-originated voids,

the compressive strength of AAMs is lower than that of the paste without SAPs, although the flexural strength and elastic modulus are hardly influenced.

Another strategy is the incorporation of metakaolin (MK). MK is also an often-used precursor for AAMs, but this is the first time that the effects of MK on the autogenous shrinkage of alkali-activated slag (AAS) and alkali-activated slag-fly ash (AASF) are studied. It is found that the incorporation of a small amount of MK can substantially reduce the autogenous shrinkage of these systems. The presence of MK is found to release extra dissolvable Si and Al to the pore solution, but decrease the concentration of Ca, Na and OH. As a result, the reaction rate of the paste becomes lower in the very early age and the formation of reaction products is retarded. The autogenous shrinkages induced by both the change of steric-hydration force and capillary tension are reduced when MK is incorporated. The results in this study suggest that SAPs and MK are promising admixtures to AAS and AASF towards a lower autogenous shrinkage.

The cracking tendency of AAMs-based concrete subjected to restrained autogenous shrinkage is evaluated. Temperature Stress Testing Machine (TSTM) is utilized to track the stress evolution and proneness to cracking of the concrete. It is found that AAMs-based concrete shows later cracking than OPC-based concrete for similar compressive strength, despite the higher autogenous shrinkage of AAMs-based concrete. The main reason for this is that a large part of the measured autogenous shrinkage belongs to creep and that the stress is reduced by the pronounced relaxation of AAMs-based concrete. It is also found that the strategies proposed above are very effective to reduce the cracking tendency of AASF concrete.

This study contributes to a better understanding of the shrinkage mechanisms of AAMs. SAPs and MK are promising ingredients for large scale use in AAMs mixtures. The numerical approaches developed in this study are also useful in future studies or applications to estimate the creep and relaxation in AAMs. Besides autogenous shrinkage, drying shrinkage and thermal shrinkage are recommended to be considered in future research.

Samenvatting

Alkali-geactiveerde materialen (AAM's), als milieuvriendelijk alternatief voor Portlandcement (OPC), hebben de afgelopen decennia steeds meer aandacht gekregen van onderzoekers. In tegenstelling tot cement, dat calcineren van kalksteen vereist, kunnen AAM's worden gemaakt van industriële bijproducten, of zelfs afval, met behulp van een alkalische activator. De productie van AAM's verbruikt 40% minder energie en stoot 25-50% minder CO₂ uit in vergelijking met de productie van OPC.

Ondanks het milieuvriendelijke karakter van AAM's, bestaan er twijfels over deze materialen als bindmiddel voor beton, bijvoorbeeld vanwege hun volumestabiliteit. Een mogelijke volumeverandering betreft autogene krimp. Autogene krimp is de volumevermindering veroorzaakt door het materiaal zelf, zonder water- of warmte-uitwisseling met de omgeving. Wanneer de autogene krimp van een bindmiddel te groot is, kunnen er scheurtjes optreden die de duurzaamheid van beton ernstig zal aantasten. Vanuit literatuur blijkt dat AAM's een hogere autogene krimp vertonen dan OPC-gebaseerde materialen. Het mechanisme achter de hoge autogene krimp van AAM's is nog onduidelijk. Bestaande krimp-mitigerende strategieën voor OPC zijn niet per definitie toepasbaar op AAM's. Vooral nog zijn er geen nieuwe strategieën ontwikkeld die specifiek voor AAM's geschikt zijn. Bovendien is de scheurgevoeligheid van op AAM's gebaseerd beton, geïntroduceerd door verhinderde autogene krimp, nog niet onderzocht.

Het doel van deze studie is daarom om de autogene krimp en de scheurgevoeligheid van AAM's te begrijpen en te verminderen.

In eerste instantie wordt de autogene krimp van AAM's experimenteel bestudeerd. Het blijkt dat AAM's gemaakt van hoogovenslakken en vliegashoudend cement een veel hogere autogene krimp vertonen dan met OPC. Hoe meer slak er in de precursor wordt gebruikt, des te groter is de autogene krimp van het bindmiddel. Om het mechanismen erachter op het spoor te komen worden de kinetische reacties, de aard van reactieproducten en de microstructuur van AAM's-pasta uitvoerig gekarakteriseerd. Er wordt aangetoond dat zelfdroging niet het exclusieve mechanisme is van autogene krimp van AAM's. Andere drijvende krachten, zoals de sterische hydratatiekracht die samenhangen met de verandering in ionenconcentraties in de porie-oplossing, spelen ook een rol, vooral op zeer jonge leeftijd. Bovendien vertonen AAM's een overduidelijke visco-elastisch karakter, wat leidt tot een grote tijdsafhankelijke vervorming / kruip. Om de tijdsafhankelijke vervorming bij autogene krimp van AAM's in te schatten, wordt een rekenmodel voorgesteld. De hiermee berekende autogene krimp is overeenkomstig het gemeten resultaat.

Op basis van de veronderstelde mechanismen worden twee strategieën voorgesteld, gericht op het verminderen van de drijvende krachten van autogene krimp. Een van de strategieën is interne nabehandeling met superabsorberende polymeren (SAP's). Met een micro-CT-scan wordt het interne uithardingsproces in AAM's-pasta vastgelegd. De vloeistof van de SAP-deeltjes wordt geleidelijk afgegeven aan de omringende pasta en er blijven grote holtes achter. De interne relatieve vochtigheid van de pasta wordt daarom op een hoog niveau

gehouden. Bij een passende dosering kunnen SAP's de autogene krimp van AAM's aanzienlijk verminderen, vooral het deel dat wordt veroorzaakt door zelfdroging. De door SAP ontstane holtes zorgen er mede voor dat de druksterkte van AAM's lager is dan die van de pasta zonder interne curing, hoewel de buigsterkte en elasticiteitsmodulus nauwelijks worden beïnvloed. Een andere strategie is de toevoeging van metakaoline (MK). MK is ook een veel gebruikte precursor voor AAM's, maar dit is de eerste keer dat de effecten van MK op de autogene krimp van alkali-geactiveerde slak (AAS) en alkali-geactiveerde slak-vliegas (AASF) zijn bestudeerd. Het is gebleken dat de opname van een kleine hoeveelheid MK de autogene krimp van deze systemen aanzienlijk kan verminderen. De aanwezigheid van MK blijkt extra oplosbaar Si en Al vrij te geven aan de poriënoplossing, maar verlaagt de concentratie van Ca, Na en OH. Dit resulteert in een lagere reactiesnelheid van de pasta op zeer jonge leeftijd, terwijl de vorming van de reactieproducten wordt vertraagd. De autogene krimp die wordt veroorzaakt door zowel de verandering van de sterische hydratatiekracht als de capillaire spanning wordt verminderd wanneer MK wordt toegepast. De resultaten in deze studie suggereren dat SAP's en MK veelbelovende opties zijn voor een lagere autogene krimp bij AAS en AASF, terwijl mechanische eigenschappen nauwelijks worden beïnvloed.

De scheurgevoeligheid van op AAMs gebaseerd beton dat is onderworpen aan verhinderde autogene krimp wordt geëvalueerd. Temperature Stress Testing Machine (TSTM) wordt gebruikt om de spanningsontwikkeling en de neiging tot scheuren van het beton te volgen. Het is gebleken dat op AAMs gebaseerd beton later scheurt dan op OPC gebaseerd beton met een vergelijkbare druksterkte, ondanks de hogere autogene krimp van op AAMs gebaseerd beton. De belangrijkste reden hiervoor is dat een groot deel van de gemeten autogene krimp uit kruip bestaat en dat de spanning wordt verminderd door relaxatie van op AAMs gebaseerd beton. Het is ook gebleken dat de hierboven voorgestelde strategieën zeer effectief zijn om de scheurgevoeligheid van AASF-beton te verminderen.

Deze studie draagt bij aan een beter begrip van de krimpmechanismen van AAM's. SAP's en MK zijn veelbelovende ingrediënten in betonmengsels om op grote schaal te worden gebruikt in AAM-mengsels. De numerieke benaderingen die in deze studie zijn ontwikkeld, zijn ook nuttig in toekomstige studies of toepassingen om de kruip en relaxatie in AAM's in te schatten. Naast autogene krimp, worden uitdrogingskrimp en thermische krimp aanbevolen om in toekomstig onderzoek in overweging te nemen.

Chapter 1

Introduction

1.1 Research background

In recent years, the concern about global warming and carbon emission has been growing. An important part of global CO₂ emission comes from the construction sector, especially the production of cement. It has been reported that cement production contributes to 5-8% CO₂ emission worldwide [1].

Figure 1.1 shows the global cement production and the consequent CO₂ emission in the past hundred years. A rapid increase in cement production can be observed in the past decades. The huge amount of cement production worldwide indicates a great demand of the society for binder materials, however, this demand conflicts with the request to reduce the emission of greenhouse gases.

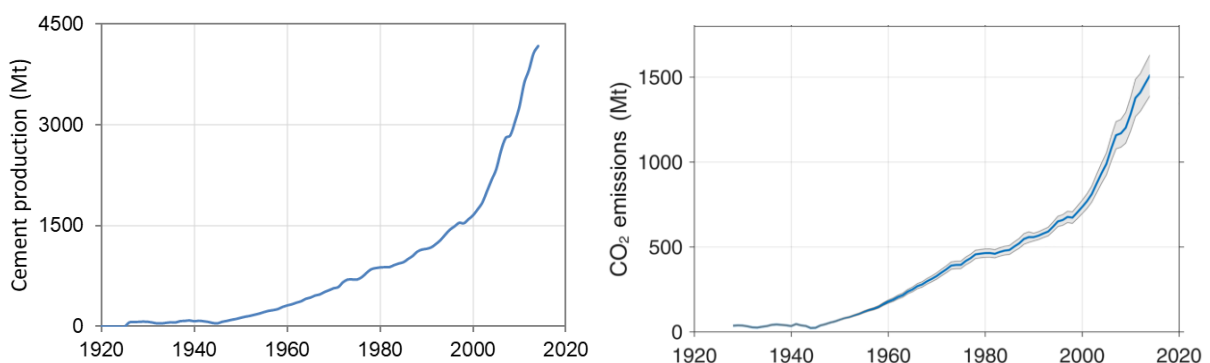


Figure 1.1 (a) Global cement production in the last 100 years (data from USGS) and (b) global CO₂ emissions from cement production in the last 100 years [2].

To resolve this conflict, increasing research attention has been paid to the development of “greener” alternative binders, which can partially or completely replace the cement in construction applications [3]. Among all the cement alternatives, alkali-activated materials (AAMs) have emerged as important candidates. Alkali-activated material is defined as a material formed by the reaction between aluminosilicate precursor(s) and alkaline activator [4]. While the cement production requires the calcination of limestone, which emits CO₂ and consumes energy, AAMs can be made from the industrial by-products, to which little environmental footprint is attributed. The activators, like NaOH and Na₂SiO₃, need to be produced from the manufacturing process, which goes along with energy consumption and CO₂ emission [5]. However, because the activator usually accounts for less than 10% by mass of the binder, the CO₂ emission per ton of binder is still much lower than that associated with OPC [4].

The two most widely utilized by-products as precursors for alkali-activated materials are ground granulated blast-furnace slag (hereinafter termed slag) from the steelmaking and fly ash from the coal-fired electricity plants. In concrete made from alkali-activated slag and fly ash materials, the ordinary Portland cement (OPC) can be 100% substituted.

A lot of research has been devoted to the investigation of the properties of AAMs, especially their mechanical properties and durability. The alkali-activated slag systems normally show high strength at ambient temperature [6,7]. However, these systems are known to harden more rapidly than usually desired [8]. Alkali-activated fly ash systems, by contrast, have very slow strength development at ambient temperature due to the low reactivity of fly ash [9]. Activating a blend of slag and fly ash can counterbalance the disadvantages of the sole precursor-based systems. It was reported that the alkali-activated slag and fly ash blended system can show reasonable setting time and good mechanical properties and are considered to be promising for widespread use in engineering [10,11]. The chemical resistance of alkali-activated concrete (AAC) against acid, chloride, sulphate, CO₂, etc., is generally reported to be similar to or even better than that of OPC concrete [12–15]. Alkali-silica reaction (ASR) could be a potential problem for AAC, but the expansion induced by the formation of ASR products of AAMs was found to be smaller compared to OPC containing the same aggregate [16]. In addition, AAC is found to have superior fire resistance as compared to OPC concrete [17].

Despite the good mechanical properties and durability of AAMs, these materials can show large autogenous shrinkage. Autogenous shrinkage is the self-created bulk shrinkage of a cementitious material system, without substance (e.g. moisture) or heat exchange with the environment [18]. Unlike drying shrinkage and plastic shrinkage, which can be eliminated by protecting the material from drying, autogenous shrinkage is a self-created shrinkage driven by internal forces and can develop fast at early age when the strength of the material is still low. When the materials are under restraint condition (e.g. the length is fixed), autogenous shrinkage may induce cracking. A schematic diagram of this is shown in Figure 1.2. The cracking can cause a series of problems with regard to aesthetics, strength, and durability. As reported in literature, AAMs show larger autogenous shrinkage than OPC-based systems, especially when the slag content is high [19,20]. The large autogenous shrinkage of AAMs has been considered a conundrum that impedes the application of AAMs as binder materials [21].

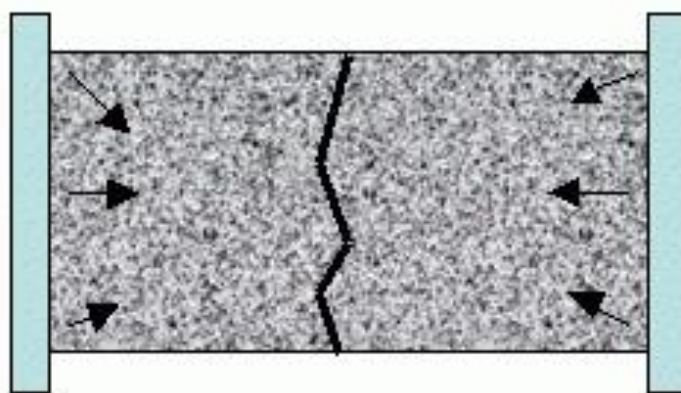


Figure 1.2 Schematic representation of cracking induced by restrained shrinkage.

Many studies can be found in the literature on autogenous shrinkage of AAMs. However, most of them were focused on the autogenous shrinkage magnitudes. The mechanism of autogenous shrinkage of AAMs remains poorly understood. For OPC systems, several shrinkage mechanisms have been proposed, such as the capillary pressure theory [18], disjoining pressure theory [22], surface tension theory [23], etc. However, according to [24,25] these theories may not be able to explain the autogenous shrinkage behaviour of AAMs. The clarification of the mechanisms of autogenous shrinkage of AAMs is required not only for a better understanding of the shrinkage-related behaviour of AAMs, but also for the development of reliable predicting models that can be used in practice.

Another important issue that has not been sufficiently studied is the cracking sensitivity of AAMs induced by the restrained autogenous shrinkage. Given the high autogenous shrinkage of AAMs, one may suppose a high cracking risk of these materials under restraint condition. However, the cracking is actually determined by multiple factors, including tensile strength, elastic modulus, and creep/relaxation. As yet, very few studies have been done to evaluate the cracking sensitivity of AAMs considering these factors.

Besides, the industrial community is in lack of effective strategies to mitigate the autogenous shrinkage of AAMs. Although efforts have been made by some researchers to use the existing strategies developed for OPC to mitigate the autogenous shrinkage of AAMs, many of the strategies were proven ineffective, due to the different chemical environments and shrinkage mechanisms of the two different systems [26–28].

In summary, a better understanding of the shrinkage mechanisms is crucial for a wider application of AAMs in the construction industry. The cracking tendency of AAM systems induced by restrained autogenous shrinkage has not been evaluated yet. Effective strategies that can mitigate the autogenous shrinkage and the consequent cracking tendency of AAMs need to be developed.

1.2 Research aim and strategy

The aim of this research is, therefore, set to understand and mitigate the autogenous shrinkage and the cracking tendency of AAMs.

As the first step, a literature survey is conducted. Published results on autogenous shrinkage obtained by researchers are reviewed and the influencing factors of the autogenous shrinkage are summarized. The autogenous shrinkage of AAM systems is then experimentally measured. To study the mechanism of autogenous shrinkage of AAMs, the reaction kinetics and microstructure of the materials are characterized. The driving forces of the autogenous shrinkage and the deformability of the paste are investigated. Based on a proposed mechanism, two innovative strategies are proposed to mitigate the autogenous shrinkage of AAMs. Autogenous shrinkage-induced stress and cracking tendency of AAC are experimentally measured and compared with those of similar OPC systems. Computational models are built to predict the stress evolution and cracking initiation of AAC. At last, the effectiveness of the strategies developed in this study for mitigating the cracking tendency of AAC is verified.

1.3 Research scope

The combination of NaOH and Na₂SiO₃ is currently the most widely used activator. Therefore, this research is focused on NaOH and Na₂SiO₃-activated slag systems and slag/fly ash blended systems. Pure fly ash-based AAMs does not set in days at ambient temperature. At elevated temperature, the slow setting and low strength of alkali-activated fly ash can be alleviated [9], but the shrinkage in that situation has been reported to be not problematic [24]. Therefore, pure fly ash-based AAMs is not considered. For the slag and fly ash blended systems, one slag to fly ash weight ratio, 50%-50%, is focused in this research. Other ratios, like 30%-70% and 70%-30%, had been found by previous work [29] not to show substantial differences in the reactions and microstructures of the paste, so these ratios are not concerned in this research.

1.4 Outline of this research

The thesis outline is shown in Figure 1.3.

In chapter 1, the background, objectives, strategy, and scope of this research are outlined.

In chapter 2, a literature survey is presented of the current state of the art in the field of autogenous shrinkage of AAMs, including the magnitude, the mechanism and the mitigating strategies of autogenous shrinkage.

In chapter 3, the autogenous shrinkage of alkali-activated paste is measured and compared with that of OPC paste. The mechanisms of autogenous shrinkage are investigated in depth. The reaction kinetics and microstructure development of AAMs paste are characterized and the driving force of the autogenous shrinkage is identified. The deformability of the paste under internal forces is also studied.

In chapters 4 and 5, the effectiveness of internal curing with SAPs and incorporation of metakaolin for mitigating the autogenous shrinkage of AAMs are studied, respectively. In both chapters, the influence of the strategies on the reactions, microstructure development, and mechanical properties of the pastes are comprehensively investigated. In chapter 4, the mitigating effect of internal curing on the drop of internal relative humidity is especially focused on, while in chapter 5, the influence of metakaolin addition on the reaction kinetics of the pastes are especially focused on.

In chapter 6, the autogenous shrinkage-induced stress in alkali-activated paste and concrete are investigated. The cracking tendency of AAC is analyzed and estimated by calculations. The strategies developed in chapters 4 and 5 are utilized to mitigate the cracking tendency of AAC.

In chapter 7, the conclusions of this work are drawn. Recommendations for structural application and standardization of AAMs concrete are given with respect to autogenous shrinkage. In the end, research perspectives for future studies are proposed.

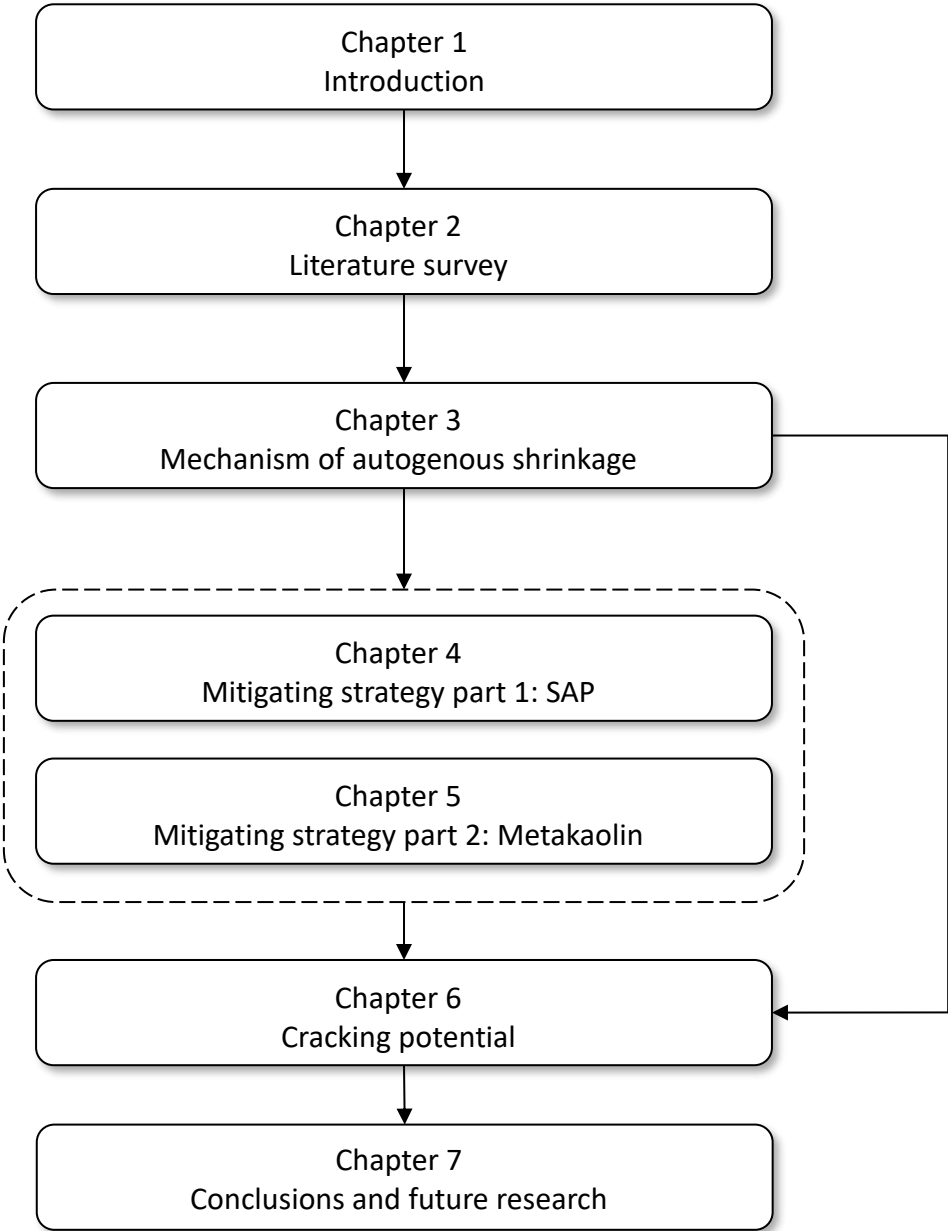


Figure 1.3. Outline of this thesis.

Chapter 2

Literature survey on autogenous shrinkage of AAMs

2.1 Introduction

This chapter provides a brief literature review on autogenous shrinkage of slag and fly ash-based AAMs. The reaction process and microstructure formation of AAMs are first briefly presented. The autogenous shrinkage of alkali-activated slag (AAS), alkali-activated fly ash (AAF) and alkali-activated slag-fly ash blends (AASF) are reviewed. The factors influencing the autogenous shrinkage of these materials and the current understanding of the autogenous shrinkage mechanisms are reviewed. The currently applied strategies to mitigate the autogenous shrinkage of AAMs are summarized and discussed.

2.2 General introduction of AAMs

The concept of AAMs as binder materials has been known since at least 1908 [30]. After that time, several studies had been conducted on the involvement of alkalis in potential cementitious materials [3]. Nonetheless, it is only since the 1990s that fundamental research on AAMs has blossomed worldwide [30], aiming at developing sustainable alternatives to OPC-based binders.

Many materials can show reactivity under alkaline condition, such as metakaolin, slag, fly ash, and other aluminosilicate materials [31,32]. Among them, slag and fly ash, as industrial by-products are the most widely utilized precursors for AAMs. Two types of fly ash have been utilized to synthesize AAMs, namely Class C and Class F according to ASTM C618 [33], depending on the calcium content in the fly ash. Class F (reactive CaO \leq 10%) fly ash is more intensively studied worldwide due to its wider availability and higher content of amorphous aluminosilicate phases [34].

Alkali activator is usually an alkali metal hydroxide and/or silicate [35]. Although Na₂CO₃ and Na₂SO₄ are also used as activators [36,37], the majority of studies have shown that activation with Na₂SiO₃ and/or NaOH provides high mechanical properties for slag and fly ash-based AAMs [10]. NaOH activators are found to accelerate early-age activation, but tend to present a barrier to advanced reactions, therefore limiting the later-age strength [38]. In contrast, the reaction of Na₂SiO₃-activated slag is comparatively slow, but results in the formation of very dense products with improved mechanical strength [39]. The molar ratio SiO₂/Na₂O, or so-called modulus, of the activator in the range of 1.0-1.5 is found to provide the densest microstructure and the highest strength for slag and fly ash-based AAMs [40,41].

A schematic illustration of alkali activation is shown in Figure 2.1. The alkali activation starts with the dissolution of the aluminosilicate source in a strongly alkaline environment (pH value above 13) [74]. A precursor with high calcium content, e.g. slag, leads to the formation of calcium-aluminosilicate-hydrate (C-A-S-H) type gels, while a precursor containing low calcium, e.g. fly ash, leads to the formation of sodium-aluminosilicate-hydrate (N-A-S-H) type gels [4]. The C-A-S-H type gels (the left-hand route in Figure 2.1) usually coexist with secondary products of the layered double-hydroxide (hydrotalcite) group. The sodium (N) in the N-A-S-H type gels (the right-hand route in Figure 2.1) can be partly substituted by potassium or even calcium, so a more complete description might be N,K-(C)-A-S-H. The H in N-A-S-H type gels is shown in parentheses to indicate that the water is not a major structural component of this gel, as it is in C-A-S-H type gels [42].

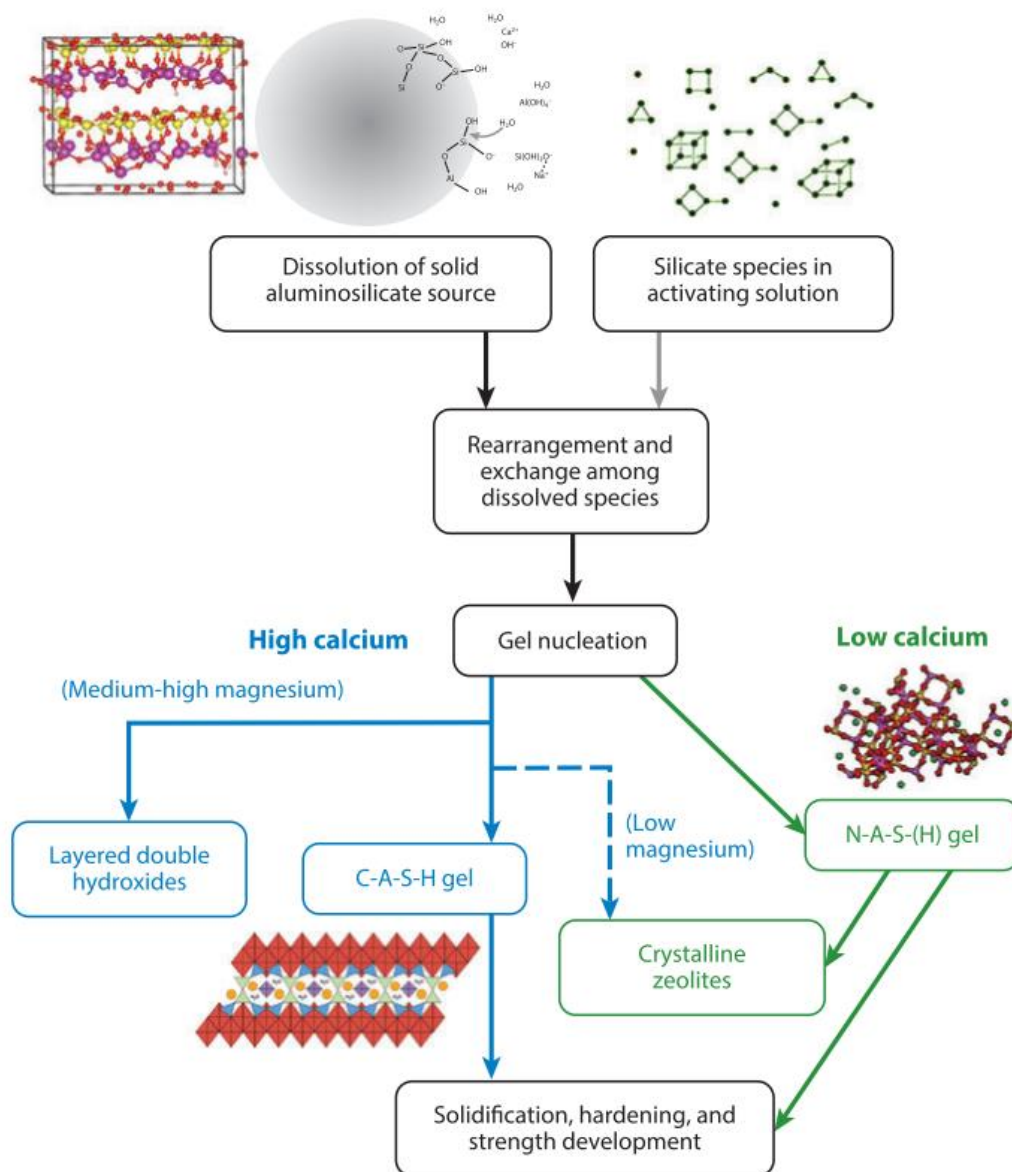


Figure 2.1 Process and reaction products of alkali activation of a solid aluminosilicate precursor [4].

AAMs, especially those activated by Na_2SiO_3 , usually show denser microstructures compared to OPC with similar liquid/binder ratios. As shown in Figure 2.2, AAS and AAF pastes show very few capillary pores, except for the cavities (marked by the arrows in Figure 2.2 (b)) in the raw fly ash. The first reason for the dense microstructure of AAMs lies in the fact that the activator of AAMs provides not only a high pH environment for the dissolution of precursors, but also nuclei (e.g. silicates) for the growth of reaction products [43,44]. The second reason is that the reaction products in AAMs, C-A-S-H or N-A-S-H type gels, normally have higher space filling capacities than calcium-silicate-hydrate (C-S-H) gels formed in OPC [45,46]. Additionally, the high reactivity of the fine-ground slag may also contribute to the dense microstructure [6].

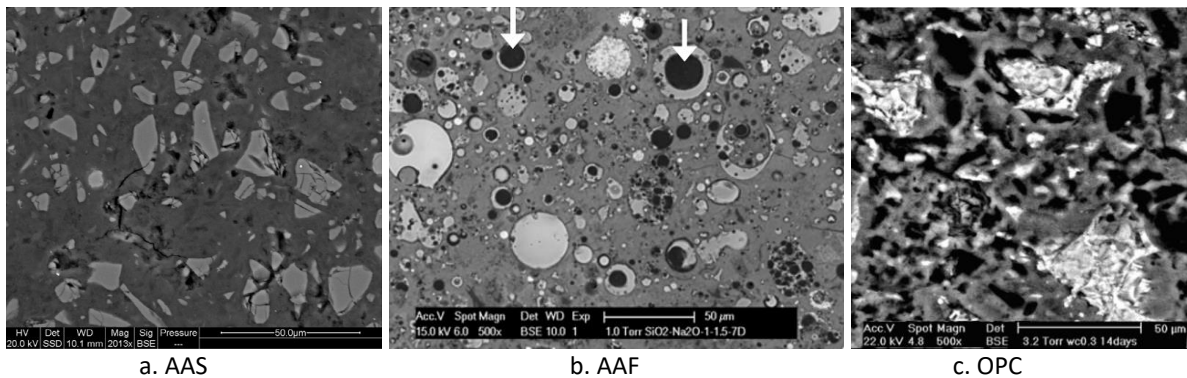


Figure 2.2 (a) BSE images of AAS ($\text{SiO}_2/\text{Na}_2\text{O} = 1.2$, cured at 20°C for 7 days) [47], (b) AAF ($\text{SiO}_2/\text{Na}_2\text{O} = 0.67$, cured at 40°C for 7 days) [9], and (c) OPC (water/cement = 0.3, cured at 20°C for 14 days) [48]. The arrows in (b) indicate the cavities in fly ash.

2.3 Autogenous shrinkage of AAMs

The phenomenon of autogenous shrinkage is known for OPC-based systems from the beginning of the 20th century [49,50], but its practical significance has been recognized only in recent decades when the high-performance concrete became widely utilized [51–53]. For traditional concrete, autogenous shrinkage is not a big problem if compared to i.e. drying shrinkage [54]. However, in high-performance concrete, the low water/cement ratio and the addition of silica fume normally cause a serious self-desiccation, and consequently a high autogenous shrinkage [55]. In AAMs, the autogenous shrinkage can be higher and is less well understood, which substantially hinders the commercialization of these materials [8,20]. Depending on the raw materials used as precursors, AAMs can show different autogenous shrinkage behaviour.

2.3.1 Autogenous shrinkage of AAS

2.3.1.1 Shrinkage magnitude

A considerable amount of literature has been published on autogenous shrinkage of AAS. It was found that autogenous shrinkage of AAS systems is pronounced even at relatively high water/binder ratios (0.4-0.5) [56,57]. For example, Cartwright et al. [57] reported that the autogenous shrinkage of AAS mortar can be 5 times as high as that of OPC mortar with a water/cement ratio of 0.4 (Figure 2.3). Similar results were obtained for AAS mortar by

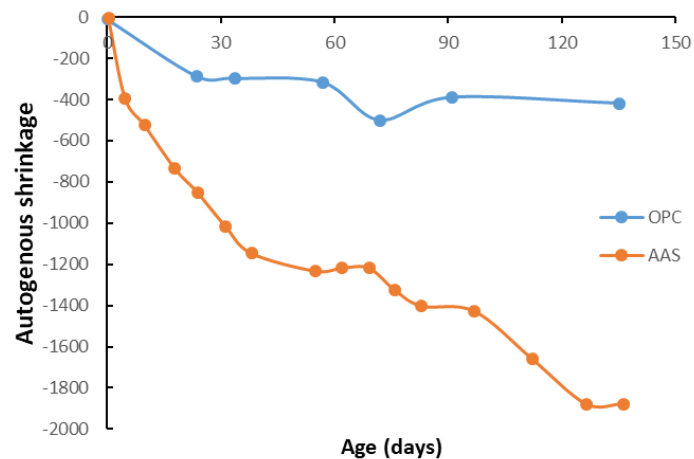


Figure 2.3 Autogenous shrinkage strains of AAS mortar with $\text{SiO}_2/\text{Na}_2\text{O}$ of 1.22 and OPC mortar with water/cement of 0.4, after [57].

Kumarappa et al. [58] and Uppalapati et al. [59]. For AAS paste, a much higher value of autogenous shrinkage, 7000 $\mu\text{m}/\text{m}$, at the age of 2 days was reported by Fang et al. [60].

Both the activator composition and the liquid/binder ratio affect the autogenous shrinkage of AAS. A number of studies have reported that the autogenous shrinkage of AAS increases with increasing Na_2O and SiO_2 content in the activator and with decreasing liquid/binder ratio [19,20,61–63]. The study by Taghvayi et al. [64] showed that increasing the alkali concentration and the silicate modulus of activator resulted in a high short-term shrinkage rate, but the silicate modulus had a more significant effect on the final amount of shrinkage, as compared to the alkali concentration. A different result was obtained by Hu et al. [27], who showed that the autogenous shrinkage of AAS mortars increased with activator modulus from 0 to 0.5, then decreased as the modulus increased from 0.5 to 1.5. The reason for the discrepancy between results from Hu et al. [27] and other studies is not known yet.

2.3.1.2 Shrinkage mechanism

Many of the researchers agreed that the mechanism responsible for autogenous shrinkage of AAS is capillary tension resulting from the chemical shrinkage of the paste [21,58,65], which is considered as one principal mechanism of autogenous shrinkage of OPC as well [18,52].

2.3.1.2.1 Mechanism of autogenous shrinkage of OPC

Chemical shrinkage is defined as the absolute volume reduction associated with the reactions forming a binder material [18]. The hydration of Portland cement is accompanied by chemical shrinkage, since the total volume of hydration products is smaller than the volume of reactants (cement and water) [50]. When the system is not set, the chemical shrinkage is converted into external shrinkage by the collapse of the paste. When the hydrates percolate to form a skeleton and the stiffness increases, gas-filled voids start to form and grow in the paste due to the ongoing chemical shrinkage (Figure 2.4). As the capillary pores are gradually emptied, the radius of the menisci decreases, which is known as self-desiccation. The curvature of the menisci results in capillary tension, which can lead to autogenous shrinkage. Wittmann et al. pointed to the relevance of “disjoining pressure” to explain the autogenous shrinkage of

cement during self-desiccation [66,67]. Despite the debate on which one is the “real” driving force of the autogenous shrinkage of OPC, some researchers believed that disjoining pressure and capillary tension must be somehow related [68] or even correlated to each other during the self-desiccation process [69,70]. In fact, the formulae for quantifying the volume changes due to disjoining pressure and capillary tension have a similar shape according to Van Breugel [71]. Therefore, the autogenous shrinkage might be described by the change in either capillary tension or disjoining pressure, both of which are closely related to the self-desiccation.

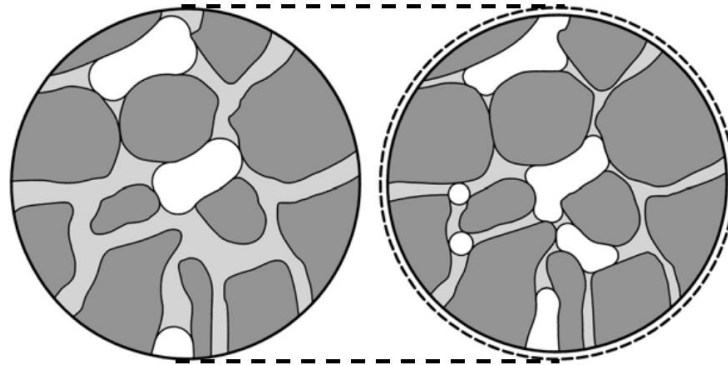


Figure 2.4 Schematic representation of a cross-section of hydrating cement paste [18]. Left: low degree of hydration. Right: high degree of hydration. Solid matter (hydrates and anhydrous cement) is shown in dark grey, pore water is light grey and empty pore volume is white.

The drop of internal relative humidity (RH) is commonly used as an indicator of the self-desiccation. Internal RH is associated with two factors, the curvature of the menisci and the ions in the pore solution, as shown in Equation 2.1.

$$RH_K = RH/RH_S \quad (2.1)$$

where RH is the internal RH of the paste, RH_S is the RH of the pore solution caused by dissolved salts and RH_K is due to the curvature of menisci at the gas-liquid interfaces.

The radius of menisci can be calculated according to the Kelvin equation (Equation 2.2). When the Kelvin radius is known, the tensile stress in the pore fluid can be calculated with the Laplace equation (Equation 2.3).

$$r = \frac{2\gamma V_w}{\ln(RH_K)RT} \quad (2.2)$$

$$\sigma = -\frac{2\gamma}{r} \quad (2.3)$$

where σ is the tensile stress in the pore fluid; r (m) is the radius of the menisci; γ (N/m) is the surface tension of the pore solution; V_w is the molar volume of the pore solution (m^3/mol); R ($\text{J}/(\text{mol}\cdot\text{K})$) is the universal gas constant; T is the temperature expressed in the absolute scale.

According to Bentz et al. [72], the linear autogenous shrinkage of a paste under the capillary pressure can be calculated by Equation 2.4.

$$\varepsilon_{lin} = \frac{S\sigma}{3} \left(\frac{1}{K} - \frac{1}{K_S} \right) \quad (2.4)$$

where S is the saturation degree of the paste, a ratio of liquid to the total pore volume (-); σ is the pore pressure (MPa); K is the bulk modulus of the whole porous body (GPa) and K_S is the bulk modulus of the solid material (GPa). Strictly speaking, this equation can only give the linear elastic deformation [73].

The abovementioned equations were extensively utilized for the simulation of autogenous shrinkage of cement systems [73], although cement is not a purely elastic solid. Taking the non-elastic behaviour, or creep, of the cement paste into account was reported to give a better estimation of the autogenous shrinkage [74].

2.3.1.2.2 Mechanism of autogenous shrinkage of AAS

Considering the similarity between the gel structures of C-A-S-H and C-S-H [75], many researchers hypothesized that the aforementioned mechanism also works for AAS systems [21,58,65]. Based on this, the autogenous shrinkage of AAS has been explained with regard to the influences of factors like pore structure, surface tension, saturation degree, elastic modulus, etc.

For example, Collins and Sanjayan [65] attributed the high autogenous shrinkage of AAS to the dense pore structure of the paste (Figure 2.5). Their results showed that up to 80% of the pores in AAS paste activated by Na_2SiO_3 were mesopores (1.25–25 nm), while OPC paste contained only 36.4% of mesopores and a larger percentage of macropores (25–5,000 nm). Given the fine pore structure of AAS, a certain chemical shrinkage would result in a small radius of menisci in the paste [76], which means high capillary pressure (see Equation 2.3). The large fraction of mesopore volume in AAS was further confirmed by Lee et al. [19]. Besides the radius of the menisci, the surface tension of the pore solution in AAS was also reported to be higher than that in OPC (Ballekere Kumarappa et al. [58]). The large quantity of ions induced a high surface tension of the pore solution in AAS and consequently resulted in a large capillary pressure (see Equation 2.3).

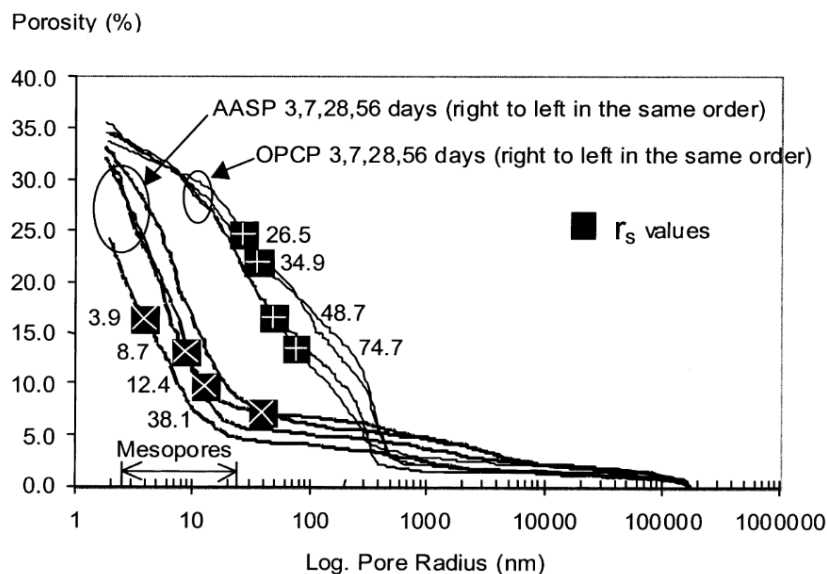


Figure 2.5 Cumulative pore size distribution of AAS paste (AASP) and OPC paste (OPCP) at 3, 7, 28, and 56 days [65].

In addition to the factors influencing the capillary pressure, a higher degree of saturation and a lower stiffness of the paste also contribute to a higher autogenous shrinkage (see Equation 2.4). Cartwright et al. [57] reported that AAS had a higher saturation degree and lower elastic modulus than OPC, and thus showed a higher autogenous shrinkage. Ye and Radlińska [21] proposed another origin of the large shrinkage of AAS from the gel structure point of view. Due to the incorporation of alkali cations, the C-A-S-H gel was found to collapse and redistribute more easily than the C-S-H gel under a certain load, which leads to a pronounced visco-elastic/visco-plastic behaviour of AAS at the macroscopic scale.

While the studies mentioned above provided different insights into the shrinkage mechanism of AAS, their common assumption is that the driving force of the autogenous shrinkage of AAS is capillary pressure, like the assumption for OPC. However, different opinions were held by other researchers. For example, Ma and Dehn [56] stated that self-desiccation seems not to be the exclusive reason why autogenous shrinkage of the AAS concrete is doubled compared to the high-strength OPC concrete, although they did not propose alternative mechanisms. Uppalapati [77] reported that apart from the self-desiccation, the autogenous shrinkage of AAS might also relate to the silica polymerization reaction during the formation of C-A-S-H gels. However, according to the reference [78–80], the polymerization degree of Si in C-A-S-H is mostly in the form of Q^2 , which is similar to that of Si in C-S-H¹. Therefore, the hypothesis based on silica polymerization seems unable to explain the much higher autogenous shrinkage of AAS than OPC. Further research is needed to figure out whether the capillary pressure resulting from self-desiccation is the only driving force of the autogenous shrinkage of AAS.

2.3.2 Autogenous shrinkage of AAF

The autogenous shrinkage of AAF has not received as much attention as that of AAS, which may be due to the smaller shrinkage value and much lower cracking proneness of this material. According to Mobili et al. [81] and Ma and Ye [24], the autogenous shrinkage of AAF is similar to or smaller than that of OPC. For 1000 g fly ash activated by 1.0 mol SiO₂ and 1.0 mol Na₂O, the autogenous shrinkage reached 1400 μm/m at 28 days, as shown in Figure 2.6 [24]. Increasing the contents of both Na₂O and SiO₂ was reported to result in a higher autogenous shrinkage [24]. For all the studied mixtures, most (nearly 90%) of the autogenous shrinkage happened in the first two days [24]. These results are in line with that obtained by Kheradmand et al. [82]. Increasing the curing temperature led to a reduced autogenous shrinkage of AAF according to Kani and Allahverdi [83]. The lower autogenous shrinkage of AAF in comparison to OPC and AAS is perhaps due to the less dramatic self-desiccation that occurred in AAF [24].

¹ Q^n denotes the connectivity of the silicate units based on the chemical shift, where n represents the number of Si–O linkages of the unit.

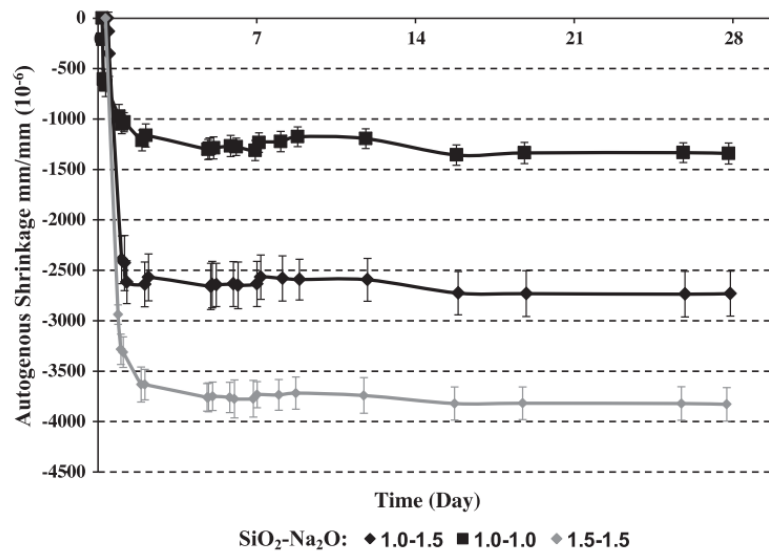


Figure 2.6 Autogenous shrinkage of AAF pastes with different SiO_2 and Na_2O contents, cured at 40°C [24].

2.3.3 Autogenous shrinkage of AASF

2.3.3.1 Shrinkage magnitude

The activation of slag and fly ash blends does not require elevated-temperature curing, which is normally necessary for AAF, and meanwhile leads to a smaller autogenous shrinkage than AAS [84]. In AASF systems, researchers have found that the lower slag/fly ash ratio led to a lower magnitude of autogenous shrinkage for any given activating solution (see Figure 2.7) [19,59,85,86]. Hu [87] found that using NaOH as activator generated much lower autogenous shrinkage than using Na_2SiO_3 as activator. This was coherent with the trends identified by Lee et al. [19]. When the $\text{SiO}_2/\text{Na}_2\text{O}$ ratio of the activator was kept constant, increasing the amount of activator led to higher autogenous shrinkage of AASF mortar [87].

Another factor influencing the autogenous shrinkage of AASF binders was the liquid/binder ratio, but on this issue, previous research findings have been contradictory. Hu [87] showed that a higher liquid/binder ratio induced a higher autogenous shrinkage for AASF mortar regardless of slag/fly ash ratio and $\text{SiO}_2/\text{Na}_2\text{O}$ ratio. By contrast, Lee et al. [19] observed a lower autogenous shrinkage of AASF mortar when the liquid/binder ratio increased.

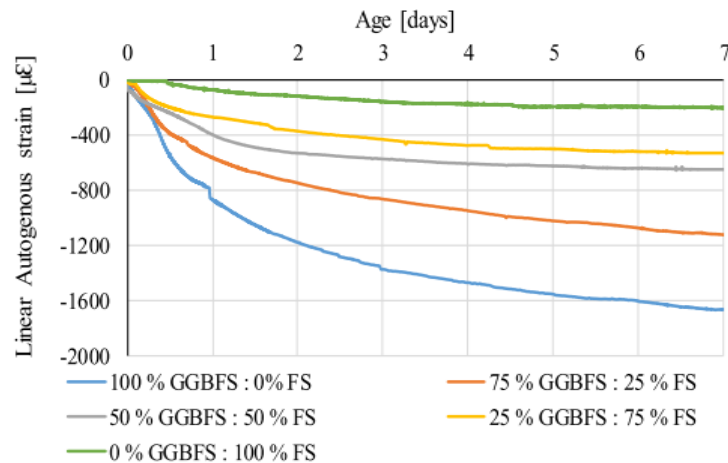


Figure 2.7 Autogenous shrinkage of AASF pastes with different slag (GGBFS) and fly ash (FS) ratios [59].

2.3.3.2 Shrinkage mechanism

In AASF systems, the reactions of alkaline with both fly ash and slag can cause autogenous shrinkage, but the reaction between alkaline and slag seems to induce higher shrinkage than that between alkaline and fly ash, mainly due to the much lower reactivity of fly ash than slag at ambient temperature [19,88,89]. Fang et al. [25] explored the autogenous shrinkage mechanism of AASF and concluded that the autogenous shrinkage in the hardening stage (from final setting time to 24 h) may not be fully attributed to the self-desiccation process resulting from the activation of slag. The reaction between fly ash and alkaline may produce N-A-S-H gels and Fang et al. [25] hypothesized, based on the mechanism proposed by Ma and Ye [24], that the reorganization and rearrangement also contribute to the autogenous shrinkage of AASF. In contrast, Aydin [90] reported that the 3D structured N-A-S-H gels produced by the activation of fly ash were stable and, therefore, reduced the autogenous shrinkage of AASF. Regarding the unreacted fly ash spheres, researchers agreed that the spheres can act as micro-aggregates, which can restrain the shrinkage of the paste [88,91].

Besides, Fang et al. [25] showed that the volume contraction by chemical shrinkage in fresh state accounts for approximately 70% of the total autogenous shrinkage in the first 24 hours. However, this finding seems contrary to the results of Lee et al. [19], who claimed that the autogenous shrinkage of AASF mortar occurs mainly due to self-desiccation in the hardened state rather than the volume contraction by chemical shrinkage in the fresh state.

Overall, the results from literature showed that AASF binders have smaller autogenous shrinkage than AAS owing to the incorporation of fly ash. However, the mechanism of autogenous shrinkage of AASF, especially with regard to the role of fly ash, is still under debate. Insufficient results are available yet to verify the hypotheses proposed by the researchers about the driving forces of autogenous shrinkage.

2.4 Strategies to mitigate the autogenous shrinkage

A considerable amount of literature has been published on strategies to mitigate the autogenous shrinkage of AAS and AASF. For fly ash-based binders, no published studies were found on this issue, which may be due to the low autogenous shrinkage shown by AAF systems [24,92,93].

Currently, there are mainly five types of strategies that have been investigated by researchers to mitigate the autogenous shrinkage of AAS or AASF, which are: adding shrinkage reducing admixtures (SRA) or other chemical admixtures, adding expansive additives, adding nanoparticles, internal curing and elevated temperature curing. It should be noted that, since AASF shows smaller autogenous shrinkage than AAS, adding fly ash can also be treated as a shrinkage mitigating strategy for AAS, but in this thesis, AASF is considered as a research object parallel to AAS, so the incorporation of fly ash will not be discussed as a strategy here.

2.4.1 SRA and other chemical admixtures

SRA is a type of chemical admixture based on neopentyl glycol $((\text{CH}_2)_2\text{-C}(\text{CH}_2\text{OH})_2)$ or other similar products [94], mostly used to reduce the shrinkage of cement-based systems [95]. The effects of SRA on shrinkage reduction originate from lowering the surface tension of the pore solution, which can decrease the capillary tension caused by self-desiccation (see Equation 2.3) [27].

Hu et al. [27] reported that the oxyalkylene alcohol-based SRA could significantly reduce the autogenous shrinkage of AAS with different modulus of the activator, as a result of a decrease in the capillary tension (Figure 2.8). SRA made from polyethylene glycol with high molecular weights show similar effects [96]. Polypropylene glycol was also found effective in mitigating the autogenous shrinkage of AAS without decreasing the strength [97,98]. However, some SRAs show side effects (e.g. strength loss) when applied in AAMs [99–101]. For example, Bílek et al. [102] studied the effects of hexylene glycol-based SRA on the shrinkage of AAS mortar and found a decrease in compressive strength. Collins and Sanjanyan [103] applied an SRA into AAS concrete to reduce the magnitude of drying shrinkage, but the cracking time of the concrete was not delayed due to the simultaneously decrease of the tensile strength.

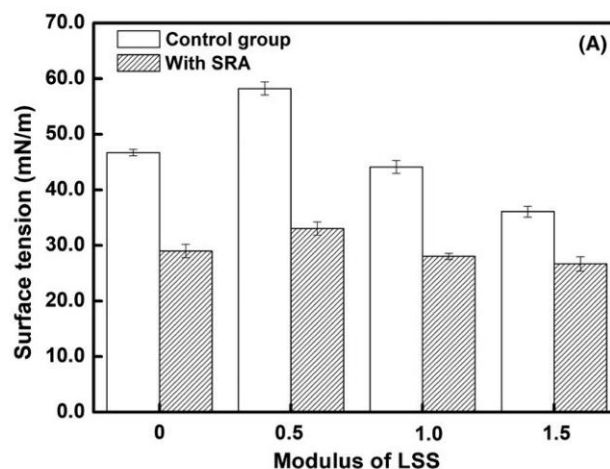


Figure 2.8 Surface tension of pore solution of AAS mortars activated by liquid sodium silicate (LSS) with different modulus [27].

Besides SRA, Bakharev et al. [104] found that an air-entraining agent with a soluble salt of an alkyl aryl sulphonate was effective in mitigating the autogenous shrinkage. Although the early age strength was reduced slightly by this admixture, the strength at 28 days was similar to that of the mixture without admixture.

Some superplasticizers that are commonly used in OPC systems were applied in AAMs [26,104,105]. However, these superplasticizers either lost their function in strong alkali media or increased the autogenous shrinkage of AAS systems. For example, Palacios and Puertas [26] studied the influence of 4 types of superplasticizers (polycarboxylates, vinyl copolymers, melamine and naphthalene-based) on the properties of AAS and found that all admixtures, except naphthalene-based product, lost their fluidifying properties in the alkaline media as a result of the changes in their chemical structures. Naphthalene-based superplasticizer was reported to increase the autogenous shrinkage of AAS concrete [104], although it can retain its chemical structure in a strong alkali environment. Hence, trial tests on the effect on autogenous shrinkage are needed when applying SRA or other chemical admixtures in AAMs.

2.4.2 Expansive additive

Hu et al. [27] added expansive MgO into AAS mortars and found that the effect was not so significant as found for the OPC systems. The reason was that AAS had a denser structure and MgO in AAS had less access to water to form $Mg(OH)_2$. Instead, it forms M-S-H or hydrotalcite-like phases and the molar volume increase was much less. In contrast, the results of Li et al. [105] showed that MgO can reduce the shrinkage of AASF and meanwhile the early age strength was improved. Their results were confirmed by Yang et al. [106], who found that the addition of reactive MgO can mitigate both the autogenous shrinkage and the drying shrinkage of AASF. Shen et al. [88] reported that the addition of 10% light-burned dolomite (containing >85% reactive MgO) reduced the shrinkage of AASF by nearly 50%. After reduction the shrinkage was only slightly higher than that of OPC.

Gypsum is another kind of expansive additive. It was found that the incorporation of gypsum coarsened the pore structure of AAS and triggered the formation of expansive sulphate-rich phases (e.g ettringite) [28]. The shrinkage was, therefore, partially compensated, as consistent with the results obtained by Bakharev [20]. However, the early-age expansion was insufficient to offset the subsequent long-term shrinkage, as reported by Ye and Radlińska [28].

The addition of CaO-type expansive additive in AAS was not effective in shrinkage compensation [28]. The reasons given by the authors were the refined pore structure and unreduced chemical shrinkage. In addition, CaO can release Ca^{2+} rapidly after contacting the activator and accelerate the setting of AAS, which is already fast [107]. Therefore, CaO was not recommended to be used for shrinkage mitigation in AAS [107]. In contrast, according to Zhu et al. [108] adding $Ca(OH)_2$ can successfully reduce the autogenous shrinkage of AAS concrete regardless of the water/binder (w/b) ratio (Figure 2.9). The mechanism was to promote the formation of expansive crystals like C_2ASH_8 and C_4AH_{13} , coarsen the meso-pores and meanwhile increase the elastic modulus [108].

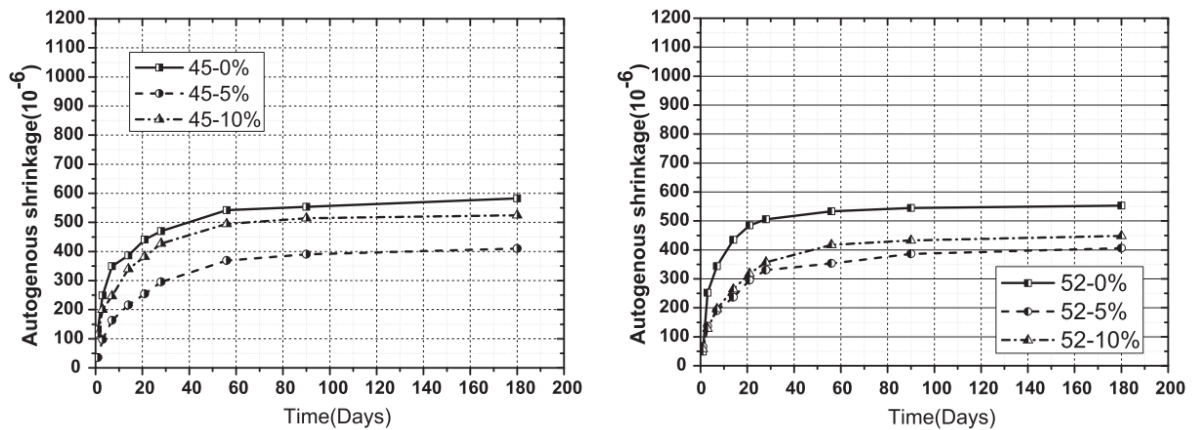


Figure 2.9 Autogenous shrinkage of AAS concrete (left: w/b=0.45, right: w/b=0.52) with different dosages (0%, 5% and 10%) of Ca(OH)_2 [108].

2.4.3 Nano-particles

Liu et al. [109] added nano C-A-S-H gel particles into AAS mortar and found that the autogenous shrinkage can be reduced by more than 20%, as shown in Figure 2.10. The reduction of autogenous shrinkage was explained by the reduced overall porosity and the increased proportion of meso-pores in the AAS mortar [109]. This explanation was opposite to the finding of Yang et al. [110], who attributed the reduced autogenous shrinkage of AAS paste with nano- TiO_2 to the reduced overall porosity and a smaller volume proportion of meso-pores.

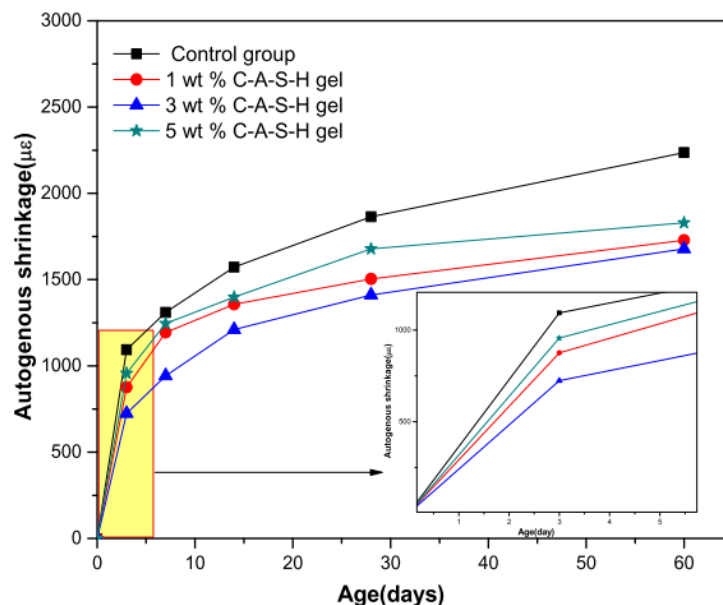


Figure 2.10 Autogenous shrinkage of AAS mortars with different amounts of nano C-A-S-H gel [109].

In fact, the volume fraction of meso-pores is never the single factor that influences the capillary pressure and the autogenous shrinkage. The diameter of menisci is determined not only by the pore size distribution, but also by the volume that is emptied due to chemical shrinkage, i.e. the degree of saturation [76]. A larger saturation degree and a coarser pore structure would lead to larger menisci (see Figure 2.4) and consequently a smaller capillary pressure. Furthermore, the pore size distribution also influences the elastic modulus of the paste, which acts as resistance to the shrinkage. Therefore, more factors such as chemical shrinkage, pore size distribution, degree of saturation, elastic modulus, etc. need to be considered in order to clearly interpret the mitigating mechanism of autogenous shrinkage.

2.4.4 Internal curing

Internal curing is normally realized by adding superabsorbent polymers (SAPs) or lightweight aggregates (LWA) (e.g., pumice or expanded clay) into a binder or concrete [111–115]. SAPs or LWA can act as liquid reservoirs for the system and extra liquid will be provided during hydration to compensate for the liquid consumption [112]. By internal curing, the capillary pressure induced by self-desiccation will be mitigated.

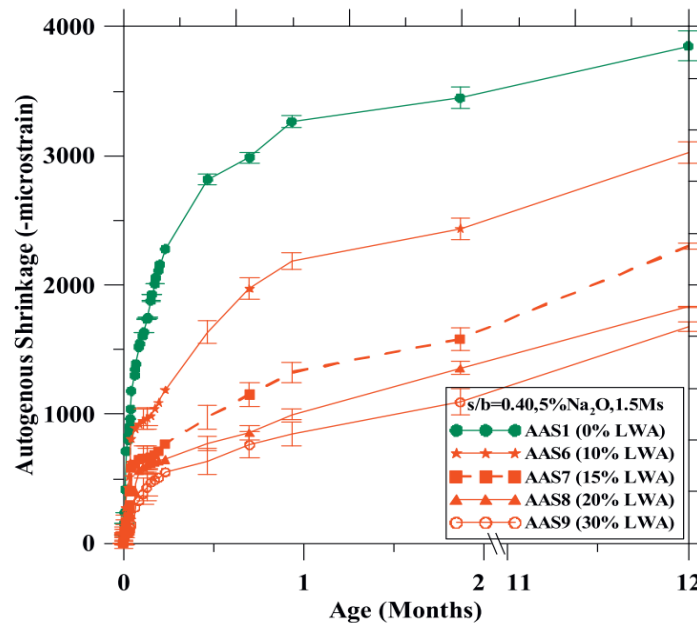


Figure 2.11 Autogenous shrinkage of AAS mortars with different LWA contents, weight % substitution to normal weight aggregate [58].

Sakulich and Bentz [116] utilized LWA to provide internal curing for AAS mortar and obtained a greatly reduced autogenous shrinkage, regardless of the liquid used for internal curing, i.e., water or alkali solution. Kumarappa et al. [58] varied the content of LWA in AAS mortar and observed an autogenous shrinkage reduction up to 50% when 30% of the aggregates were replaced by LWA (Figure 2.11). However, a reduced compressive strength was observed for all the LWA-containing mixtures studied in [116] and [58].

Lee et al. [117] investigated the feasibility of using recycled concrete as internal curing aggregates for AAS concrete and found that the autogenous shrinkage of AAS concrete can be

reduced by more than 30%. Along with the reduced autogenous shrinkage, the degree of hydration was decreased due to the dilution effect on the alkali activator, which was caused by the additional water supplied from the recycled aggregates [117].

Oh and Choi [118] and Song et al. [119] found that using SAPs as internal curing agents also led to lower autogenous shrinkage of AAS mortar. For AASF systems, internal curing was also effective in reducing the autogenous shrinkage according to Tu et al. [120]. However, the compressive strength of the samples studied in [118–120] was reduced in all cases due to internal curing.

These studies indicate that internal curing has a promising potential for mitigating the autogenous shrinkage of AAS and AASF, although the strength can be compromised.

2.4.5 Elevated-temperature curing

Ye and Radlińska [28] and Bakharev et al. [121] reported that elevated temperature curing at 60 °C – 80 °C was helpful to reduce the drying shrinkage of AAS. The reduction was because the visco-elastic/visco-plastic compliance of C-A-S-H gels was reduced at elevated temperatures. This indicates that elevated temperature curing may also be effective in mitigating the autogenous shrinkage of AAS, since the autogenous shrinkage is also critically influenced by the deformability of the gels [21]. However, this strategy may be unsuitable for cast-in-situ concrete due to the high requirement for the curing condition. Besides, the elevated temperature curing would accelerate the reaction [122] and cause a faster setting of AAS and AASF. Hence, applying elevated-temperature curing seems not to be a recommendable strategy for reducing the autogenous shrinkage of slag-based AAMs.

2.5 Problem definition

AAMs have reaction processes different from the hydration of cement. The microstructures of AAMs and OPC are also substantially different. While the autogenous shrinkage of AAFA seems not problematic, AAS and AASF usually show much higher autogenous shrinkage than OPC systems. The influencing factors of autogenous shrinkage of AAMs have been studied by many researchers. Various strategies have been explored to mitigate the autogenous shrinkage of AAS and AASF. Despite the preliminary results obtained in the literature, guidelines or standards for design of AAMs concerning the autogenous shrinkage are not available. In the field of autogenous shrinkage of AAMs, three main knowledge gaps exist:

1. The mechanisms of autogenous shrinkage of AAS and AASF are not clear. Although capillary pressure resulting from the self-desiccation is highly possible to be one of the driving forces of autogenous shrinkage, it has not been clarified whether there are other driving forces taking effect and how much these driving forces contribute individually. The role of fly ash in influencing the autogenous shrinkage of AASF has not been well understood.
2. Effective strategies to mitigate the autogenous shrinkage of AAS and AASF are still lacking. Due to the differences in microstructure and chemical environment between AAMs and OPC, the shrinkage-mitigating admixtures like SRA, expansive additive and nano-additive that are widely adopted in OPC may be ineffective or cause side effects

(e.g. strength loss) in AAMs. Admixtures that can effectively mitigate the autogenous shrinkage without compromising other properties of AAS and AASF need to be identified. Internal curing is most likely a promising shrinkage-mitigating strategy, but further research is needed to figure out the mitigating mechanism and investigate the influences of internal curing on the cracking tendency of restrained AAS and AASF systems.

3. The cracking tendency induced by the autogenous shrinkage of AAS and AASF concrete has not been reported yet. The cracking tendency of building materials under restrained condition is a more crucial criterion for the serviceability evaluation of these materials than the magnitude of free autogenous shrinkage. The cracking tendency is determined not only by autogenous shrinkage, but also by elastic modulus, creep/relaxation and tensile strength [103]. However, very few data are available in the literature about the cracking tendency of AAS and AASF systems.

2.6 Conclusions

Based on the presented state of the art on autogenous shrinkage of AAMs, the following conclusions can be drawn:

- The autogenous shrinkage of AAMs is substantially influenced by the composition of the precursor. AAF systems show lower autogenous shrinkage and lower cracking tendency under restrained condition than OPC systems. In contrast, AAS and AASF systems show much higher autogenous shrinkage than OPC systems, especially when the slag content is high. Critical attention needs to be paid to the autogenous shrinkage of AAS and AASF systems before these materials can be standardized and widely utilized in construction.
- The autogenous shrinkage of AAS and AASF increases with the increase of Na_2O and SiO_2 contents in the activator. Regarding the influence of liquid/binder ratio, no consensus has yet been reached in literature. The driving force of autogenous shrinkage of AAS and AASF has not been well understood. Nonetheless, it is likely that the capillary pressure resulting from self-desiccation is one of the main driving forces. Further research is required to clarify the autogenous shrinkage mechanism of AAS and AASF systems. The role of fly ash in AASF system needs to be specially focused on.
- Cracking tendency of restrained alkali-activated concrete is an important parameter for evaluating the suitability of these materials in structural applications. However, very few studies have been published on the autogenous shrinkage-induced cracking of AAS and AASF systems.
- Various strategies have been explored to mitigate the autogenous shrinkage of AAS and AASF systems. Most SRAs are proven effective in shrinkage mitigation, but many of them caused a strength reduction of the matrix. Superplasticizers either lose their function in the strong alkali media or increase the autogenous shrinkage of alkali-activated concrete. Expansive additives like MgO , CaO and gypsum are not as effective as they are in OPC systems. Internal curing seems a promising autogenous shrinkage-mitigating strategy, but the mitigating mechanism needs to be better understood. In

addition, internal curing usually causes a decrease in strength. Therefore, new strategies that can effectively mitigate the autogenous shrinkage of AAS and AASF without compromising their mechanical properties need to be developed.

Chapter 3

Mechanisms of autogenous shrinkage of AAMs

3.1 Introduction

Previous studies have shown that AAMs can show high autogenous shrinkage [84,87,88,91,123,124]. However, the mechanisms behind the high autogenous shrinkage are still unknown. For OPC systems, three principal mechanisms have been proposed, including the capillary pressure theory [18,52], disjoining pressure theory [22,66], and surface tension theory [23,125,126]. For AAMs, in contrast, no convincing hypothesis has been proposed yet to completely explain the autogenous shrinkage of AAMs, as discussed in Chapter 2. A better understanding of the shrinkage mechanisms is a prerequisite for the prediction of the cracking proneness of AAMs under restrained condition and the development of shrinkage mitigating strategies.

In this chapter, the autogenous shrinkage of AAS and AASF pastes is experimentally measured. Various techniques are applied to characterize the microstructure formation of AAS and AASF pastes with regard to the reaction products, reaction kinetics and pore structures. The parameters that influence the autogenous shrinkage of AAMs, e.g., chemical shrinkage, internal relative humidity (RH) and elastic modulus evolution of the pastes, are comprehensively investigated. The driving force of the autogenous shrinkage of AAMs and the deformability of the pastes are then clarified. Based on the experimental results, the autogenous shrinkage of AAMs is modelled considering both elastic and time-dependent/creep deformations. The comparison between the calculated and the measured results can in return indicate the validity of the mechanism identified in this chapter.

The results obtained in this chapter will act as the basis for the development of shrinkage mitigating strategies for AAMs in chapters 4 and 5, and the analysis of the cracking tendency of AAMs concrete under restraint condition in Chapter 6.

3.2 Materials and experiments

3.2.1 Raw materials and mixture proportions

The main raw materials used in this study were blast furnace slag (indicated as slag hereafter) supplied by Ecocem Benelux BV and fly ash from Vliegassunie BV. The chemical compositions of slag and fly ash were determined by X-ray fluorescence (XRF) and shown in Table 3.1. The

Parts of this chapter have been published in:

Zhenming Li, Tianshi Lu, Xuhui Liang, Hua Dong, Guang Ye. Mechanisms of autogenous shrinkage of alkali-activated slag and fly ash pastes. *Cement and Concrete Research*. 135 (2020). 106107.

fly ash complies with Class F (EN 450, ASTM C618) since it has low CaO content (< 10% reactive CaO) and a “SiO₂ + Al₂O₃ + Fe₂O₃” content higher than 70%.

Table 3.1 Chemical compositions of slag, fly ash, and cement.

Raw materials	Oxide (wt. %)									
	SiO ₂	Al ₂ O ₃	CaO	MgO	Fe ₂ O ₃	SO ₃	K ₂ O	TiO ₂	Other	L.O.I
Slag	31.77	13.25	40.50	9.27	0.52	1.49	0.34	0.97	0.21	1.31
Fly ash	56.8	23.8	4.8	1.5	7.2	0.3	1.6	1.2	1.6	1.2

L.O.I= Loss on ignition

The particle size of slag, as determined by laser diffraction analyzer, ranges from 0.1 to 50 μm, with a d₅₀ of 18.3 μm. The particle size of fly ash is between 0.14 and 138 μm, with a d₅₀ of 48.1 μm.

The mineralogical composition of slag and fly ash was studied with X-ray diffraction (XRD). XRD patterns were acquired using a Philips PW 1830 powder X-ray diffractometer, with Cu Kα (1.5406 Å) radiation, tube setting of 40 kV and 40 mA, a step size of 0.030° and a 2θ range of 5–70°. The XRD pattern of slag and fly ash presents a hump around 30.5° and 24° (marked by the dashed lines), respectively, indicating the presence of amorphous phases. While the slag is mainly amorphous, several crystalline phases are detected in fly ash, such as mullite ((Al₂O₃)_{1.136}(SiO₂)_{0.728}), quartz (SiO₂) and hematite (Fe₂O₃).

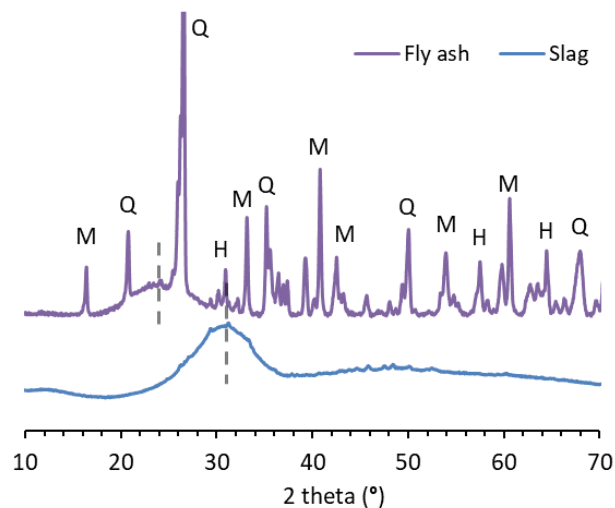


Figure 3.1 XRD patterns of slag and fly ash. M, Q and H stand for mullite, quartz and hematite, respectively.

The alkaline activator was prepared by mixing anhydrous pellets of sodium hydroxide with deionized water and commercial sodium silicate solution (27.5 wt. % SiO₂ and 8.25 wt. % Na₂O). The solution was allowed to cool down for 24 h to room temperature before mixing with the precursors. The mix design of the pastes is shown in Table 3.2. The liquid/binder (l/b) ratio of the alkali-activated paste is 0.5, while the water/solid (w/s) ratio of the paste is 0.344 if the

SiO₂ and Na₂O in the activator are considered parts of solid. The water/cement ratio of the cement paste is 0.4.

A Hobart mixer was used to make AAS and AASF pastes. After the premixing of the raw materials for 1 min, the activator was added at low-speed mixing. The mixing continued at low speed for 1 min and another 2 min at high speed. All the samples were cured in sealed condition at 20° C.

Table 3.2 Mixture proportions of the pastes.

Mixture	Slag (g)	Fly ash (g)	Cement (g)	SiO ₂ (mol)	Na ₂ O (mol)	H ₂ O (g)
AAS	1000	-	-	1.146	0.76	384
AASF	500	500	-	1.146	0.76	384

3.2.2 Experimental methods

3.2.2.1 Setting time

The times of initial and final setting were measured by an automatic Vicat setup with a measurement interval of 5 minutes [127].

3.2.2.2 Autogenous shrinkage

The autogenous shrinkage of the paste was measured using the corrugated tube method [128]. Compared to other methods (e.g. the methods used in [20] and [25]), the corrugated tubes method allows the earliest starting point of the measurement (20-30 min after casting). Three corrugated tubes of 425 mm (Ø28.5 mm) were used for each mixture. After mixing, the fresh paste was cast into the corrugated tubes and sealed by plugs. The specimens and the tubes were stored in a climate chamber, the temperature of which was controlled at 20°C. The autogenous shrinkage of specimens was measured by linear variable differential transformers (LVDTs) with an accuracy within ±1 µm. The deformation was recorded every 5 min from the final setting time measured by Vicat method to 7 days. The automatic measurements show a low scatter for triplicate samples, with the relative standard error in the range of 1–2% after the final set of the materials.

3.2.2.3 Shrinkage under saturated condition

To investigate the role of self-desiccation in autogenous shrinkage of AAMs, the deformation of the pastes under saturated condition was measured by a modified corrugated tube method [129,130]. Puertas et al. [89] and Feng et al. [131] measured the deformation of the samples under a RH close to 100%. However, in their methods, the deformation of the paste/mortar can only be measured after the demoulding at 24 hours. In this study, the paste was cast into a corrugated tube but only to fill 80% volume of the tube. After that, the top end plug was mounted and the tube was vibrated horizontally. The upper part (20% volume) of the tube was then occupied by air. The length change of the tube was measured following the same procedure as the autogenous shrinkage measurement. After the final setting of the mixture,

three tiny holes were pricked on top of the tube by a needle along the length direction. Drops of activator were then gently added into the tubes through these holes by a syringe until the upper surface of the sample was submerged in liquid (as shown in Figure 3.2). Special attention was paid when adding the liquid such that the measurement was not disturbed. According to Tian and Jensen [129], filling only 80% of the tube does not influence the deformation results after the final setting of the paste relative to the case that the tube is fully filled up. With the method proposed in this study, the deformation can be measured without changing the geometry of the specimen or delaying the starting time of the experiment. An error involved in this method is that the actual reaction degree of the samples could be a bit different from that of the samples under sealed condition, due to externally supplied activator. However, this error is evitable as long as there is exchange of substances between the sample and the environment (e.g. supply of moisture to the sample to keep a high enough RH).

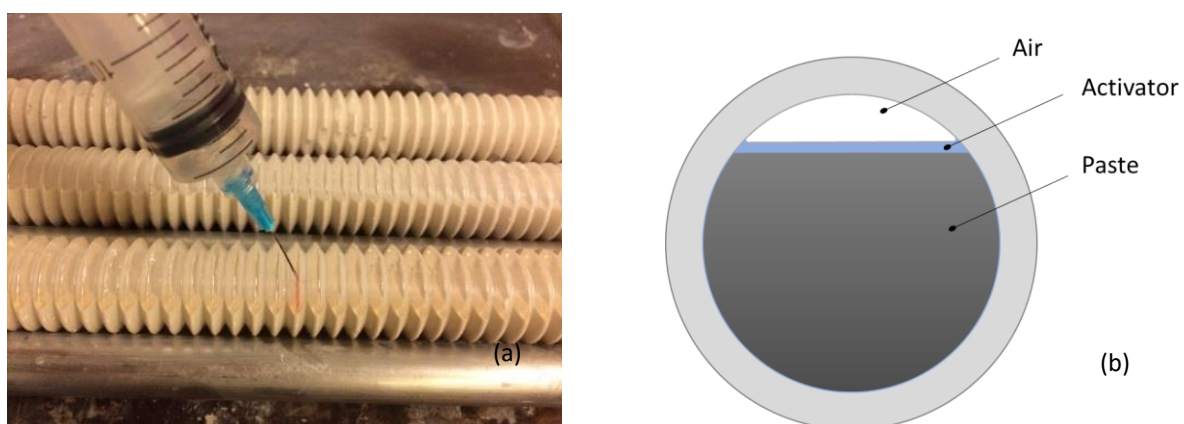


Figure 3.2 Using a syringe to add alkali solution into the corrugated tubes (a) which are 80% filled by the paste (b).

3.2.2.4 Characterization of the microstructure

X-ray diffraction (XRD) measurement was conducted to examine the crystalline phases in the pastes using a Philips PW 1830 powder X-ray diffractometer with Cu K α (1.5406 Å) radiation, tube setting of 40 kV and 40 mA, a step size of 0.030° and a 2 θ range of 5–70°.

Fourier transform infrared spectroscopy (FTIR) measurement was performed with a TM 100 Optical ATR-FTIR spectrometer over the wavelength range of 600 to 4000 cm⁻¹ with a resolution of 4 cm⁻¹.

The TAM-Air-314 isothermal conduction calorimeter was used to measure the heat flow and cumulative heat of the alkali-activated pastes. Before measurements, the calorimeter was calibrated at 20 °C for 1 week. About 6 grams of freshly mixed pastes were poured into the glass vials with an internal diameter of 18 mm. The vials were then sealed and placed in the calorimeter. The whole procedure took approximately 15 min from the moment of adding activator. During the test, the measuring cells within the calorimeter were kept at 20 ± 0.1 °C. The data was recorded every 1 min until 7 days. The calorimetry results were normalized by the weight of the paste.

Nitrogen adsorption was utilized to characterize the pore size distributions of the pastes. The test was conducted using a Micrometrics Gemini VII 2390 V1.03 with a relative pressure

ranging from 0.05 to 0.998. Based on the nitrogen adsorption data, Barrett-Joyner-Halenda (BJH) model was used to derive the pore size distribution curve [132].

3.2.2.5 Chemical shrinkage and internal RH

Dilatometry was used to measure the chemical shrinkage of the pastes as suggested by ASTM C 1608 [133]. Only the water was replaced by activator, to be added onto the surface of the paste [46].

The internal RH of the pastes was measured by Rotronic hygroscopic DT station equipped with HC2-AW measuring cells [134]. Two replicates were tested for each mixture. The nominal error of the sensor was within 2% RH. The sensors were calibrated before and after each measurement using four saturated salt solutions (NaCl, KCl, KNO₃ and K₂SO₄) with equilibrium RH in the range 75–98%. At the curing age of 1 day, 3 days and 7 days, the paste was crushed into small pieces around 0.5 cm³ and immediately inserted into the hermetic measuring chambers. To consider the influence of dissolved ions on the internal RH, the pore solution was extracted from the paste by a steel die under high pressure and the RH of the pore solution was measured [135].

3.2.2.6 Elastic modulus measurement

Elastic modulus is an important parameter to analyse the autogenous shrinkage of the paste. Moreover, the evolution of elastic modulus helps to understand the time-zero of the autogenous shrinkage of AAMs, from when tensile stress can be potentially induced in the restrained material. In this chapter, the elastic modulus was measured automatically using Elasticity Modulus Monitoring through Ambient Response Method (EMM-ARM) from casting until 7 days. The EMM-ARM method applied herein is based on the continuous monitoring of the first resonant frequency of a 450mm span composite cantilevered beam with a circular cross-section (outer shell with a 20mm thick acrylic tube, and inner 16mm corresponding to the material under testing). Based on the knowledge of all geometric and mass features of the testing system, it is possible to infer the elastic modulus of the tested material through the application of the dynamic equation of motion of the beam. The detailed measuring procedure was shown in [136]. Three replicates were tested for each mixture.

3.3 Results and discussion

3.3.1 Autogenous shrinkage

The setting time of the pastes determined by Vicat needle is shown in Table 3.3. The autogenous shrinkage curves plots starting at the final setting time of the paste.

Table 3.3 Vicat setting time of the pastes (min).

Mixture	AAS	AASF
Initial setting	25	63
Final setting	35	103

As shown in Figure 3.3, the autogenous shrinkage of AAS paste develops rapidly after the final setting, reaching 3560 $\mu\text{m}/\text{m}$ at 1 day and around 6600 $\mu\text{m}/\text{m}$ at 7 days. The autogenous shrinkage of AASF is around 40% lower than that of AAS, reaching 1700 $\mu\text{m}/\text{m}$ at 1 day and around 3700 at 7 days, but is still much larger than that of the commonly used OPC pastes (related results can be found in [52,68]). These findings are in line with the data reported in the literature [56–58,60,137].

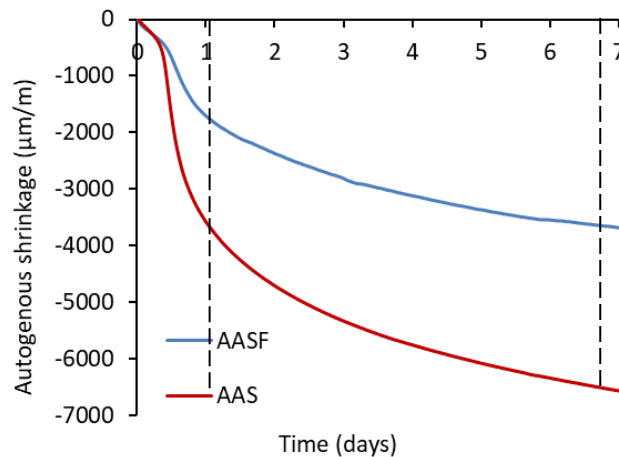


Figure 3.3 Autogenous shrinkage of AAS and AASF pastes.

3.3.2 Microstructure characterization

3.3.2.1 XRD analysis

The XRD patterns of pastes at curing age 1 day and 7 days are shown in Figure 3.4, where XRD patterns of the precursors were also plotted for comparison. Apart from the background hump related to the unreacted slag, additional diffraction peaks at 29° and 49.8° can be observed in the diffractograms for AAS paste, which is attributed to the formation of C-A-S-H type gels [39]. The intensity of these peaks decreases when half of the slag is replaced by fly ash. No new crystals are formed in the two pastes. In OPC-based paste, an expansion can be shown due to the formation of expansive crystals (e.g. ettringite) [138].

With increasing curing age, the main band (29°) for C-A-S-H gel in AAS becomes more intensive. Meanwhile, the peaks for crystals, e.g., the one at 26.5° , become relatively weaker. This indicates that more amorphous reaction products are formed. The spectra for AASF pastes show lower intensity at the humps representing C-A-S-H gel than those for AAS pastes at both 1 day and 7 days. This indicates that the amount of C-A-S-H gel formed in the first week is lower when slag is substituted by fly ash.

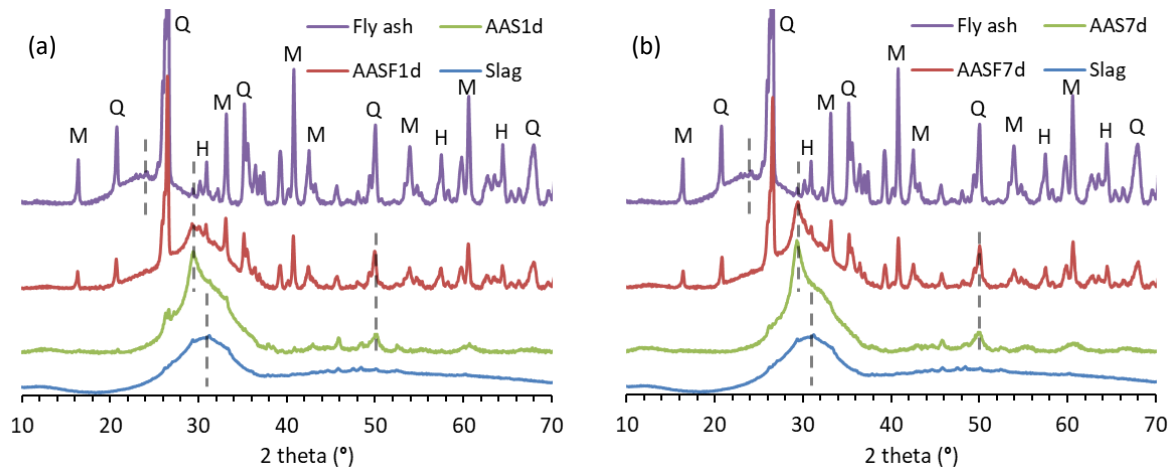


Figure 3.4 XRD patterns of AAS and AASF pastes cured for (a) 1 day and (b) 7 days, in comparison with precursors (slag and fly ash). M, Q and H stand for mullite, quartz and hematite, respectively.

3.3.2.2 FTIR analysis

The main bands of the FTIR spectra for AAS and AASF pastes are all near 950 cm^{-1} (Figure 3.5), which is assigned to the vibration of Si–O bonds [139]. More specifically, it is associated with the asymmetrical stretching vibrations of Si–O–T (T=Si or Al) bonds and/or Si–O–M bonds (M being alkali metal element) generated by Q^2 units¹³, which is the representative structure of aluminosilicate chains containing C–A–S–H type gel [140,141]. The shoulder in the range of $1040 - 1070\text{ cm}^{-1}$ is also assigned to the asymmetrical stretching of Si–O–T (T=Si or Al) bonds and/or Si–O–M bonds, with a lower extent of Al substitution [101]. The bands located at around 900 cm^{-1} and 660 cm^{-1} can be assigned to the deformational vibrations of Si–O–Si or Si–O–Al [140,142]. The band at around 815 cm^{-1} is typical for Si–O (Q^1) symmetric stretching vibrations [142]. The small band at 855 cm^{-1} originates from slag, and the intensity of this band becomes smaller in the spectra for AAS and AASF pastes due to the dissolution of slag and/or the substitution of slag by fly ash.

In Figure 3.5, the signals at 950 cm^{-1} , 900 cm^{-1} , 815 cm^{-1} and 660 cm^{-1} are visible in all spectra for the pastes, but their intensities are lower when fly ash is present. Besides, the spectra for AASF paste show higher intensity in the range of $1000 - 1200\text{ cm}^{-1}$ than that for AAS paste, due to the presence of unreacted fly ash particles (see the spectrum for fly ash). These findings indicate that the main reaction products in AAS and AASF are C–A–S–H type gel. The amount of this gel decreases when slag is partially substituted by fly ash, which confirmed the observations from XRD analysis. No signal representative for N–A–S–H type gel is detected in the spectra. These findings agree with the results obtained by Nedeljković [29] using energy-dispersive X-ray spectroscopy and thermogravimetric analysis.

³ Q^n denotes the connectivity of the silicate units based on the chemical shift, where n represents the number of Si–O linkages of the unit.

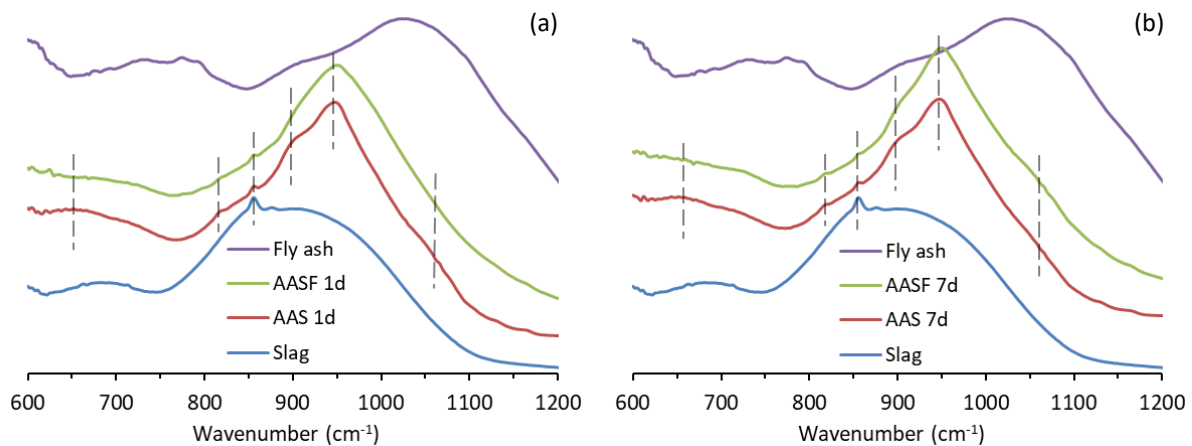


Figure 3.5 FTIR spectra of AAS and AASF pastes cured for (a) 1 day and (b) 7 days, in comparison with precursors (slag and fly ash).

The first reason why the typical reaction products in heat-cured fly ash-based geopolymer, N-A-S-H gel and zeolites, are not formed in AASF system lies in the low reactivity of fly ash at ambient temperature. The second reason is the instability of N-A-S-H gel in the presence of Ca^{2+} at high alkalinity [140]. Even though the dissolution of fly ash can release a small amount of Si and Al, these elements tend to involve in the formation of C-A-S-H gel rather than N-A-S-H gel, since a large amount of Ca is present in the system due to the dissolution of slag [140]. The fact that similar reaction products are formed in AAS and AASF pastes suggests that the two systems should follow similar mechanisms of autogenous shrinkage.

Comparing the spectra for AASF in Figure 3.5 (a) and (b), we can see that the bands at 950 cm^{-1} , 1050 cm^{-1} , 900 cm^{-1} and 815 cm^{-1} become more intensive at 7 days, which indicates more C-A-S-H gel is formed with the increase of curing age. In contrast, the intensities of the band at 855 cm^{-1} and the region from $1000 - 1200\text{ cm}^{-1}$ in the spectra for AASF decrease. This means that part of the fly ash starts to dissolve during the 7th days. These changes are less apparent in the spectra for AAS, implying a small change of the molecular structures of the phases in AAS paste from 1 day to 7 days. The reason can be the high reactivity of slag in alkali environments, which does not need 7 days to produce characteristic products [143]. The higher reaction degree of AAS paste compared to AASF paste at 1 day will be confirmed by the results discussed in the next section.

3.3.2.3 Isothermal heat release

Isothermal calorimetry tests are conducted to investigate the reaction kinetics of AAS and AASF, as shown in Figure 3.6. For reason of clarity, the heat flow curves are plotted up to 40 hours, while the cumulative heat in the whole measuring period of 168 hours is presented. It can be seen from Figure 3.6 (a) that both pastes experience a dormant period after the initial peak caused by wetting of the raw materials and initial reactions (mainly dissolution). After that, both curves show one main peak, corresponding to the acceleration period of the reaction. The main heat flow peak indicates the rapid formation of the major products, i.e. C-A-S-H gel, from the reaction of the ions in the activator and new ions dissolved from the precursor. The decrease of the reaction rate after the main peak is normally attributed to the inhibited

dissolution of the precursors due to the continuous formation of reaction products surrounding the unreacted particles and the gradually blocked pore space [144].

Compared with AAS, AASF shows a later acceleration period and a lower intensity of the main heat release peak. Accordingly, the cumulative heat released by AASF is lower than that released by AAS. Given the similar reaction products (C-A-S-H type gels) in the two systems, the lower total heat release of AASF paste indicates a lower overall reaction degree of the paste.

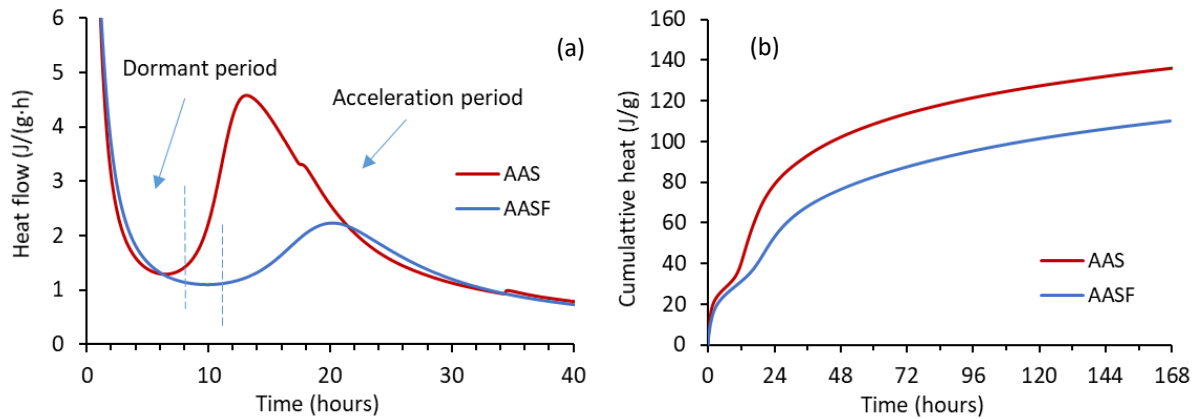


Figure 3.6 (a) Heat flow and (b) cumulative heat of AAS and AASF pastes.

The main reason for the lower overall reaction degree of AASF paste lies in the low reactivity of fly ash at ambient temperature [9]. It is well known that the fly ash particles are relatively hard to dissolve, no matter in cementitious systems or alkali-activated systems, despite the existence of amorphous phases in fly ash [9,145]. A longer time or a higher temperature is normally required for fly ash to show an evident reaction degree in alkali environments [146].

3.3.2.4 Pore structure

The pore volume and pore size distribution of AAS and AASF pastes characterized by nitrogen absorption are shown in Figure 3.7. At the age of 1 day, the total pore volume in AAS is higher than in AASF due to a faster formation of gel structures in AAS paste. AAS paste shows a critical pore size at around 4.5 nm and 20 nm at this age, while AASF paste does not show characteristic pores within the measuring range of nitrogen absorption. This indicates that a dense microstructure has not formed yet in AASF pastes. After 7 days, a critical pore size of 3.5 nm can be identified for AAS, indicating the formation of a large amount of gel pores (pore diameter $d < 10$ nm) [147,148]. Compared with AAS, AASF shows coarser gel pores, with the critical pore size at around 5 nm, and a larger total porosity. The coarser pore structure, when slag is replaced by fly ash, is consistent with the findings from the literature [29,149], and also with the cumulative heat release results shown in Figure 3.6. The denser pore structure of AAS paste would contribute to a smaller radius of the menisci formed within the paste given similar degrees of saturation, thus leading to a larger pore pressure (either capillary or disjoining pressure) that can generate autogenous shrinkage. This point will be further discussed in section 3.3.4.

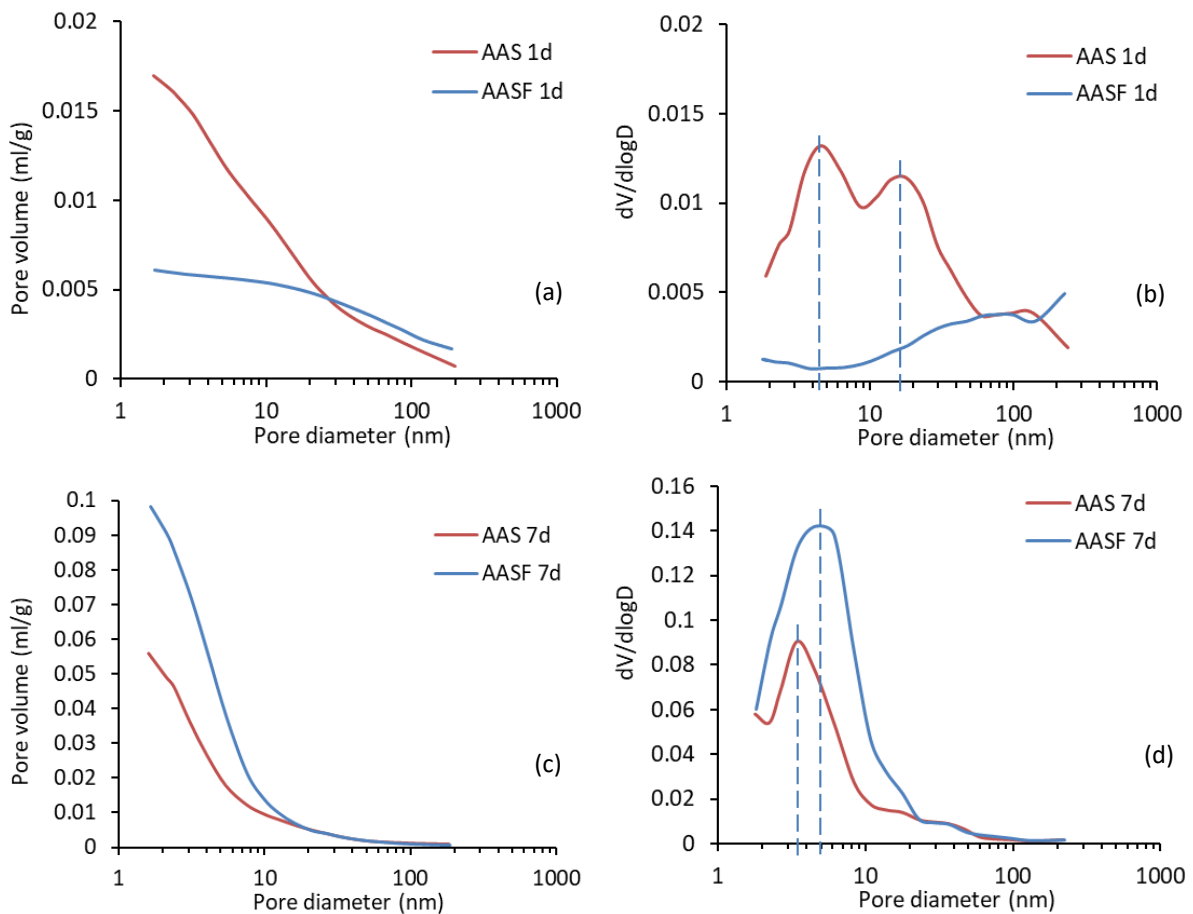


Figure 3.7 Pore volume and differential curves for AAS and AASF cured for 1 day (a,b) and 7 days (c,d).

By summarizing the characterization results shown above, it can be found that AAS and AASF systems have the same type of reaction products. The substitution of slag by fly ash leads to a lower reaction degree of the paste and a coarser microstructure. Consequently, the magnitude of the driving force of the autogenous shrinkage and the deformability of the pastes are expected to be different. In the following sections, the driving forces of the autogenous shrinkage and the deformability of the pastes will be investigated.

3.3.3 Chemical shrinkage

Chemical shrinkage is believed to be the primary reason for self-desiccation in OPC-based systems [18,52]. Since the total volume of hydration products is smaller than the volume of reactants (cement and water) [50], internal voids would form when the paste is stiff enough. As a result, negative pore pressure is built up in the internal voids and autogenous shrinkage of the paste is generated (see Figure 2.4 in Chapter 2) [150]. In order to study whether AAMs follow similar mechanisms, the chemical shrinkage of AAS and AASF is measured, as shown in Figure 3.8.

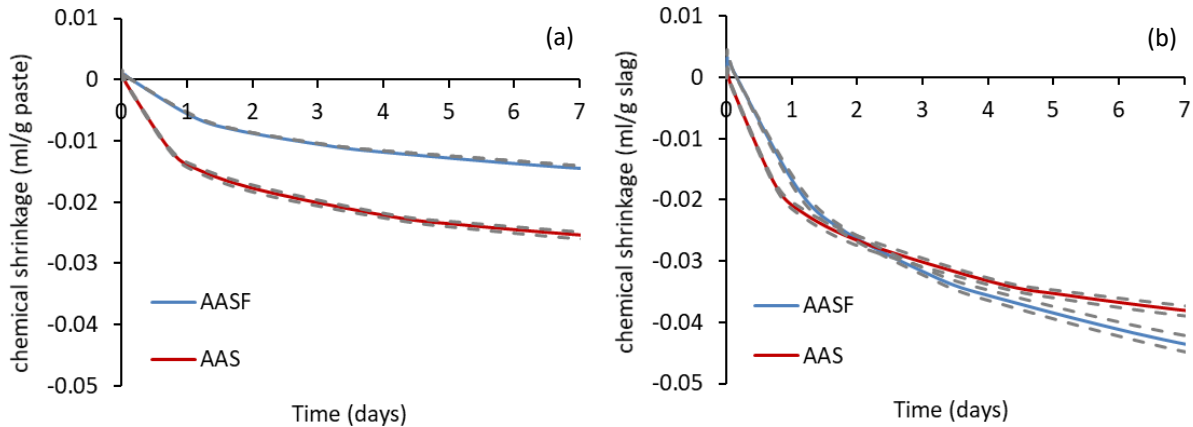


Figure 3.8 (a) Chemical shrinkage of AAS and AASF pastes, in ml per gram of paste and (b) chemical shrinkage of AAS and AASF paste in ml per gram of slag. The results of the two replicates for each mixture are shown in dashed lines while the average data is shown in solid line.

It can be seen from Figure 3.8 (a) that both AAS and AASF pastes show chemical shrinkage after the final setting (35 min for AAS paste and 103 min for AASF paste). The lower chemical shrinkage of AASF paste than of AAS paste is consistent with the lower reaction degree of AASF indicated by the cumulative reaction heat results as shown in Figure 3.6 (b). However, the chemical shrinkages of the two pastes are rather similar in the unit of ml per gram of slag, as shown in Figure 3.8 (b). This confirms the hypothesis proposed above that the slag dominates the reactions in AASF at ambient conditions. At the age of 7 days, AASF shows a slightly higher chemical shrinkage (ml/g slag) than AAS, which may be due to the higher reaction degree of slag in AASF system than in AAS system (see [151]) and the contribution of the reaction of fly ash.

The chemical shrinkage of the two pastes indicates that internal voids are formed in the systems and the pore pressure generated by liquid-gas menisci might be one of the driving forces of the formation of autogenous shrinkage.

3.3.4 Internal RH and pore pressure

In order to confirm the occurrence of self-desiccation in AAMs and quantify the pore pressure, the internal RH of the pastes is measured. The RH that indicates the curvature effect of the meniscus (RH_K) can be calculated according to Equation 3.1 [73].

$$RH_K = RH/RH_S \quad (3.1)$$

where RH is the relative humidity of the paste, RH_S is due to the dissolved salts in the pore solution and RH_K is due to the curvature effect of the liquid-gas menisci.

Figure 3.9 shows the measured RH of AAS and AASF pastes and RH_S of the pore fluid. The calculated RH_K is also shown in Figure 3.9.

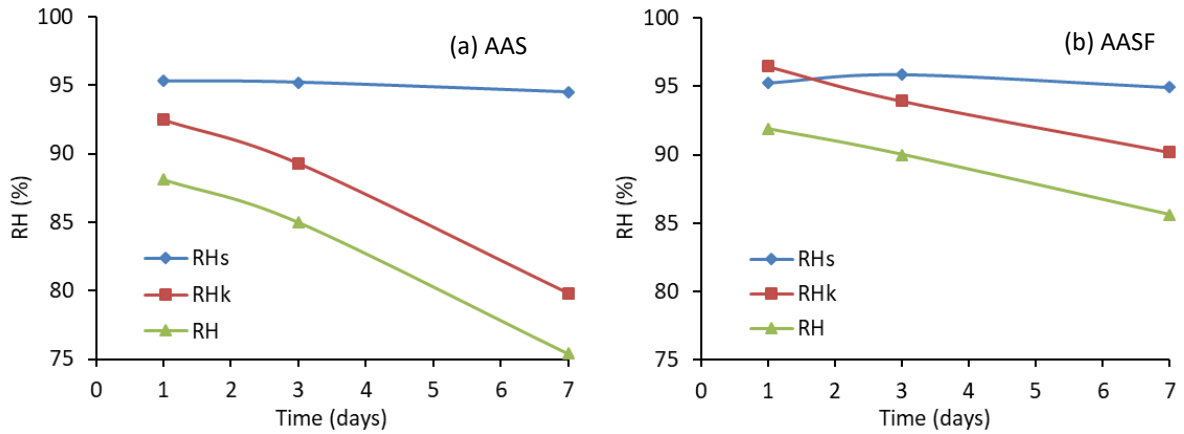


Figure 3.9 Internal RH results of AAS (a) and AASF (b). RH is the measured RH of the paste, RH_s is due to the dissolved salts in the pore solution and RH_k is due to the curvature effect of the liquid-gas menisci as calculated with Equation 3.1.

It can be seen that the RH_s of the pore solutions of the pastes is lower than 100% due to the presence of ions. The similar RH_s values (around 95%) of AAS and AASF indicate similar ions concentrations in the pore solutions. Both AAS and AASF show a decrease in RH_k with time indicating the occurrence of self-desiccation in the paste. The RH_k drop in AAS is more evident than in AASF.

The extent of RH_k drop in AAS and AASF pastes can be analysed according to Kelvin equation (Equation 3.2).

$$\ln(RH_k) = \frac{2\gamma V_w}{rRT} \quad (3.2)$$

where γ (N/m) and V_w (m³/mol) are the surface tension and the molar volume of the pore solution, respectively; r (m) is the radius of the menisci; R (8.314 J/(mol·K)) is the ideal gas constant and T (K) is the absolute temperature, in this study 293.15 K.

In Equation 3.2, R and T are constants. According to Lura [52], the ions have a limited effect on V_w . Thus the value of V_w can be considered as a constant and taken as that for water, i.e. 18.02×10^{-6} m³/mol. Then, it is the surface tension of the pore solution and the menisci radius that control the RH_k . The surface tensions of the pore solutions of AAS and AASF are believed to be similar since they have similar ions concentrations in the pore solution, as indicated by the RH_s results (see Fig. 3.9). According to Figures 3.7 and 3.8, AAS paste shows higher chemical shrinkage and higher extent of pore refinement than AASF paste. Therefore, the diameter of menisci in AAS is supposed to be smaller [18], which qualitatively explains the larger RH_k drop in AAS paste compared to AASF paste.

Combining the Kelvin equation (Equation 3.2) and the Laplace equation (Equation 3.3), the pore pressure σ (MPa), induced by the drop of RH_k , can be calculated with Equation 3.4.

$$\sigma = -\frac{2\gamma}{r} \quad (3.3)$$

$$\sigma = -\frac{\ln(RH_k)RT}{V_w} \quad (3.4)$$

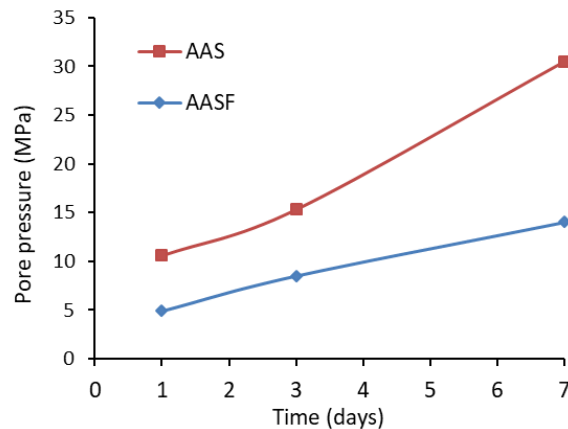


Figure 3.10 Calculated pore pressure in AAS and AASF according to Equation 3.4.

The calculated pore pressure for AASF and AAS at the age of 1 day, 3 days and 7 days is shown in Figure 3.10. It can be seen that larger pore pressure is generated in AAS than in AASF, which results in a larger autogenous shrinkage in AAS paste.

Compared with the measured pore pressure in OPC paste [52,68], the pore pressure generated in AASF paste is around two times higher than that in OPC paste with a w/c of 0.4. This might be one reason why AASF shows larger autogenous shrinkage than OPC. However, the two times larger pore pressure in AASF may not fully explain the 6 times larger autogenous shrinkage of AASF compared to OPC. It is, therefore, assumed that other driving forces besides the pore pressure induced by self-desiccation may also exist. More information on this will be given in the next section.

3.3.5 Shrinkage under saturated condition.

In order to investigate the existence of other driving force besides pore pressure, the autogenous shrinkage of AAS and AASF under saturated condition is measured (set up as shown in Figure 3.11 (a) and (b)). OPC paste was also tested for comparison. The autogenous shrinkage under saturated condition is compared with the deformation (i.e., autogenous shrinkage) of the pastes under sealed condition.

It can be seen from Figure 3.11 (c) that OPC shows expansion under saturated condition. The mechanism behind this phenomenon is that the formation of internal voids is compensated by the externally supplied water. Hence, no meniscus would form and no capillary tension would exist in the paste. Meanwhile, the formation of crystals (e.g. ettringite) can exert pressure on the microstructure and as a result, expansion of the paste is generated [138,152]. By contrast, AAS and AASF show a noticeable shrinkage even under saturated condition, especially on the first day. This finding is consistent with the results obtained by Yang et al. [110], who observed considerable shrinkage of AAS cured in an environment with RH above 90%. After the age of 1 day, the shrinkage of AAM pastes under saturated condition develops much slower. A similar trend on AAS mortar was observed by Palacios and Puertas [97]. The results in Figure 3.11 indicate that besides self-desiccation, there is another mechanism that can induce autogenous shrinkage of AAMs, especially at early age.

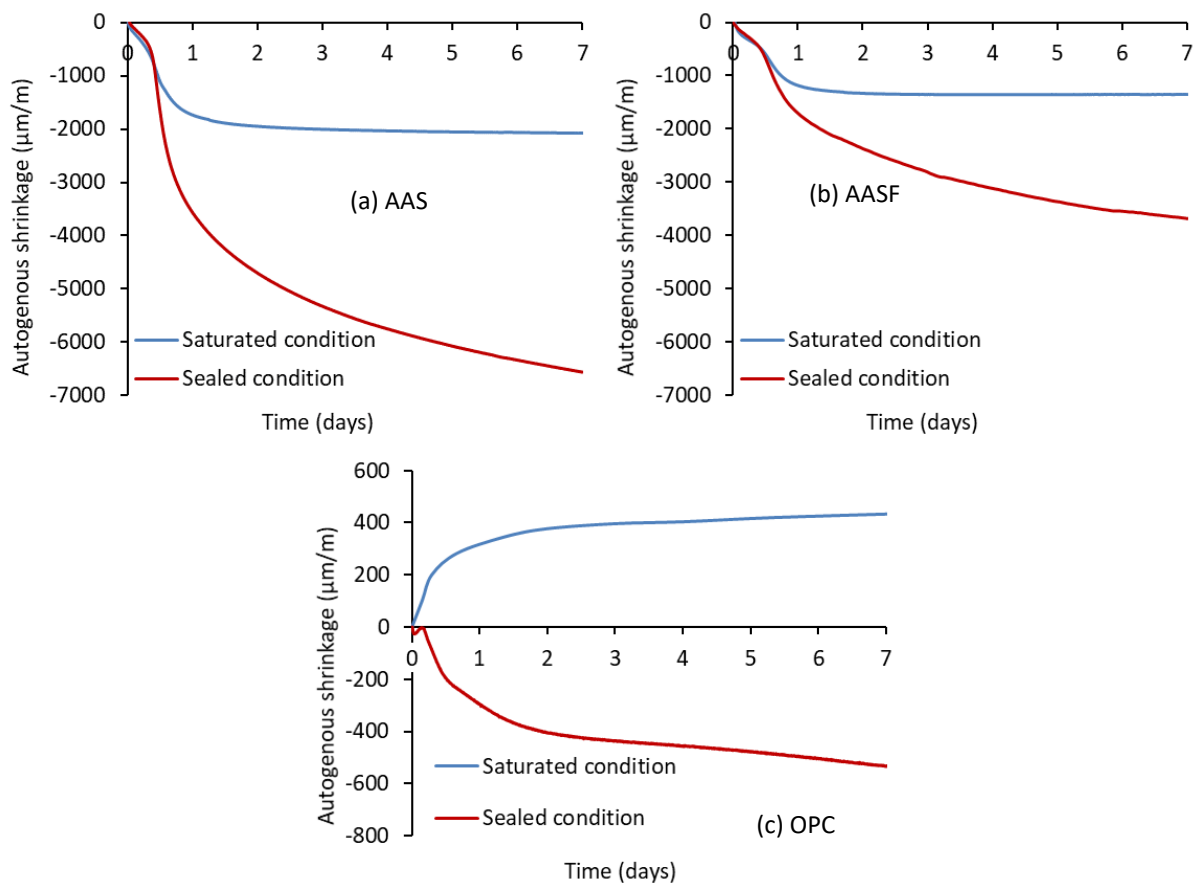


Figure 3.11 Shrinkage of AAS (a), AASF (b) and OPC (c) under saturated condition in comparison with the autogenous shrinkage (under sealed condition). The OPC paste is with a w/c of 0.4. Detailed information on the chemical composition of cement can be found in [68].

Several studies proposed the possibility of the existence of various mechanisms of autogenous shrinkage of AAMs other than self-desiccation. For example, Fang et al. [25] found that a large part of the early age autogenous shrinkage of AASF is associated with the development of chemical shrinkage. However, they did not define the driving force behind it. Uppalapati [77] hypothesized that the autogenous shrinkage of AAS may be related to the polymerization reaction during the formation of C-A-S-H gel. However, this mechanism may not explain the different autogenous shrinkage behaviours of AAS and OPC, since the polymerization degree of Si in C-A-S-H (mostly in the form of Q^2 [78,79]) is actually similar to that of Si in C-S-H.

In the sub-micro level, several forces are active between the gel surfaces, including attractive forces, e.g., van der Waals force, and impulsive forces, e.g., double-layer force and steric-hydration force [153,154]. DLVO theory (named after Derjaguin, Landau, Verwey and Overbeek [155,156]) provides a framework for the balance between van der Waals force and double-layer force [157,158]. However, for distances smaller than about 5 nm and concentrated solutions (10^{-2} - 10^{-1} M) especially when divalent or multivalent ions, e.g., Ca^{2+} , Al^{3+} , and SiO_3^{2-} , are present in the electrolytic solution, DLVO theory was also found unable to interpret the interparticle forces [158–161]. In these situations, non-DLVO forces such as the steric-hydration force play more important roles. The steric-hydration force is an impulsive force generated by the hydration shells surrounding individual ions (see Figure 3.12 (a)). In the

electrolytic solution, ions (especially divalent ions) would absorb neighbouring water molecules to form hydration shells and the counter overlap of the shells of individual ions would provide strong repulsive steric force to avoid the solid surfaces reaching closer [162]. As reported in [158] and [153], the repulsive steric-hydration force is stronger than either of the two DLVO forces. Unlike DLVO forces, the steric-hydration force increases with the increase of concentration of ions, as illustrated in Figure 3.12 (b).

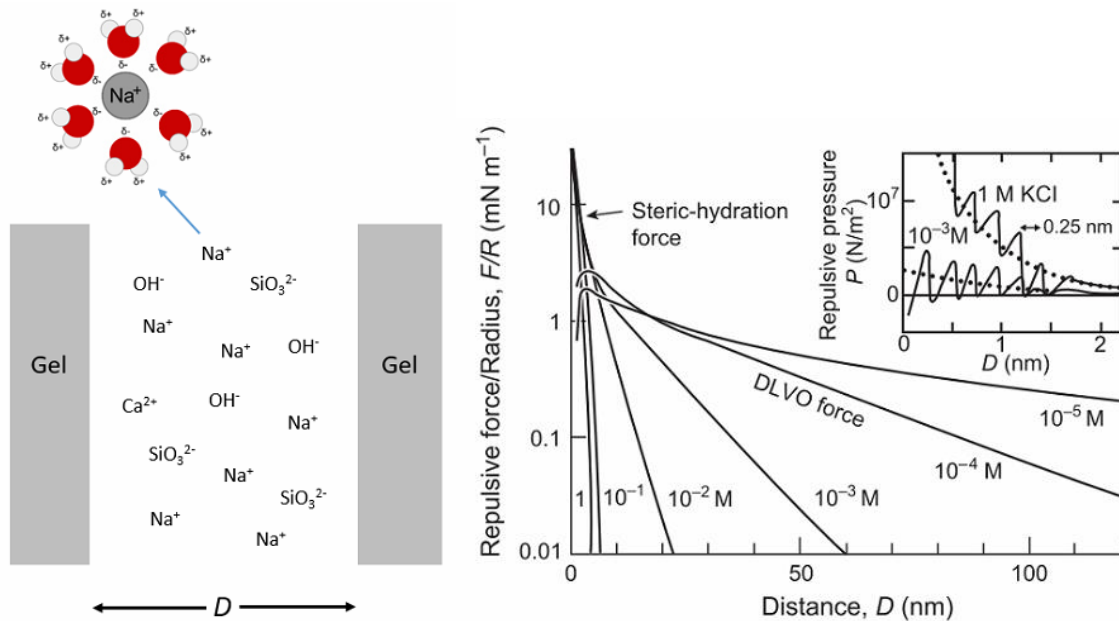


Figure 3.12 (a) Schematic representation of the ions and hydration shells between gel particles in AAMs. (b) An example of steric-hydration force in comparison with DLVO force, after [162]. The forces were measured between curved mica surfaces in KNO_3 or KCl solutions (qualitatively similar results are obtained in other electrolyte solutions). In 10^{-5} and 10^{-4} M the force follows the theoretical DLVO force law at all separations. At 10^{-3} M and higher concentrations more cations adsorb (bind) onto the surfaces and bring with them their water of hydration. This gives rise to an additional short-range hydration force below 3–4 nm (see inset for details).

In AAMs systems, there are large amounts of ions, such as Na^+ , OH^- and SiO_3^{2-} , in the initial pore solution. Schematic representation of the ions and the hydration shell between gel particles and is shown in Figure 3.12 (b). The hydration shells within the interstitial space counterbalance the attractive forces between gel particles to resist the densification of the gel structure. From the start of the acceleration period, the reaction is progressing rapidly and the concentrations of ions decrease dramatically. For example, according to [163] the concentration of SiO_3^{2-} in similar AAM systems decreases from more than 2 M to 100–200 mM. The reduced concentrations of the ions and the hydration shells lead to a substantial reduction in the steric-hydration force, while the attractive forces like van der Waals force remain unchanged. As a result, the gel particles surrounding the pores come closer to each other, which results in a rearrangement or densification of the gel [21]. This effect, together with the continuous formation of new products, contributes to the formation of a denser and stronger skeleton (which can be inferred from Figure 3.7). The correlation between the shrinkage under saturated condition and the reaction heat of AAS and AASF is presented in Figure 3.13. The large shrinkage of AAS than AASF closely relates to the faster reaction in AAS in the acceleration period.

After the acceleration period, the reactions slow down and the concentrations of the ions become stable [163]. Hence, the steric-hydration force also stabilizes. As a result, AAS and AASF show little shrinkage under saturated condition in the deceleration period, as shown in Figure 3.13. For the samples in sealed condition, the autogenous shrinkage keeps increasing after the acceleration period due to the increasing pore pressure (see Figure 3.3).

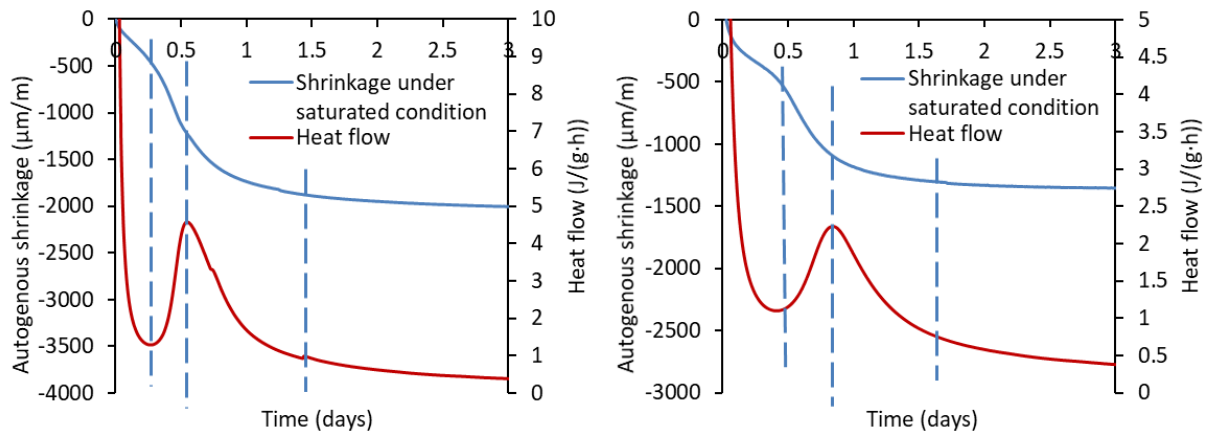


Figure 3.13 Shrinkage of AAS (a) and AASF (b) under saturated condition, plotted with the reaction heat.

The mechanism proposed above is a possible explanation of the shrinkage of AAS and AASF under saturated condition. This kind of shrinkage was not observed in OPC for two reasons. First, the concentrations of the ions in the pore solution of OPC are much lower than in alkali-activated systems and are relatively stable during the acceleration and subsequent periods [164,165]. Second, the shrinkage induced by steric-hydration force, if any, can be compensated by the expansion of the paste after the final setting caused by the formation of crystals, e.g. ettringite [152]. Future study is needed to quantify the decrease of the steric-hydration force in different reaction processes.

3.3.6 Elastic modulus evolution

The elastic modulus of AAS and AASF, determined by EMM-ARM, is shown in Figure 3.14. It is seen that the elastic modulus of AAS and AASF remains at a low level during the dormant period (until 8 hours for AAS and 11 hours for AASF, see Figure 3.6 (a)). After that, the elastic modulus of the two systems experiences a sudden increase. After 1 day, when the reaction rate slows down, the elastic moduli of the two systems continue to develop at a slower speed. AAS shows a higher elastic modulus than AASF after the dormant period due to the larger amount of reaction products and the denser pore structure formed in the paste as shown in section 3.3.2. The elastic modulus of AAMs is slightly lower than that of OPC paste made from similar water/binder ratios according to the results reported in [52] and [166].

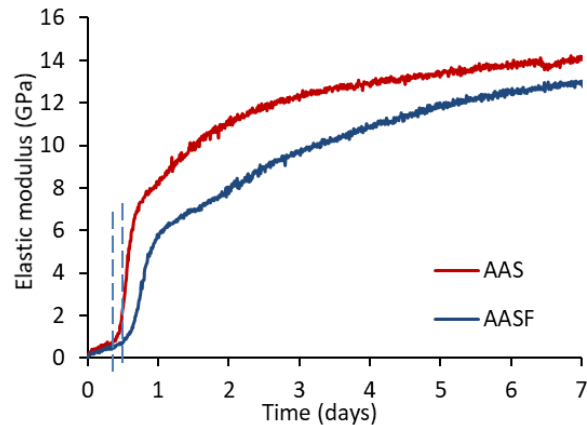


Figure 3.14 Evolution of elastic modulus of AAS and AASF pastes (L/B ratio 0.5). The dashed line indicates the instants when the elastic modulus starts to rapidly increase.

A phenomenon different from what has been observed in OPC systems is that the elastic modulus of AAMs starts to rapidly develop at the start of the acceleration period, which is far beyond the final setting time (see Table 3.3). For OPC, the final setting time normally indicates the formation of solid percolation, when the reaction products surrounding the cement particles start forming a solid cluster that spans the whole sample [48]. Therefore, the elastic modulus of OPC was observed to rapidly increase after the final setting [136]. For AAMs, in contrast, the final setting is probably the result of flowability loss of the paste due to the formation of initial products from the alkali and silicate ions in the interstitial space [167]. At such a short time (within one hour after mixing), a solid skeleton with loadbearing capacity has not formed yet.

This statement can find support in the shrinkage data. As can be seen from Figure 3.11 (a) and (b), the shrinkages under different conditions are nearly identical in the dormant period. This indicates that no considerable pore pressure is generated in this stage yet in sealed cured AAMs. Otherwise, they will show higher autogenous shrinkage than those under saturated condition. As the chemical shrinkage progresses, the liquid should have started to be consumed in the dormant period, but the paste is not stiff enough to enable the formation of menisci. Therefore, the shrinkage in this stage is likely to be viscous or even plastic deformation.

This finding is also in agreement with the results obtained by Ma et al. [168], who measured the internal pore pressure in AAMs and found that the pore pressure starts to develop only after the dormant period. Therefore, it seems the starting point of the acceleration period is a better definition of the “time-zero” of the autogenous shrinkage for AAMs.

3.3.7 Modelling of the autogenous shrinkage

In this section, results of early age properties of AAM pastes, presented in previous sections, are used as inputs for calculating autogenous shrinkage of AAS and AASF pastes. Based on the analyses above, the autogenous shrinkage of AAMs can be divided into two parts (Equation 3.5), the part induced by pore pressure and the part induced by other driving forces such as the steric-hydration force, as discussed in section 3.3.5.

$$\varepsilon_{AS} = \varepsilon_{pore} + \varepsilon_{ste} \quad (3.5)$$

ε_{ste} can be experimentally measured under saturated condition, as shown in Figure 3.11.

ε_{pore} can be considered as the sum of two parts, namely the elastic part and the time-dependent/creep part, as shown in Equation 3.6. The starting point of the acceleration period as discussed in section 3.3.6 instead of final setting time is used as the time-zero of the autogenous shrinkage in the calculations below:

$$\varepsilon_{pore} = \varepsilon_{elas} + \varepsilon_{creep} \quad (3.6)$$

According to Bentz et al. [72], the elastic deformation of a paste induced by pore pressure can be calculated by Equation 3.7:

$$\varepsilon_{elas} = \frac{S\sigma}{3} \left(\frac{1}{K} - \frac{1}{K_S} \right) \quad (3.7)$$

where S (m^3 liquid/ m^3 pore) is the saturation fraction; σ (MPa) is the stress in the pore solution calculated by Equation 3.4; K (MPa) is the bulk modulus of the paste and K_S (MPa) is the bulk modulus of the solid material.

The saturation degree S can be calculated from the non-evaporable water content and chemical shrinkage, according to Equation 3.8 [52]:

$$S = \frac{V_l}{V_p} = \frac{V_{il} - V_{nl}}{V_{il} - V_{nl} + V_{cs}} \quad (3.8)$$

where V_l (ml) is the liquid volume in the paste, V_p (ml) is the total pore volume in the paste, V_{il} (ml) is the initial liquid content, V_{nl} (ml) is the non-evaporable liquid volume, and V_{cs} (ml) is the volume of chemical shrinkage, see Figure 3.8.

In Equation 3.8, the air content of the paste is not considered. The non-evaporable water is determined by measuring the weight loss per gram of the sample when heated from 105 °C up to 950 °C. To obtain the volume of the non-evaporable liquid through the non-evaporable water content, it is assumed that the water proportion in the liquid and the density of the liquid are equal to those of the activator, which are 384 g water/500 g activator solution (see Table 3.2) and 1.23 g/ml (measured by pycnometer), respectively. The saturation degrees of the three mixtures at 1 day and 7 days are shown in Table 3.4. In general, AAS shows a lower saturation degree than AASF and the saturation degree of the two systems decreases with reaction time.

Table 3.4 Saturation degree of AAS and AASF pastes.

Mixture	AAS 1d	AAS 7d	AASF 1d	AASF 7d
S	0.933	0.881	0.974	0.931

The bulk modulus K of AAS and AASF pastes is calculated using the following formula:

$$K = \frac{E}{3(1-2\nu)} \quad (3.9)$$

where E (GPa) is elastic modulus and ν is Poisson's ratio (-).

The elastic modulus results is shown in Figure 3.14. The Poisson's ratio of AAS and AASF pastes is taken as 0.2 according to [169]. The bulk modulus K_S is taken as 44 GPa [170].

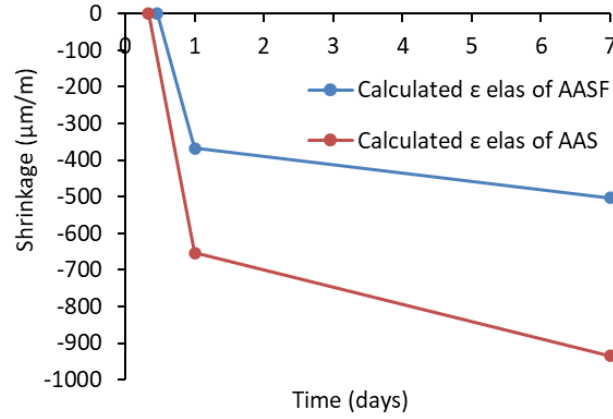


Figure 3.15 Calculated ϵ_{elas} of AAS and AASF paste. The time-zero of the curves is the start of the acceleration period of the paste (8 hours and 12 hours for AAS and AASF, respectively).

The elastic part of the autogenous shrinkage induced by pore pressure is calculated and shown in Figure 3.15. The elastic deformation between the age 1 day and 7 days is obtained by linear interpolation. It can be seen that the elastic deformation (ϵ_{elas}) only accounts for a small part of the total autogenous shrinkage (compare Figure 3.15 with Figure 3.3).

To calculate the creep part of the autogenous shrinkage of AAMs, the available models developed for OPC systems are applied, as shown in Equation 3.10.

$$\epsilon_{creep}(t, \tau) = \epsilon_{elas}(\tau)\varphi(t, \tau) \quad (3.10)$$

where $\varphi(t, \tau)$ is the creep factor. τ (days) is the time when the load is applied.

According to van Breugel [171], the creep of a hardening cementitious material at time t can be calculated with Equation 3.11.

$$\varphi(t, \tau) = \left(\frac{\alpha(t)}{\alpha(\tau)} - 1 \right) + 1.34 * \omega^{1.65} \tau^{-d} (t - \tau)^n \frac{\alpha(t)}{\alpha(\tau)} \quad (3.11)$$

where α is the degree of reaction; ω is the water-binder ratio (0.344, see section 3.2.1); n is a constant whose value is taken as 0.3 and d is the constant whose value is taken as 0.35 [172].

The reaction degree α of a cement or AAM paste can be calculated by Equation 3.12 [144,173,174].

$$\alpha(t) = \frac{Q(t)}{Q_{max}} \quad (3.12)$$

where $Q(t)$ is the reaction heat and Q_{max} is the ultimate total heat at the completion of reaction. Since only $\frac{\alpha(t)}{\alpha(\tau)}$ in the first week is needed in Equation 3.11, there is in fact no need to predict Q_{max} . The reaction degree term $\frac{\alpha(t)}{\alpha(\tau)}$ can be calculated directly from experimental results of $Q(t)$ and $Q(\tau)$ as shown in by Equation 3.13.

$$\frac{\alpha(t)}{\alpha(\tau)} = \frac{Q(t)}{Q(\tau)} \quad (3.13)$$

where $Q(t)$ and $Q(\tau)$ are the reaction heats of the paste at time t and τ . The reaction heat results in the first week have been shown in Figure 3.6.

Since the pore pressure is increasing with time, the creep part of the autogenous shrinkage at a certain age needs to be considered as the accumulation of increments of creep deformations that formed at previous time intervals, e.g. from τ_1 to τ_{n-1} . Within each time interval, the load can be treated as constant. Therefore, the creep induced by pore pressure can be calculated by Equation 3.14.

$$\varepsilon_{creep} = \sum_{k=1}^{n-1} \Delta\varepsilon_{creep}(t_k, \tau_k) \quad (3.14)$$

where $\Delta\varepsilon_{creep}(t_k, \tau_k)$ is the increment of creep from τ_k to τ_{k+1} .

A schematic representation of the calculation process mentioned above is shown in Figure 3.16.

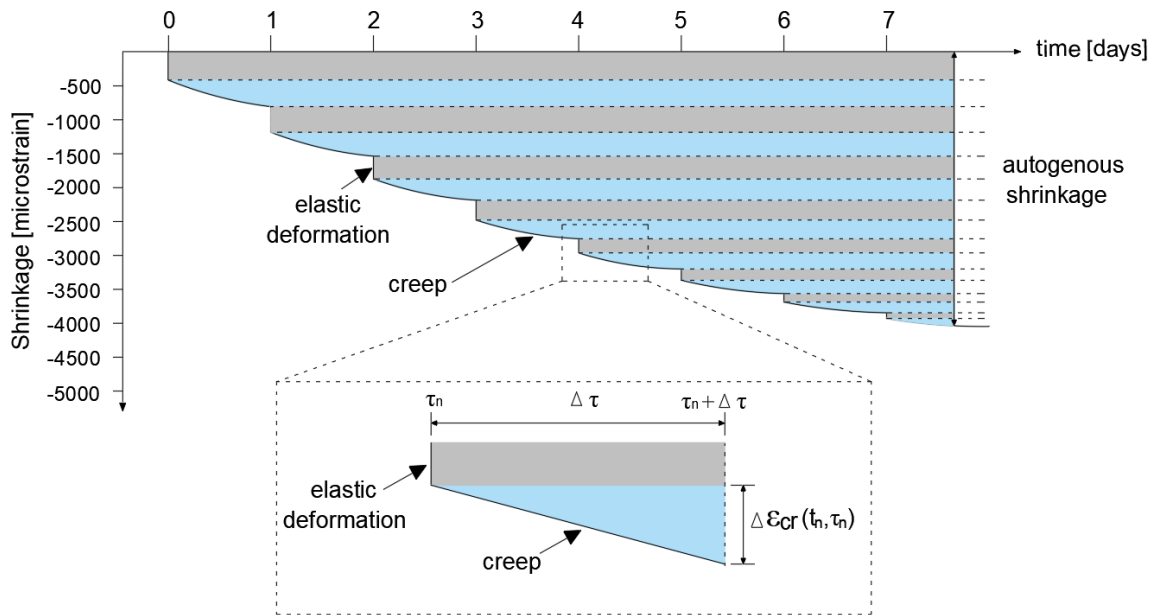


Figure 3.16 Schematic representation of pore pressure induced autogenous shrinkage of the paste, after [68].

Based on the Equations above, the creep part of the autogenous shrinkage induced by pore pressure, ε_{creep} , is calculated and compared with ε_{elas} , as shown in Figure 3.17. It can be seen that the calculated ε_{creep} of AAMs is more than three times higher than ε_{elas} . For plain OPC paste, the creep part was generally reported to be with a similar magnitude to that of the elastic part of the autogenous shrinkage. For hardening OPC paste blended with fly ash or slag, the creep coefficient (creep part/elastic part) can reach 2 [52,68,87]. Hence, it seems that AAM systems show more evident viscosity than OPC-based systems. This finding is in line with the evident creep/relaxation of AAM paste and concrete reported by Ye and Radlińska [21], Li et al. [175] and Kostiuhenko et al. [176]. According to Ye et al. [21], the evident viscous deformation of AAMs is due to the rearrangement of C-A-S-H gel. The reason why C-A-S-H gel appears more viscoelastic compared with C-S-H gel lies in the structural incorporation of alkali cations in C-A-S-H, which reduces the stacking regularity of C-A-S-H layers and makes the gel easier to collapse and redistribute [21].

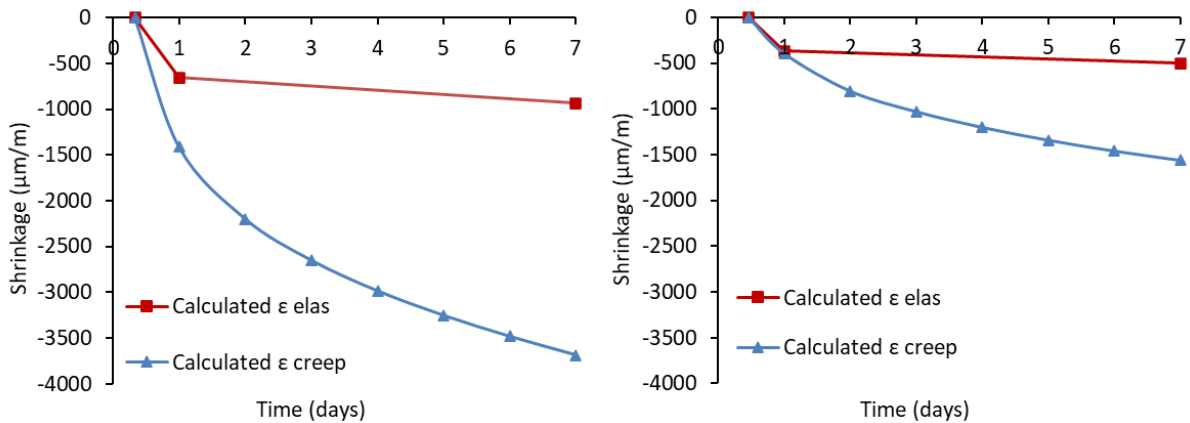


Figure 3.17 Calculated ε_{creep} of AAS (a) and AASF (b) paste, in comparison with ε_{elas} . The time-zero of the curves is 8 hours and 11 hours for AAS and AASF, respectively.

With the calculated ε_{elas} and ε_{creep} , and the measured ε_{ste} , the total autogenous shrinkage can be calculated by combining Equations 3.5 and 3.6. The calculated autogenous shrinkage of the pastes is compared with the measured one as shown in Figure 3.18.

In Figure 3.18, the calculated autogenous shrinkage curves of AAM paste agree fairly well with the measured ones, especially for AAS paste. This also supports the hypothesis of the autogenous shrinkage mechanism proposed in this chapter. The results also indicate that the creep model developed in [171] for OPC-based systems can also be used to predict the pore pressure induced-creep of AAMs.

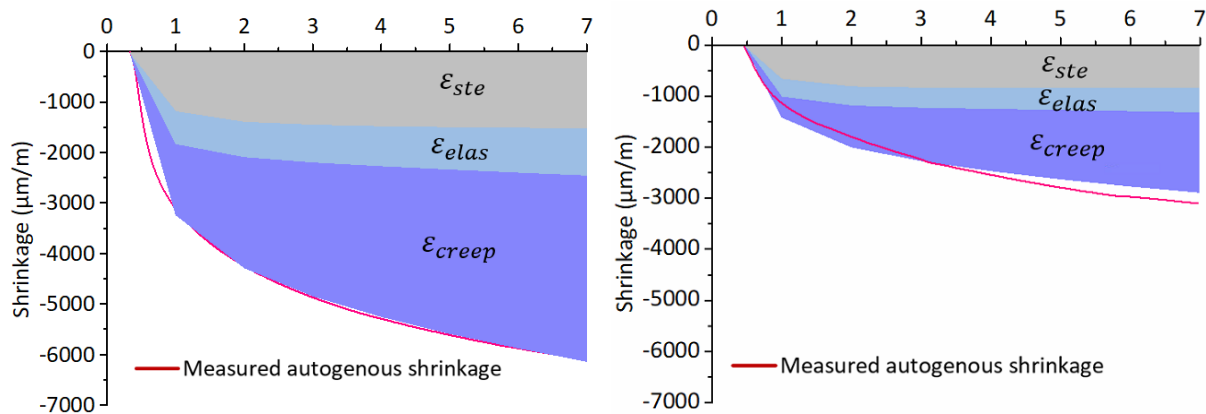


Figure 3.18 Calculated and measured autogenous shrinkage of AAS paste (a) and AASF paste (b).

The formulation well estimated the autogenous shrinkage within the age of 7 days. For AASF paste, the calculated ε_{AS} underestimates the autogenous shrinkage within 3 days, and overestimates it in later age. However, the discrepancies are within 20% in the whole period studied.

This section provides a useful strategy for academia and industrial users to predict the autogenous shrinkage of AAMs. The important input parameters that need to be known first are the evolution of: internal RH, saturation degree, elastic modulus, reaction heat evolution and shrinkage under saturated condition (ε_{ste}). The good agreement between the calculated

and the measured autogenous shrinkage of AAMs, in turn, supports the mechanism identified in this study. Of course, future study is still needed to clarify the nature of ε_{ste} (elastic or creep) in order to deepen the understanding of the deformation of AAMs.

3.4 Concluding remarks

In this chapter, the autogenous shrinkage of AAS and AASF pastes is measured and the mechanisms of the autogenous shrinkage are investigated. The role of fly ash in AASF paste is clarified. A model for calculating the autogenous shrinkage of AAMs is proposed. The autogenous shrinkage of AAMs is calculated and compared with the measured results. The following remarks can be made:

1. AAM pastes show larger autogenous shrinkage than OPC paste. The more slag is used in the precursor, the larger is the autogenous shrinkage of the AAM pastes.
2. The main reaction products in AAS and AASF are C-A-S-H type gel. Compared with AAS, AASF shows a longer dormant period, a smaller amount of reaction products and a coarser pore structure in the first 7 days. From the early-age reaction kinetics point of view, the role of fly ash is similar to that of inert filler.
3. In the dormant period, the stiffness of the paste remains low and the autogenous shrinkage is mainly viscous/plastic deformation. From the start of the acceleration period, the elastic modulus of the paste increases rapidly and the pore pressure starts to develop due to a drastic drop of internal RH. No significant change in the reaction kinetics or stiffness evolution is observed around the final setting time determined by Vicat needle. It is suggested, therefore, that the moment when the acceleration period starts is a more proper indication of the time-zero for the autogenous shrinkage of AAMs than the Vicat final setting time.
4. It has been shown for the first time that self-desiccation is not the only mechanism of autogenous shrinkage of AAMs. Besides self-desiccation, it is believed that the reduction of steric-hydration force due to significant consumption of ions also induces a certain amount of shrinkage, especially in the acceleration period. In the deceleration period, pore pressure becomes the dominant driving force of the autogenous shrinkage.
5. AAS and AASF pastes show pronounced viscoelasticity in comparison with OPC paste. Creep deformation of the solid skeleton under the action of pore pressure plays an important role in the autogenous shrinkage of AAMs.
6. A computational model is proposed to estimate the autogenous shrinkage of AAMs pastes based on the mechanisms clarified. By summing the shrinkage under saturated condition, the elastic and creep shrinkage induced by the pore pressure, the calculated autogenous shrinkage agrees very well with the measured results.

Chapter 4

Mitigation strategies of autogenous shrinkage of AAMs

Part 1: internal curing with SAPs

4.1 Introduction

As shown in Chapter 2, effective strategies to mitigate the autogenous shrinkage of AAMs are still lacking. Due to the differences in microstructure and chemical environment between AAMs and OPC, many shrinkage-mitigating admixtures like SRA, expansive additive and nano-additive, which are widely adopted in OPC, are ineffective in AAMs. According to the results presented in Chapter 3, the pore pressure resulting from the self-desiccation process seems one of the important driving forces that cause autogenous shrinkage in AAMs. To mitigate the extent of self-desiccation in AAM paste, internal curing might be a promising way, by which extra liquid could be supplied to the matrix of AAM paste to compensate for the moisture loss in AAM paste, like in cement-based materials [177].

Lightweight aggregates and superabsorbent polymers (SAPs) are the two most widely used types of liquid reservoirs to provide internal curing. As reported by Jensen [112], SAPs normally have a cross-linked structure, which can absorb water many times its weight. The water stored in SAPs will be released to the surrounding matrix during the hardening of the paste. Compared with lightweight aggregates, the use of SAPs will cause a lower strength loss of the matrix and is of lower cost. Therefore, SAPs are widely used as an internal curing agent in cement-based materials [178,179].

For cement-based systems, internal curing by SAPs has been widely reported to be effective in mitigating the self-desiccation and the associated autogenous shrinkage [111–115,180]. For AAMs, in contrast, few studies have been conducted on this topic [118–120]. Oh and Choi [118] and Song et al. [119] reported that using SAPs as internal curing agent led to lower autogenous shrinkage of AAS mortar. Tu et al. [120] found that internal curing by SAPs was effective in mitigating the autogenous shrinkage of AASF paste. Despite the preliminary results reported in these studies, the absorption behaviour of SAPs in alkali solution and the shrinkage-mitigating mechanism of SAPs in AAMs are poorly understood.

In this chapter, the effectiveness and mechanism of internal curing by SAPs to mitigate the autogenous shrinkage of AAS and AASF pastes is investigated. The absorption capacity of SAPs in alkali solutions is first measured by the tea-bag method and the dosages of SAPs in AAS and

Parts of this chapter have been published in:

Zhenming Li, Mateusz Wyrzykowski, Hua Dong, José Granja, Miguel Azenha, Pietro Lura, Guang Ye. Internal curing by superabsorbent polymers in alkali-activated slag. *Cement and Concrete Research*. 135 (2020). 106123.

AASF pastes are accordingly determined. The influence of internal curing on the reaction kinetics is examined through isothermal calorimetry. X-ray computed tomography (CT) and scanning electron microscopy (SEM) are utilized to monitor the liquid desorption from the SAPs and the microstructure of the SAPs-containing pastes. The internal relative humidity (RH) evolution of the plain AAM pastes and internally cured pastes is measured. At last, the mechanical properties (compressive and bending strength, elastic modulus) of the pastes are measured.

4.2 Materials and methods

4.2.1 Raw materials

The precursors used in this chapter are slag and fly ash. The chemical compositions and physical properties of the precursors can be found in Table 3.1. The composition of the alkali activator was shown in Table 3.2.

The SAPs used is based on a cross-linked copolymer of acrylamide and acrylate obtained in bulk polymerization and were anionic. The SAPs had particles with irregular shapes and sizes up to 500 μm , with a dominant size around 200 μm , see Figure 4.1. No SAPs degradation (dissolution) was evident during the teabag tests in the activator (the activator remained clear without any traces of SAPs leaching out and there was no self-release of the absorbed fluid).

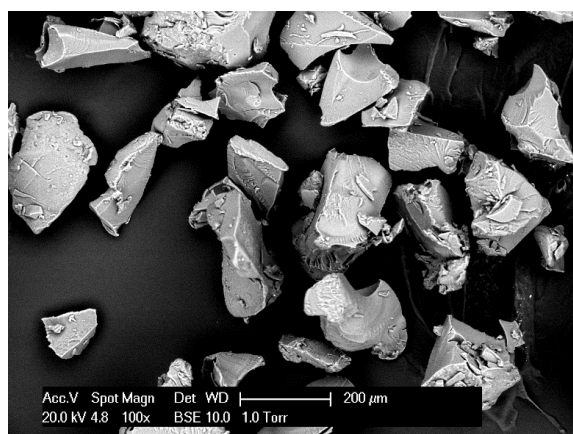


Figure 4.1 Scanning Electron Microscopy of SAPs particles in the dry state.

4.2.2 Determination of SAPs content

4.2.2.1 Absorption capacity of SAPs

The absorption capacity of SAPs in the activator ($\text{NaOH}/\text{Na}_2\text{SiO}_3$ solution) was measured by the teabag method according to [181]. To understand better the absorption behaviour of the SAPs in different solutions, the absorption capacities of the SAPs in deionized water and NaOH solution were also measured. The NaOH solution had the same $\text{Na}_2\text{O}/\text{H}_2\text{O}$ ratio as the activator. To measure the free absorption potential of the SAPs, each teabag was filled with 0.2 g of dry SAP particles. Three individual teabags were prepared for each solution to ensure reliable results. The teabag containing the SAPs was hung in a beaker filled with the fluid (about 100 ml). The beaker was tightly covered with a paraffin stretch film to avoid

carbonation and evaporation of the fluid. After 15 min, 30 min, 60 min, 3 h and 24 h of contact time, the teabag (with the hydrogel inside) was removed and weighed. The detailed testing procedure and formulas used to calculate the absorption capacity can be found in [182]. Considering the fast setting of the AAS pastes, the absorption capacity in the activator at 3 h, equal to 20 g/g, was used to calculate the necessary amount of dry SAPs.

It should be noted that in an AAS paste, Ca^{2+} also exists in the initial pore solution of the paste and may influence the actual absorption capacity of SAPs as reported e.g. in [183,184]. In addition, the concentrations of the ions in the pore solution can change with time. Therefore, the absorption capacity of the SAPs in the activator may be different from that in the AAS paste. In order to take those effects into account, the initial pore solution of the paste before the SAPs complete the absorption process, instead of the activator, should be used for the absorption capacity test. However, it is difficult to obtain pore solution from the paste in the first hours after casting by the hydraulic piston method, since the paste has not obtained enough stiffness yet (the stiffness evolution will be discussed in detail in section 4.3). In this case, a slurry of paste instead of fluid will be obtained by hydraulic pressing. Moreover, due to the fast setting of the paste (around 0.5 h, as has been shown in section 3.3), the release of Ca^{2+} from the dissolution of slag and the changes in the concentrations of ions are supposed to be limited by the time the SAP cavities have formed [163]. Therefore, the activator instead of the actual pore solution of the paste was used to measure the absorption capacity of the SAPs.

To investigate whether the SAPs preferentially absorb ions or water when they are immersed in the activator, 0.4 g of SAPs (which were expected to absorb about 8 g of solution) were put into 20 g of activator and the concentrations of the ions in the activator before and after SAPs absorption were measured. 20 g of activator was chosen because the amount of solution should be as low as possible to magnify the possible influence of SAPs absorption on the concentrations of the ions of the surrounding solution, but in the meantime, the solution should be enough to submerge the SAPs during absorption. Three individual solutions and teabags were prepared for each absorption time (30 min, 60 min, 3 h and 24 h). After absorbing for a given time, the teabag with the SAPs was taken out, and the ion concentrations of the left solution were measured. The concentration of OH^- was measured by titration against diluted HCl acid solution (0.1 mol/L). Phenolphthalein was used as an indicator. The elemental concentrations of Na and Si were measured by a PerkinElmer Optima 5300 DV ICP-OES (Inductively Coupled Plasma Optical Emission Spectrometry). The average values of three replicates are presented.

4.2.2.2 SAPs content design

In order to prevent self-desiccation, the amount of liquid absorbed by SAPs should compensate for the chemical shrinkage during and after the hardening of paste [184]. This approach was assumed here also for the AAM binder. The desired liquid/binder ratio provided by SAPs (l/b_{SAP}) can be calculated by the following equation:

$$l/b_{SAP} = CS \cdot \alpha_{max} \cdot \rho_a \quad (4.1)$$

where CS (ml/g) is the chemical shrinkage of the paste, α_{max} (-) is the estimated maximum degree of reaction of the paste, ρ_a (g/cm^3) is the density of the activator.

Since there has been no theoretical ultimate chemical shrinkage of AAM pastes reported in the literature, the measured chemical shrinkage of the pastes till the age of 28 days, 0.042 ml/g for AAS paste and 0.026 ml/g for AASF paste, is used here to replace $CS \cdot \alpha_{max}$. The chemical shrinkage of AAM pastes was measured by the dilatometry method suggested by ASTM C 1608 [133]. Only the water was replaced by the activator to be added onto the surface of the paste [46]. ρ_a is 1.23 g/cm³ as measured by pycnometry [185]. Accordingly, l/b_{SAP} is calculated to be 0.052 for AAS and 0.032 for AASF.

The amount of SAPs to be added to the precursor, m_{SAP} [g], is determined according to the absorption capacity, AC, of the SAPs in the activator (emulating the initial pore solution absorbed by the SAPs during mixing) and the desired amount of the internal curing liquid, $l/b_{SAP} \cdot m_{binder}$:

$$m_{SAP} = \frac{l/b_{SAP} \cdot m_{binder}}{AC} \quad (4.2)$$

where m_{SAP} (g) is the amount of SAPs needed; m_{binder} (g) is the mass of the binder; AC is the absorption capacity of SAPs in the activator, 20 g/g, as described in section 4.2.2.1.

Accordingly, the desired amount of SAPs is calculated to be 0.26% and 0.16% by mass of the binder for the AAS paste and AASF paste studied in this thesis, respectively.

4.2.3 Mixtures

The liquid/binder (l/b) ratio of the plain AAM paste was 0.5 (the control mixture). The l/b ratio in the internally cured AAM pastes was designed so that the *basic* l/b ratio (corresponding to the liquid not absorbed by the SAPs, i.e. the initially effective liquid) was the same. The total l/b ratio of the internally cured AAS and AASF pastes were, therefore, the sum of the basic l/b ratio and l/b_{SAPs} ratio = 0.5 + 0.052 = 0.552, and 0.5 + 0.032 = 0.532, respectively. Additionally, higher amounts of SAPs (0.5% and 1%) and correspondingly higher amounts of internal curing activator were also applied in AAS paste (it was assumed that the SAPs absorb the same amount of activator, 20 g/g, in mixtures with higher l/b ratio). The goal was to obtain a maximal autogenous shrinkage reduction and a minimal strength reduction. For each total l/b ratio, a mixture without SAPs was also tested as a reference. The compositions of all mixtures are shown in Table 4.1. The casting procedure was given in section 3.2.1.

Table 4.1 Mixture compositions (by mass proportion) of AAM pastes with and without SAPs.

Mixture	Slag	Fly ash	Total l/b ratio	Basic l/b ratio	Entrained l/b ratio	SAPs
AAS0.5	1	0	0.5		0	-
AAS0.552	1	0	0.552		0	-
AAS0.552SAP	1	0	0.552		0.052	0.0026
AAS0.6	1	0	0.6		0	-
AAS0.6SAP	1	0	0.6	0.5	0.1	0.005
AAS0.7	1	0	0.7		0	-
AAS0.7SAP	1	0	0.7		0.2	0.01
AASF0.5	0.5	0.5	0.5		0	-
AASF0.532	0.5	0.5	0.532		0	-
AASF0.532SAP	0.5	0.5	0.532		0.032	0.0016

4.2.4 Experimental methods

4.2.4.1 Autogenous shrinkage measurement

The autogenous shrinkage of the pastes was measured according to the procedure described in section 3.2.2.

4.2.4.2 Setting time, heat release of reaction and internal RH

The setting time, reaction heat flow and internal RH of the pastes were measured according to the procedures described in section 3.2.2. The calorimetry results were normalized by the weight of the binder.

4.2.4.3 X-ray micro-computed tomography

To study the absorption and desorption behaviour of SAPs in AAMs paste, the mixtures AAS0.552SAP and AASF0.532SAP were scanned with X-ray tomography using a Micro-CT-Scanner (Phoenix Nanotom). The paste was first cast into a small plastic container with a diameter of 4 mm and a height of 6 mm. Immediately after casting, the container was sealed by paraffin film and put into the CT scanner. During the first week after casting, the same sample was scanned 4 times, at the age of 1 h (nominally, in reality starting immediately after mixing), 8 h, 1 day and 7 days, respectively. The X-ray source tube worked at 120 keV/60 mA. 1900 images were acquired on a digital GE DXR detector (2304 × 2304 pixels). The duration of each scan was one hour. The reconstructed dataset had a voxel size of 5 μm. The 3D Reconstruction of the slices was carried out with VG Studio Max.

4.2.4.4 Scanning electron microscopy analysis

The fracture surface of internally cured pastes and the voids left by desorption of SAPs were observed using SEM by a Philips-XL30-ESEM in secondary electron mode under high vacuum

condition. The pastes AAS0.552SAP and AASF0.532SAP were cast into a PVC cylinder bottle with a diameter of 24 mm and a height of 50 mm. At the age of 7 days, the sample was taken out from the bottle and knocked into pieces with a size of around 1 cm³. These pieces were then immersed in isopropanol to stop the reaction. During that period, the isopropanol was replaced every two days until 2 weeks. Afterwards, the samples were put into a freeze dryer until a constant weight was obtained. After carbon coating, the samples were imaged with an environmental scanning electron microscope (Philips- XL30-ESEM) in secondary electron mode in high vacuum.

4.2.4.5 Mechanical properties

The flexural and compressive strength of AAS and AASF pastes were tested in accordance with NEN-196-1 [186]. The elastic modulus was measured according to the procedure described in section 3.2.2.

4.3 Results

4.3.1 Absorption behaviours of SAPs

The time-resolved free (teabag) absorption curve of SAPs in the activator (3.8M NaOH and 2.9M Na₂SiO₂) within 24 hours is shown in Figure 4.2. For comparison, the absorption curves in NaOH solution and deionized water are also shown. It can be seen that the SAPs in all liquids exhibit increasing absorption with time. The absorption capacity of SAPs in deionized water is much higher than in alkali solutions and the SAPs absorbs the least in the activator. From this curve, the absorption capacity of the SAPs in the activator was assumed to be the absorption at 3 h, 20 g/g. As mentioned in section 4.2.2.1, this value was used to calculate the amount of SAPs in the mix design of the internally cured mixtures.

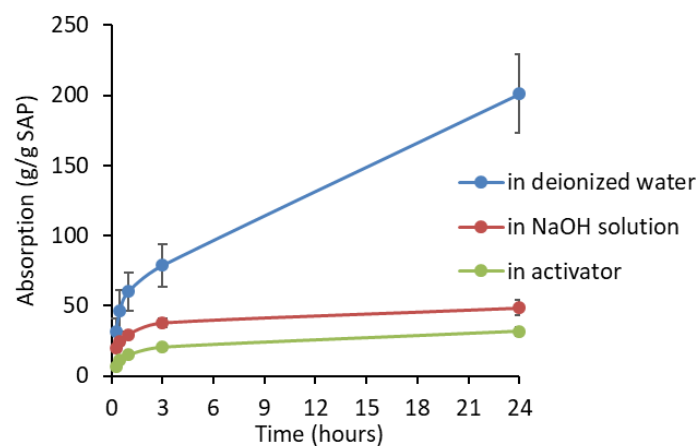


Figure 4.2 Absorptions of SAPs in deionized water, NaOH solution and activator, measured with the tea bag method.

To investigate whether the absorption of SAPs leads to a change in ion concentration of the activator solution, the ion concentrations in the activator before and after exposure to the SAPs were measured. As shown in Figure 4.3, the concentrations of Na, Si, and OH⁻ of the activator change slightly (within 3.5%) after absorption by SAPs for different lengths of time.

Considering the relative standard deviation of the results (0.2-3%), the concentration differences among the solutions are rather small. That allows assuming that the SAPs absorb the alkali solution approximately as a whole and the preference ions during absorption can be neglected in the paste.

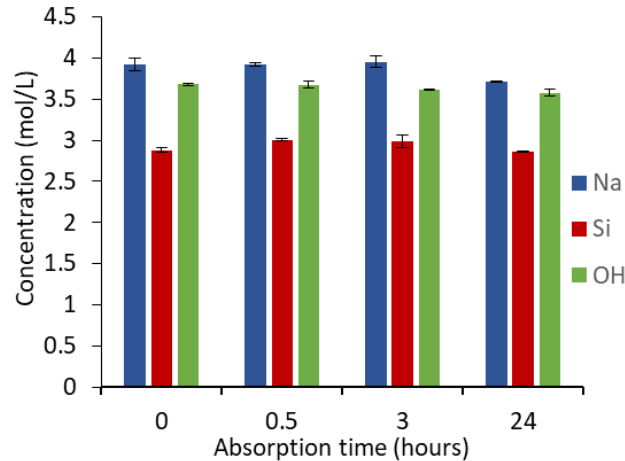


Figure 4.3 Concentrations of Na, Si and OH⁻ in activator before (0 h) and after (0.5, 3 and 24 h) absorption by SAPs.

4.3.2 Reaction heat

In Figure 4.4, the heat evolution rate and the cumulative heat of AAS pastes with different l/b ratios, with and without SAPs, are presented. For reasons of clarity, the heat evolution curves are plotted from 6 hours up to 24 hours, while the cumulative heat in the whole measuring period of 168 hours is presented. A dormant period of around 8-9 hours (depending on the l/b ratio and the presence of SAPs) is followed by an acceleration period and by the main peak, which manifests between 13 hours to 15 hours (Figure 4.4 (a)). The decrease of the reaction rate after the main peak is normally attributed to the inhibited dissolution of precursors because of the continuous formation of reaction products surrounding the precursors and the gradually blocked pore space [144]. For pastes without SAPs, the main heat release peaks appear later with increasing l/b ratio from 0.5 to 0.7, while becoming broader at the same time. With the addition of SAPs at the same total l/b ratio, the main peaks appear later and are lower in amplitude. The dormant period also becomes a bit longer for SAPs-containing mixtures, especially for AAS0.6SAP and AAS0.7SAP, of which the liquid contents are much higher than the control mixture AAS0.5.

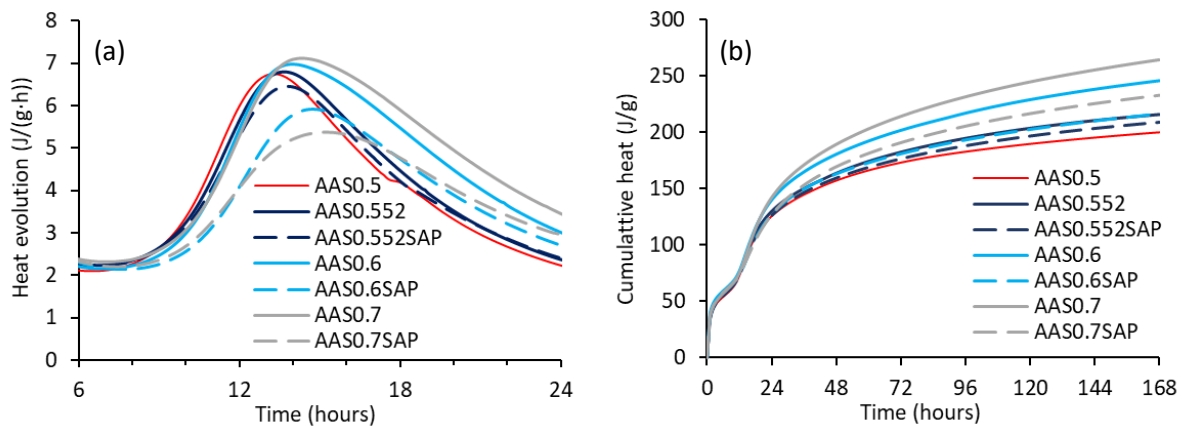


Figure 4.4 (a) Heat evolution and (b) cumulative heat of AAS pastes with different l/b ratios and different amounts of SAPs. Same colours correspond to the same total liquid amount; dashed lines denote samples with SAPs.

As shown in Figure 4.4 (b), AAS0.5 shows the lowest cumulative heat. The cumulative heat increases with increasing l/b ratio, and the pastes without SAPs generate more hydration heat than the pastes with SAPs and the same l/b ratio. All pastes, with and without SAPs, generate very similar cumulative heat in the dormant period. After that, the differences among the curves start to become evident.

As for the heat evolution of AASF pastes with different l/b ratio with and without SAPs, similar trends can be observed. As shown in Figure 4.5 (a), the main heat release peak of AASF0.532 appears later and has a higher intensity than that of AASF0.5. The cumulative heat of AASF paste increases with l/b ratio when SAPs is absent, similar to what has been found for AAS paste. With the addition of SAPs, the amplitude of the main peak becomes lower and the dormant period is a bit longer than those of the mixtures without SAPs. Accordingly, the accumulative heat of AASF0.532SAP is lower than that of AASF0.532, but is similar to that of AASF0.5.

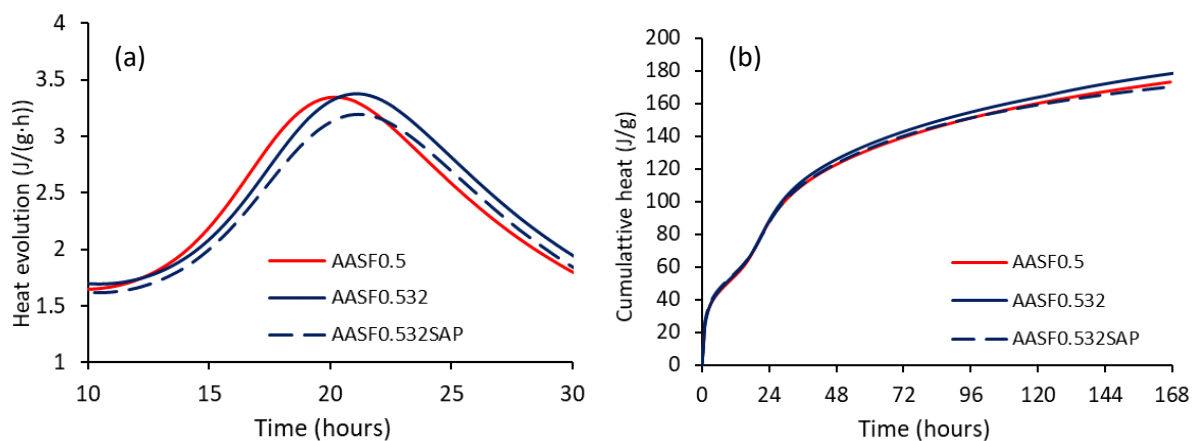


Figure 4.5 (a) Heat evolution and (b) cumulative heat of AASF pastes with and without SAPs. Same colours correspond to the same total liquid amount; dashed lines denote samples with SAPs.

4.3.3 Setting time

The initial and final setting times determined by Vicat test are shown in Table 4.2. For both AAS and AASF pastes, the initial and final setting occur later for pastes with higher I/b ratios without SAPs. However, for pastes with SAPs, the time of initial setting is similar to the control mixture, which may be due to the similar basic I/b ratio of these mixtures. The times of final setting of SAPs-containing pastes are a bit longer than the control mixture but much shorter than the non-SAPs mixtures with the same total I/b ratio.

Table 4.2 Times of initial and final setting for AAS and AASF pastes with and without SAPs.

Mixture	Initial setting (min)	Final setting (min)
AAS0.5	25	35
AAS0.552	36	51
AAS0.552SAP	24	39
AAS0.6	40	65
AAS0.6SAP	25	56
AAS0.7	55	80
AAS0.7SAP	35	70
AASF0.5	63	103
AASF0.532	68	133
AASF0.532SAP	64	109

4.3.4 Internal RH

Figure 4.6 shows the development of the internal RH in the internally cured mixture AAS0.552SAP and AASF0.532SAP. The measured RH_s of the pore solutions of the mixtures and the calculated RH_k (see Equation 3.1) are also shown in Figure 4.6. The RH results of non-SAP mixtures AAS0.5 and AASF0.5 had been shown in Figure 3.9.

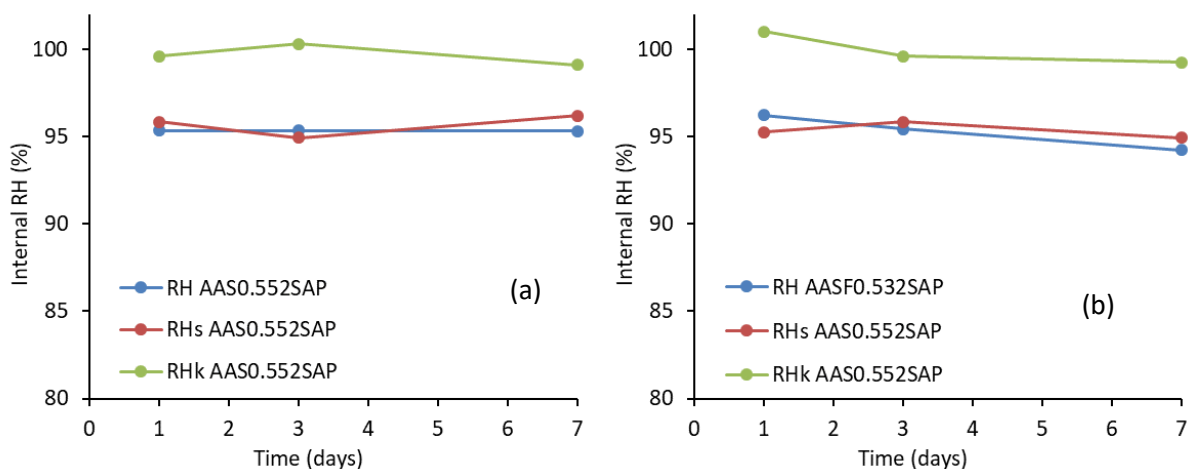


Figure 4.6 Internal RH results of AAS0.552SAP (a) and AASF0.532SAP (b). The RH_k was calculated with Equation 3.1.

It can be seen in Figure 4.6 that the RH_S of the pore solutions of the pastes is lower than 100% due to the presence of ions. The internally cured mixtures keep a RH_K close to 100% in the period studied. This indicates that the self-desiccation in AAS and AASF paste is successfully mitigated by the addition of SAPs.

4.3.5 Autogenous shrinkage

Figure 4.7 shows the autogenous shrinkage of the plain and internally cured AAS pastes in the first week of reaction. The starting times of the curves are Vicat setting time and the start of the acceleration period (8h and 11h for AAS and AASF pastes, according to chapter 3) in Figure 4.7 (a) and (b), respectively. To investigate the influence of higher SAPs contents, the autogenous shrinkage of mixtures with 0.5% and 1% of SAPs and correspondingly higher l/b ratios are also shown in Figure 4.7.

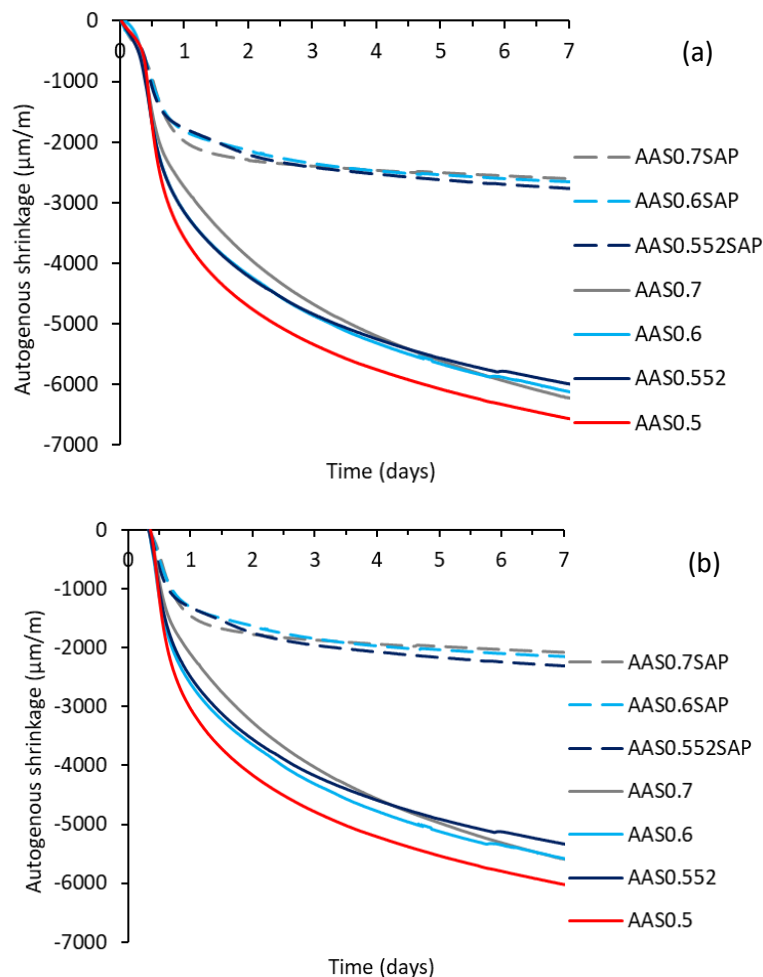


Figure 4.7 Autogenous shrinkage of AAS pastes with different l/b ratios and different amounts of SAPs, starting at Vicat final setting (a) or the start of the acceleration period (b). Same colours correspond to the same total liquid amount; dashed lines denote samples with SAPs.

It can be seen that increasing the liquid content (AAS0.6, and AAS0.7) without adding SAPs in AAS reduces the autogenous shrinkage only slightly. By adding 0.26 wt. % SAPs (AAS0.552) in AAS, the autogenous shrinkage is dramatically reduced, reaching only 1780 $\mu\text{m}/\text{m}$ 1 day and 2760 $\mu\text{m}/\text{m}$ at 7 days. The reduction proportions at 1 day and 7 days are 51% and 58%, respectively. Increasing the SAPs dosage (together with the corresponding absorbed liquid amount) to 0.5% or 1% (AAS0.6SAP and AAS0.7SAP), however, does not lead to any significant change in the measured shrinkage. Although the internally cured samples still shrink for nearly 1800 $\mu\text{m}/\text{m}$ within the first day, the absolute change of the autogenous shrinkage from 1 to 7 days is significantly lower compared to the ones for non-SAP samples.

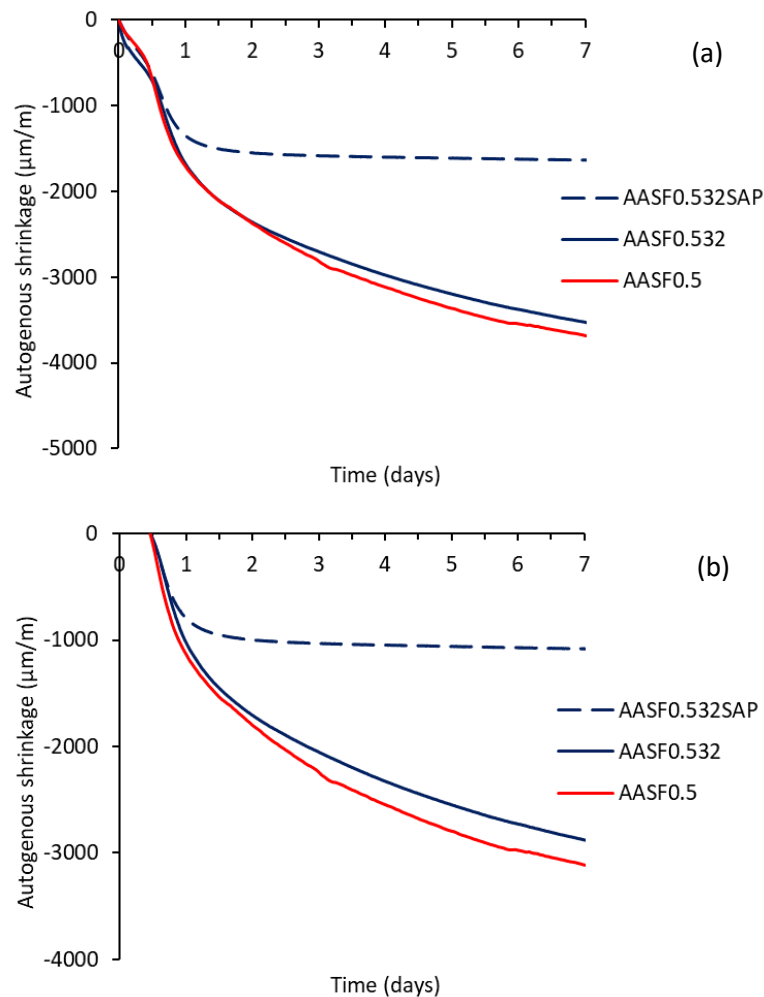


Figure 4.8 Autogenous shrinkage of AASF pastes with and without SAPs, starting at Vicat final setting (a) or the start of the acceleration period (b). Same colours correspond to the same total liquid amount; dashed lines denote samples with SAPs.

Since adding more SAPs than needed only brings a limited effect on the shrinkage mitigation, higher contents of SAPs than 0.16 wt. % were not considered for AASF pastes. The autogenous shrinkage of AASF with 0.16 wt. % of SAPs (AASF0532SAP) is shown in Figure 4.8 in comparison with the control mixture (AASF05) and the mixture with the same water content as SAPs-containing sample (AASF0532). Similar to AAS pastes, AASF paste with higher l/b ratio generates only slightly lower autogenous shrinkage compared to the control mixture after one

day. In the first hours, AASF0.532 shows even larger autogenous shrinkage than AASF0.5, however, this discrepancy disappears if the curves start at the beginning of the acceleration period (Figure 4.8 (b)). With the addition of SAPs, the autogenous shrinkage is reduced by more than 50% at 7 days. At a very early age, in contrast, the mitigating effect is less dominant.

4.3.6 CT scan

The evolution of the microstructure of a representative cross-section of AAS0.552SAP and AASF0.532SAP obtained by X-ray microtomography is shown in Figures 4.9 and 4.10, respectively. Based on the grey levels, several phases can be clearly distinguished within the paste (light grey in general), including unreacted slag particles (white and irregular), unreacted fly ash particles (white and spherical), SAPs with liquid (deep grey), entrapped air or hollow voids in fly ash (black and spherical) and newly formed voids within the SAPs-originated voids (black, marked by the arrows).

Figure 4.9 (a) and 4.10 (a) show the randomly distributed swollen SAPs particle in freshly cast AAS0.552SAP and AASF0.532SAP, respectively, indicating that the SAPs absorbed liquid before solidification of the paste. The size of SAPs after absorption can reach more than 0.5 mm. The irregular shape of SAPs after absorbing liquid is consistent with the shape of dry SAPs shown in Figure 4.1. Figure 4.9 (b) and 4.10 (b) show that at the age of 8h, voids are already formed within the cavities originally occupied by the swollen SAPs (marked by the arrows), indicating the liquid release from SAPs to the surrounding paste, i.e. internal curing. At the age of 1 day, the volume of newly formed voids increases, indicating that more liquid is released from the SAPs. It can be seen from Figure 4.9 (d) and 10 (d) that at the age of 7 days, most of the SAPs located in the chosen cross-section have been emptied, while some of them still have liquid stored inside, indicated by the dark grey colour of these SAPs-originated voids. This part of liquid may be useful for further reaction after 7 days. At the given resolution, no reaction products forming inside the SAPs voids could be identified.

Comparing Figures 4.9 and 4.10, we can see that AASF consumes less liquid from SAPs than AAS (marked by arrows), which is consistent with the lower chemical shrinkage of AASF compared to AAS.

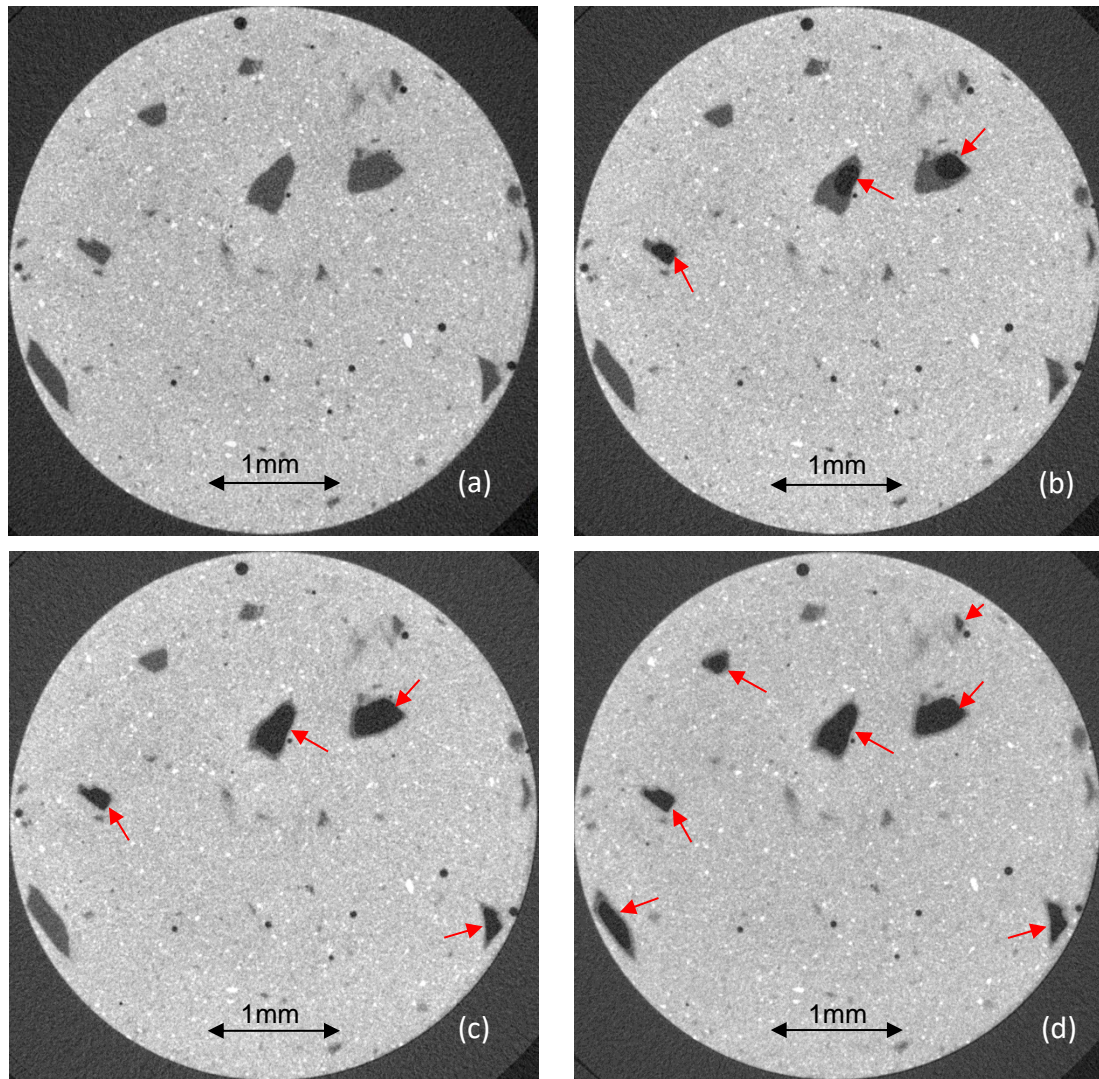


Figure 4.9 A representative cross-section of AAS0.552SAP paste obtained by X-ray tomography at the curing age of (a) 0h, (b) 8h, (c) 1d and (d) 7d. Several phases can be clearly distinguished within the paste (light grey) including unreacted slag particles (white and irregular), SAPs with liquid (deep grey), entrapped air (black and spherical) and newly formed voids within the SAPs-originated voids (black, marked by the arrows).

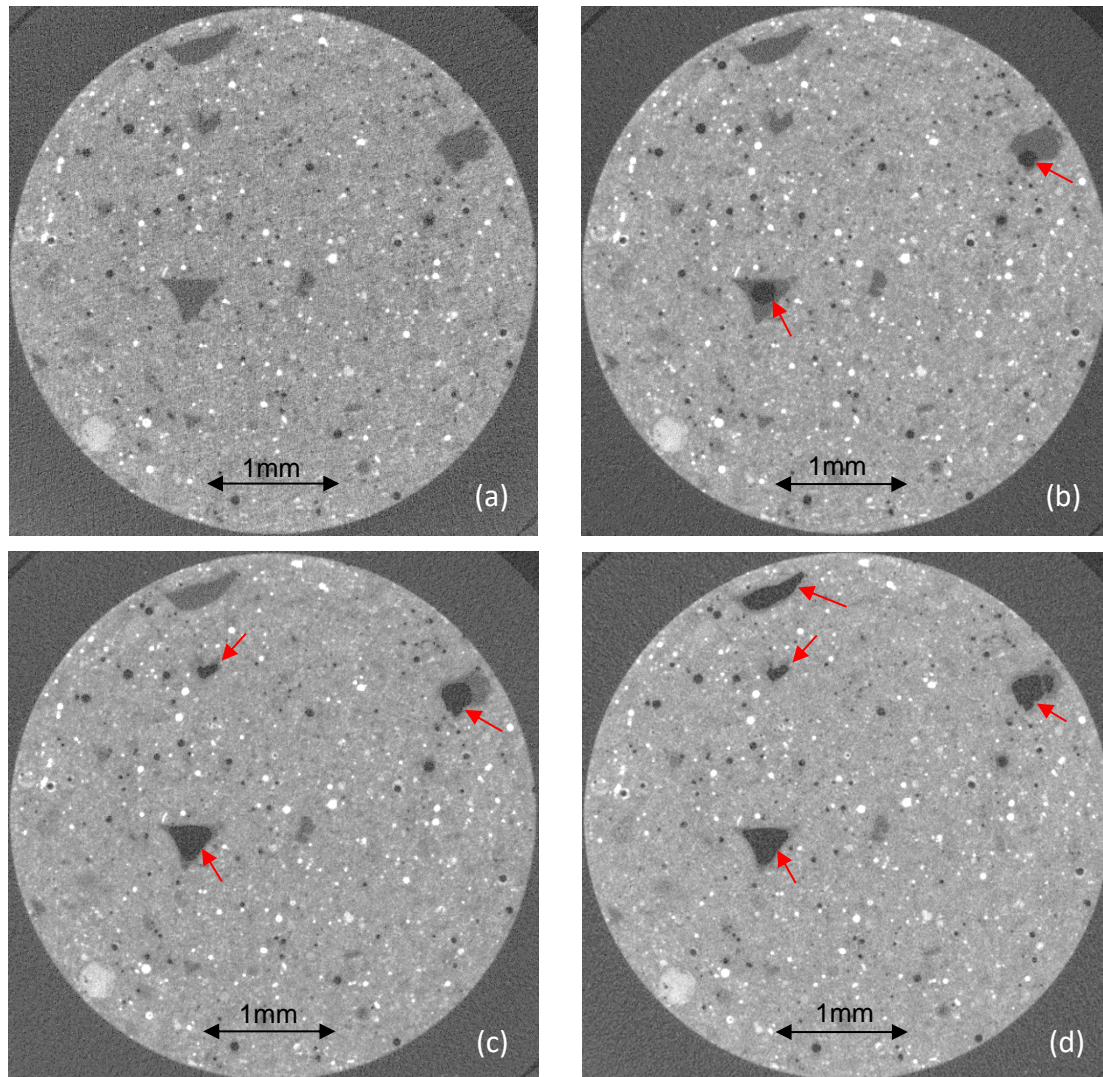


Figure 4.10 A representative cross-section of AASF0.532SAP paste obtained by X-ray tomography at the curing age of (a) 0h, (b) 8h, (c) 1d and (d) 7d. Several phases can be clearly distinguished within the paste (light grey) including unreacted slag particles (white and irregular), unreacted fly ash particles (white and spherical), SAPs with liquid (deep grey), entrapped air or hollow voids in fly ash (black and spherical) and newly formed voids within the SAPs-originated voids (black, marked by the arrows).

4.3.7 SEM analysis

Figure 4.11 (a) shows a representative SEM image of the microstructure of AAS0.552SAP paste cured for 7 days. Figure 4.11 (b) shows a representative interface between SAPs and the surrounding paste. From the images, the dry SAPs and the surrounding paste can be clearly distinguished based on the characteristics of the phases: SAPs have a locally porous microstructure while the paste is dense and homogenous. The SAP particle shown in Figure 4.11 (a) has a big void inside, with a smooth curved surface, as consistent with what has been observed from the CT results in Figure 4.10. A rim of paste can be observed surrounding the SAPs particle, with a relatively smooth surface and fewer unreacted slag particles embedded. This could be due to the liquid released from the SAP particle, resulting in a local increase of l/b ratio in the rim.

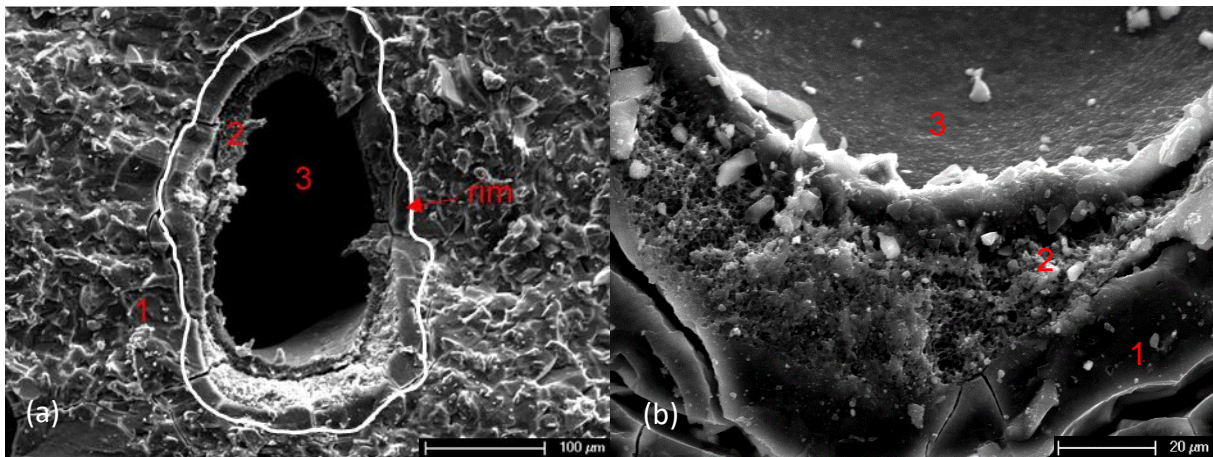


Figure 4.11 SEM images of the SAPs-originated voids in paste AAS0.552SAPs cured for 7 days. (a) shows a void that is partly filled by dry SAPs with a big emptied void inside. An interface between SAPs and surrounding paste is amplified in (b) showing the dense microstructure of the paste in comparison with the porous structure of dry SAPs. The red coloured number 1 indicates the paste, 2 indicates the dry SAPs and 3 indicates the SAPs-originated voids.

Two representative SEM images of the microstructure of internally cured AASF paste are shown in Figure 4.12. The dry SAPs in AASF0.532SAP show similar features to the ones in AAS0.552SAP. Unreacted fly ash particles can be observed embedded on the fractured surface. Besides the SAPs-originated voids, surrounding AASF paste also shows a dense microstructure with no big capillary pores. A difference from AAS0.552SAP is that AASF0.532SAP does not show clear rims surrounding the SAPs voids. As discussed above, the rim in AAS paste is probably due to the locally increased l/b ratio resulting from the liquid desorption from SAPs. For AASF paste, the basic l/b ratio is the same, 0.5; however, due to the much lower reactivity of fly ash compared to slag, the liquid-to-“real” binder ratio in AASF paste is actually much higher than in AAS. Therefore, the extra supply of liquid from SAPs does not make a significant difference to the surrounding.

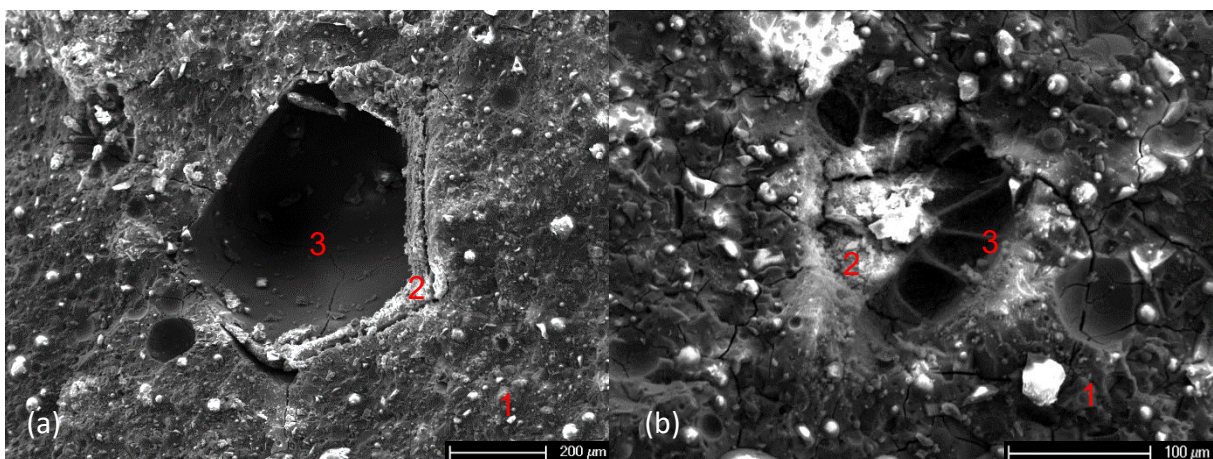


Figure 4.12 SEM images of the SAPs-originated voids in paste AASF0.532SAP cured for 7 days. (a) shows a void that is partly filled by dry SAPs with a big emptied void inside and (b) shows a void that is mostly filled with dry SAPs. The red coloured number 1 indicates the paste, 2 indicates the dry SAPs and 3 indicates the SAPs-originated voids.

4.3.8 Mechanical properties

The compressive and flexural strength of AAS and AASF pastes are shown in Figure 4.13 and 4.14, respectively. For both systems, the compressive strength decreases with increased l/b ratio, and decreases are more significant for pastes with SAPs. The difference in compressive strength between AAM pastes with and without SAPs does not decrease with time.

The flexural strength of the paste slightly decreases with increasing l/b ratio at 14 h. When SAPs are incorporated, a similar or even higher flexural strength is shown at a very early age for both systems. For AAS, the internally cured mixtures do not show a flexural strength much different from the control mixture at 6 days, considering the scatter in the results. For AASF, in contrast, a considerably higher flexural strength is seen for internally cured paste at 7 days. It is also noted that the flexural strength of AASF0.5 and AASF0.532 decreases with time, which is not observed for other mixtures. A discussion about the influences of SAPs on the strength developments will be given in session 4.4.4.

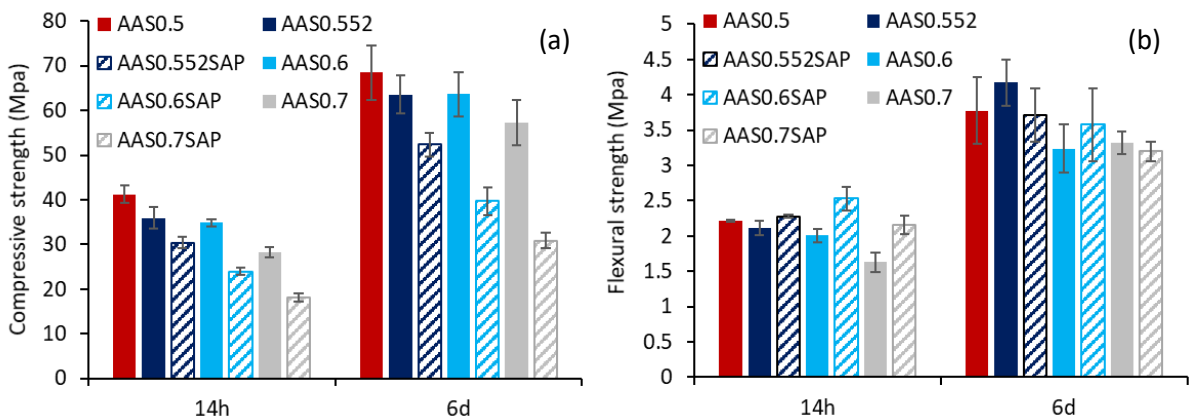


Figure 4.13 Compressive strength (a) and flexural strength (b) of AAS pastes with and without SAPs.

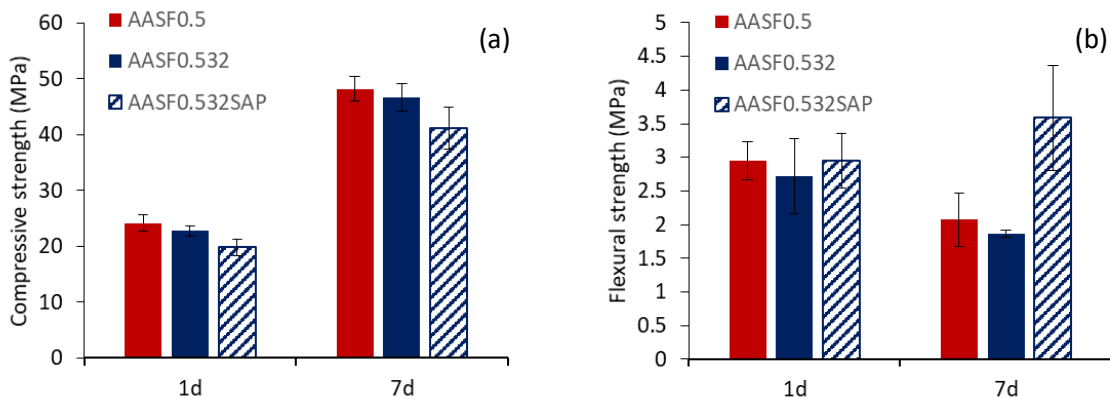


Figure 4.14 Compressive strength (a) and flexural strength (b) of AASF pastes with and without SAPs.

The evolution of elastic moduli of internally cured AAM pastes is shown in Figure 4.15 in comparison with the control mixtures. It can be seen that the incorporation of SAPs into the system does not result in a decrease in the elastic modulus. The elastic modulus of the internally cured pastes develops at the same pace as the control mixtures.

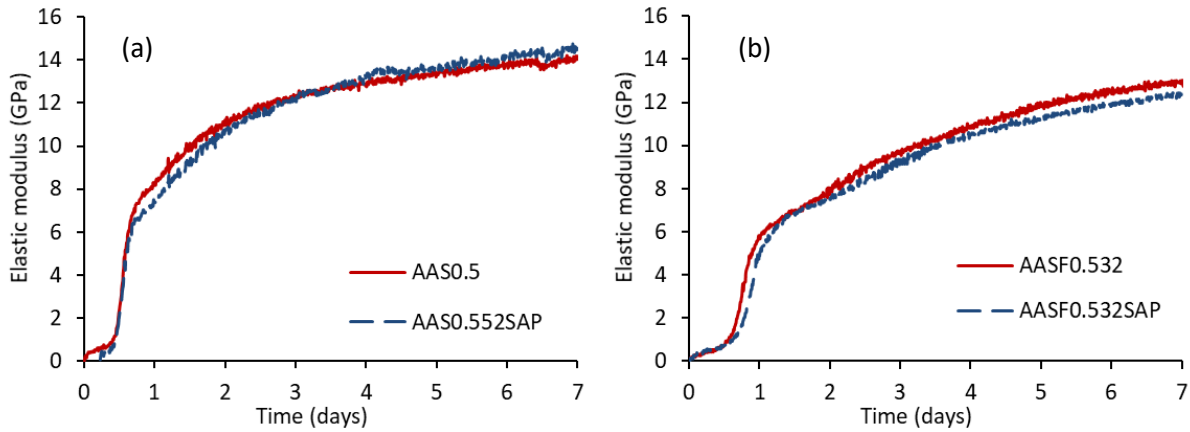


Figure 4.15 Elastic modulus of AAS paste and AASF paste with and without SAPs.

4.4 Discussion

4.4.1 Absorbing and releasing behaviours of SAPs

According to Figure 4.2, the SAPs absorb the most in deionized water and the least in the activator. This is consistent with the lower absorption capacity of SAPs in cement filtrate solution than in deionized water [187], since different ion concentrations result in different osmotic pressures of the solution. The absorption capacity of SAPs in water, 200 g/g at 24 hours, is comparable with the data reported in the literature for similar types of SAPs [115]. In NaOH solution, in contrast, there are large amounts of Na^+ and OH^- , which lead to screening of the repulsive interactions between charged groups within the polymer network and thus reduce the osmotic pressure. Therefore, the SAPs absorb much less NaOH solution than deionized water.

Compared with the NaOH solution, the activator contains the same amount of Na^+ , but part of the OH^- is substituted by SiO_3^{2-} . According to [188–190], divalent ions (e.g. Ca^{2+} and SO_4^{2-}) can better screen the charges of SAPs than monovalent ions (e.g. Na^+ , K^+ , OH^- and NO_3^-), thus reduce the swelling of SAPs. The SiO_3^{2-} in the activator may have a similar effect, which would result in a lower absorption capacity of SAPs than in NaOH solution. Besides SiO_3^{2-} , part of Si in the activator exists as monomer (SiO_2 or $\text{Si}(\text{OH})_4$) or even oligomers [191,192], but the influence of these species on the absorption capacity of the SAPs is not known.

Besides the absorption capacity, the influence of SAPs on the ion concentrations in the alkali solution also needs to be considered. For alkali-activated materials, the reaction kinetics and the microstructure development largely depend on the ion concentrations of the pore solution. If SAPs preferentially absorbed water or ions, the concentration of the ions in the pore solution would be affected. For example, the SAPs used in [193] were found to release Na^+ and OH^- and affect the hydration kinetics. As shown in Figure 4.3, the ion concentrations

in the activator remain nearly unchanged after absorption by SAPs, indicating that the internal curing by SAPs influences the paste mainly by providing extra activator rather than affecting the initial ion concentrations of the pore solution. This information helps to understand the reaction kinetics of the internally cured mixtures, which will be discussed in detail in the next section.

The SAPs start to release liquid in the initial hours (before 8 h from mixing) as indicated by the CT scan results (Figure 4.9-4.10). Voids start to form inside the SAPs particles, similar to the phenomenon observed in SAPs-containing OPC-based systems [194]. What is different is that not much reaction products are formed within the voids left by SAPs in AAM systems in the first week of curing, as indicated in Figure 4.9-4.12. In OPC systems, reaction products, especially portlandite, can grow or even fill the voids left by SAPs [114]. In AAM systems, in contrast, amorphous C-A-S-H gels, which are the main reaction products (as proven in chapter 3), usually do not grow in large voids. Nonetheless, it is not excluded that a layer of reaction products can form at the original interface between SAPs particles and the paste, which cannot be clearly distinguished in the CT scan (Figures 4.9 and 4.10) at the current resolution. Due to the large size of the empty pores within SAPs voids, the internal RH in the paste with SAPs during the first week would be kept very close to 100% if the ions' effect is not considered. This is in line with the RH results shown in Figure 4.6.

4.4.2 Reaction kinetics and setting

The initial reaction rate of the paste is critically influenced by the alkalinity of the activator, which controls the dissolution of the precursors [195]. Since the composition of the activator was kept constant with different l/b ratios and the absorption of SAPs does not change the ions concentration of the surrounding solution, the heat evolution and total heat release of different mixtures in the initial hours are rather similar (Figure 4.4). The main heat evolution peak indicates the formation of a large amount of reaction products, i.e. C-A-S-H gels, from the ions in the activator and new ions dissolved from the slag and/or fly ash. The l/b ratio and the presence of SAPs have major influences on the reaction in this stage. To explain this, a schematic diagram on the pore structure of pastes with and without SAPs is shown in Figure 4.16.

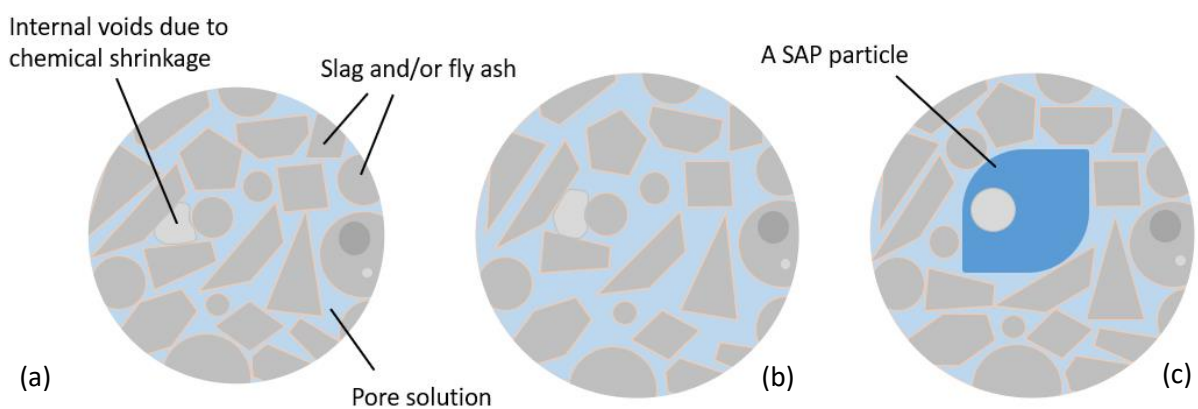


Figure 4.16 Schematic representation of the pore structure of the control paste (a), paste with extra liquid but without internal curing by SAPs (b) and paste with extra liquid with internal curing by SAPs (c).

Plain pastes (without SAPs)

For the pastes without SAPs, the activator is evenly distributed in the interstitial space. At higher liquid content, the space between the precursor particles is enlarged (comparing Figure 4.16 (a) and (b)) and more silicates and alkali ions are present in the pore solution. Hence, more ions, such as Ca^{2+} and Al^{3+} , need to be dissolved from the precursor to reach critical Ca/Si and Al/Si in the pore solution before the reaction rate reaches a peak. For this reason the heat evolution peak appears later for mixtures with higher l/b ratios without SAPs. Due to the presence of a higher amount of ions at the heat peak, the amplitudes of the heat release peak becomes higher. Since the mixtures with higher l/b ratios without SAPs have larger initial interstitial porosity, more time is needed before the transport of ions can be inhibited. Therefore, the mixtures with higher l/b ratios without SAPs show longer acceleration periods, as indicated by the broader heat flow peaks (Figure 4.4 (a) and 4.5 (a)). The higher amount of reactants from the activator and the longer acceleration period contribute to the higher total heat release of the mixture with higher l/b ratio without SAPs (Figure 4.4 (b) and 4.5 (b)). The delayed appearance of the reaction peak and the increased total reaction degree of the pastes with higher l/b ratios are similar to what has been reported for OPC paste [48,196,197].

Pastes with SAPs

For the pastes with SAPs, in contrast, the extra activator is stored in the SAPs particles before being released (comparing Figure 4.16 (a) and (c)). The ions in SAPs are not instantaneously available for the reactions with the precursor compared to the ions in the interstitial space [196]. The activator will gradually be released from SAPs, on one hand, providing more ions that are reactants to the adjacent paste and, on the other hand, increasing the water content that can dilute the concentrations of Ca^{2+} and Al^{3+} dissolved from the precursors. The increment of Ca/Si and Al/Si in the pore solution till which the C-A-S-H gels can rapidly form is, therefore, delayed. Hence, compared to the control mixture with the same basic l/b ratio, the start of the acceleration period is a bit delayed and the magnitude of the peak reaction rates is slightly lowered when SAPs is present (Figure 4.4 (a) and 4.5 (a)). Nonetheless, the buffering effect decreases as the activator is continuously released from the SAPs. Due to the higher activator content of SAPs-containing mixtures than in the control mixtures, the reaction degrees are higher at 7 days, as indicated in Figure 4.4(b). For AASF paste, the liquid-to-“real” binder (slag) ratio is already very high. The reaction rate is dominated by the content of slag rather than the amount of activator. Therefore, the extra liquid from SAPs does not induce an apparent increase in the total reaction heat.

Pastes with the same liquid content

Compared with the mixtures with the same liquid content but without SAPs, SAPs-containing mixtures have the same initial total porosity, but different pore size distribution. Since a large amount of liquid is stored in the SAPs, internally cured mixtures have, besides the macro voids induced by SAPs, finer interstitial pore space in between the precursor particles (comparing Figure 4.16 (b) and (c)). The finer interstitial pore size means a smaller space for the formation of reaction products around slag particles and thus a faster solid-phase percolation. After a large amount of reaction products are formed in the interstitial space, the further dissolution of precursors and the transportation of ions would be inhibited (see the dense microstructure of the pastes in Figure 4.11 and 4.12). Therefore, the reaction rate of SAPs-containing paste is

slower than in the paste with the same total l/b ratio without SAPs, especially after the acceleration period. The smaller amount of activator that is instantaneously available for the reaction and the limited interstitial space for transport and formation of reaction products induce a lower reaction rate after the acceleration period, and thus a lower total reaction degree of internally cured mixtures compared to the mixtures with the same l/b ratio but without SAPs.

The time of the initial and final setting of the pastes is also delayed for mixtures with higher l/b ratios. However, it should be noted that the delay in setting time is not directly associated with the delayed heat flow peak, since the setting of the pastes happened much earlier than the beginning of the acceleration period, as discussed already in chapter 3. In the setting mechanism, the initially effective l/b ratio plays a more important role since it determines the initial interstitial porosity of the paste. A finer interstitial porosity between the precursor particles ensures a shorter distance for the diffusion of Ca^{2+} and Al^{3+} from the precursor to form reaction products that can fill the space. Although internally cured mixtures contain large voids initially occupied by SAPs, these voids matter much less than the interstitial pores for the setting of the paste. For internally cured pastes, the basic l/b ratio is similar to the control mixture, so the initial setting times of the internally cured pastes are quite close to that of the control mixture. This phenomenon is consistent with the finding for internally cured OPC pastes [114]. For the paste without SAPs, however, the final setting time increases significantly with increased l/b ratio. The delay of setting by internal curing is beneficial to AAM systems, which are known to set too fast, but this beneficial delay comes at the expense of a loss in compressive strength, as shown in Figure 4.13 and 4.14.

4.4.3 Mitigating effect of internal curing on autogenous shrinkage

It has already been proven through internal RH results and CT scan that the incorporation of SAPs with extra activator successfully provides internal curing to the AAM pastes. Within the first 7 days, the liquid stored in the SAPs particles is enough to compensate for the liquid consumption in the systems (Figure 4.9 and 4.10). However, as shown in section 4.3.5, the internal curing cannot eliminate the autogenous shrinkage of AAM pastes regardless of the SAPs content. This finding confirms the suggested existence of a part of autogenous shrinkage that is not induced by self-desiccation. According to chapter 3, the autogenous shrinkage induced by a steric-hydration force highly correlates with the reaction rate and the early-age microstructure formation in AAMs. To this part of autogenous shrinkage, internal curing cannot contribute much, since the incorporation of liquid reservoirs into the system has limited effects on the reaction rate and the micro-scale pore structure, as shown in this chapter.

In Figure 4.17, the autogenous shrinkage of internally cured pastes is plotted together with the shrinkage under externally saturated condition (ε_{ste} , see Figure 3.11). It can be seen that the autogenous shrinkage of internally cured AAS and AASF is slightly higher than the corresponding ε_{ste} , which indicates that AAM pastes shrink less with externally provided liquid than with internal curing. For AAS paste, the difference between ε_{ste} and the autogenous shrinkage of SAPs-containing pastes is relatively small at 1 day, and becomes larger with elapse of time, reaching around 600 $\mu\text{m}/\text{m}$ at 7 days. For AASF paste, in contrast, the difference mainly arises on the first day and becomes more stable at a later age.

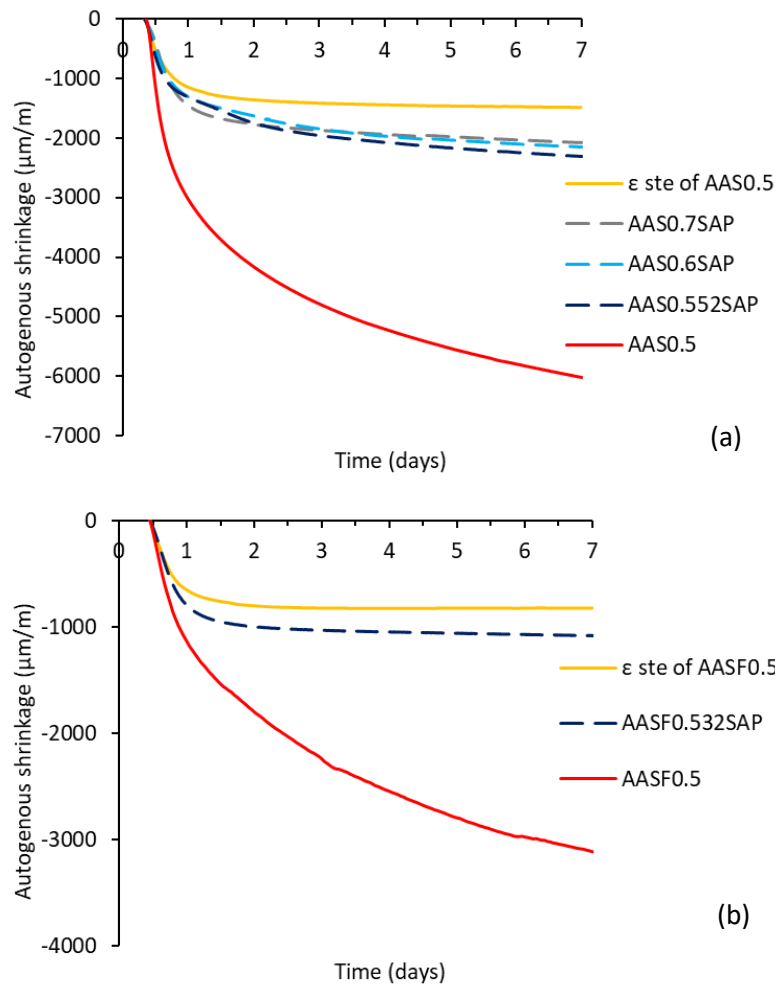


Figure 4.17 Autogenous shrinkage of internally cured AAS paste (a) and AASF paste (b), in comparison with the shrinkage under saturated condition (see Figure 3.11).

There are two possible reasons for the higher autogenous shrinkage of internally cured pastes than the corresponding ϵ_{ste} . First, there may be a part of the paste that cannot be readily cured by SAPs when the microstructure becomes dense. Due to the big particle size of the SAPs utilized (Figure 4.1), the number of SAPs particles added into AAM pastes is limited. Some residual pore pressure due to self-desiccation may exist in some parts of the paste that is relatively far from the SAPs [198]. The second reason may lie in that the air pressure in and out of the corrugated tube are different. Unlike ϵ_{ste} , that is measured with externally added solution, the shrinkage of internally cured samples is measured under sealed condition (what “autogenous” means), and the continuous formation of internal voids in the paste would inevitably induce a lower air pressure in the system. The air pressure difference between inside and outside the sealed tube can be close to 0.1 MPa (atmospheric pressure) depending on the vacuum degree in the paste. Due to the relatively low elastic modulus and evident viscosity of AAMs, the influence of the air pressure difference on the autogenous shrinkage might not be negligible.

It is likely that the ϵ_{ste} indicates an ultimate mitigating effect on autogenous shrinkage that can be reached by internal curing. In other words, the part of autogenous shrinkage that is not

induced by self-desiccation cannot be mitigated by internal curing, however high is the dosage of SAPs. To further mitigate the autogenous shrinkage of AAM pastes, attention needs to be paid to strategies that can reduce ε_{ste} . This will be the aim of chapter 5.

4.4.4 Mechanical properties

As shown in Figures 4.13 (a) and 4.14 (a), the compressive strength of AAM pastes is decreased with increased l/b ratio. This phenomenon is generally in line with what is observed in OPC, since higher l/b ratio normally means higher porosity and, therefore, lower compressive strength [114,199,200]. The presence of SAPs decreases the compressive strength of AAM pastes further due to the incorporation of macro-level voids. Later, the difference in the compressive strength between mixtures with higher l/b ratio without SAPs and the control mixture decreases, while the difference between the SAPs-containing mixtures and the control mixture does not. This is because the larger interstitial spaces in mixtures with higher l/b ratios without SAPs can be more easily filled by reaction products during further reaction, compared to the voids originated from SAPs. With the reaction going on, the microstructure of pastes with higher l/b ratios without SAPs becomes denser and denser, but the SAPs-originated voids will mostly remain as defects, as shown in Figure 4.9 and Figure 4.10. This finding has been confirmed by the higher total reaction heat of non-SAPs samples compared to that of SAPs-containing samples with the same l/b ratio (Figure 4.4 and 4.5).

Figures 4.13 (b) and 4.14 (b) show that the internally cured samples show comparable or even higher flexural strength relative to the control mixture. The reason why the flexural strength is not significantly reduced by SAPs-originated voids may lie in their mitigation effect on the development of microcracking. While compressive strength depends mainly on the porosity of the paste, the three-point bending flexural strength is more sensitive to the microcracking. As reported in many studies [90,201,202], AAM paste is prone to shrinkage-induced microcracking. Although the pastes are not under externally restrained condition during curing, the unreacted precursor particles can act as local restraints to the autogenous shrinkage of surrounding gels [203]. Due to the large autogenous shrinkage of the paste, microcracks may have developed, especially at an early age when the strain capacity of the paste remains low. When internal curing is applied to the paste, the autogenous shrinkage is mitigated, and so is the development of microcracking. Therefore, the flexural strength of internally cured samples is not reduced, although their liquid contents are higher than the control mixture.

Shrinkage-induced microcracking can also be the reason why AASF0.5 shows higher flexural strength at 1 day than at 7 days. From 1 day to 7 days, the autogenous shrinkage of AASF paste experiences a rapid increase, which contributes to the development of microcracking, and hence a reduced flexural strength. Hence, it seems the reaction time has a coupled effect on the flexural strength: on one hand, the microstructure becomes denser, but on the other hand, microcracking can develop due to continuing autogenous shrinkage. With internal curing, the detrimental effect of autogenous shrinkage is mitigated, so AASF0.532SAPs shows the higher flexural strength among AASF mixtures at 7 days. This may also explain why the SAPs incorporation does not result in a lower elastic modulus of AAM pastes (Figure 4.15), since the elastic modulus is sensitive not only to the porosity but also to the microcracking [204,205].

Considering the detrimental impact on the compressive strength of internal curing and the limited mitigation of autogenous shrinkage by higher contents of SAPs, it seems that the dosage determined based on chemical shrinkage is the optimal dosage to provide internal curing to AAS paste. Further increasing the dosage would not have any significant positive effect.

4.5 Concluding remarks

In this chapter, the absorption and desorption behaviour of SAPs in AAM systems are studied and the mechanism of mitigation effect on autogenous shrinkage of AAMs is clarified. The influences of SAPs incorporation on the mechanical properties of AAM pastes are also studied. Based on the results obtained, the following remarks can be made:

1. The SAPs show a lower absorption capacity in alkali-activator than in water and pure NaOH solution. Little absorption preference for water or ions is observed. In the internally cured samples, the SAPs start to release liquid to the surrounding paste from before 8 h. After the first week, there is still a certain amount of liquid left in SAPs for mixtures AAS0.552SAP and AASF0.532SAP, indicating a further internal curing potential for later reactions. In the period studied, there is a negligible amount of reaction products filling the SAPs voids.
2. Internal curing by SAPs prolongs the time of final setting and the time at which the peak of reaction heat occurs, but it increases the total reaction degree of AAS paste at longer-term due to the higher content of activator. For AASF paste, increasing the liquid content has a minor influence on the total reaction degree, regardless of the presence of SAPs.
3. Internal curing by 0.26 wt. % and 0.16 wt. % of SAPs can effectively mitigate the autogenous shrinkage of AAS and AASF paste. These dosages are designed on basis of the chemical shrinkage of the paste and the absorption capacity of SAPs measured by the teabag method. Larger contents of SAPs are found not to bring further mitigation of autogenous shrinkage.
4. While the flexural strength and elastic modulus of AAMs are only slightly influenced by the addition of SAPs, the compressive strength can exhibit substantial reduction.

Chapter 5

Mitigation strategies of autogenous shrinkage of AAMs Part 2: incorporation of metakaolin

5.1 Introduction

The results of chapter 4 show that the autogenous shrinkage of AAMs induced by self-desiccation can be effectively mitigated by internal curing with SAPs. However, the internal curing has a very limited effect on the autogenous shrinkage in the very early age, e.g. in the first day. According to chapter 3, a significant part of the early age autogenous shrinkage of AAMs is not induced by self-desiccation and highly correlates with the reaction rate and the early-age microstructure formation in AAMs. To further mitigate the autogenous shrinkage of AAMs, strategies that can modify the reaction kinetics and the microstructure evolution of the paste at the early age needs to be identified.

In fact, replacing slag by fly ash is already a way to reduce the reaction rate and to coarsen the pore structure. As shown in chapter 3, for example, AASF paste shows a slower reaction rate (Figure 3.5) and a coarser pore structure (Figure 3.7) than AAS paste. As a result, the autogenous shrinkage of AASF paste with slag/fly ratio of 50/50 is 40% lower than that of AAS paste (Figure 3.2). Similar reductions on autogenous shrinkage by incorporation of fly ash can be found in [19,87,88,123]. However, this reduction is mainly due to the lower content of slag and the role of fly ash in AASF is mainly as a filler in the early age reactions, as clarified in chapter 3. Therefore, the strategy of replacing slag by fly ash is not promising enough to mitigate the autogenous shrinkage of AAMs.

Metakaolin (MK) is another widely used type of aluminosilicate material for synthesizing AAMs or geopolymers [13,14,206]. Compared with fly ash, MK is more reactive at ambient temperature upon alkali activation, so it may have advantages over fly ash in terms of influencing the reaction kinetics and microstructure of AAS. Besides, it was found that the alkali activation of MK can generate chemical expansion during geopolymerization [46]. Therefore, MK may have a promising potential to mitigate the autogenous shrinkage of slag-based AAMs.

Regarding slag and MK blended AAM systems, many studies have been carried out on their microstructural characteristics and engineering properties [207–210]. For the reaction products, the coexistence of C-A-S-H gel and N-A-S-H gel was found when the blended system

Parts of this chapter have been published in:

Zhenming Li, Marija Nedeljković, Boyu Chen, Guang Ye. Mitigating the autogenous shrinkage of alkali-activated slag by metakaolin. *Cement and Concrete Research*. 122 (2019) 30–41.

was cured at elevated temperature [207–209]. At ambient temperature, the reaction products were found to be dominated by C-A-S-H type gel, part of which can be C-(N)-A-S-H where Ca was replaced by Na, but the 2D gel structure remained [140,211]. The addition of a small amount of MK in AAS was found to improve the workability [212], postpone the final setting [212], enhance the flexural strength [213], and decrease the chloride permeability of AAS [213]. Moreover, MK also helps to mitigate the alkali-silica reaction and enhance the high-temperature stability of AAS mortar [214]. A disadvantage induced by addition of MK is the increase of the carbonation rate of AAS [215]. MK addition also leads to a potential reduction in the compressive strength, but that is only to a limited extent, especially when the content of MK is low (e.g. 10% - 20%) [213,216]. Given the improvements in the properties of AAS by addition of MK, it would be very interesting to know its potential to mitigate the autogenous shrinkage of AAS and AASF.

The aim of this chapter is, therefore, to investigate the effectiveness of MK in mitigating the autogenous shrinkage of AAS and AASF, and to study the underlying mechanisms. For this purpose, the development of autogenous shrinkage, microstructure, chemical shrinkage and shrinkage under the saturated condition of AAM pastes with and without MK are comprehensively investigated. The mechanical properties of the pastes are also measured.

5.2 Methodological approach

5.2.1 General framework of this chapter

Firstly, the autogenous shrinkage of AAM pastes with and without MK is tested and discussed. Secondly, the mitigation mechanism of autogenous shrinkage by MK was explored. The framework of this part is shown in Figure 5.1. According to the conclusions of chapter 3, the autogenous shrinkage of AAM consists of two parts: shrinkage induced by decreasing steric-hydration force and shrinkage induced by increasing pore pressure. The elastic modulus of the paste reflects the resistance to the driving forces of the autogenous shrinkage [58,65]. These parameters are all dependent on the microstructure development of the paste. Therefore, the reaction kinetics, reaction products, ions concentrations of the pore solution and pore structures of AAM with and without MK were comprehensively studied. The evolution of ε_{ster} , chemical shrinkage and internal RH were measured. The elastic modulus of the pastes was tested as well.

Thirdly, the compressive and flexural strength of the pastes were measured to evaluate the influence of MK incorporation on these mechanical properties of AAM pastes.

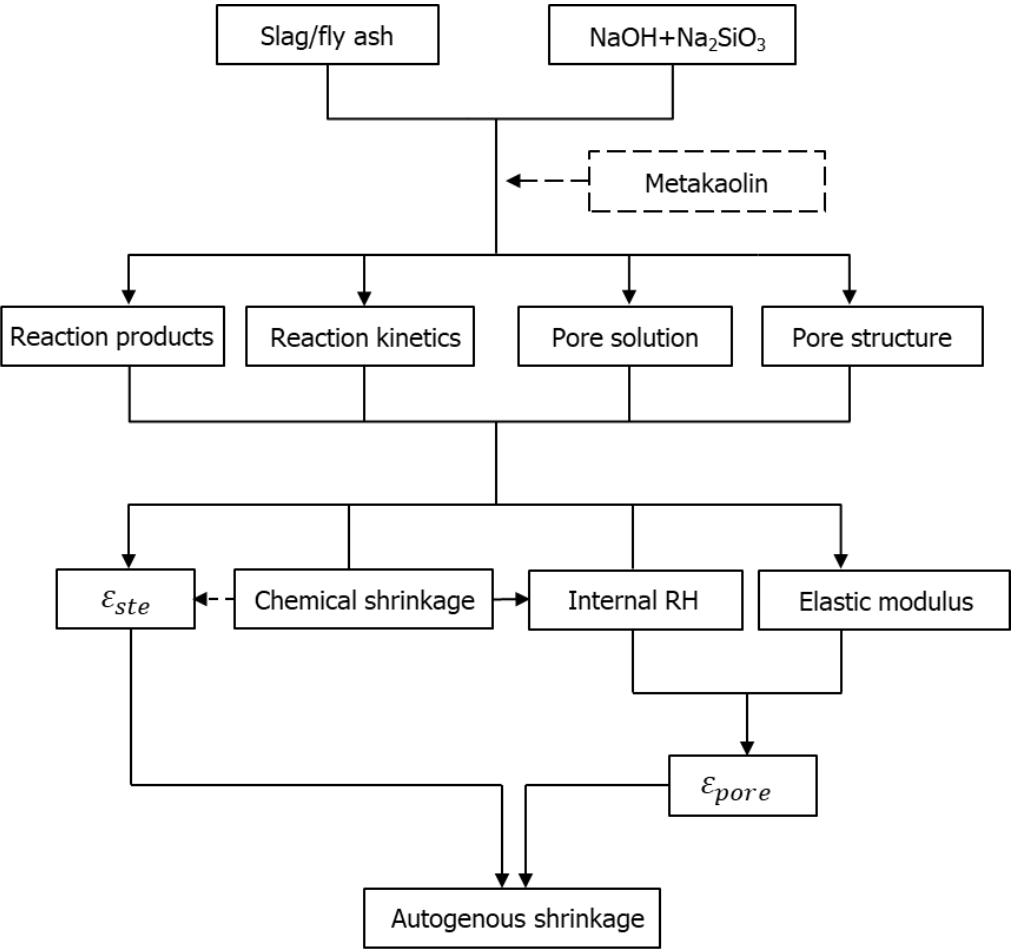


Figure 5.1 Approach to study the autogenous shrinkage-mitigating mechanism of MK addition.

5.2.2 Raw materials and mixture proportions

The raw materials used in this chapter are slag, fly ash and MK. The chemical compositions and physical properties of slag and fly ash can be found in chapter 3. MK was supplied by Argeco (France). The particle size of the MK is between 0.15 and 142 μm, with a d₅₀ of 69.4 μm. The chemical composition of MK determined by XRF is shown in Table 5.1. Part of the high percentage of silica content is due to the presence of quartz (43% in weight) in the raw material, which remains inert during the reaction process [217]. The mineralogical composition of MK determined with XRD is shown in Figure 5.2.

Table 5.1 Chemical compositions of MK measured by XRF.

Precursor	Component (mass% as oxide)									
	SiO ₂	Al ₂ O ₃	CaO	MgO	Fe ₂ O ₃	SO ₃	K ₂ O	TiO ₂	Other	LOI
MK	55.14	38.43	0.55	-	2.6	-	0.17	1.12	0.14	1.85

LOI= Loss on ignition

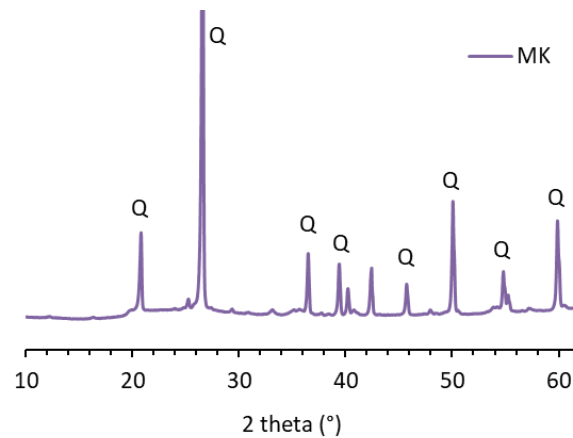


Figure 5.2 XRD pattern of MK. Q stands for quartz.

The alkaline activator was prepared in the way as described in chapter 3. A relatively high alkaline environment (9.3% Na_2O by mass of the binder) was created to attain good mechanical properties of the mixtures (according to [38,39,213]). The mix design of the pastes is shown in Table 5.2. Slag is substituted by MK by 10% - 20% in AAS pastes and AASF pastes. The fly ash content is kept constant in AASF pastes. All the samples were cured in sealed condition at 20°C.

Table 5.2 Mixture proportions of AAS and AASF pastes with and without MK.

Mixture	Slag (g)	Fly ash (g)	MK (g)	SiO_2 (mol)	Na_2O (mol)	H_2O (g)
S100	1000	-	-	1.146	1.5	420
S90MK10	900	-	100	1.146	1.5	420
S80MK20	800	-	200	1.146	1.5	420
S50F50	500	500	-	1.146	1.5	420
S45F50MK5	450	500	50	1.146	1.5	420
S40F50MK10	400	500	100	1.146	1.5	420

5.2.3 Experimental methods

5.2.3.1 Autogenous shrinkage measurement

The autogenous shrinkage of the pastes was measured according to the procedure as described in section 3.2.2.1.

5.2.3.2 Characterization of the paste

The pastes were characterized by XRD, FTIR, isothermal calorimetry and nitrogen adsorption according to the procedures described in section 3.2.2. The calorimetry test results were normalized by the weight of the paste. Initial and final setting times of the mixtures were determined by using the Vicat needle method [218].

Pore solution chemistry of paste was measured by using ICP-OES with Optima 5300 DV. The

concentrations of Na, Ca, Si and Al in the pore solutions extracted from the pastes cured for 1 day and 7 days were determined. The titration method with 0.1M HCl solution was used to measure the concentration of OH⁻ in the pore solutions. Three replicates were tested and the average results are presented.

5.2.3.3 Chemical shrinkage and shrinkage under saturated condition (ε_{ste})

The chemical shrinkage of the pastes was measured according to the gravimetry method. The detailed procedure was described in [46]. The average chemical shrinkage of three replicates is presented for each mixture.

The volume change under saturated condition (ε_{ste}) of the pastes was measured according to the procedures described in section 3.2.2.

The internal RH of the pastes was measured according to the procedures described in section 3.2.2. The calculation of the pore pressure from the RH results was shown in Equations 3.1-3.4.

5.2.3.4 Mechanical properties

The flexural and compressive strength of the pastes at the age of 1 day and 7 days were tested as per NEN-196-1 [186].

The quasi-static elastic modulus of the pastes was measured on 40 × 40 × 160 mm³ prisms at the age of 1 day and 7 days. The loading was provided by a hydraulic actuator with a maximum load of 100 kN. The strain was measured by four transducers (LVDTs) on each side of the sample. The loading consisted of four cycles with the load ranges from 5% to 30% of the compressive strength and only the stress and strain obtained from the latter three cycles were used to calculate the mean elastic modulus. The loading and unloading were under displacement control and the rate was 0.004 mm/second (around 0.6 MPa/second) [219]. Three specimens were tested for each mixture at each age.

5.3 Results and discussion

5.3.1 Autogenous shrinkage

The autogenous shrinkage of AAS pastes with and without MK is shown in Figure 5.3. The curves shown in Figure 5.3 (a) start at the traditional time-zero, i.e. Vicat setting time, while the ones in Figure 5.3 (b) start at the beginning of the acceleration period, as suggested in chapter 3. It can be seen that the plain AAS paste shrinks rapidly after the final set. When 10% slag is substituted by MK, the autogenous shrinkage is reduced by 45% at 1 day and 38% at 7 days. A larger content of MK to 20% leads to a further reduction in autogenous shrinkage, irrespective of the time-zero of the curves.

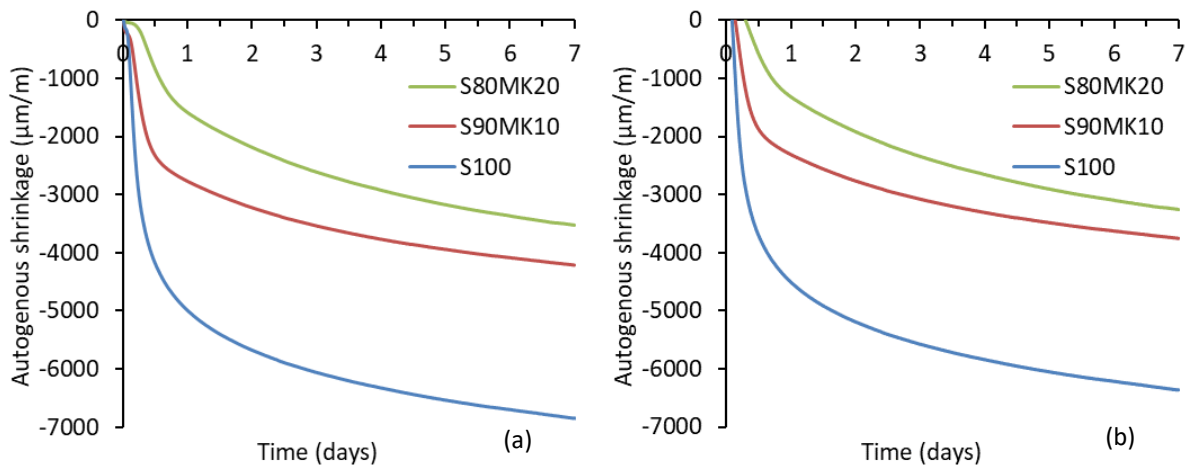


Figure 5.3 Autogenous shrinkage of AAS pastes with and without MK, starting at Vicat setting time (a) or the start of the acceleration period (b). Detailed results on setting time and reaction heat are shown in section 5.3.2.3.

The autogenous shrinkage of AASF pastes with and without MK is shown in Figure 5.4. The autogenous shrinkage of plain AASF paste is lower than that of AAS paste. Substituting slag by MK leads to a reduction of autogenous shrinkage. When 20% of slag is replaced by MK, the autogenous shrinkage is reduced by 65% at 1 day and 24% at 7 days, if the curves start at the final setting times. If the curves are zeroed at the start of the acceleration period, the mitigation effect by MK is even more pronounced.

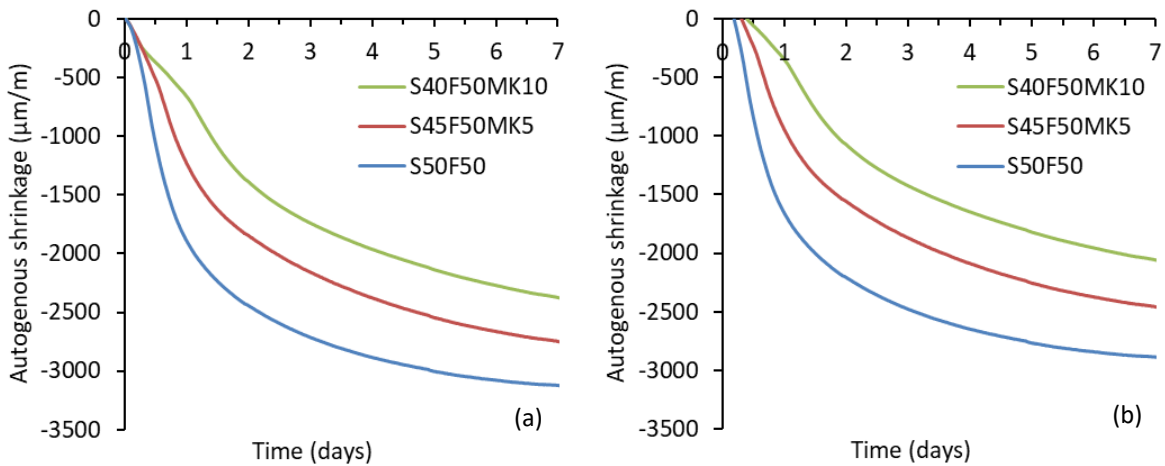


Figure 5.4 Autogenous shrinkage of AASF pastes with and without MK, starting at Vicat setting time (a) or the start of the acceleration period (b). Detailed results on setting time and reaction heat are shown in section 5.3.2.3.

The above results clearly show that the incorporation of MK can substantially reduce the early-age autogenous shrinkage of AAMs paste, irrespective of the time-zero of the curves. To explain the mechanisms behind, the influences of MK addition on the microstructure of AAS and AASF pastes are investigated in the next section.

5.3.2 Microstructure characterization

5.3.2.1 XRD analysis

The XRD patterns of pastes at curing age 1 day and 7 days are shown in Figure 5.5, where XRD patterns of the precursors were also plotted for comparison. The plain AAS paste is mainly amorphous. The crystalline phases in fly ash are mullite ($(Al_2O_3)_{1.136}(SiO_2)_{0.728}$), quartz (SiO_2) and hematite (Fe_2O_3), as already shown in Figure 3.3. The crystalline phase identified in the spectra of S90MK10 and S80MK20 is basically quartz originating from the MK. In S45F50MK5 and S40F50MK10, the crystals are from both MK and fly ash.

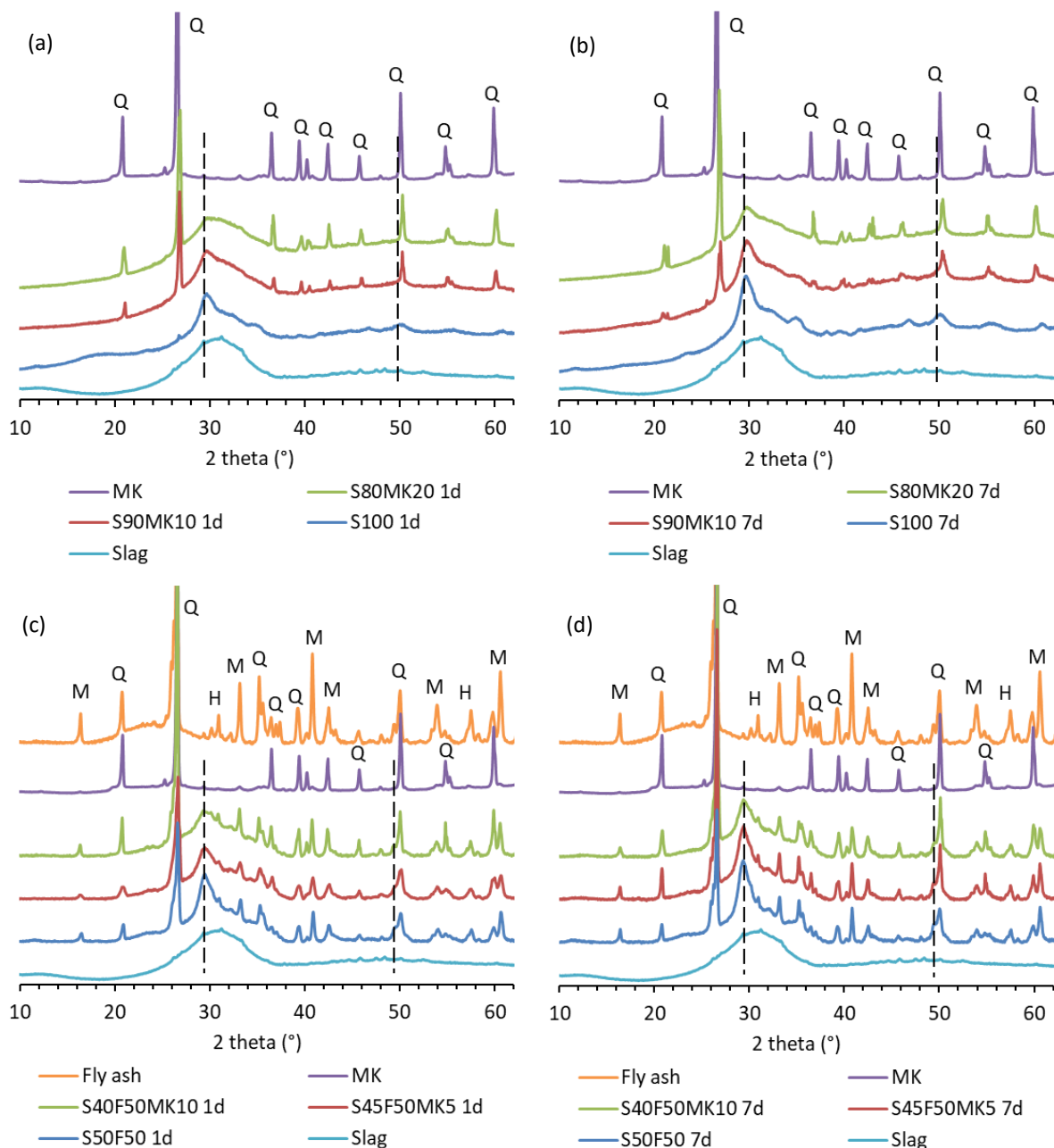


Figure 5.5 XRD patterns of AAS pastes (a, b) and AASF pastes (c, d) in comparison with the precursors (slag, fly ash and MK). M, Q and H stand for mullite, quartz and hematite, respectively.

Apart from the background hump related to the unreacted slag, additional diffraction peaks at 29° and 49.8° (as marked by the dashed lines) can be observed in the curves of S100 and S50F50, which can be attributed to the formation of C-A-S-H type gel [39]. These signals become less evident in the mixtures with MK incorporation. With the increase of curing time, the small hump for C-A-S-H gels become more intensive than the intensity for quartz peaks, indicating the formation of larger amounts of amorphous reaction products. The intensities of the humps representing C-A-S-H gel in the XRD spectra of MK-incorporated pastes are smaller than that of the mixture without MK at both 1 day and 7 days. This suggests that the amount of C-A-S-H gels formed in the first week decreases with the increasing content of MK.

5.3.2.2 FTIR analysis

FTIR spectra of AAS pastes and AASF pastes with and without MK at 1 day and 7 days is plotted in Figure 5.6. It is found that the main bands of the FTIR spectra of AAS pastes are all near 942 cm^{-1} (Figure 5.6 (a) and (b)). These bands are associated with the asymmetrical stretching vibrations of Si–O bonds generated by Q^2 units, which is the representative structure of aluminosilicate chains containing C-A-S-H type gel [140,142,220]. For the spectra of AASF pastes, the main band is located at slightly higher wavenumbers due to the incorporation of unreacted fly ash (Figure 5.6 (c) and (d)) [221]. With the increase of reaction time, the intensities of all main bands increase.

The bands located at around 895 cm^{-1} and 660 cm^{-1} can be assigned to the deformational vibrations of Si-O-Si or Si-O-Al [140,142]. The band at around 815 cm^{-1} is typical for Si–O ($Q1$) symmetric stretching vibrations [142]. The shoulder in the range of $1040 - 1070\text{ cm}^{-1}$ is also assigned to the asymmetrical stretching of Si-O-T (T=Si or Al) bonds and/or Si-O-M bonds, with a lower extent of Al substitution than the bulk gel [101]. The signals at 895 cm^{-1} , 815 cm^{-1} , and 660 cm^{-1} are visible in all spectra for AAS pastes, and their intensities decrease with increasing content of MK (Figure 5.6 (a) and (b)). These results indicate that the dominant reaction product in AAS remains as C-A-S-H gel, but the amount of this gel decreases when more MK is introduced to the system, which confirmed the observation in XRD. This finding is also in line with the previous studies on alkali-activated slag/MK blends [211].

In AASF pastes, the presence of MK in AASF pastes has similar effects. The intensities of the peaks in AASF pastes are generally lower than in AAS pastes, indicating relatively lower amounts of reaction products formed (Figure 5.6 (c) and (d)). With the increase of reaction time, the intensities of all main bands increase as well.

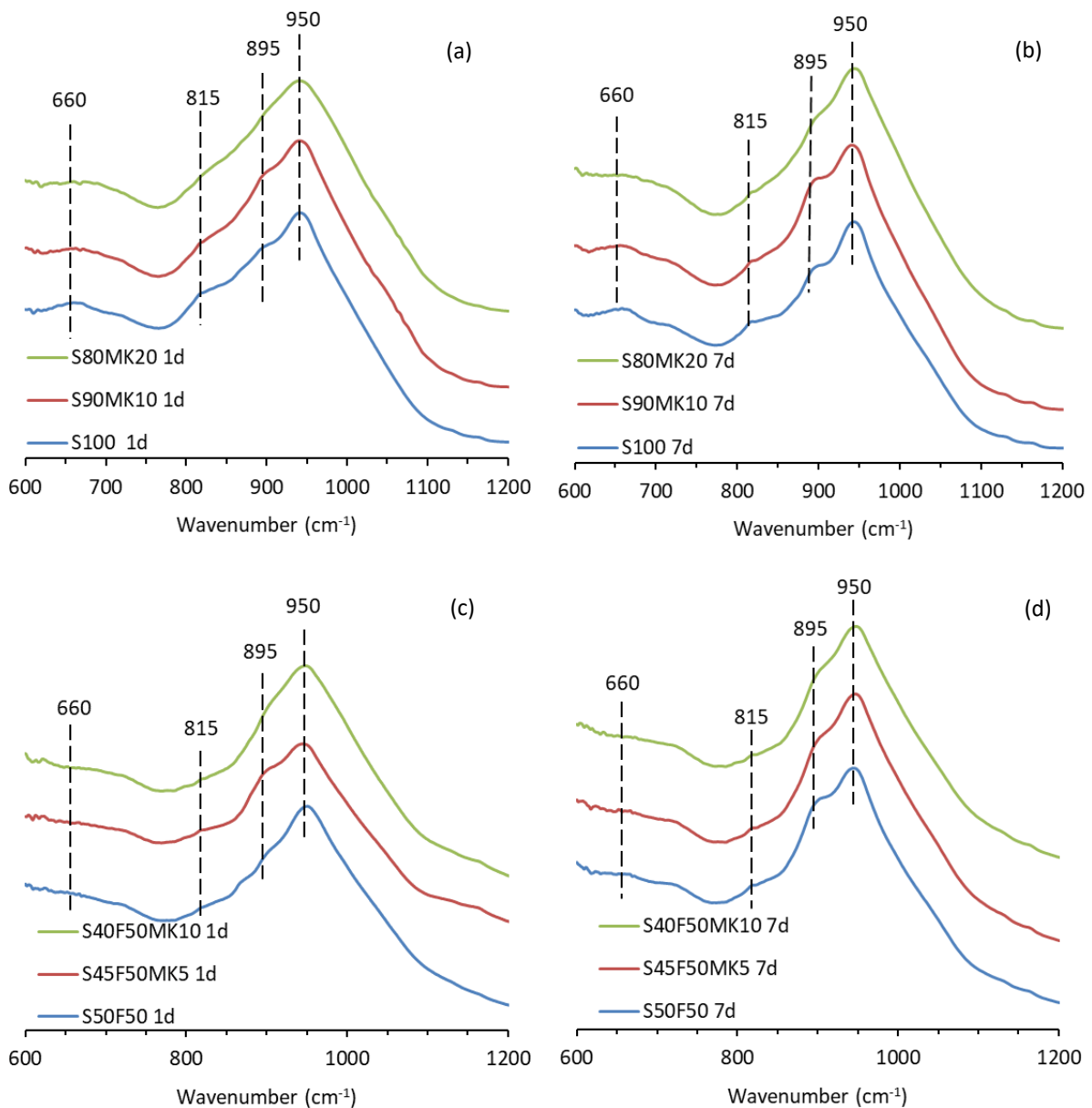


Figure 5.6 FTIR spectra of AAS pastes (a, b) and AASF pastes (c, d) with and without MK.

5.3.2.3 Isothermal heat release and setting time

The heat flow curves of the mixtures are shown in Figure 5.7. The initial peak detected during the first few minutes of reaction may be caused by wetting and initial dissolution of the precursors. The main peak identified at the later stage of reaction represents the reactions among the dissolved species, corresponding to the acceleration period. The starting time of the acceleration period is marked by the dashed line (for S80MK20 and S40F50MK10, the marking is somehow arbitrary since their main reaction peaks are not pronounced). As shown in Figure 5.7 (a), S100 shows a very short dormant period. Replacing 10% slag with MK delays the occurrence of the main peak and decreases its intensity, suggesting that the formation of the majority of reaction products slows down due to the presence of MK. This effect becomes

more significant when 20% of MK is added to the system. In AASF pastes, the presence of MK also significantly reduces the reaction rate in the acceleration period (Figure 5.7 (c)). For S40F50M10, the main peak can even hardly be distinguished. These results are in agreement with the XRD and FTIR results, where MK-containing mixtures show less intensive and less sharp main band compared to the plain mixtures (see Figures 5.4 and 5.5).

The cumulative heat of the pastes is shown in Figure 5.7 (b) and (d). The amounts of heat release of the AAS mixtures are similar during the first 3 hours. Although the heat flow of S90MK10 is lower than that of S100 during the acceleration period, the two mixtures have released a similar total amount of heat after 120 hours. The total heat release of S80MK20 is lower than those of the other two mixtures in the whole period studied, except for the first 3 hours. The cumulative heat released by AASF pastes is generally lower than that of AAS pastes, which is consistent with the results in chapter 3. The incorporation of MK reduces the total heat of AASF pastes after the dormant period, but at the age of 5 days, the cumulative heat curves of different AASF pastes start to develop in similar rates. It can also be noticed that the heat releases of AAM mixtures are lower than the heat release of OPC pastes, which is normally higher than 200 J/g at ambient temperature within 5 days [222]. This finding is in line with the results reported by Krizan and Zivanovic [223].

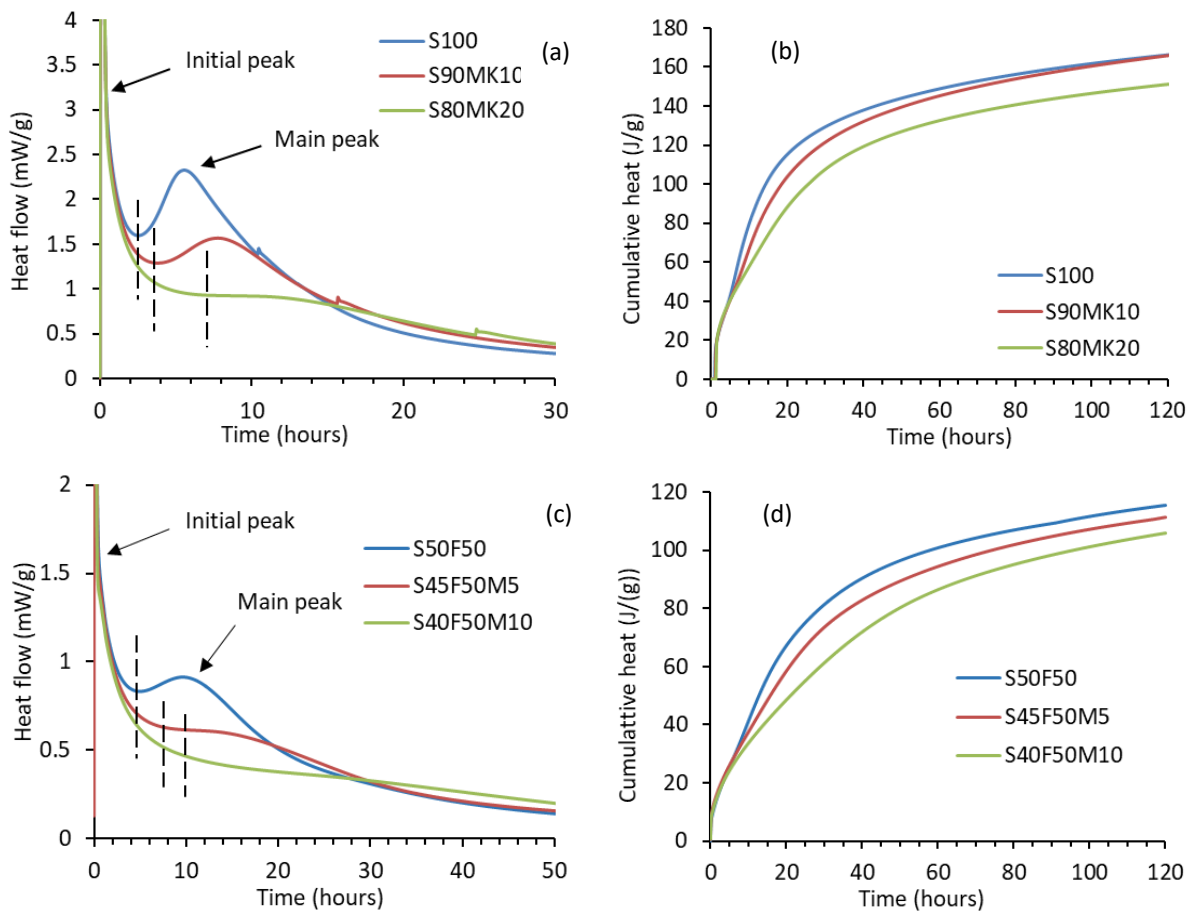


Figure 5.7 Heat release of AAS pastes (a, b) and AASF pastes (c, d) with and without MK.

The Vicat setting time of the mixtures is presented in Table 5.3. When 10% of MK is incorporated into AAS paste, the initial setting time and final setting time of AAS are increased by 7 min and 23 min, respectively. Increasing the content of MK from 10% to 20% results in longer setting time, but the effect is not pronounced. The delaying effect of MK on the setting time of AASF paste is also evident. For example, the incorporation of 5% of MK into AASF pastes results in a delay of around 40 min of the final set.

Table 5.3 Setting times of AAS and AASF pastes with and without MK measured by Vicat method.

Mixtures	Initial setting (min)	Final setting (min)
S100	33	59
S90MK10	40	82
S80MK20	45	85
S50F50	117	175
S45F50MK5	132	213
S40F50MK10	133	223

5.3.2.4 Pore solution compositions

The elemental concentrations of Ca, Na, Si and Al and the concentration of OH⁻ of the pore solutions of AAM pastes are shown in Figures 5.7 and 5.8.

It can be seen from Figure 5.8 (a) that the concentrations of Na⁺ and OH⁻ in the pore solutions of S90MK10 and S80MK20 are lower than those in S100 at both 1 day and 7 days. This is probably due to the consumption of these ions during the dissolution of MK [224]. Figure 5.8 (b) shows that the concentration of Ca in the pore solutions decreases with the increase of MK content. The much lower Ca concentrations in MK-containing samples indicate either retarded dissolution of slag or faster precipitation of the ions to form C-A-S-H gels. The latter one seems not to be the case here as can be inferred from the longer induction periods of S90MK10 and S80MK20 shown in Figure 5.7. Therefore, it's highly probable that the dissolution of slag is prohibited when MK is present. The reason of the retarded dissolution of slag will be discussed in section 5.3.2.6. Besides, the dissolution of MK releases more Si and Al to the pore solution, especially at the early age, as shown in Figure 5.8 (c).

At the age of 7 days, the divergence of the concentrations of Ca, Si and Al in different mixtures is less distinct than at 1 day. This is in line with the FTIR and calorimetry results, which show that the three AAS systems have similar final reaction products (C-A-S-H gel) and reach similar reaction degrees at the age of 7 days.

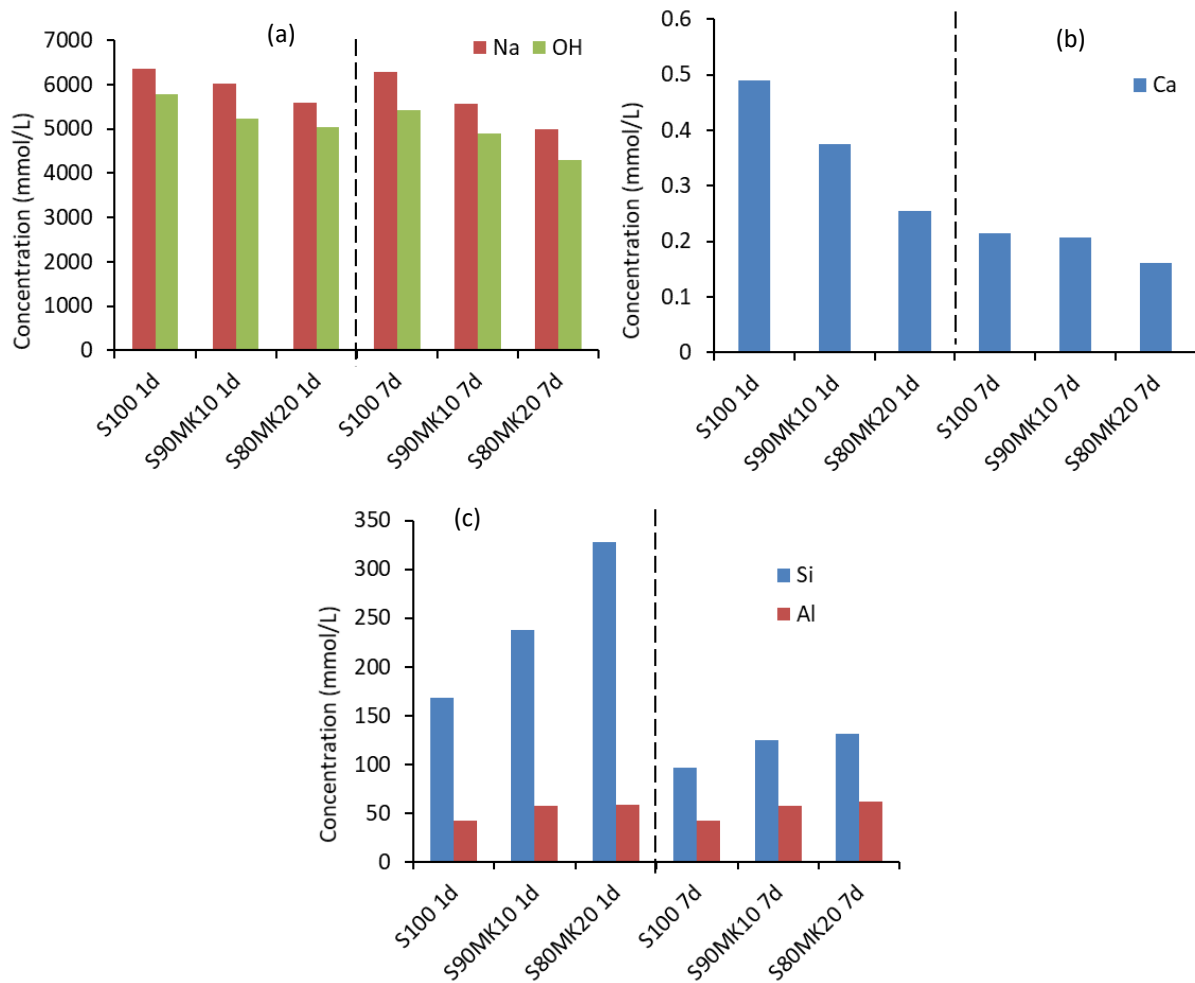


Figure 5.8 Concentrations of (a) Na and OH, (b) Ca, (c) Si and Al of the pore solutions of AAS pastes with and without MK at 1 d and 7 d.

While the concentrations of Na^+ and OH^- in S100 remain nearly unchanged with time, these ion concentrations in S50F50 decrease, as shown in Figure 5.9 (a). The effect of fly ash is similar to that of MK in AAS. Due to the lower content of slag, less calcium is available in the system, while more alumina-silicate ions are introduced. Therefore, more sodium would involve in C-A-S-H gel in place of calcium, resulting in the formation of more C-(N)-A-S-H gel [225].

The incorporation of MK into AASF paste further decreases the concentrations of Na^+ and OH^- in the pore solution. As shown in Figure 5.9 (b), the concentration of Ca in AASF decreases when MK is present, which is similar to what has been observed in AAS. Not like AAS, the concentrations of Ca in AASF pastes with MK are much lower at the age of 1 day but increase with the reaction time, indicating the dissolution of slag is retarded at the very early age, but not afterwards. This is consistent with the calorimetry results (Figure 5.7), which show that the presence of MK significantly reduced the reaction rate at the acceleration period, but after that the reaction rates of S45F50MK5 and S40F50MK10 exceed the one of S50F50. The effect of MK on the concentrations of Si and Al in AASF pastes is similar to that in AAS pastes, only the concentrations of Si and Al in AASF pastes are generally lower than those in AAS pastes due to the lower amount of reactive slag and MK.

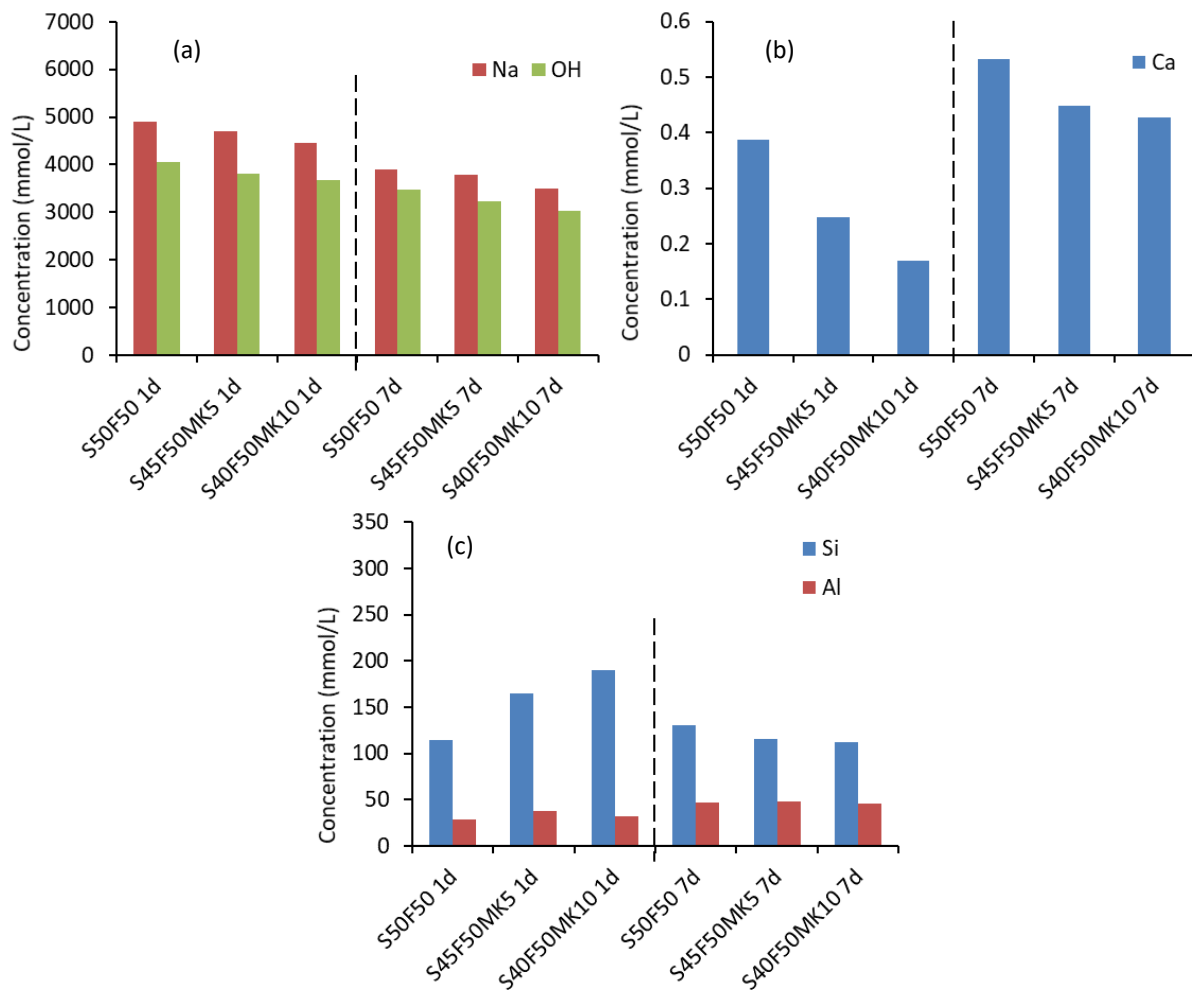


Figure 5.9 Concentrations of (a) Na and OH, (b) Ca, (c) Si and Al of the pore solutions of AASF pastes with and without MK.

5.3.2.5 Pore size distribution

Figure 5.10 shows the pore size distribution and differential curves, determined by nitrogen adsorption tests, for AAS pastes with and without MK at the curing ages of 1 day and 7 days. The pore sizes detected by N_2 adsorption range from 2 nm to 200 nm.

It can be observed that a large part of the pores in the mixtures are small pores within the pore diameter range of 2 nm-10 nm, corresponding to the gel pores. The differential curves of the pore size distribution show one main peak (as marked by the dashed lines). The curves for S90MK10 and S80MK20 also show some small peaks at the pore diameter between 30 nm to 90 nm, which are in the range of capillary pores. As curing age increases, the main peaks of the three mixtures all shift to smaller pore diameters, and the amplitudes decrease, indicating the formation of denser structures, and the pore volume decreases. By comparing the pore size distribution in S100, S90MK10 and S80MK20, it can be seen that the introduction of MK results in a coarser pore structure of the paste in the first week of reaction.

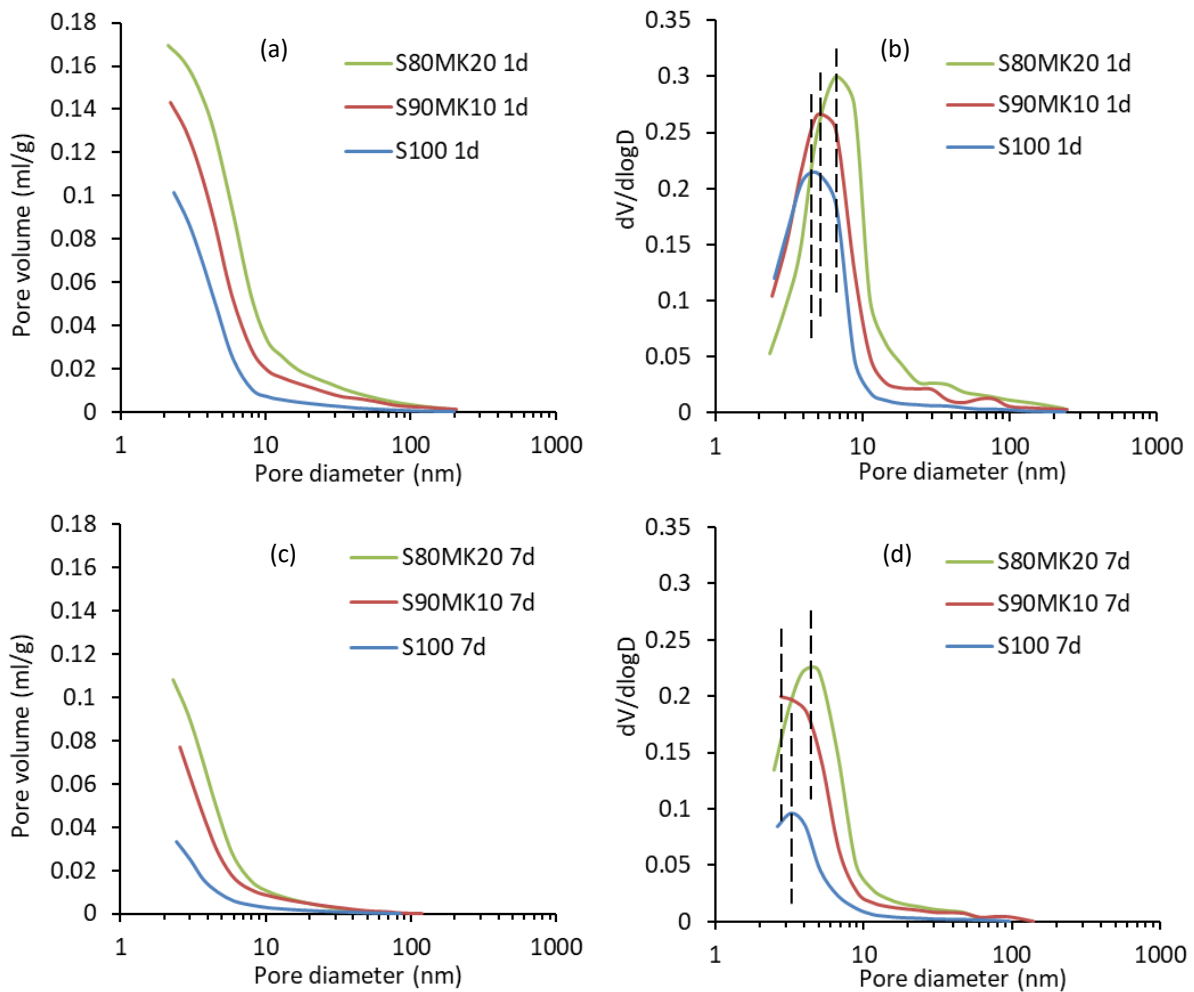


Figure 5.10 Pore size distribution and differential curves, derived from nitrogen adsorption, for AAS pastes with and without MK cured for 1 day (a,b) and 7 days (c,d).

The pore size distribution of AASF pastes with and without MK is shown in Figure 5.11. It can be seen that the gel porosities of AASF pastes are substantially lower than those of AAS pastes during the first week of curing. As shown in Figure 5.11 (a), (c) and (e), the incorporation of MK increases the porosity of the paste in the whole period studied, as in AAS pastes. The characteristic pore sizes of AASF pastes at the age of 1 day and 7 days are not, according to the pore differential curves shown in Figure 5.11 (b) and (d), in the measuring range of nitrogen adsorption. At the age of 28 days, the three pastes show similar critical pore sizes at around 3 nm, although the porosity of S40F50MK10 is still the largest.

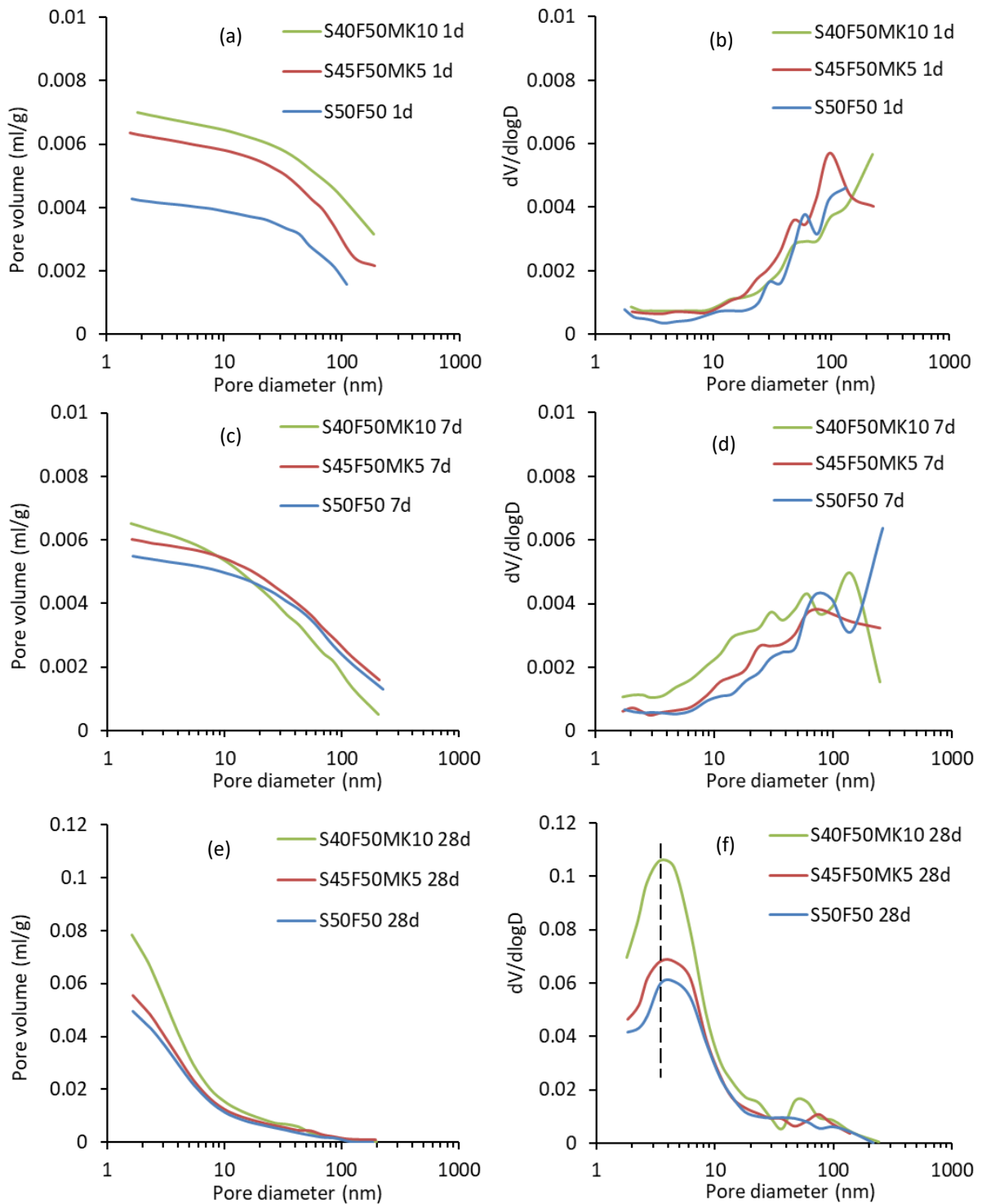


Figure 5.11 Pore size distribution and differential curves, derived from nitrogen adsorption, for AASF pastes with and without MK cured for 1 day (a,b), 7 days (c,d) and 28 days (e,f).

5.3.2.6 Discussion of the influence of MK on reaction process and microstructure formation of AAS and AASF

By combining the characterization results, a comprehensive understanding of the influence of MK addition on the reaction process and microstructure evolution of AAM paste can be obtained. This influence will further affect the shrinkage of AAMs.

The XRD and FTIR results show that the major reaction products formed in the studied mixtures are C-A-S-H (Figure 5.5 and 5.5). Little N-A-S-H gels are detected in the blended systems despite the higher content of Si and Al. This is because the N-A-S-H gels are not stable in the presence of Ca at high alkalinity. Even if N-A-S-H gels are formed, they tend to gradually convert into C-A-S-H gel when Ca is available until all the N-A-S-H gel is consumed.

The XRD and FTIR results, together with the calorimetry results (Figure 5.7), show that the formation of the major reaction products is retarded when MK is incorporated into the system. This effect can be explained through the pore solution composition results as shown in Figure 5.8 and 5.9. It can be seen that the concentrations of Na^+ and OH^- in the pore solution only slightly change with time in plain AAS paste. This finding is confirmed by the RH_s data of the S100 pore solution, which varies little from 1 day (73.9%) to 7 days (74.1%), since the RH_s is linearly related to the molar fraction of the water in the pore solution according to Raoult's law [226]. In MK-containing systems, in contrast, the concentration of Na^+ and OH^- is more significantly reduced with elapse of time, due to the dissolution of MK and formation of C-(N)-A-S-H gel [224]. The reduced OH^- hinders the dissolution of slag and formation of C-A-S-H gels as reported by Zuo et al. [227]. The retarded dissolution of slag is confirmed by the Ca concentration results shown in Figure 5.8 (b) and 5.8 (b). In the meantime, the dissolution of MK releases additional Si and Al to the system (Figure 5.8 (c) and 5.8 (c)). Evidence of the retarding effect of extra Si and/or Al on the formation C-A-S-H gels can be found in many studies that investigated the reaction kinetics of AAS system modified by incorporation of fly ash or by activator with higher modulus ($\text{SiO}_2/\text{Na}_2\text{O}$) [143,144,223,228,229]. For example, Ismail et al. [229] reported that the incorporation of fly ash, as an additional source of Si and Al, into AAS system decreases the rate of formation of C-A-S-H gels (the main binding gels). Higher Al_2O_3 content in the precursor, i.e. slag, can also slow down the hydration of slag as reported by Ben Haha et al. [230]. These results corroborate the retarding effect of MK on the hydration of slag observed in this study.

Due to the delayed formation of the major reaction products, the pore refinement in the paste is also retarded when MK is present, as shown in Figures 5.9 and 5.10. The final setting time is delayed by MK addition, as shown in Table 5.3. A similar effect of MK on the setting time of AAS was also found by Cheng and Chiu [231]. The prolonged setting time is beneficial for the application of AAM systems since they are known to harden more rapidly than usually desired [8].

It is worth noting that the influence of MK on the reaction process of AAM becomes less predominant at 7 days compared with 1 day. As indicated by Figure 5.5 – 5.8, the reaction products, ion concentrations in the pore solution and the total heat release of the mixtures with and without MK become closer with ongoing reactions. This is at odds with the results obtained by Bernal et al. [212] and Buchwald et al. [208], who found a clear difference between the long-term reaction products in plain AAS (C-A-S-H gels) and in slag/MK blends

(coexistence of C-A-S-H gels and N-A-S-H gels or zeolite). This discrepancy is probably due to two reasons. First, the MK content in this study is lower. Second, the curing temperature utilized in this study is 20 °C, while 27 °C and 40 °C were used in [212] and [208], respectively. The elevated temperature is favourable or even necessary for the formation of N-A-S-H gels or zeolites, especially when a large amount of Ca is present [9,140]. At ambient temperature, however, C-A-S-H gels are more stable in slag-based systems [232], as in the case of this study.

5.3.3 Autogenous shrinkage induced by steric-hydration force

To study the influence of MK on the autogenous shrinkage induced by the change in steric-hydration force, the shrinkage of the pastes under saturated condition is measured (detailed procedure was shown in chapter 3). As shown in Figure 5.12, the dashed lines indicate the autogenous shrinkage of the mixtures (as already shown in Figures 5.3 (b) and 5.4 (b)), while the solid lines indicate the ϵ_{ste} of paste containing MK. It can be seen that the ϵ_{ste} accounts for a considerable amount of the total autogenous shrinkage, which is consistent with the results in chapter 3. The incorporation of 10% and 20% MK reduces the ϵ_{ste} of AAS paste by 50% and 68%, respectively, at the age of 1 day. For AASF paste, the mitigating effect of MK is less evident, with the reductions at 1 day reaching 24% and 60%, when 5% and 10% MK is present, respectively. The significant reductions on ϵ_{ste} by MK contributes to the overall mitigation of the autogenous shrinkage.

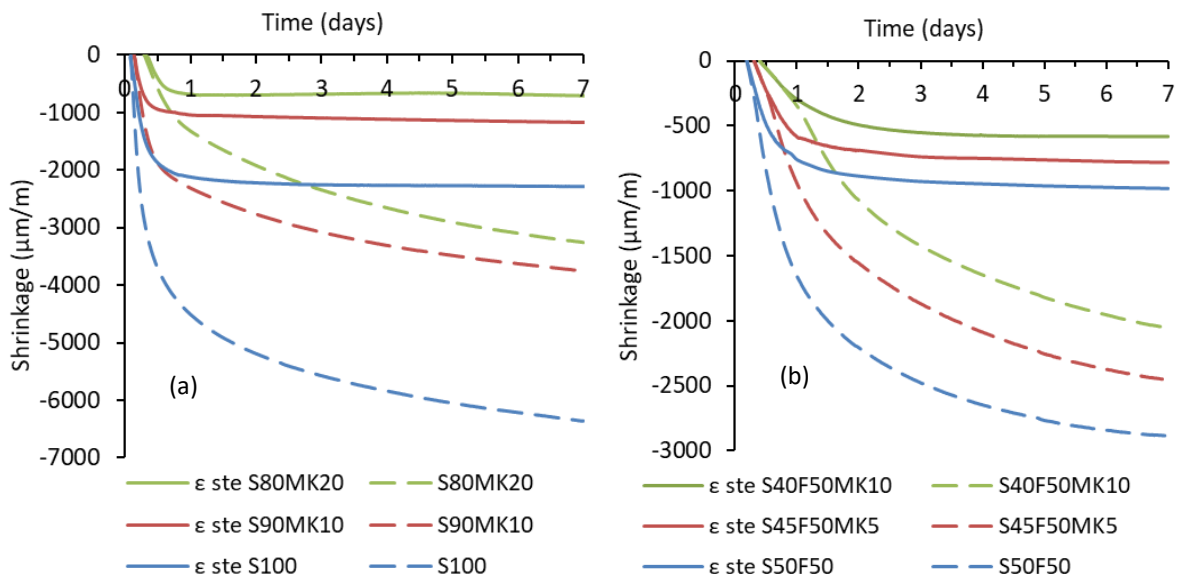


Figure 5.12 Shrinkage of AAS pastes (a) and AASF pastes (b) with and without MK under saturated condition (shown in solid lines). The autogenous shrinkage of the pastes is shown in dashed lines as reference. The curves start at the beginning time of the acceleration period.

5.3.4 Autogenous shrinkage induced by pore pressure

Based on Equation 5.1 (the same as equation 3.5), the autogenous shrinkage induced by pore pressure of the pastes is calculated and shown in Figure 5.13.

$$\varepsilon_{AS} = \varepsilon_{pore} + \varepsilon_{ste} \quad (5.1)$$

It can be seen that the incorporation of MK greatly decreases the ε_{pore} of AAS and AASF paste. The reasons for the mitigating effect will be explained based on the results on chemical shrinkage, internal RH and elastic modulus.

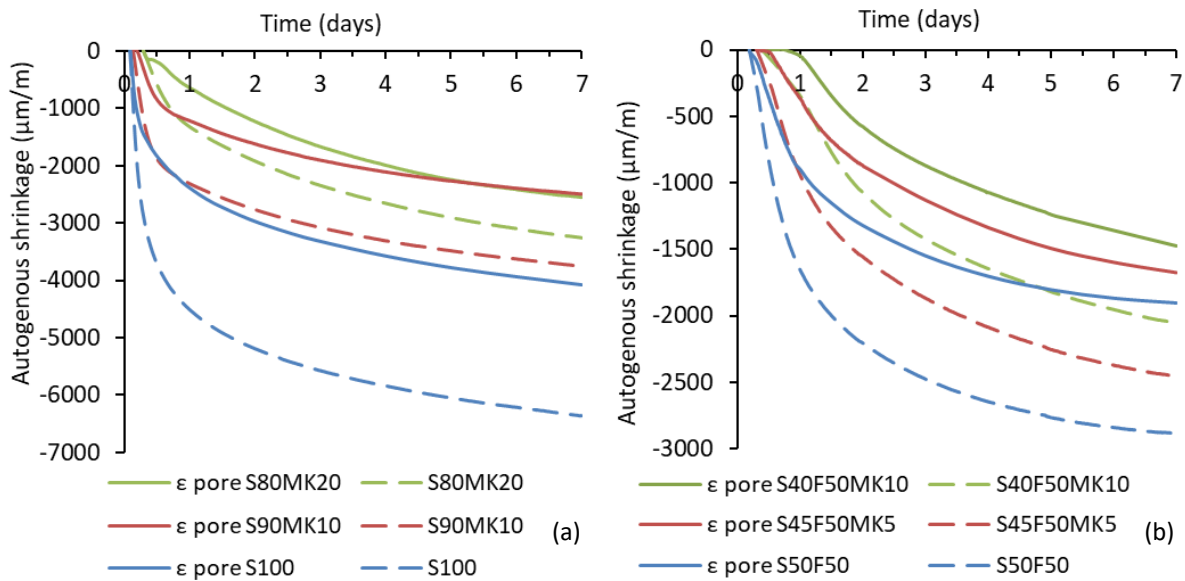


Figure 5.13 Shrinkage of AAS pastes (a) and AASF pastes (b) with and without MK induced by pore pressure (shown in solid lines). The autogenous shrinkage of the pastes is shown in dashed lines as reference. The curves start at the beginning time of the acceleration period.

5.3.4.1 Chemical shrinkage

Chemical shrinkage is the root reason for the self-desiccation and the consequent pore pressure in a binder material [18,73]. To investigate the influence of MK on the self-desiccation, the chemical shrinkage of the pastes with and without MK needs to be measured first.

Figure 5.14 shows the chemical shrinkage evolution of AAS pastes with and without MK. It can be seen that the chemical shrinkage of the mixtures experiences two stages of rapid development. The first stage of chemical shrinkage is due to the fast dissolution of the precursors, while the second stage represents the formation of reaction products. The turning instant between the two stages (determined as the moment when the second derivative of the curve reaches the minimum) is found to correspond well with the moment when the heat release rate of the mixture reaches the peak, as shown in Figure 5.14 (a).

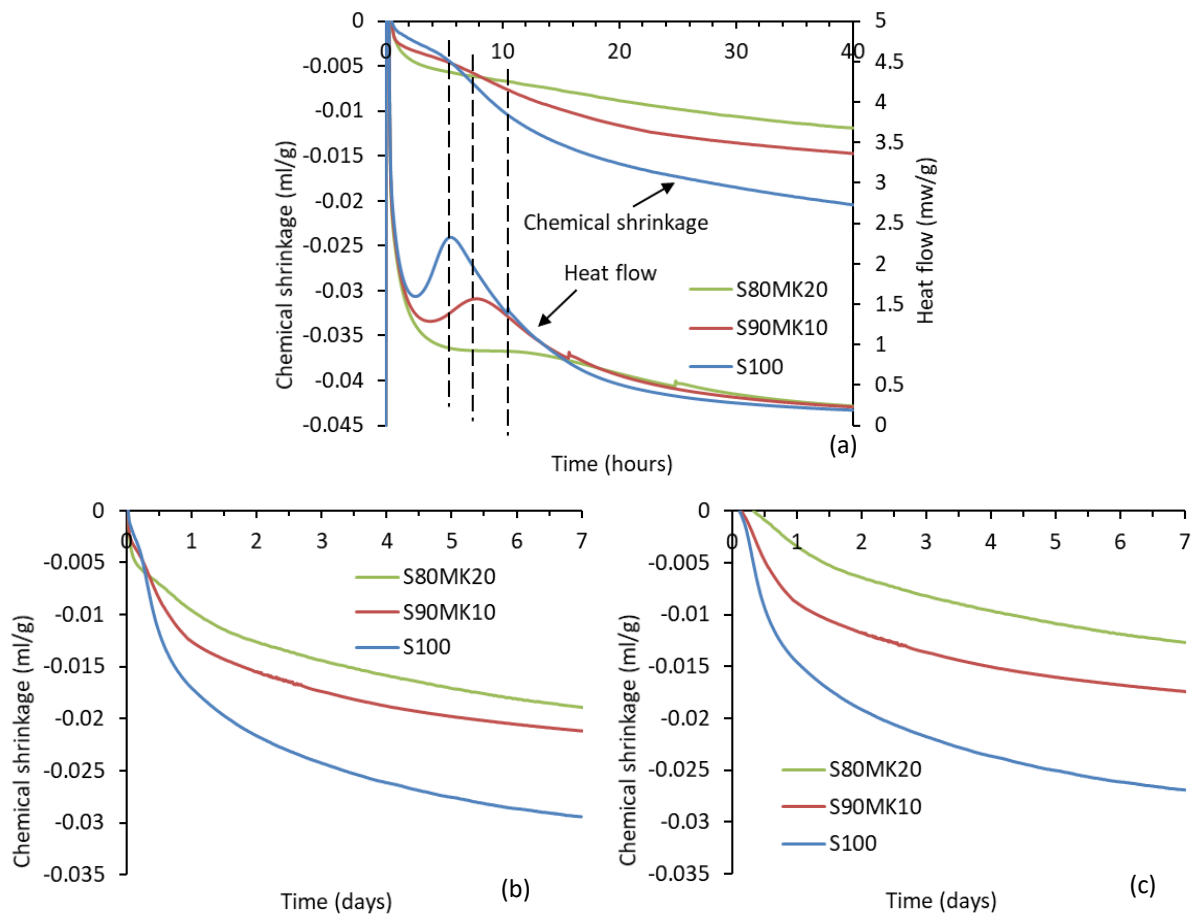


Figure 5.14 (a) Chemical shrinkage of AAS pastes with and without MK (shown in the primary axis) plotted together with the heat evolution of the pastes (shown in the secondary axis). (b) Chemical shrinkage starting at 20 mins after casting. (c) Chemical shrinkage starting at the beginning of acceleration period.

In the first stage, the mixtures with a higher content of MK show higher chemical shrinkage, which may be attributed to the fast dissolution of MK [46]. After the turning point, the chemical shrinkage of S100 surpasses the other two mixtures, which is probably due to the retarded reaction process in S90MK10 and S80MK20, as also shown in Figure 5.5 – 5.6. Similarly, the chemical shrinkage of S90MK10 develops faster than that of S80MK20, after the occurrence of the heat flow peak.

As shown in Figure 5.14 (b), the pastes with 10% and 20% MK show a chemical shrinkage that are 28% and 36% lower than that of the reference mixture, respectively, at the age of 7 days. If the chemical shrinkage curves are starting at the end of the dormant period, the difference between the chemical shrinkage curves is more evident, as shown in Figure 5.14 (c).

The chemical shrinkage of AASF pastes with and without MK show similar trends as those of AAS pastes, only with lower amplitudes, as shown in Figure 5.15. The moments when the chemical shrinkage rate experiences the second increase (the first increase occurs immediately after casting) also correspond well with the peaks of the heat flow. The mitigating effect of MK on the chemical shrinkage of AASF pastes is not as evident as in AAS pastes, which is probably due to the lower extents of substitution of binder by MK. When the curves are

shown from the start of the acceleration period, the differences between the chemical shrinkage of paste with and without MK become more distinct.

The reduced chemical shrinkage, together with the coarsened pore structure of the paste due to the incorporation of MK, would lead to a lower drop in the RH [18,76] and, therefore, a lower pore pressure. This point will be verified by the internal RH results in the next section.

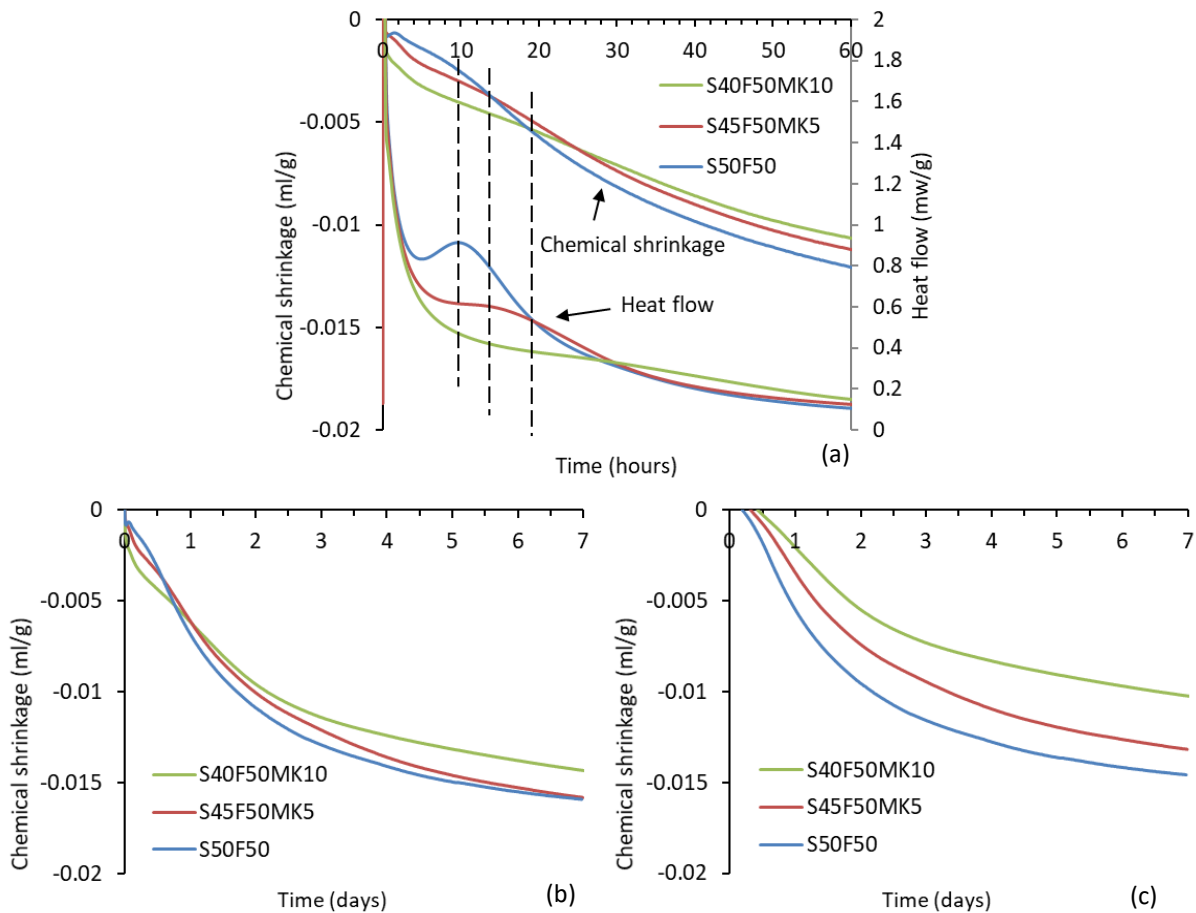


Figure 5.15 (a) Chemical shrinkage of AASF pastes with and without MK (shown in the primary axis) plotted together with the heat evolution of the pastes (shown in the secondary axis). (b) Chemical shrinkage starting at half an hour after casting. (c) Chemical shrinkage starting at the beginning of acceleration period.

5.3.4.2 Internal RH and pore pressure

The measured internal RH and RH_S and the calculated RH_K (see Equation 3.1), and computed pore pressure (according to Equation 3.4) at 1 day and 7 days, are shown in Table 5.4.

The RH of the pore solutions of AAM pastes with and without MK are in the range of 70% - 80%. This is much lower than that of the pore solution in cement paste, where an RH of above 95% was usually reported [76,233]. This is due to the high concentrations of Na^+ and OH^- in the pore solution of AAMs as previously shown in Figure 5.8 and 5.8. The RH_K values of the

three mixtures decrease with time, indicating the self-desiccation process takes place in all mixtures.

By comparing the RH_K values of different pastes, it can be seen that the drop of internal RH due to the formation of menisci and the pore pressure are mitigated by adding MK. For AAS pastes, 10% replacement of slag by MK results in a decrease in the pore pressure by 50% and 40% on day 1 and day 7, respectively. In a paste with a higher amount of MK, i.e. 20%, the pore pressure is even lower. For AASF pastes, the pore pressure can be reduced by more than half at 1 day and 7 days by the incorporation of 10%MK. The smaller RH reduction and pore pressure in AAM pastes when MK is present are consistent with the smaller chemical shrinkage and coarser pore structure of the pastes.

Table 5.4 Internal RH and pore pressure within AAS pastes with and without MK

Mixture	Specimens cured for 1 day				Specimens cured for 7 days			
	$RH(\%)$	$RH_S(\%)$	$RH_K(\%)$	$\sigma(\text{MPa})$	$RH(\%)$	$RH_S(\%)$	$RH_K(\%)$	$\sigma(\text{MPa})$
S100	71.6	73.9	96.8	4.4	65.9	74.1	89.0	15.8
S90MK10	76.7	77.9	98.4	2.2	73.9	78.9	93.6	8.95
S80MK20	79.1	80.2	98.6	1.9	77.6	82.0	94.5	7.61
S50F50	81.1	83.2	97.5	3.4	83.6	90.5	92.4	10.7
S45F50MK5	83.4	84.5	98.6	2.0	86.8	91.2	94.5	7.66
S40F50MK10	86.1	87.0	99.0	1.4	91.1	94.8	96.2	5.24

5.3.4.3 Elastic modulus

With pore pressure acting as a driving force, the autogenous shrinkage induced by pore pressure (ε_{pore}) also depends on the compressibility of the paste, in particular on the elastic modulus [52]. It can be seen from Figure 5.16 (a) that the elastic modulus of all AAS pastes is above 14 GPa at the age of 1 day. The fast development of the elastic modulus of AAS pastes is consistent with their high reaction rate in the first day (see Figure 5.7 (b)). During the following 6 days, the elastic modulus of AAS pastes experienced a slight increase. Compared with the S100 mixture, a paste with 10% of MK has a slightly higher elastic modulus at 1 day, while 20% of MK addition is beneficial to the elastic modulus only at 7 days. Nonetheless, the differences between the elastic modulus values for the three mixtures at the same age are smaller than 5%. This means that the addition of MK has minor influence on the elastic modulus of AAS paste.

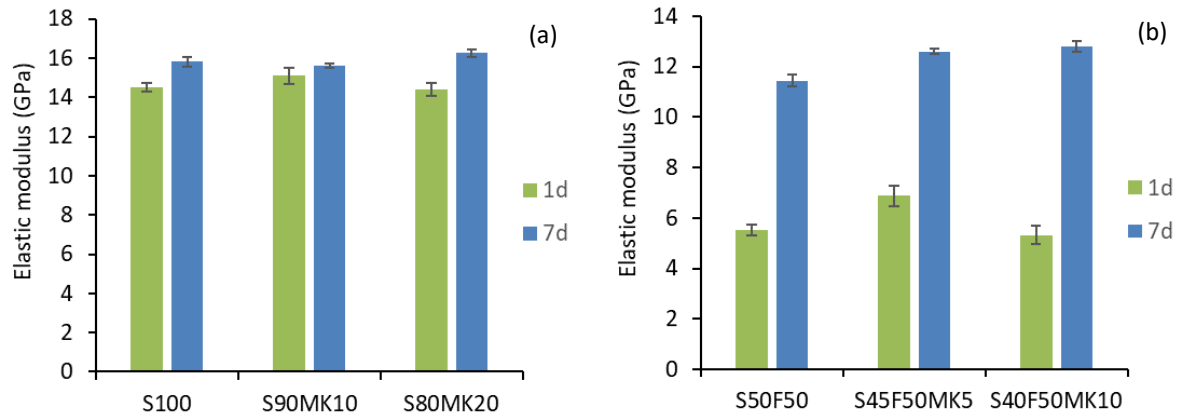


Figure 5.16 Elastic modulus of AAS pastes (a) and AASF pastes (b) with and without MK.

As shown in Figure 5.16 (b), the elastic modulus of all AASF pastes at 1 day is around 6 GPa, which is much lower than those of AAS pastes. The incorporation of 5% MK into AASF paste leads to the highest elastic modulus at 1 day among three AASF mixtures. At the age of 7 days, the elastic modulus of all mixtures increases substantially, and S40F50MK10 shows the highest elastic modulus.

Generally, the incorporation of MK does not interfere with the elastic modulus development of AAM pastes, as shown in Figure 5.16. This can be explained by the coupled effects induced by MK on the porosity and microcrack development (see the discussion in section 4.4). Unlike the compressive strength that is mainly depended on the porosity of the solid skeleton, the elastic modulus is also influenced by the development of microcracking [204,205]. Although the pastes are not under external restrained condition, the unreacted particles can act as local restraints to the autogenous shrinkage of the surrounding gels [203]. Since AAM pastes without MK show high autogenous shrinkage, microcracks may have developed within the paste, as also reported intensively in literature [11,103,122,234], and therefore harm the elastic modulus of AAM paste [11,235]. When MK is present, the autogenous shrinkage is greatly mitigated and so would be the development of microcracking. Thus, the elastic modulus of AAM pastes does not decrease with the addition of MK, in spite of the lower amount of reaction products and the coarser pore structure of the pastes.

The significantly decreased pore pressure, combined with the slightly influenced stiffness, explain the lower ε_{pore} (Figure 5.13) of AAM pastes with MK. Due to the lower ε_{ste} and ε_{pore} exhibited by AAM pastes with MK, the total autogenous shrinkage is lower as a result. So far the mechanism behind the mitigating effect of MK on the autogenous shrinkage of AAMs is interpreted.

5.3.5 Compressive and flexural strength

Besides autogenous shrinkage, also the strength is an important property of binder materials. As shown in Figure 5.17 (a), the compressive strength of pastes with MK is lower than of AAS paste. For example, the compressive strength at 7 days is by 8% and 20% lower when 10% and 20% of MK are incorporated, respectively. Nonetheless, all mixture experienced large

increase in compressive strength with elapse of time and the differences between different mixtures at 28 days are smaller than 20%.

Figure 5.17 (b) shows that S80MK20 has the lowest flexural strength at 1 day, but it exceeds the flexural strength of S100 after 7 days. The flexural strength of S100 and S90MK10 decreases after one day and increases after curing for 7 days. Figure 5.17 (b) also illustrates that the substitution of 10% and 20% slag by MK can lead to higher 28-days flexural strength by around 50% and 45%, respectively, compared to AAS paste.

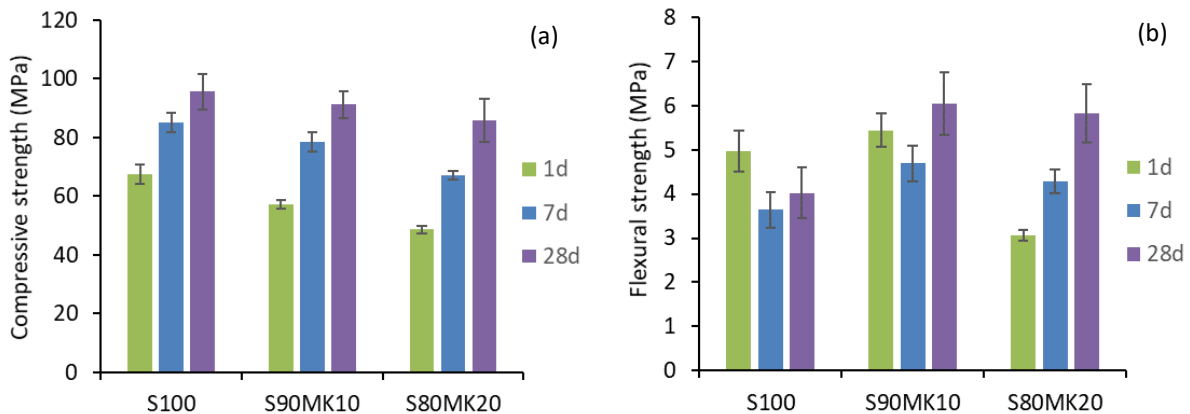


Figure 5.17 (a) Compressive strength and (b) flexural strength of AAS pastes with and without MK.

For AASF pastes, the incorporation of 5% MK induces very slight changes in the compressive strength (Figure 5.18 (a)). When MK accounts for 10% of the binder, the compressive strength of AASF paste decreases in the whole studied period. In general, AASF pastes show lower compressive strength than AAS pastes, but experience larger increase from 1 day to 28 days.

Figure 5.18 (b) shows that the flexural strength of pastes containing MK is lower than that of the reference mixture. However, at the age of 7 days and 28 days, the flexural strength is higher when 5% of MK is present. The incorporation of 10% MK leads to higher flexural strength than S50F50 only at the age of 7 days.

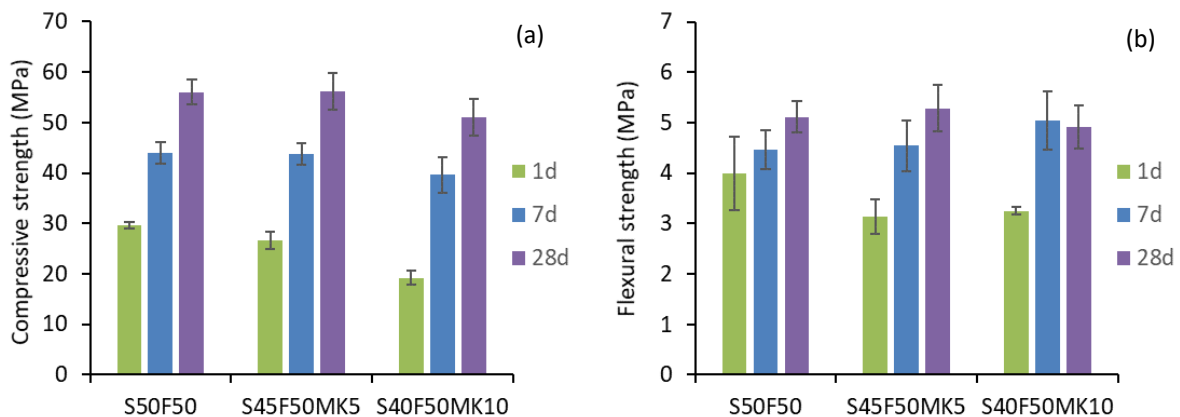


Figure 5.18 (a) Compressive strength and (b) flexural strength of AASF pastes with and without MK.

The decrease in compressive strength of the paste when MK is present is mainly due to the smaller amount of reaction products and coarser pore structure of the paste as shown in section 5.3.2. For flexural strength, in contrast, an increase is generally shown when MK is incorporated, especially at a later age. This can also be explained by the mitigating effect of the MK on the microcrack development. On one hand, AAMs with MK have a coarser pore structure which has a detrimental effect on the flexural strength. On the other hand, the addition of MK mitigates the development of microcracking in the paste, which is beneficial for the development of flexural strength. As a result, the MK-containing mixtures exhibit a comparable or higher elastic modulus at later age. It should be noted that the higher flexural strength of pastes containing MK is significant for slag-based alkali-activated systems, which are reported to be strong in compression, but relatively weak in tension [236,237]. This, besides the shrinkage mitigating effect, is another advantage of MK as admixture in AAM systems.

Considering the influence of MK on autogenous shrinkage, microstructure, setting and mechanical properties of AAM paste, it seems that 10% substitution of slag by MK leads to an optimal overall performance of AAS and AASF pastes studied in this chapter. A higher amount of MK results in pastes with a lower compressive strength. Nonetheless, the 28-days compressive strength of S40F50MK10, the weakest mixture in this chapter, exceeds 50 MPa, which is already adequate for most structural applications as specified, for example, in the standard ACI 318 [238]. Therefore, higher amounts of MK may also be suitable for some applications, especially for those which require longer setting time and an enhanced shrinkage-mitigation effect. Considering also the wide availability of MK as a low-cost product, there is good potential for utilizing MK in alkali-activated concrete.

5.4 Concluding remarks

In this chapter, the effect of MK incorporation on the autogenous shrinkage of AAM pastes is investigated. It is found that the presence of MK can effectively mitigate the autogenous shrinkage, especially at the early age. This result indicates that the incorporation of MK can be good complementary shrinkage-mitigating strategy to internal curing for example, by SAP, which has limited mitigating effect on early-age autogenous shrinkage as discussed in Chapter 4. In the next chapter, the effect of the combination of these two strategies will be investigated.

The mitigation mechanism of the addition of MK lies in the modification of the reaction kinetics and microstructure formation of AAM pastes due to the presence of MK. Based on the presented results and discussion, the following conclusions can be drawn:

1. The incorporation of MK provides extra dissolvable Si and Al to the system and decreases the concentration of Ca^{2+} , Na^+ and OH^- in the pore solution. As a result, the reaction rate of the paste is delayed and the formation of C-A-S-H gels, the major reaction products, is retarded. The autogenous shrinkage of AAMs induced by the reduction of steric-hydration force (ϵ_{ste}) is mitigated by MK.
2. The development of chemical shrinkage and the refinement of the pore structure are hindered by the incorporation of MK. The self-desiccation process and the pore pressure developed in the paste are considerably mitigated. Meanwhile, the elastic

modulus is only slightly influenced when MK is incorporated. As a result, the autogenous shrinkage of AMMs induced by pore pressure, ε_{pore} , is effectively mitigated by MK.

3. The compressive strength of AAMs is slightly decreased by the incorporation of MK, while the flexural strength is improved. For AAS paste, 10% replacement of slag by MK leads to a larger increase of the flexural strength compared with 20% replacement. For AASF paste, 5% replacement of slag by MK gives the highest flexural strength at 28 days.
4. The lower autogenous shrinkage, longer setting time and higher flexural strength of the paste with incorporation of MK suggest that MK is a very promising admixture for AAMs systems. The dosages of MK studied in this chapter can be used for the design of alkali-activated blended materials in future studies.

Chapter 6

Cracking tendency of alkali-activated concrete subjected to restrained autogenous shrinkage

6.1 Introduction

The main reason why academia and industrial communities are interested in autogenous shrinkage is that it can potentially cause cracking of concrete [222,239]. In practice, concrete is often under restrained condition. The restraint can be either external (e.g. caused by adjoining structures) or internal (e.g., caused by reinforcement or non-shrinking aggregates) [52,240]. The volume change of the concrete will be, therefore, hindered to a certain extent and, consequently, tensile stress will develop. When the tensile stress in concrete exceeds the tensile strength, cracking will occur. Such cracks can cause a series of problems with regard to serviceability, durability and aesthetics [241]. Therefore, the cracking tendency of AAMs has to be evaluated and the strategies for reducing the cracking risk need to be identified before the materials can be widely utilized.

According to the results in chapter 3 (Figure 3.3) and in the literature [56–58,60,137], the autogenous shrinkage of AAMs systems is generally higher than that of OPC-based systems. One may suspect that alkali-activated concrete (AAC) has higher crack tendency. However, the cracking tendency is determined not only by autogenous shrinkage, but also by creep/relaxation, elastic modulus, and tensile strength of the material. For this reason, an integrated study is required to investigate the cracking tendency of AAC by considering these parameters.

The main aim of this chapter is, therefore, to evaluate the autogenous shrinkage-induced cracking tendency of AAS and AASF concrete. The Temperature Stress Testing Machine (TSTM) is utilized to follow the internal stress evolution and the probability of cracking of the concrete under restrained condition. With the measured autogenous shrinkage and elastic modulus as inputs, the internal stresses in AAS and AASF concrete are calculated and compared with the experimental results. The roles of creep and relaxation on stress evolution and cracking proneness of concrete are highlighted.

The results in chapters 4 and 5 suggest that the incorporation of MK and SAPs can effectively mitigate the early-age and later-age autogenous shrinkage of AAMs, respectively. The combination of MK and SAPs may have an enhanced effect on mitigating the autogenous

shrinkage and the cracking tendency of AAMs at concrete scale. Therefore, in this last chapter, SAPs and MK are applied together into AASF concrete, aiming at producing a practically applicable AAM concrete with sufficient strength and meanwhile a very low cracking tendency.

6.2 Materials and methods

6.2.1 Raw materials and mixtures

The primary precursors used in this chapter were slag and fly ash, as already used in previous chapters. The composition of the activator was shown in Table 3.2. The mixture compositions of AAS and AASF concrete are shown in Table 6.1. Internal curing with SAPs and incorporation of MK are applied into AASF concrete to mitigate its autogenous shrinkage and cracking tendency. The physical and chemical properties of SAPs and MK are presented in sections 4.2 and 5.2, respectively. Since AAS concrete show fast setting and low workability (see [242] and section 4.3.2 of [169]), AAS concrete with SAPs and MK are not studied here. According to the results in chapters 4 and 5 and considering the balance between the shrinkage mitigating effect and the mechanical properties of the matrix, the dosages of SAPs and MK are chosen as 0.16 wt. % and 5 wt. % of the binder, respectively. The mixture design of AASF concrete with internal curing and MK (hereinafter termed AASFICMK) is also shown in Table 6.1.

Table 6.1 Mixture design of AAS, AASF and AASFICMK concrete (kg/m³).

Mixtures	AAS	AASF	AASFICMK
Slag	400	200	180
Fly ash	0	200	200
Activator	200	200	200
SAP	-	-	0.64
Extra activator for internal curing	-	-	12.8
MK	-	-	20
Aggregate [0-4 mm]	789	789	789
Aggregate [4-8 mm]	440	440	440
Aggregate [8-16 mm]	525	525	525
Admixtures	-	-	-

6.2.2 Experimental methods

6.2.2.1 Mechanical properties of concrete

Concrete cubes (150 × 150 × 150 mm³) for compressive and splitting strength tests and prisms (100 × 100 × 400 mm³) for elastic modulus test were cast and cured in sealed and temperature-controlled steel moulds. The moulds were connected with cryostats by parallel circulation tubes and the upper surface was sealed by plastic film. The temperature of the concrete cubes was controlled at 20 °C.

Compressive strength and splitting strength of the concrete were measured according to NEN-EN 12390 [243]. The measurements were conducted at the age of 1, 3, 7, 28 days and the day when the beam in TSTM cracked. Three cubes were tested for compressive strength and splitting strength.

The elastic modulus of the concrete was tested by a Tonibank hydraulic Instron (Figure 6.1). The strain during loading was measured by linear variable differential transducers (LVDTs) aligned vertically on the four sides of the concrete prism. The loading and unloading of each sample went through four cycles with the stress ranging from 5% to 30% of the compressive strength of the concrete. The results obtained from the latter three cycles were used in the calculation of the elastic modulus. The loading and unloading rates were 1 kN/s [219]. Two samples were tested for each mixture at each age.



Figure 6.1 Testing set-up for elastic modulus measurement on AAS and AASF concrete.

6.2.2.2 *Autogenous shrinkage of concrete*

The autogenous shrinkage of the concrete was measured with an Autogenous Deformation Testing Machine (ADTM) [244]. The prismatic mould for the concrete is made of thin steel plates and external insulating materials. The size of the mould is $1000 \times 150 \times 100 \text{ mm}^3$, which is illustrated in Figure 6.2. The mould was connected with cryostats by a series of circulation canals located between the plates and the insulating material (see Figure 6.2). The temperature of the beam was controlled at 20 °C.

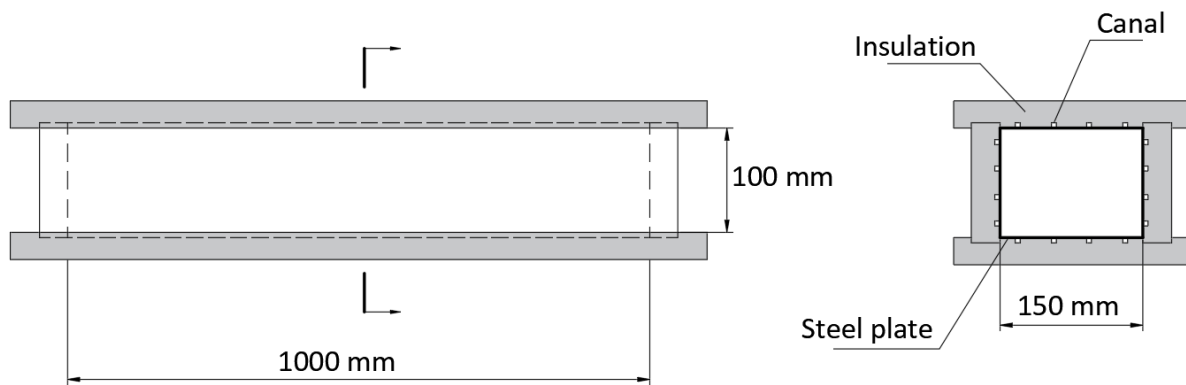


Figure 6.2 Front view (left) and cutaway view (right) of the mould of ADTM.

The length change of the concrete was measured with two external quartz rods located next to the side mould. LVDTs were installed at both ends of the rods. The LVDTs measured the movement of the steel bars which were cast in the concrete. The distance between the two cast-in steel bars was 750 mm. The instalment of LVDTs was conducted when the concrete had reached sufficient strength to support them (see Figure 6.3). The measurement of the deformation of AAS and AASF concrete starts at 8h and 11h (time-zero for the two systems as suggested by chapter 3), respectively. Attention was paid to the sealing of the moulds in order to avoid moisture loss to the environment.

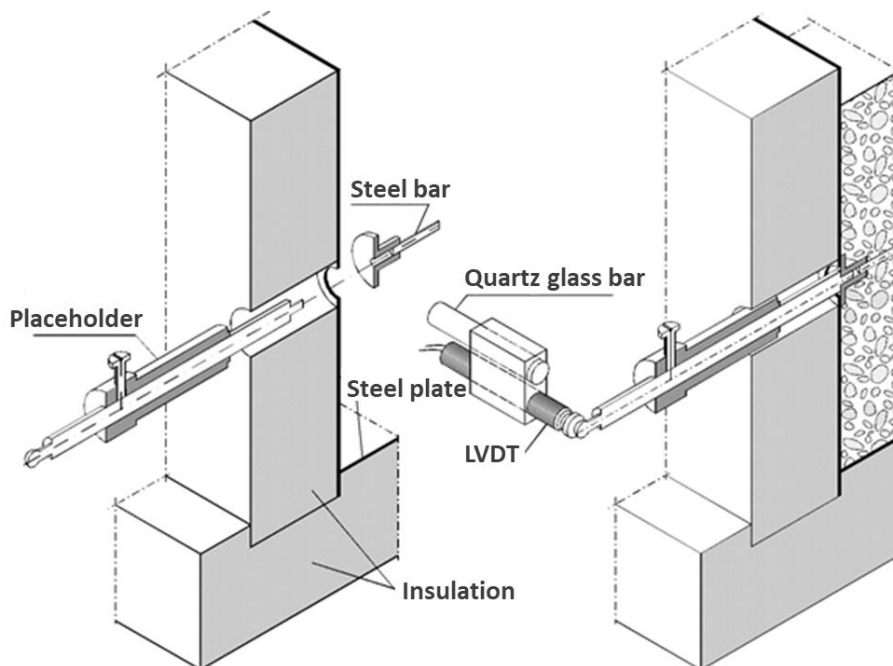


Figure 6.3 Installation of measuring bars and placeholders before casting (left) and installation of LVDTs when the concrete is stiff enough to support the bars (right), after [244].

6.2.2.3 Autogenous shrinkage-induced cracking of concrete

The internal tensile stress in the concrete induced by restrained autogenous shrinkage was monitored by a TSTM. The TSTM was equipped with a horizontal steel frame (Figure 6.4) in which the concrete specimen can be loaded in compression or in tension while the concrete hardens under any imposed temperature regime. Both load-controlled and deformation-controlled experiments can be performed. Thus, the TSTM can be used to determine stress development due to restrained deformations, but also to determine the creep and relaxation behaviours (in compression and in tension) under prescribed thermal conditions. To obtain the prescribed thermal conditions, the specimen is cast in a temperature controlled mould, similar to the ADTM mould as described in Section 6.2.2.2.

The specimen is of a dog-bone shape and the testing area of interest is of prismatic shape ($1000 \times 150 \times 100 \text{ mm}^3$). Two rigid steel claws were used to grip the concrete specimen. One of the claws was fixed to the steel frame, while the other one lied on roller bearings and can move with the hydraulic actuator to provide a compressive or tensile force onto the testing specimen. A short formwork was attached to the claws to provide a smooth and curved transition between the straight insulated mould and the slanting inner sides of the claws.

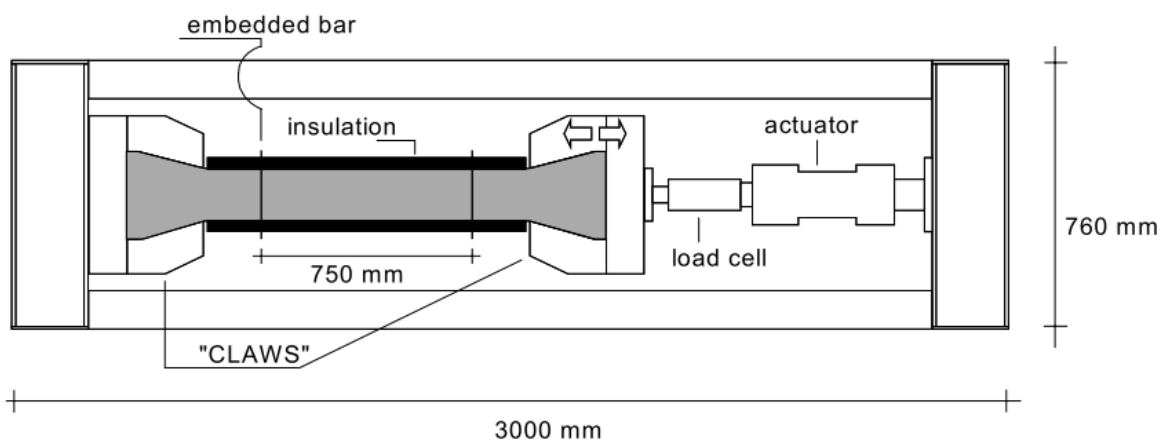


Figure 6.4 Top view of TSTM [245].

In this study, the TSTM is used to measure the autogenous shrinkage-induced stress in restrained AAC. During the first 8 hours after casting, LVDTs were used to control the deformation between the two claws because it was not yet possible to measure the deformations of the fresh concrete with the embedded steel bars. After that, the deformation control was switched to the LVDTs that measure the displacement between the embedded bars. The deformation of the concrete was kept at zero (nominally, in reality within $1 \mu\text{m}$ range) so that a full restraint condition was provided. When the total deformation of the concrete went beyond the threshold, a load was applied to pull or push the concrete back to the original position. The load was recorded with the load-cell with a loading capacity of 100 kN and a resolution of 0.049 kN. A sudden drop of the load to around zero indicated the occurrence of cracking of the concrete.

The whole set-up including TSTM, ADTM, cubes and controlling systems are schematically shown in Figure 6.5. Various thermocouples were used to monitor the temperatures of the samples. To minimize the influence of thermal deformation on the autogenous shrinkage, the temperatures of the middle parts of the specimen, i.e. T3 for TSTM, T7 for ADTM, T9 for prisms and T10 for cubes, were controlled at 20 °C.

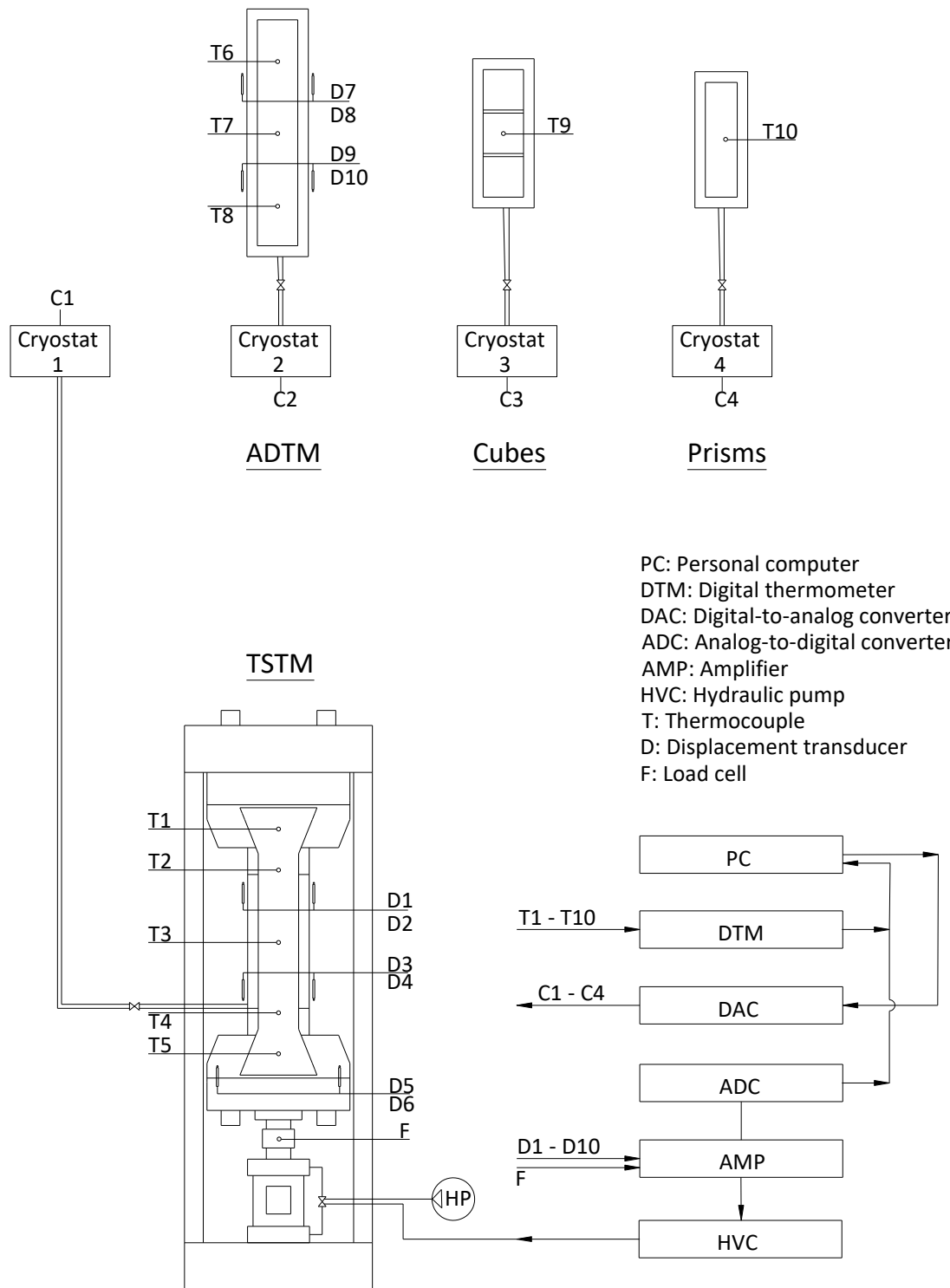


Figure 6.5 Overview of the set-up for the concrete properties, after [240].

6.2.3 Prediction of the autogenous shrinkage-induced stress

The autogenous shrinkage-induced stress in restrained concrete can be monitored by TSTM, but the test is very time-consuming and labour-intensive. It would be meaningful if the stress evolution can be predicted with the help of numerical models.

6.2.3.1 Calculation of the stress based on autogenous shrinkage

If the autogenous shrinkage is assumed to be a purely elastic deformation [52], the stress (σ_{AS}) generated in the concrete due to restrained shrinkage can be calculated using Equation 6.1. A schematic representation of the calculation process is shown in Figure 6.6.

$$\sigma_{AS}(t) = \Sigma \Delta \varepsilon_{AS}(t) \times E(t) \quad (6.1)$$

where $\Delta \varepsilon_{AS}(t)$ and $E(t)$ is the measured autogenous shrinkage increment and elastic modulus of the concrete at a certain age t .

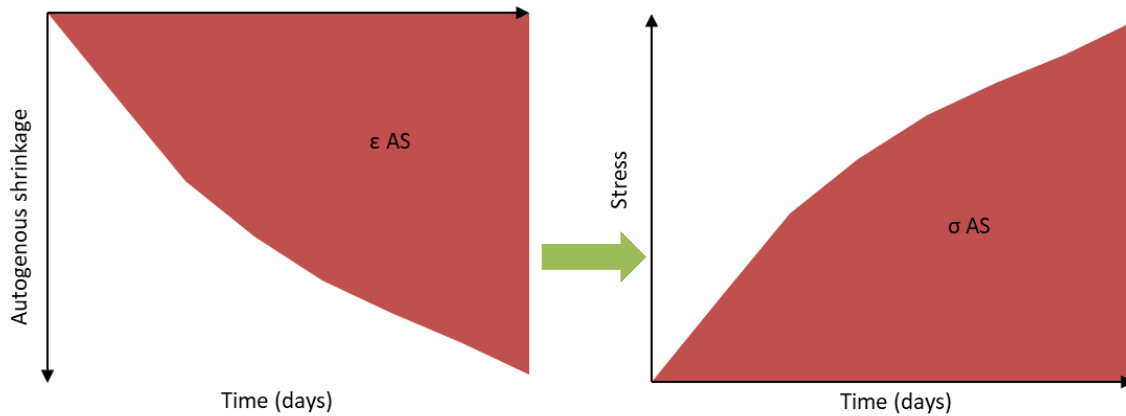


Figure 6.6 Schematic representation of stress calculated based on autogenous shrinkage.

6.2.3.2 Calculation of the stress based on the elastic part of the autogenous shrinkage

In fact, the concrete, either OPC-based concrete or AAC, is not a purely elastic material. Under external or internal load, the concrete tends to generate time-dependent deformation, or so-called creep, due to the viscoelasticity of the material. Therefore, a part of the autogenous shrinkage of the concrete measured under free condition actually belongs to creep deformation driven by internal forces, which does not generate additional external force when the concrete is under restrained condition [21,68,246]. Therefore, only the increase in the elastic part of the autogenous shrinkage shall be considered in calculating the shrinkage-induced stress, as shown in Equations 6.2.

$$\varepsilon_{elas} = \varepsilon_{AS} - \varepsilon_{creep} \quad (6.2)$$

where ε_{AS} is the measured autogenous shrinkage of the concrete. ε_{elas} and ε_{creep} are the elastic part and creep part of the autogenous shrinkage of the concrete, respectively. The stress can be then calculated as:

$$\sigma_{elas}(t) = \Sigma \Delta \varepsilon_{elas}(t) \times E(t) \quad (6.3)$$

where σ_{elas} is the stress induced by the increment of elastic part of the autogenous shrinkage ($\Delta \varepsilon_{elas}$).

A schematic representation of the calculation process is shown in Figure 6.7.

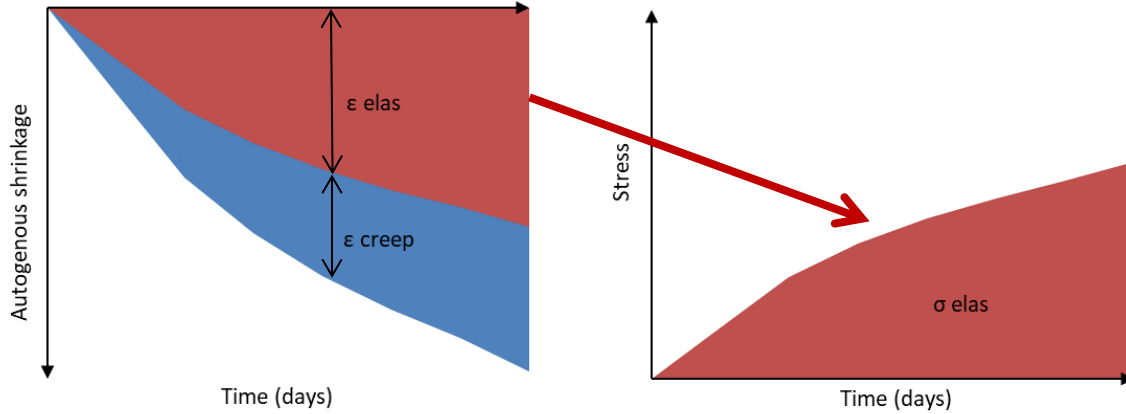


Figure 6.7 Schematic representation of stress calculated based on the elastic part of the autogenous shrinkage.

The relationship between the creep deformation and the elastic deformation under a load can be expressed by Equation 6.4 (the same as Equation 3.10) [222,247].

$$\varepsilon_{creep}(t, \tau) = \varepsilon_{elas}(\tau) \varphi(t, \tau) \quad (6.4)$$

where $\varphi(t, \tau)$ is the creep coefficient. τ (days) is the time when the load is applied.

From Equations 6.2 and 6.4, we can see in each time step:

$$\varepsilon_{elas}(\tau) = \frac{\varepsilon_{AS}}{(1 + \varphi(t, \tau))} \quad (6.5)$$

The creep coefficient can be calculated according to Equation 6.6 (the same as Equation 3.11).

$$\varphi(t, \tau) = \left(\frac{\alpha(t)}{\alpha(\tau)} - 1 \right) + 1.34 * \omega^{1.65} \tau^{-d} (t - \tau)^n \frac{\alpha(t)}{\alpha(\tau)} \quad (6.6)$$

where α is the degree of reaction. ω is the water-to-solid ratio (0.344, see section 3.2.1). n is the relaxation factor which value is taken as 0.3 and d is the constant which value is taken as 0.35 [172].

The reaction degree α of the concrete can be calculated with Equation 6.7 (the same as Equation 3.12) [144,173,174].

$$\alpha(t) = \frac{Q(t)}{Q_{max}} \quad (6.7)$$

where $Q(t)$ is the reaction heat at time t , and Q_{max} is the ultimate total heat when the reaction degree reaches 100%. The detailed procedure to calculate $Q(t)$ and Q_{max} is described in Appendix A.

With Equations 6.2 and 6.4–6.7, the elastic part and creep part of the autogenous shrinkage of AAS and AASF concrete can be calculated and with Equation 6.3, the stress generated in the concrete can be obtained.

6.2.3.3 Calculation of the stress by taking relaxation into account

In the previous section, the stress due to increasing elastic autogenous shrinkage is calculated. However, the stress decrease due to relaxation has not been considered. Like creep, stress relaxation is another result of the viscoelasticity of the material. While the concrete does not show displacement under restrained condition, the local viscous deformation of the material can cause relief of the stress with the elapse of time. Therefore, a factor smaller than one is normally needed to consider the relaxation effect in calculating the stress, as shown in Equation 6.8 [171]. A schematic representation of the calculation process of the stress considering the relaxation effect is shown in Figure 6.8.

$$\sigma_{rel}(t, \tau) = \sigma_{elas}(\tau)\psi(t, \tau) \quad (6.8)$$

where $\psi(t, \tau)$ is the relaxation factor. τ (days) is the time when the load is applied.

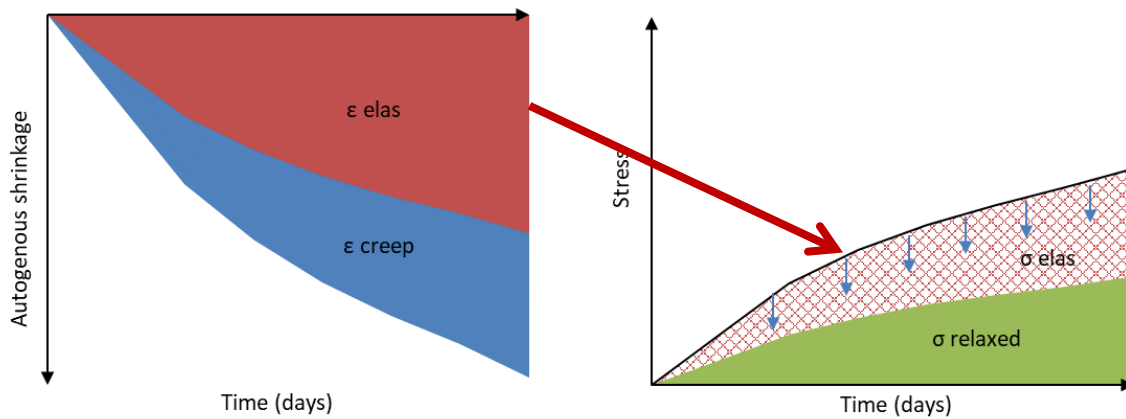


Figure 6.8 Schematic representation of stress calculated based on the elastic part of the autogenous shrinkage by taking relaxation into account.

The relaxation coefficient of concrete can be calculated from the creep coefficient $\varphi(t, \tau)$ using Equation 6.9, according to van Breugel [171].

$$\psi(t, \tau) = e^{-\varphi(t, \tau)} \quad (6.9)$$

From Equations 6.3, 6.5, 6.8 and 6.9, we get Equation 6.10, where the stress is directly expressed as a function of the autogenous shrinkage, elastic modulus and creep coefficient. It should be noted that all these parameters change with time.

$$\sigma_{rel}(t, \tau) = \varepsilon_{AS}(t) \cdot E(t) \cdot \frac{e^{-\varphi(t, \tau)}}{(1 + \varphi(t, \tau))} \quad (6.10)$$

The stress generated in the concrete after a certain curing age can be considered as the summation of the stress increments that occurred at previous time intervals, e.g. from τ_1 to τ_{n-1} , as shown in Equation 6.11.

$$\sigma_{rel} = \sum_{k=1}^{n-1} \Delta\sigma_{rel}(t_k, \tau_k) \quad (6.11)$$

where $\Delta\sigma_{rel}(t_k, \tau_k)$ is the increment of elastic shrinkage-induced stress after relaxation from τ_k to τ_{k+1} .

A schematic representation of the calculation process mentioned above is shown in Figure 6.9.

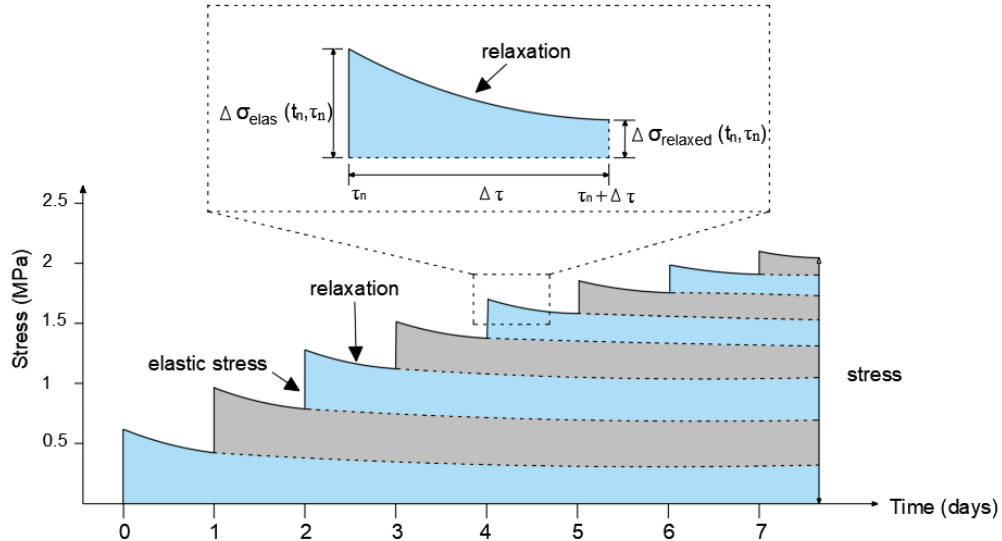


Figure 6.9 Schematic representation of stress generated in concrete.

In section 6.4, the three calculation approaches provided in sections 6.2.3.1-6.2.3.3, respectively, will be used to calculate the stress in AAC and the results will be compared and discussed.

6.3 Experimental results on cracking tendency of AAC

6.3.1 Mechanical properties

6.3.1.1 Compressive and splitting tensile strength

The strength development of the concrete is shown in Figure 6.10. It can be seen that AAS and AASF concrete generally shows high strength. At the age of 28 days, the compressive strength of AAS and AASF concretes is around 90 MPa and 75 MPa, respectively. According to EN 206 [248], the strength can be classified as C60 or higher.

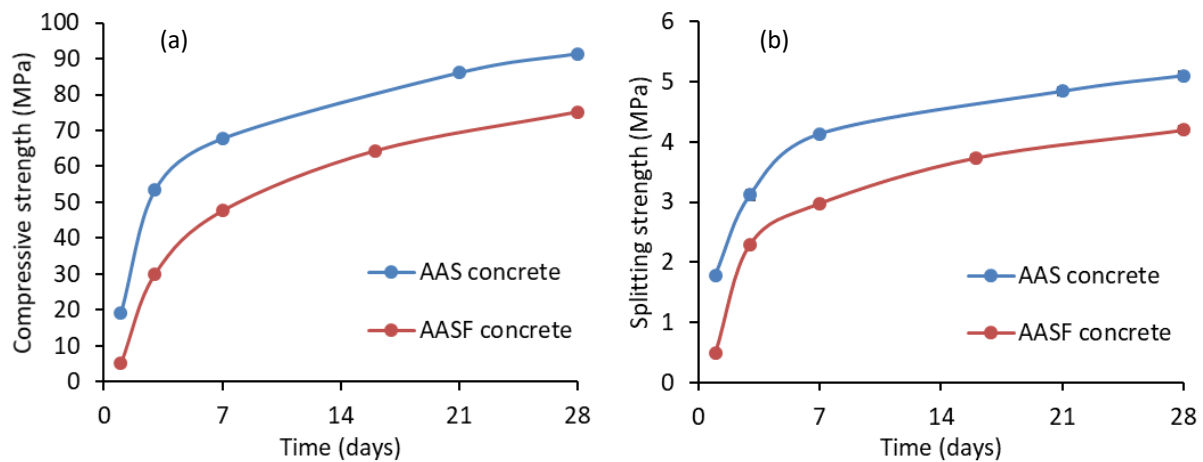


Figure 6.10 Compressive (a) and splitting strength (b) of AAS and AASF concrete. The error bar is shown in the diagram, but it is too small to be clearly distinguished from the marker.

AAS concrete shows higher compressive and splitting strength than AASF concrete, which is consistent with the findings in the literature [29,249,250]. The lower strength of AASF concrete is due to the replacement of slag by fly ash, which has a low reactivity at ambient temperature [9]. The dissolution of fly ash particles is slow, no matter in cementitious systems or in alkali-activated systems [9,145]. Nonetheless, with the elapse of time the amorphous phases in fly ash would eventually contribute to the strength growth [145], which can be reflected by the considerable increase of the compressive strength of AASF concrete from 7 days to 28 days.

Despite the high compressive strength of the concrete, its splitting tensile strength (Figure 10 (b)) is not remarkably high. This point can be seen more clearly in Figure 6.11, in which the splitting tensile strength-to-compressive strength (f_t/f_c) ratios of the concrete are plotted. The f_t/f_c ratio is an important parameter that allows the estimation of f_t by knowing f_c or vice versa [251]. The ratio also provides insight into the failure type (in compression or in tension) to which the concrete is more prone. It can be seen from Figure 6.11 that AAS and AASF concretes showed nearly identical f_t/f_c except at the age 3 days.

The f_t/f_c ratios of AAS and AASF concrete decrease from around 0.1 at the first day to only 0.055 at 28 days. This decrease might be due to the development of microcracking within the concrete, resulting from restrained autogenous shrinkage of the material [252]. Although the samples for strength test were not subject to external restraint, the aggregates can act as local restraints to the autogenous shrinkage of the surrounding paste [203]. Due to the large autogenous shrinkage of the concrete (as will be discussed in the following section), microcracks may have developed within the concrete, although no visual cracks were observed on the surface of the sample. The development of microcracking can harm the (increase of) tensile strength. Although the absolute tensile strength of the concrete increased with the curing age as shown in Figure 6.10, the developing rate of the tensile strength became lower than that of the compressive strength as indicated by the decreasing f_t/f_c .

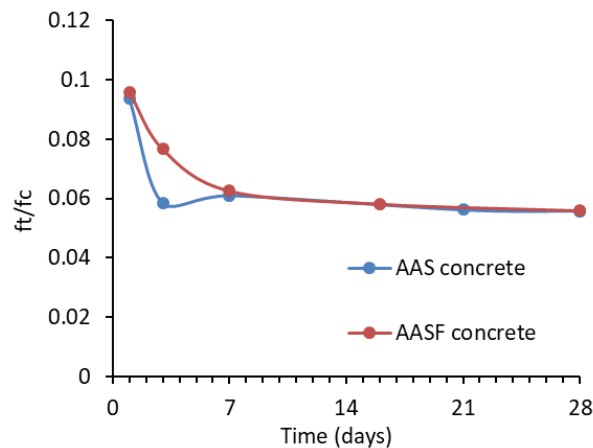


Figure 6.11 Splitting tensile strength-to-compressive strength (f_t/f_c) ratios of AAS and AASF concrete.

6.3.1.2 Elastic modulus

The elastic modulus of the concrete is shown in Figure 6.12. AAS concrete showed higher elastic modulus than AASF concrete at early age. After 7 days, however, the elastic modulus of AAS concrete started to decrease slightly, while the one of AASF concrete kept increasing. At 28 days, AAS and AASF concrete showed similar magnitudes of elastic modulus.

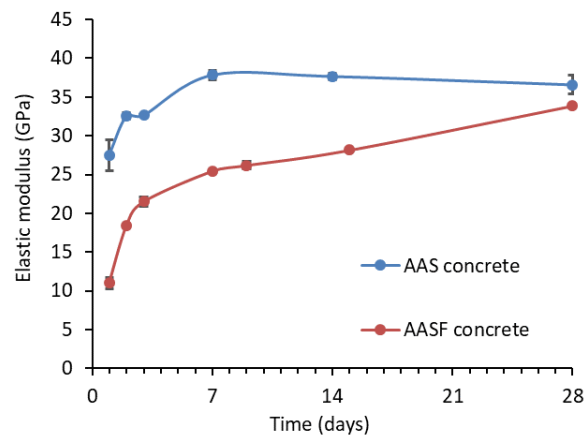


Figure 6.12 Elastic modulus of AAS and AASF concrete.

6.3.2 Autogenous shrinkage

The autogenous shrinkage of the concrete is shown in Figure 6.13. AASF concrete showed lower autogenous shrinkage than AAS concrete in the whole period of the study. These findings are consistent with the autogenous shrinkage results on corresponding AAS and AASF pastes as shown in Figure 3.3. The autogenous shrinkage of AAS and AASF concrete develops rapidly at the first one to two days, which is in line with the accelerated reaction stages of the mixtures (see Figure 3.6). At the age of 21 days, the autogenous shrinkage of AAS and AASF concrete reaches 609 and 325 $\mu\text{m}/\text{m}$, respectively.

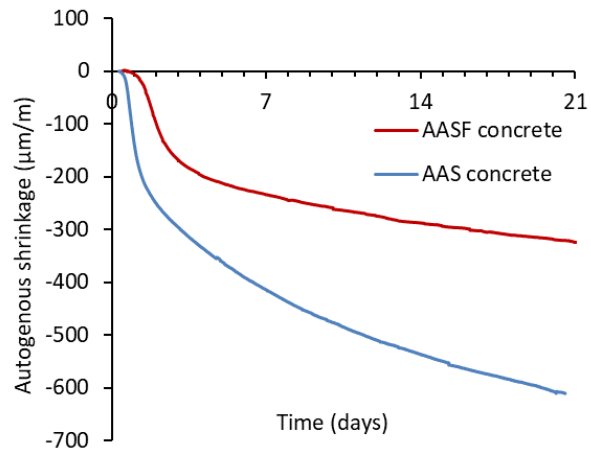


Figure 6.13 Autogenous shrinkage (AS) of AAS and AASF concrete measured by ADTM (details of ADTM were shown in section 6.2.2.2).

6.3.3 Autogenous shrinkage-induced stress

Figure 6.14 shows the stress development in AAS and AASF concrete tested by TSTM. The sudden drop in the stress to around zero indicates the occurrence of cracking in concrete. It can be seen that AAS concrete showed a rapid stress development due to the high autogenous shrinkage. The stress in AASF concrete remained low in the first 1.5 days due to low shrinkage (see Figure 6.13). The tensile stress generated in AASF concrete was substantially lower than in AAS concrete. The lower autogenous shrinkage, and also the lower elastic modulus of AASF concrete, results in a stress in AASF concrete lower than in AAS concrete. The tensile strength (1.4 MPa) tested by TSTM of AASF concrete was also lower than that of AAS concrete (2.7 MPa). Eventually, AASF concrete cracked even earlier and at a lower stress than AAS concrete.

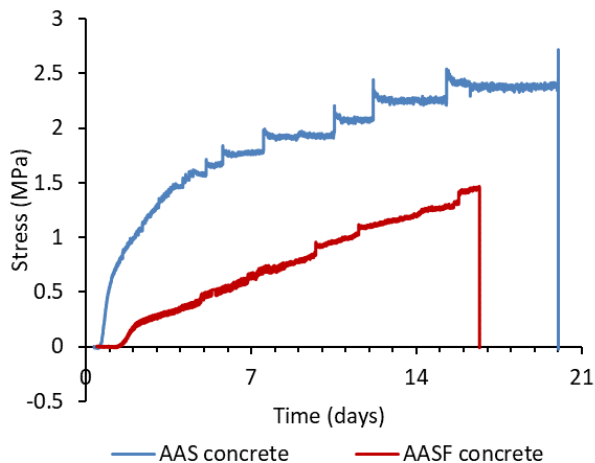


Figure 6.14 Autogenous shrinkage-induced stress in AAS and AASF concrete measured by TSTM (details of TSTM were shown in section 6.2.2.3).

By comparing the results in Figures 6.14 and 6.10 (b), we see that the measured tensile strength of the concrete beam is much lower than the splitting tensile strength of the cubes. There are mainly two reasons for this. First, the beam is much longer than the cube, so there is a high probability that some cross-sections in the beam have lower strength than the middle cross-section of the cube. Moreover, the concrete beam in the TSTM was under tensile stress in the whole period before failure, while the cubes were free from loading. The continuous increase in tensile stress, even if it did not break the beam, can induce stress concentration in the concrete and aggravate the development of microcracking within the beam. As a result, local failure within the concrete can be induced, which reduces the tensile strength [253,254].

The classification of the cracking tendency according to ASTM C1581 [245] is shown in Table 6.2, where the cracking time (in days) and average stress rate (in MPa/day) were considered. According to Table 6.2, the cracking tendency of the two concrete mixtures belongs to the category “moderate-low”. Compared with the results obtained by TSTM on OPC-based concrete in the literature [241,255,256], the AAS and AASF concretes show actually lower stress and later cracking than OPC-based concrete with similar strength. The lower cracking tendency of AAC than OPC-based concrete with similar or even lower strength is very positive information in view of the application of AAC as a building material.

The reason why AAC showed higher autogenous shrinkage but lower cracking tendency than OPC-based concrete, is believed to be mainly due to the stress relaxation. The evident stress relaxation of AAC is in line with the large creep of AAM paste identified in chapter 3. These two phenomena, creep and relaxation, are both associated with the viscoelasticity of the material [257]. In the next section, the creep part of the autogenous shrinkage will be quantified.

Table 6.2 Classification of potential for cracking according to ASTM C1581 [245].

Cracking time t_{cr} (days)	Average stress rate S (MPa/day)	Potential for cracking
$0 < t_{cr} \leq 7$	$S \geq 0.34$	High
$7 < t_{cr} \leq 14$	$0.17 \leq S < 0.34$	Moderate-High
$14 < t_{cr} \leq 28$	$0.10 \leq S < 0.17$	Moderate-Low
$t_{cr} > 28$	$S < 0.10$	Low

6.4 Prediction of the autogenous shrinkage-induced stress in AAC

6.4.1 Calculated stress based on autogenous shrinkage

The calculated evolution of stresses with Equation 6.1, based on the autogenous shrinkage (see Figure 6.13) and the elastic modulus (see Figure 6.12) of the concrete, are presented and compared with measured stress in Figure 6.15. It can be seen that the calculated stress in AAC is around 7-8 times higher than the experimentally measured one. These results confirm that the creep/relaxation plays an important role in the stress development in the AAC specimen. The stress is greatly overestimated when the creep part in the autogenous shrinkage and the stress relaxation are not considered.

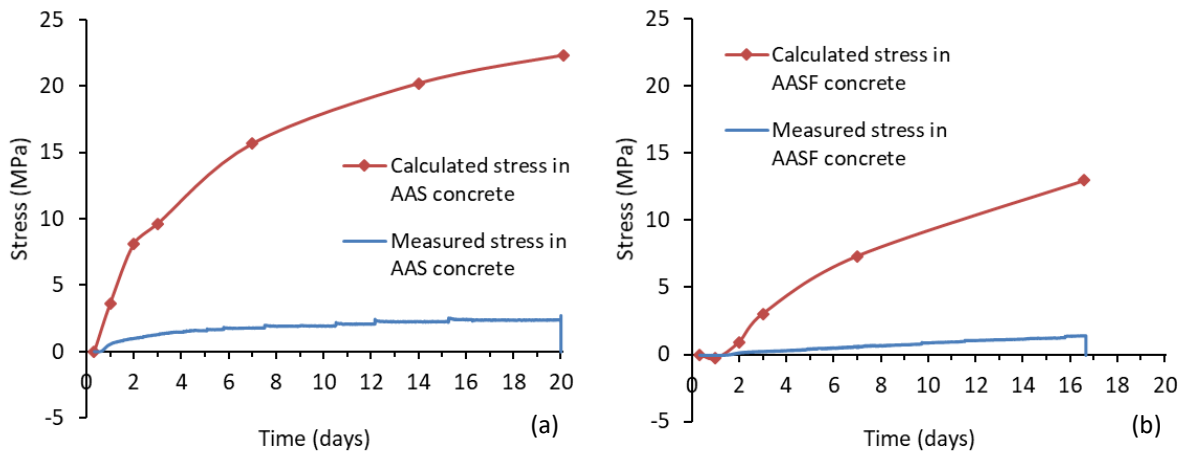


Figure 6.15 Calculated stress in AAS (a) and AASF (b) concrete from the autogenous shrinkage and the elastic modulus of the concrete. Calculations were according to Equation 6.1.

6.4.2 Calculated stress based on the elastic part of autogenous shrinkage

According to Equations 6.2 and 6.4–6.7, the elastic part and creep part of the autogenous shrinkage of AAC can be calculated, as shown in Figure 6.16.

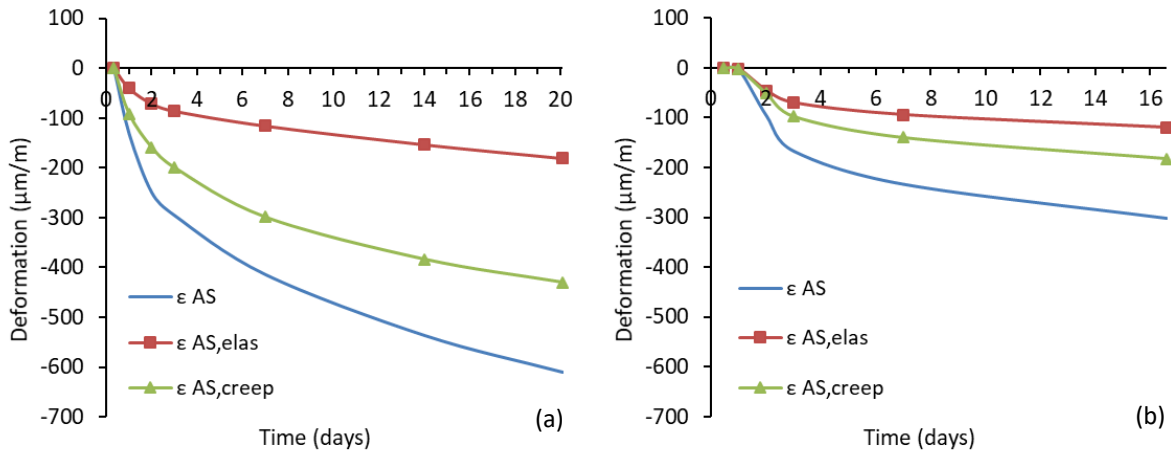


Figure 6.16. Calculated elastic part and creep part of autogenous shrinkage of AAS (a) and AASF (b) concrete.

The calculated stress in the AAC specimen according to Equation 6.3 is shown in Figure 6.17. It can be seen that considering only the elastic part of autogenous shrinkage for calculating the stresses gives a much better prediction of the shrinkage-induced stress than the results shown in Figure 6.15, where the total autogenous shrinkage was used as input. Nonetheless, the calculated stress is still two times higher than the stress measured by TSTM, indicating that the relaxation of the stress has also to be considered in order to estimate the time-dependent stress.

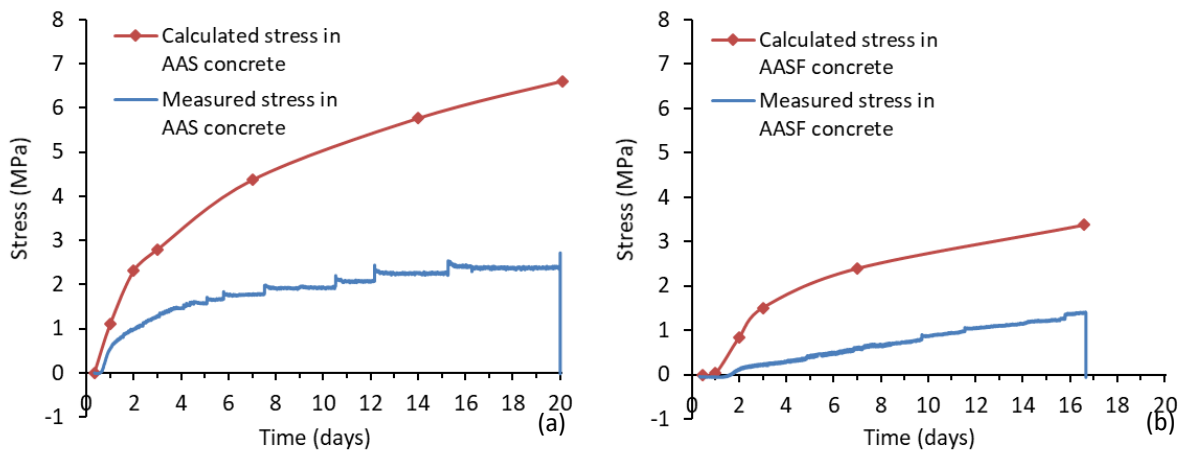


Figure 6.17 Calculated stress in AAS (a) and AASF (b) concrete from the elastic part of the autogenous shrinkage and the elastic modulus of the concrete. Calculations were according to Equation 6.3.

6.4.3 Calculated stress by taking into account creep and relaxation

According to Equations 6.8-6.11, the stress in the AAC specimen by taking both creep and relaxation into account is calculated and shown in Figure 6.18. It can be seen that the calculation considering the elastic part of the autogenous shrinkage and the relaxation of the stress with time provides a fairly good agreement between calculated and measured stress evolutions in AAC. For AAS concrete, the calculation underestimates the stress in the first 7 days while overestimates the stress at 20 days. For AASF concrete, an opposite trend is observed.

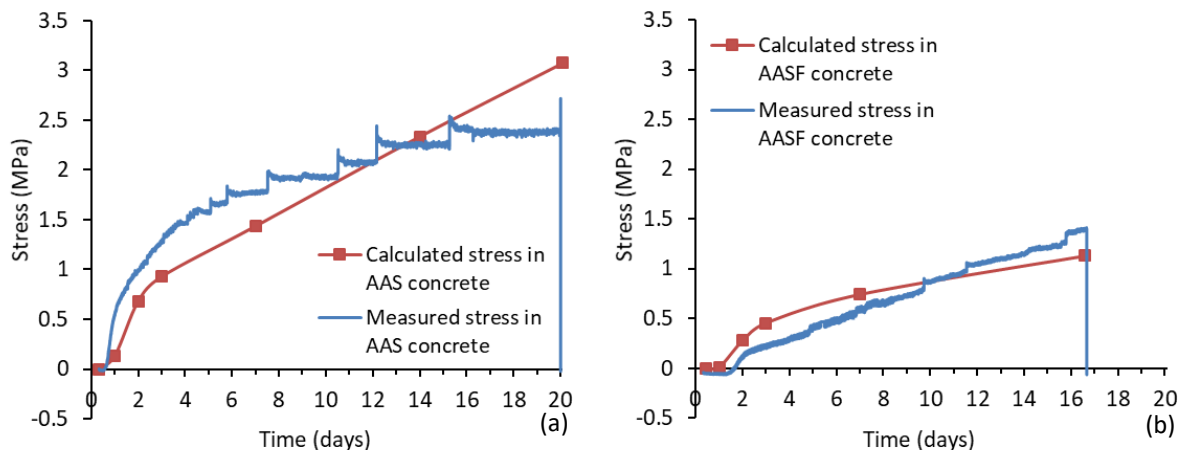


Figure 6.18 Calculated stress in AAS (a) and AASF (b) concrete from the elastic part of the autogenous shrinkage and the elastic modulus of the concrete, with the stress relaxation taken into account. Calculations were according to Equation 6.8.

Despite the discrepancies between the calculated and measured results as shown in Figure 6.18, the calculations in this section have clearly shown the important roles played by relaxation in the stress evolution of restrained AAC. Neglecting the creep and relaxation behaviours would lead to an overestimation of the self-induced stress in AAC.

With the estimated stress, the probability of cracking of AAC can be predicted if the evolution of the tensile strength of concrete is known. In section 6.3.1, the splitting tensile strength of the concrete was shown. However, the tensile strength of the concrete beam is normally lower than the splitting tensile strength of the cubes, as discussed in section 6.3.3. Therefore, a reducing factor of the splitting tensile strength needs to be considered when estimating the cracking time, as shown in Figure 6.19.

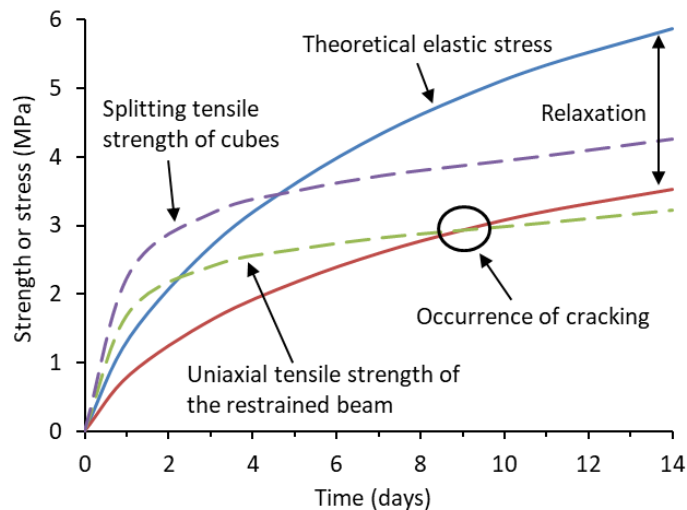


Figure 6.19 A schematic diagram of the stress development and the resultant cracking of concrete due to restrained shrinkage.

For OPC-based concrete, the failure stress-to-splitting strength ratios were in the range of 0.7 - 0.8 [244,258,259]. Based on experiments on a dozen specimens, Lokhorst [244] found OPC-based concrete, on average, failed at 75% of the actual tensile splitting strength, irrespective of the age at cracking. However, the ratios of failure stress (Figure 6.14) to splitting tensile strength (Figure 10 (b)) for AAS concrete and AASF concrete in this study were only 0.56 and 0.37, respectively. These ratios were lower than those for OPC concretes, possibly because of the more evident creep/relaxation in AAC. Besides, it should be noted that these ratios are also dependent on the quality of concrete casting. In this chapter, only a limited number of samples were tested. Therefore, it is not possible to conclude that the ratio 0.56 or 0.37 is representative and a reliable input for predicting the cracking time of all AAC mixtures. To obtain representative reduction factors of the tensile strength of AAC under restrained condition, intensive experimental work in future on numerous mixtures and samples is required.

6.5 Effectiveness of internal curing and incorporation of MK

According to Table 6.2, the cracking tendency of AAC is classified as “moderate-low”. Both AAS and AASF concrete cracked within one month due to restrained autogenous shrinkage. Strategies to reduce the cracking tendency of AAC is needed in order to widen its acceptance by the market in structural applications. In chapters 4 and 5, two shrinkage-mitigating strategies, internal curing with SAPs and incorporation of MK, were discussed. In this section, the effectiveness of these two strategies for mitigating the proneness to cracking of AASF

concrete will be verified. The properties of AASFICMK concrete (see the composition in Table 6.1) are shown below.

6.5.1 Workability and strength

The measured slump of AASFICMK concrete was 280 mm. The concrete quickly spread over the whole flow table ($700 \times 700 \text{ mm}^2$) after the cone was lifted up (Figure 6.20). This slump-flow value corresponds to the class SF2 for self-compacting concrete [260]. The initial and final setting times of AASFICMK paste were 58 min and 117 min, respectively. The long setting time and the large slump-flow indicate very good workability of the concrete.

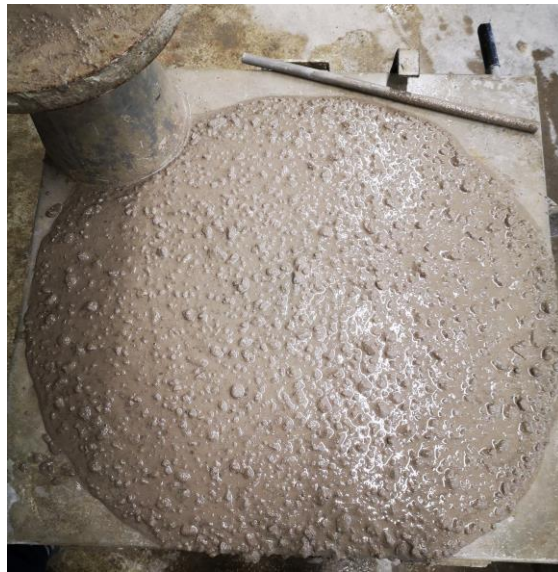


Figure 6.20 Flowability of AASFICMK concrete immediately after lifting up of the cone.

The strength development of AASFICMK concrete is shown in Figure 6.21. The 1-day compressive strength is 2.1 MPa, which enables a successful demoulding at that age. Due to the incorporation of SAPs and MK, the strength of AASFICMK concrete is generally lower than that of AASF concrete (see the discussion in section 4.3.8 and 5.3.5). However, the 28 days compressive strength of AASFICMK concrete still reaches 51 MPa, which is sufficient for many structural applications[238].

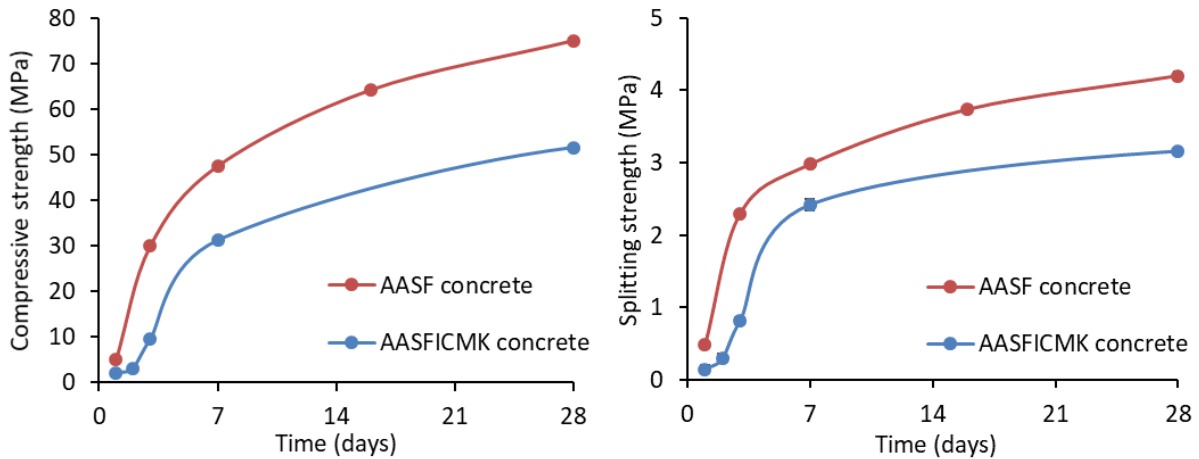


Figure 6.21 Compressive (a) and splitting strength (b) of AASFICMK concrete, in comparison with AASF concrete. For splitting strength, the error bar is shown in the diagram, but it is too small to be clearly distinguished from the marker.

The f_t/f_c ratio of AASFICMK concrete is compared with that of AASF concrete in Figure 6.22. In the first day, the f_t/f_c ratio of AASFICMK concrete is lower than that of AASF concrete. Probably this is because the bonding between the aggregate and the paste in AASFICMK is still weak due to the retarding effect of MK and SAPs on the reactions in the very early age (see Figures 4.4 and 5.7). After the first day, however, the f_t/f_c ratios of AASFICMK concrete is always higher than that of AASF concrete. As mentioned in section 6.3.1, f_t/f_c ratios are affected by the development of microcracking in the concrete. The higher f_t/f_c ratio of AASFICMK indicates that the incorporation of MK and SAPs can mitigate the microcracking development in AASF concrete induced by locally restrained autogenous shrinkage. This point will be verified in the following sections.

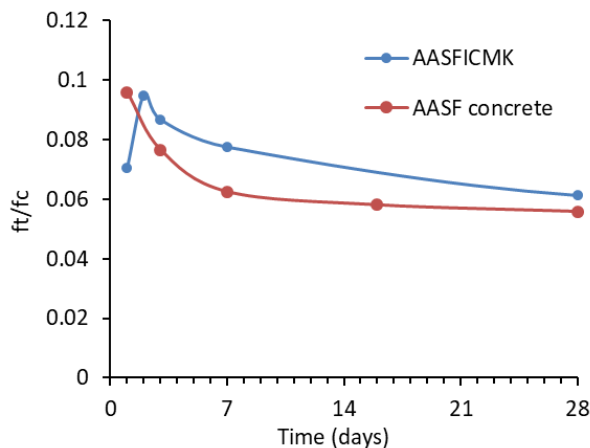


Figure 6.22 Splitting tensile strength-to-compressive strength (f_t/f_c) ratios of AASFICMK concrete, in comparison with AASF concrete.

6.5.2 Autogenous shrinkage

Figure 6.23 shows that the autogenous shrinkage of AASFICMK concrete is less than 20% of the autogenous shrinkage of AASF concrete after one month of sealed curing. This indicates that the combination of internal curing and MK can effectively mitigate the autogenous shrinkage of AASF concrete. The slight expansion shown by AASFICMK concrete at the very early age is probably an artefact of the measurement, such as the pushing force from the LVDTs on the measuring bars, since the corresponding paste does not show autogenous expansion (see Figure 3.3).

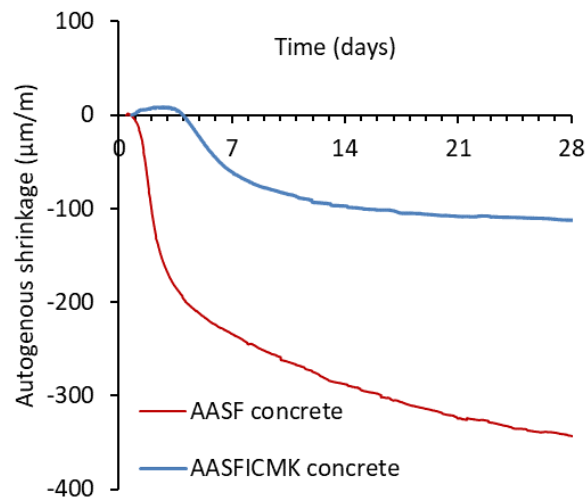


Figure 6.23 Autogenous shrinkage of AASF and AASFICMK concrete.

6.5.3 Autogenous shrinkage-induced stress

The stress evolutions in the plain AASF concrete and AASFICMK concrete are shown in Figure 6.24. The figure shows that the stress generated in AASFICMK was much lower than that in AASF. In the first 4 days, a small compressive stress was detected in AASFICMK due to the restrained expansion of the concrete (see Figure 6.23). Afterwards, a tensile stress started to develop. The stress in AASFICMK was only 35% and 25% of the stress in plain AASF concrete at 7 days and 14 days, respectively.

With the internal curing by SAPs and incorporation of MK, AASFICMK concrete did not crack within 56 days. The stress development rate after the first week was lower than 0.01 MPa/day, indicating a very “low” cracking tendency of the concrete (see Table 6.2). These results indicate that the strategies developed in chapters 4 and 5 are effective in mitigating the autogenous shrinkage and the cracking tendency of AAC.

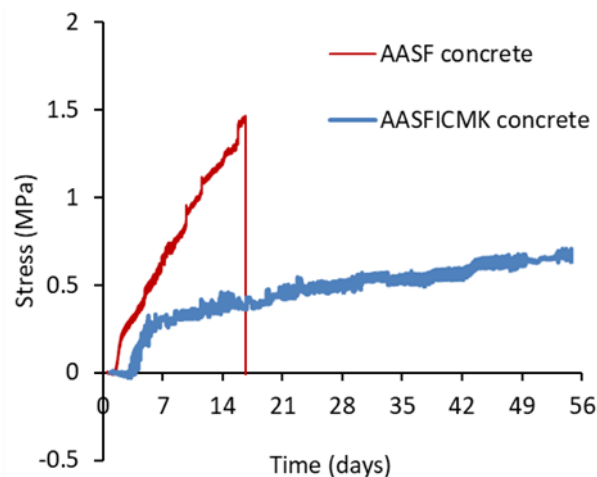


Figure 6.24 Self-induced stress in AASF and AASFICMK concrete.

The superior workability (self-compacting), the high 28 days-strength (51 MPa) and the low cracking tendency indicate that AASFICMK concrete can be considered as a highly competitive construction material. Furthermore, due to the very low cracking tendency of AASFICMK concrete, there is much room for further tailoring the current mixture design according to different engineering requirements. For example, for the cases where the autogenous shrinkage is not very critical, lower liquid/binder ratios, lower dosages of SAPs and MK or higher amounts of slag could be used, by which a higher strength of the concrete can be easily achieved.

6.6 Concluding remarks

In this chapter, the cracking tendency of AAC subjected to restrained autogenous shrinkage is evaluated. The effectiveness of the strategies proposed in chapters 4 and 5 to reduce the cracking tendency of AASF concrete is shown plausible. Based on the results of this chapter, the following remarks can be made:

1. AAC shows generally high compressive strength. The f_t/f_c ratio and the elastic modulus of AAC decrease with the curing age, which may be due to the development of microcracking resulting from the continuous autogenous shrinkage.
2. TSTM is utilized to track the stress evolution and proneness to cracking of AAC caused by autogenous shrinkage. AAC is found to show later cracking than OPC-based concrete with similar compressive strength, despite the higher autogenous shrinkage of AAC. This is mainly because a large part of the measured autogenous shrinkage belongs to creep and that the stress is reduced by the pronounced relaxation of the concrete.
3. With the elastic part of the autogenous shrinkage and the stress relaxation taken into account, a very good prediction of the stress evolution in AAC is obtained. In contrast, calculations without considering the creep and relaxation would lead to a significant overestimation of the stress in AAC.

4. Internal curing and incorporation of MK can dramatically mitigate the cracking tendency of AAC. An AAC concrete mixture (AASFICMK) with good workability, high strength, and very low autogenous shrinkage-induced cracking tendency is developed. Based on the mixture AASFICMK, tailored designs are allowed to reach optimal overall performances for specific applications.

Chapter 7

Retrospection, conclusions, contributions and future research

7.1 Retrospection

Alkali-activated materials (AAMs) have emerged as eco-friendly alternatives for ordinary Portland cement (OPC)-based binders [232]. Compared to cement production, the production of AAMs entails around 25-50% lower CO₂ emissions and more than 40% lower embodied energy [261,262]. However, a wide utilization of AAMs in infrastructures has not been realized yet due to insufficient knowledge of the performance of AAMs. While it has been known that AAMs can show high strength, good chemical resistance and fire resistance [13,14,206], the autogenous shrinkage of AAMs is not well understood yet. According to the experimental results in several preliminary studies [56–58,81], AAMs can show high autogenous shrinkage, which may hinder the application of AAMs as binder materials.

The research question therefore arises that “whether autogenous shrinkage is a problem for AAMs as binder materials?” The immediately following question is that “if so, can we solve it?” To answer these questions, this research was conducted to understand and mitigate the autogenous shrinkage and cracking tendency of AAMs and the sub-tasks of this thesis were set.

In chapter 3, the autogenous shrinkage of AAMs paste was measured and compared with that of OPC paste. The mechanism of autogenous shrinkage of AAMs was then investigated through characterizations of the reaction products, reaction kinetics, pore structures and internal relative humidity of AAMs. The role of fly ash in slag and fly ash-blended system was discussed. In this chapter, the driving force of autogenous shrinkage and the deformability of the paste were clarified. A computation model was built to calculate the elastic part and creep part of autogenous shrinkage of AAMs.

In chapters 4 and 5, targeting at the driving forces of the autogenous shrinkage, two mitigating strategies were developed. In these two chapters, the effectiveness of internal curing with superabsorbent polymers (SAPs) and incorporation of small amounts of metakaolin (MK) on mitigating the autogenous shrinkage of AAMs were explored, respectively. The mechanisms of the mitigation effect were elaborated. The mechanical properties of AAMs paste with SAPs and MK were also studied.

In chapter 6, the proneness to cracking of alkali-activated concrete (AAC) induced by restrained autogenous shrinkage was evaluated. The self-induced stress development and cracking time of AAC were then modelled by considering creep and relaxation and the

evolution of the tensile strength. The strategies proposed in chapters 4 and 5 were utilized in chapter 6 to produce an AAC with sufficient strength and very low cracking tendency.

With the results obtained in the chapters, the original questions can be answered: “autogenous shrinkage can be a problem for AAMs as a binder material”, but, “we can solve it”.

7.2 Conclusions

The conclusions of this thesis are summarized as follows:

Magnitude and mechanism of autogenous shrinkage of AAMs

- The autogenous shrinkage AAMs pastes was generally larger than that of OPC paste. The more slag is used in the precursor, the larger autogenous shrinkage will be.
- In the dormant period of the reaction, the stiffness of AAMs paste was low and the autogenous shrinkage was mainly viscous or even plastic deformation. From the start of the acceleration period, the stiffness of the paste increased rapidly, and the self-desiccation resulted in the build-up of pore pressure in the paste. It was hypothesized that the reduction of steric-hydration force due to the consumption of ions in the pore solutions also induced a certain amount of autogenous shrinkage. In the deceleration period, the pore pressure became the dominant driving force of autogenous shrinkage.
- A large part of the autogenous shrinkage of AAMs paste belonged to creep under internal forces. By employing van Breugel’s model, the creep part of the autogenous shrinkage can be well estimated from the elastic deformation.

Mitigating the autogenous shrinkage of AAMs by internal curing

- The SAPs showed lower absorption capacity in alkali activator than in water. Nonetheless, one gram of the SAPs could still absorb 20 grams of activator, with no absorption preference for water or ions observed.
- The dosage of SAPs was designed based on the chemical shrinkage of the paste and the absorption capacity of the SAP. With the internal curing by SAPs, the autogenous shrinkage of AAMs paste was effectively mitigated, especially the part of autogenous shrinkage that occurred during the deceleration period. Higher SAPs amounts did not bring a further mitigating effect on the autogenous shrinkage.
- While the flexural strength and elastic modulus of AAMs paste were only slightly influenced by the addition of SAP, the compressive strength can decrease by more than 15%.

Mitigating the autogenous shrinkage of AAMs by incorporation of MK

- The incorporation of MK provided extra dissolvable Si and Al to the system and decreased the concentration of Ca^{2+} , Na^+ and OH^- . As a result, the reaction rate in the acceleration period was delayed and the pore refinement was retarded. Nonetheless, the primary reaction product remains C-A-S-H type gel.
- The autogenous shrinkage of AAMs induced by pore pressure and by reduction of steric-hydration force was both significantly mitigated by incorporation of MK.

- The compressive strength of AAM pastes was slightly decreased by incorporation of MK, while the flexural strength was improved. The setting time was prolonged when MK was present.

Cracking tendency of AAC induced by restrained autogenous shrinkage

- AAS and AASF concrete show high compressive strength but relatively low tensile strength.
- Thanks to their pronounced relaxation, AAS and AASF concretes showed much later cracking time than OPC base concrete with similar compressive strength, although the autogenous shrinkage of AAMs concrete was higher. A numerical approach is proposed to predict the evolution of autogenous shrinkage-induced stresses in AAC.
- Combining internal curing agent SAPs and incorporation of MK, an AAC with good workability, high strength and very low autogenous shrinkage-induced cracking tendency was designed.

7.3 Contributions of this study

In this study, the magnitude, the mechanisms and the mitigating strategies of autogenous shrinkage of slag and fly ash-based AAMs systems were comprehensively investigated. The following contributions were made by this thesis to the science, the engineering application and the standardizations of AAMs as alternative binder materials.

Shrinkage measurement

- While the time-zero of the autogenous shrinkage of OPC-based paste is suggested to be at the final setting time [128], this study revealed that the start of the acceleration period indicated by the calorimetry test is a better time-zero for AAS/AASF pastes. Before that, the stiffness of the paste and the self-induced stress develop rather slowly, even though the paste already sets according to the Vicat method [127].
- The procedure for measuring chemical shrinkage of AAMs paste needs a slight modification compared to the method for OPC-based paste. Alkali solution instead of pure water should be put onto the surface of the paste before paraffin oil is added, in order to avoid dilution of the early age pore solution of the paste. The details of the modified method for chemical shrinkage measurement of AAMs have been published elsewhere [46].

Mechanisms of autogenous shrinkage of AAMs

- In this study, the mechanism of autogenous shrinkage of slag and fly ash-based AAMs was proposed. It was found that the pore pressure induced by self-desiccation is not the only driving force of the autogenous shrinkage of AAMs. Based on the understanding of the mechanisms, more mitigating strategies of autogenous shrinkage of AAMs can be developed.
- AAMs systems were found to show more pronounced viscous deformation/creep than OPC-based systems. This behaviour helps to explain the large long-term creep of AAC

measured at external load [263]. The evident creep of AAMs systems is an important factor to be considered in the future design of AAMs concrete as structural element.

- Thanks to the pronounced creep/relaxation, AAC showed lower cracking tendency than OPC-based concrete with similar compressive strength. This finding is important in view of the market acceptance of AAC.

Mixture design

- The role of slag and fly ash in influencing the autogenous shrinkage of AAMs was clarified. At ambient temperature, slag was found to be a dominant precursor for the formation of reaction products, while fly ash acted more like fillers (to dilute the slag content).
- In order to mitigate the autogenous shrinkage, internal curing by SAPs and incorporation of MK were found to be promising ways. The dosage of SAPs is suggested to be designed from the chemical shrinkage of the paste and the absorption capacity of the SAP. The content of MK is suggested to be less than 20 wt. % of the slag since MK can significantly retard the formation of C-A-S-H type gels. For the formation of a considerable amount of N-A-S-H type gel, an elevated temperature might be required.
- An AAC mixture with superior workability, high strength and very low autogenous shrinkage-induced cracking tendency was designed. For slag and fly ash-based AAC (in fact even for OPC concrete), low shrinkage and good workability are hard to realize without compromising the strength. With the help of SAPs and MK, the dilemma was resolved.

Models

- The creep part of the autogenous shrinkage of AAMs paste was estimated by a numerical approach. Using the calculated creep factor as input, the relaxation factor could be calculated. Considering the creep and relaxation, the stress evolution and cracking time of restrained AAC can be well predicted. These approaches have promising potential to be used in future studies or applications where shrinkage and cracking estimations are needed.

7.4 Future research

The following are indications about possible future research in the field of shrinkage of AAMs:

- In this study, only the autogenous shrinkage of NaOH and Na₂SiO₃-activated AAMs was concerned. The autogenous shrinkage of AAMs activated by other types of activators, such as Na₂CO₃ or Na₂SO₄, is worth studying.
- In this study, no admixtures besides SAPs and MK were utilized. More alternative chemical admixtures, like shrinkage reducing admixtures (SRA), which can mitigate the autogenous shrinkage of AAMs need to be identified in the future.
- In this study, the steric-hydration force was only preliminarily investigated. It is necessary to quantify the effects of ion concentrations, pore diameters, and elastic modulus on this force and the resulting shrinkage.

- This study only focused on the autogenous shrinkage of AAMs. Drying shrinkage, which might be more problematic in some cases, needs to be investigated in the future. It should be noted that the autogenous shrinkage accounts for an important part of the drying (total) shrinkage and the creep of the material will still play a critical role in drying condition. What needs special attention is that drying can cause larger driving force of shrinkage, while the force and deformation can be unevenly distributed in the materials.
- The specimens of AAMs paste and concrete tested in this study were all cured at 20 °C. The thermal deformation and the corresponding cracking tendency of AAMs need to be studied in the future. For example, the cracking tendency of AAC under restrained and (semi-)adiabatic conditions would be important in view of the probability of cracking in massive concrete structures.

Appendix A

Ultimate total heat and overall reaction degree

In chapters 3 and 6, the reaction degree α was used to calculate the creep coefficient of the paste or concrete. The reaction degree α of the paste or concrete can be calculated with Equation A.1 [144].

$$\alpha(t) = \frac{Q(t)}{Q_{max}} \quad (\text{A.1})$$

where $Q(t)$ is the reaction heat and Q_{max} is the ultimate total heat at the completion of the reaction.

$Q(t)$ of AAS and AASF pastes during the first week of reaction has been experimentally measured as shown in Figure 3.5. Therefore, in chapter 3, where only the creep coefficient during the first week was needed, the ratio $\frac{\alpha(t)}{\alpha(\tau)}$ was calculated directly from the experimental results of $Q(t)$ and $Q(\tau)$ as shown in Equation A.2.

$$\frac{\alpha(t)}{\alpha(\tau)} = \frac{Q(t)}{Q(\tau)} \quad (\text{A.2})$$

In chapter 6, in contrast, the reaction degree α until the age of 21 days was needed in order to calculate the creep coefficient. To estimate $Q(t)$ after the first week and Q_{max} , the method of curve fitting is needed.

According to [144,264,265], the exponential model shown in Equation A.3 can provide a good prediction of Q_{max} for AAMs.

$$Q(t) = Q_{max} \exp\left[-\left(\frac{\theta}{t}\right)^\beta\right] \quad (\text{A.3})$$

where θ and β are the fitting parameters associated with the time and the shape of the exponential model.

According to the trend of the heat flow curves of AAMs paste, a piecewise approximation by two functions is needed for the fitting. The fitted curves of the heat flow of AAS and AASF pastes are presented in Figure A.1, in comparison with the experimental results. The fitting parameters and the accuracy of the fitting (indicated by the adjusted R-square) are shown in Table A.1.

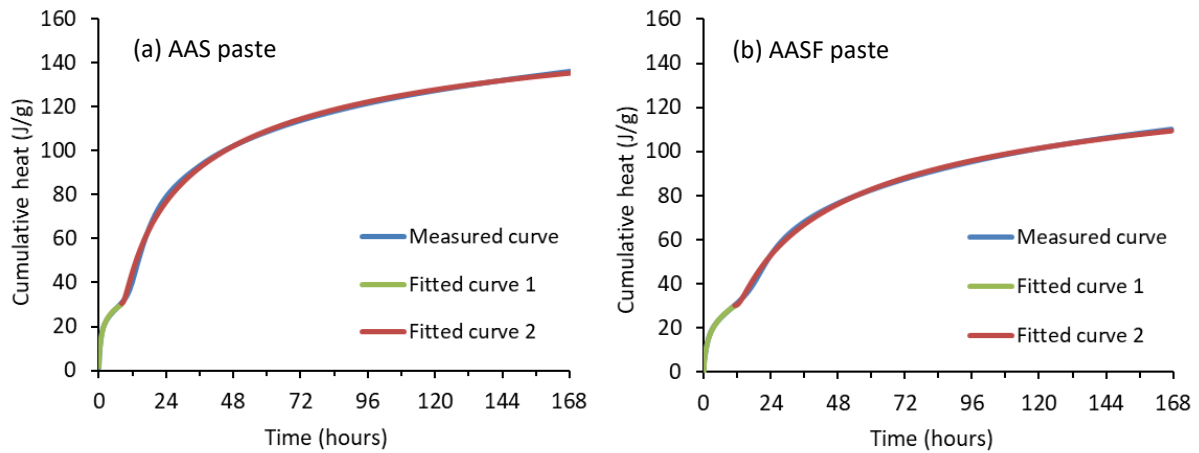


Figure A.1 Fitted heat of AAS paste (a) and AASF paste (b), in comparison with the experimental results.

Table A.1 Fitted parameters of the exponential model for the heat flow of AAS and AASF paste.

Mixtures	Q_{max} (J)	θ (days)	β (-)	R-square
AAS curve 1	56.17	0.08	0.33	0.998
AAS curve 2	155.04	0.99	0.49	0.998
AASF curve 1	115.57	1.83	0.218	0.999
AASF curve 2	139.128	1.92	0.47	0.999

Figure A.1 and Table A.1 indicate a very good fitting of the curves. It can be seen in Table A.1 that AAS paste has a higher Q_{max} than AASF paste, which is consistent with the results in section 3.3.2. Due to the same curing condition (iso-thermal) of the paste and concrete samples, we assume the reaction degrees of the paste and the concrete are the same all the time. Hence, with the fitted parameters, the $Q(t)$ and the reaction degree α of AAS and AASF concrete at different curing ages can be then calculated, as shown in Table A.2. The results were used to in chapter 6 to calculate the creep coefficient.

Table A.2 $Q(t)$ and α of AAS and AASF concrete at different ages.

AAS concrete	8h	1d	2d	3d	7d	14d	20d
$Q(t)$ (J)	30.53	78.90	102.09	113.70	135.98	148.63	153.70
α (-)	0.20	0.51	0.66	0.73	0.88	0.96	0.99
AASF concrete	8h	1d	2d	3d	7d	16.6d	-
$Q(t)$ (J)	26.93	53.65655	77.03087	88.11111	110.6487	126.955	-
α (-)	0.193563	0.385663	0.553669	0.63331	0.795302	0.912505	-

References

- [1] E. Worrell, L. Price, N. Martin, C. Hendriks, L.O. Meida, Carbon dioxide emissions from the global cement industry, *Annu. Rev. Energy Environ.* 26 (2001) 303–329.
- [2] R.M. Andrew, Global CO₂ emissions from cement production, 1928-2017, *Earth Syst. Sci. Data.* 10 (2018) 2213–2239. doi:10.5194/essd-10-2213-2018.
- [3] C. Shi, A.F. Jiménez, A. Palomo, New cements for the 21st century: The pursuit of an alternative to Portland cement, *Cem. Concr. Res.* 41 (2011) 750–763. doi:10.1016/j.cemconres.2011.03.016.
- [4] J.L. Provis, S. a Bernal, Geopolymers and Related Alkali-Activated Materials, *Annu. Rev. Mater. Res.* 44 (2014) 299–327. doi:doi:10.1146/annurev-matsci-070813-113515.
- [5] M. Fawer, M. Concannon, W. Rieber, Life cycle inventories for the production of sodium silicates, *Int. J. Life Cycle Assess.* 4 (1999) 207.
- [6] C. Shi, D. Roy, P. Krivenko, *Alkali-activated cements and concretes*, CRC press, 2003.
- [7] O.N. Petropavlovsky, *Slag alkaline binding systems and concretes based on steelmaking slag*, Thesis, Kiev Civil Engineering Institute, 1987.
- [8] S. Wang, X. Pu, K.L. Scrivener, P.L. Pratt, Alkali-activated slag cement and concrete: a review of properties and problems, *Adv. Cem. Res.* 7 (1995) 93–102. doi:10.1680/adcr.1995.7.27.93.
- [9] Y. Ma, *Microstructure and Engineering Properties of Alkali Activated Fly Ash -as an environment friendly alternative to Portland cement*, Delft University of Technology, 2013.
- [10] J.L. Provis, J.S.J. Van Deventer, *Alkali Activated Materials*, 2014. doi:10.1007/978-94-007-7672-2.
- [11] M. Nedeljković, Z. Li, G. Ye, Setting, Strength, and Autogenous Shrinkage of Alkali-Activated Fly Ash and Slag Pastes: Effect of Slag Content, *Materials (Basel)*. 11 (2018) 2121. doi:10.3390/ma11112121.
- [12] M. Nedeljković, Y. Zuo, K. Arbi, G. Ye, Carbonation resistance of alkali-activated slag under natural and accelerated conditions, *J. Sustain. Metall.* 4 (2018) 33–49.
- [13] K. Arbi, M. Nedeljković, Y. Zuo, G. Ye, A Review on the Durability of Alkali-Activated Fly Ash/Slag Systems: Advances, Issues, and Perspectives, *Ind. Eng. Chem. Res.* 55 (2016) 5439–5453. doi:10.1021/acs.iecr.6b00559.
- [14] M.C.G. Juenger, F. Winnefeld, J.L. Provis, J.H. Ideker, Advances in alternative cementitious binders, *Cem. Concr. Res.* 41 (2011) 1232–1243. doi:10.1016/j.cemconres.2010.11.012.
- [15] S.A. Bernal, J.L. Provis, Durability of alkali-activated materials: progress and

- perspectives, *J. Am. Ceram. Soc.* 97 (2014) 997–1008.
- [16] Z. Shi, C. Shi, S. Wan, Z. Ou, Effect of alkali dosage on alkali-silica reaction in sodium hydroxide activated slag mortars, *Constr. Build. Mater.* 143 (2017) 16–23. doi:10.1016/j.conbuildmat.2017.03.125.
- [17] D.L.Y. Kong, J.G. Sanjayan, Effect of elevated temperatures on geopolymer paste, mortar and concrete, *Cem. Concr. Res.* 40 (2010) 334–339. doi:10.1016/j.cemconres.2009.10.017.
- [18] O.M. Jensen, P.F. Hansen, Autogenous deformation and RH-change in perspective, *Cem. Concr. Res.* 31 (2001) 1859–1865. doi:10.1016/S0008-8846(01)00501-4.
- [19] N.K. Lee, J.G. Jang, H.K. Lee, Shrinkage characteristics of alkali-activated fly ash/slag paste and mortar at early ages, *Cem. Concr. Compos.* 53 (2014) 239–248. doi:10.1016/j.cemconcomp.2014.07.007.
- [20] A.A. Melo Neto, M.A. Cincotto, W. Repette, Drying and autogenous shrinkage of pastes and mortars with activated slag cement, *Cem. Concr. Res.* 38 (2008) 565–574. doi:10.1016/j.cemconres.2007.11.002.
- [21] H. Ye, A. Radlińska, Shrinkage mechanisms of alkali-activated slag, *Cem. Concr. Res.* 88 (2016) 126–135. doi:10.1016/j.cemconres.2016.07.001.
- [22] F.H. Wittmann, Heresies on shrinkage and creep mechanisms, *Proc. 8th Int. Conf. Creep, Shrinkage Durab. Mech. Concr. Concr. Struct. (CONCREEP 8)*. 8 (2008) 3–9. doi:10.1201/9780203882955.pt1.
- [23] W. Hansen, Drying shrinkage mechanisms in Portland cement paste, *J. Am. Ceram. Soc.* 70 (1987) 323–328.
- [24] Y. Ma, G. Ye, The shrinkage of alkali activated fly ash, *Cem. Concr. Res.* 68 (2015) 75–82. doi:10.1016/j.cemconres.2014.10.024.
- [25] G. Fang, H. Bahrami, M. Zhang, Mechanisms of autogenous shrinkage of alkali-activated fly ash-slag pastes cured at ambient temperature within 24 h, *Constr. Build. Mater.* 171 (2018) 377–387. doi:10.1016/j.conbuildmat.2018.03.155.
- [26] M. Palacios, F. Puertas, Effect of superplasticizer and shrinkage reducing admixtures on alkali-activated slag pastes and mortars, *Cem. Concr. Res.* 35 (2005) 1358–1367. doi:10.1016/j.cemconres.2004.10.014.
- [27] X. Hu, C. Shi, Z. Zhang, Z. Hu, Autogenous and drying shrinkage of alkali-activated slag mortars, *J. Am. Ceram. Soc.* (2019) 1–13. doi:10.1111/jace.16349.
- [28] H. Ye, A. Radlińska, Shrinkage mitigation strategies in alkali-activated slag, *Cem. Concr. Res.* 101 (2017) 131–143. doi:10.1016/j.cemconres.2017.08.025.
- [29] M. Nedeljković, Carbonation mechanism of alkali-activated fly ash and slag materials: In view of long-term performance predictions, Delft University of Technology, 2019.
- [30] S.A. Bernal, J.L. Provis, A. Fernández-jiménez, P. V Krivenko, E. Kavalerova, M. Palacios, C. Shi, *Alkali Activated Materials*, 2014. doi:10.1007/978-94-007-7672-2.
- [31] S. Songpiriyakij, T. Kubprasit, C. Jaturapitakkul, P. Chindaprasirt, Compressive strength

- and degree of reaction of biomass- and fly ash-based geopolymer, *Constr. Build. Mater.* 24 (2010) 236–240. doi:10.1016/j.conbuildmat.2009.09.002.
- [32] S.A. Bernal, E.D. Rodríguez, A.P. Kirchheim, J.L. Provis, Management and valorisation of wastes through use in producing alkali-activated cement materials, *J. Chem. Technol. Biotechnol.* 91 (2016) 2365–2388.
- [33] ASTM C618 - 19, Standard specification for coal fly ash and raw or calcined natural pozzolan for use in concrete, (2008). doi:10.1520/C0618-19.2.
- [34] N. Gamage, K. Liyanage, S. Fragomeni, S. Setunge, Overview of different types of fly ash and their use as a building and construction material, in: *Int. Conf. Struct. Eng. Constr. Manag.*, Sri Lanka, 2011.
- [35] J.L. Provis, Activating solution chemistry for geopolymers, in: *Geopolymers*, Elsevier, 2009: pp. 50–71.
- [36] F. Collins, J.G. Sanjayan, Early age strength and workability of slag pastes activated by NaOH and Na₂CO₃, *Cem. Concr. Res.* 28 (1998) 655–664.
- [37] H. Tan, X. Deng, X. He, J. Zhang, X. Zhang, Y. Su, J. Yang, Compressive strength and hydration process of wet-grinded granulated blast-furnace slag activated by sodium sulfate and sodium carbonate, *Cem. Concr. Compos.* 97 (2019) 387–398. doi:https://doi.org/10.1016/j.cemconcomp.2019.01.012.
- [38] B.S. Gebregziabihier, R.J. Thomas, S. Peethamparan, Temperature and activator effect on early-age reaction kinetics of alkali-activated slag binders, *Constr. Build. Mater.* 113 (2016) 783–793. doi:10.1016/j.conbuildmat.2016.03.098.
- [39] M. Ben Haha, G. Le Saout, F. Winnefeld, B. Lothenbach, Influence of activator type on hydration kinetics, hydrate assemblage and microstructural development of alkali activated blast-furnace slags, *Cem. Concr. Res.* 41 (2011) 301–310. doi:10.1016/j.cemconres.2010.11.016.
- [40] X. Gao, Q. Yu, H.J.H. Brouwers, Development of alkali activated slag-fly ash mortars : mix design and performance assessment Development of Alkali Activated Slag-Fly Ash Mortars : Mix Design, in: *4th Int. Conf. Sustain. Constr. Mater. Technol.*, Las Vegas, 2016: p. S167.
- [41] S.-D. Wang, K.L. Scrivener, P.L. Pratt, Factors affecting the strength of alkali-activated slag, *Cem. Concr. Res.* 24 (1994) 1033–1043.
- [42] A.J. Allen, J.J. Thomas, H.M. Jennings, Composition and density of nanoscale calcium-silicate-hydrate in cement., *Nat. Mater.* 6 (2007) 311–316. doi:10.1038/nmat1871.
- [43] J.L. Provis, G.C. Lukey, J.S.J. Van Deventer, Do geopolymers actually contain nanocrystalline zeolites? a reexamination of existing results, *Chem. Mater.* 17 (2005) 3075–3085. doi:10.1021/cm050230i.
- [44] S.A. Bernal, J.L. Provis, B. Walkley, R. San Nicolas, J.D. Gehman, D.G. Brice, A.R. Kilcullen, P. Duxson, J.S.J. Van Deventer, Gel nanostructure in alkali-activated binders based on slag and fly ash, and effects of accelerated carbonation, *Cem. Concr. Res.* 53 (2013) 127–144. doi:10.1016/j.cemconres.2013.06.007.

- [45] Y. Zuo, G. Ye, Pore Structure Characterization of Sodium Hydroxide Activated Slag Using Mercury Intrusion Porosimetry , Nitrogen Adsorption, and Image Analysis, (2018). doi:10.3390/ma11061035.
- [46] Z. Li, S. Zhang, Y. Zuo, W. Chen, G. Ye, Chemical deformation of metakaolin based geopolymer, *Cem. Concr. Res.* 120 (2019) 108–118. doi:10.1016/j.cemconres.2019.03.017.
- [47] H. Ye, Mechanisms and Mitigation of Shrinkage in Alkali-activated Slag, The Pennsylvania State University, 2016.
- [48] G. Ye, Experimental Study and Numerical Simulation of the Development of the Microstructure and Permeability of Cementitious Materials, Delft University of Technology, 2003.
- [49] H.A. Neville, H.C. Jones, The study of hydration changes by a volume-change method, in: *Colloid Symp. Monogr. VI*, 1928: pp. 309–318.
- [50] H. Le Chatelier, Sur les changements de volume qui accompagnent le durcissement des ciments, *Bull. Soc. l'encouragement Pour l'industrie Natl.* 5 (1900).
- [51] E. ichi Tazawa, S. Miyazawa, Influence of cement and admixture on autogenous shrinkage of cement paste, *Cem. Concr. Res.* 25 (1995) 281–287. doi:10.1016/0008-8846(95)00010-0.
- [52] P. Lura, Autogenous Deformation and Internal Curing of Concrete, Delft University of Technology, 2003.
- [53] A. Paillere, M. Buil, J.J. Serrano, Effect of fiber addition on the autogenous shrinkage of silica fume, *Mater. J.* 86 (1989) 139–144.
- [54] H.E. Davis, Autogenous volume change of concrete, *Proc. ASTM*, 40. (1940) 1103–1110.
- [55] M. Jensen, P.F. Hansen, Autogenous deformation and change of the relative humidity in silica fume-modified cement paste, *Mater. J.* 93 (1996) 539–543.
- [56] J. Ma, F. Dehn, Shrinkage and creep behavior of an alkali-activated slag concrete, *Struct. Concr.* 18 (2017) 801–810. doi:10.1002/suco.201600147.
- [57] C. Cartwright, F. Rajabipour, A. Radli, Shrinkage Characteristics of Alkali-Activated Slag Cements, *J. Mater. Civ. Eng.* 27 (2014) 1–9. doi:10.1061/(ASCE)MT.1943-5533.0001058.
- [58] B.D. Kumarappa, S. Peethamparan, M. Ngami, Autogenous shrinkage of alkali activated slag mortars: Basic mechanisms and mitigation methods, *Cem. Concr. Res.* 109 (2018) 1–9. doi:10.1016/j.cemconres.2018.04.004.
- [59] S. Uppalapati, S. Joseph, Ö. Cizer, AUTOGENOUS SHRINKAGE AND STRENGTH DEVELOPMENT OF ALKALI-ACTIVATED SLAG/FLY ASH MORTAR BLENDS, in: *5th Int. Slag Valor. Symp.*, 2017: pp. 393–396.
- [60] G. Fang, W. Tu, Y. Zhu, M. Zhang, AUTOGENOUS SHRINKAGE OF ALKALI-ACTIVATED FLY ASH-SLAG PASTES WITH AND WITHOUT SAP, in: *4th Int. Conf. Serv. Life Des. Infrastructures*, 2018: pp. 449–455.
- [61] A. Allahverdi, B. Shaverdi, K.E. Najafi, Influence of sodium oxide on properties of fresh

- and hardened paste of alkali-activated blast-furnace slag, *Int. J. Civ. Eng.* 8 (2010).
- [62] S.H. Oh, S.H. Hong, K.M. Lee, Autogenous shrinkage properties of high strength alkali activated slag mortar, *J. Korean Recycl. Constr. Resour. Inst.* 2 (2014) 60–65.
- [63] N.J. Hu, G. Hüsken, G.J.G. Gluth, H.C. Kühne, The influence of activator composition on the strength, shrinkage and chloride migration resistance of alkali-activated slag mortars, in: *Key Eng. Mater.*, 2018: pp. 61–64.
- [64] H. Taghvayi, K. Behfarnia, M. Khalili, The Effect of Alkali Concentration and Sodium Silicate Modulus on the Properties of Alkali-Activated Slag Concrete, *J. Adv. Concr. Technol.* 16 (2018) 293–305.
- [65] F. Collins, J.. Sanjayan, Effect of pore size distribution on drying shrinking of alkali-activated slag concrete, *Cem. Concr. Res.* 30 (2000) 1401–1406. doi:10.1016/S0008-8846(00)00327-6.
- [66] F. Beltzung, F.H. Wittmann, Role of disjoining pressure in cement based materials, *Cem. Concr. Res.* 35 (2005) 2364–2370. doi:10.1016/j.cemconres.2005.04.004.
- [67] C.F. Ferraris, F.H. Wittmann, Shrinkage mechanisms of hardened cement paste, *Cem. Concr. Res.* 17 (1987) 453–464.
- [68] T. Lu, Autogenous shrinkage of early age cement paste and mortar, Delft University of Technology, 2019.
- [69] C. Di Bella, M. Wyrzykowski, P. Lura, Evaluation of the ultimate drying shrinkage of cement-based mortars with poroelastic models, *Mater. Struct.* (2017). doi:10.1617/s11527-016-0870-0.
- [70] Z.C. Grasley, C.K. Leung, Desiccation shrinkage of cementitious materials as an aging, poroviscoelastic response, *Cem. Concr. Res.* 41 (2011) 77–89.
- [71] K. van Breugel, Numerical modelling of volume changes at early ages-Potential, pitfalls and challenges, *Mater. Struct.* 34 (2001) 293–301. doi:10.1007/bf02482209.
- [72] D.P. Bentz, E.J. Garboczi, D.A. Quenard, Modelling drying shrinkage in reconstructed porous materials: application to porous Vycor glass, *Model. Simul. Mater. Sci. Eng.* 6 (1998) 211.
- [73] P. Lura, O.M. Jensen, K. Van Breugel, Autogenous shrinkage in high-performance cement paste: An evaluation of basic mechanisms, *Cem. Concr. Res.* 33 (2003) 223–232. doi:10.1016/S0008-8846(02)00890-6.
- [74] K. Kovler, S. Zhutovsky, Overview and future trends of shrinkage research, *Mater. Struct.* 39 (2006) 827–847. doi:10.1617/s11527-006-9114-z.
- [75] S.D. Wang, K.L. Scrivener, Hydration products of alkali activated slag cement, *Cem. Concr. Res.* 25 (1995) 561–571. doi:10.1016/0008-8846(95)00045-E.
- [76] H. Chen, M. Wyrzykowski, K. Scrivener, P. Lura, Prediction of self-desiccation in low water-to-cement ratio pastes based on pore structure evolution, *Cem. Concr. Res.* 49 (2013) 38–47. doi:10.1016/j.cemconres.2013.03.013.
- [77] S. Uppalapati, O. Cizer, Understanding the autogenous shrinkage in alkali-activated

- slag/fly-ash blends, in: *Int. Conf. ALKALI Act. Mater. GEOPOLYMERS VERSATILE Mater. Offer. HIGH Perform. LOW Emiss.*, 2018: p. 27.
- [78] X. Gao, Q.L. Yu, H.J.H. Brouwers, Apply²⁹Si,²⁷Al MAS NMR and selective dissolution in identifying the reaction degree of alkali activated slag-fly ash composites, *Ceram. Int.* 43 (2017) 12408–12419. doi:10.1016/j.ceramint.2017.06.108.
- [79] F. Puertas, M. Palacios, H. Manzano, J.S. Dolado, A. Rico, J. Rodríguez, A model for the CASH gel formed in alkali-activated slag cements, *J. Eur. Ceram. Soc.* 31 (2011) 2043–2056.
- [80] I. Garcia-Lodeiro, A. Fernandez-Jimenez, D.E. Macphee, I. Sobrados, J. Sanz, A. Palomo, Stability of synthetic calcium silicate hydrate gels in presence of alkalis, aluminum, and soluble silica, *Transp. Res. Rec.* 2142 (2010) 52–57.
- [81] A. Mobili, A. Belli, C. Giosuè, T. Bellezze, F. Tittarelli, Metakaolin and fly ash alkali-activated mortars compared with cementitious mortars at the same strength class, *Cem. Concr. Res.* 88 (2016) 198–210. doi:10.1016/j.cemconres.2016.07.004.
- [82] M. Kheradmand, Z. Abdollahnejad, F. Pacheco-Torgal, Shrinkage Performance of Fly Ash Alkali-activated Cement Based Binder Mortars, *KSCE J. Civ. Eng.* 22 (2018) 1854–1864. doi:10.1007/s12205-017-1714-3.
- [83] E.N. Kani, A. Allahverdi, Investigating shrinkage changes of natural pozzolan based geopolymer cementpaste, *Iran. J. Mater. Sci. Eng.* 8 (2011) 50–60.
- [84] N. Marjanović, M. Komljenović, Z. Baščarević, V. Nikolić, R. Petrović, Physical-mechanical and microstructural properties of alkali-activated fly ash-blast furnace slag blends, *Ceram. Int.* 41 (2015) 1421–1435. doi:10.1016/j.ceramint.2014.09.075.
- [85] M. Hojati, Shrinkage characteristics of alkali activated fly ash-slag binders, The Pennsylvania State University, 2014.
- [86] M. Hojati, A. Radlińska, Shrinkage and strength development of alkali-activated fly ash-slag binary cements, *Constr. Build. Mater.* 150 (2017) 808–816. doi:10.1016/j.conbuildmat.2017.06.040.
- [87] Z. Hu, Early hydration and shrinkage of alkali-activated slag/fly ash blend cement, Hunan University, 2013.
- [88] W. Shen, Y. Wang, T. Zhang, M. Zhou, J. Li, X. Cui, Magnesia modification of alkali-activated slag fly ash cement, *J. Wuhan Univ. Technol. Mater. Sci. Ed.* 26 (2011) 121–125. doi:10.1007/s11595-011-0182-8.
- [89] F. Puertas, T. Amat, A. Fernández-Jiménez, T. Vázquez, Mechanical and durable behaviour of alkaline cement mortars reinforced with polypropylene fibres, *Cem. Concr. Res.* 33 (2003) 2031–2036. doi:10.1016/S0008-8846(03)00222-9.
- [90] S. Aydin, A ternary optimisation of mineral additives of alkali activated cement mortars, *Constr. Build. Mater.* 43 (2013) 131–138. doi:10.1016/j.conbuildmat.2013.02.005.
- [91] A.M. Rashad, Properties of alkali-activated fly ash concrete blended with slag, *Iran. J. Mater. Sci. Eng.* 10 (2013) 57–64.

- [92] Y. Ling, K. Wang, C. Fu, Shrinkage behavior of fly ash based geopolymer pastes with and without shrinkage reducing admixture, *Cem. Concr. Compos.* 98 (2019) 74–82. doi:<https://doi.org/10.1016/j.cemconcomp.2019.02.007>.
- [93] M. Mastali, P. Kinnunen, A. Dalvand, R. Mohammadi Firouz, M. Illikainen, Drying shrinkage in alkali-activated binders – A critical review, *Constr. Build. Mater.* 190 (2018) 533–550. doi:[10.1016/j.conbuildmat.2018.09.125](https://doi.org/10.1016/j.conbuildmat.2018.09.125).
- [94] N.P. Mailvaganam, M.R. Rixom, *Chemical admixtures for concrete*, Crc Press, 2002.
- [95] N.S. Berke, L. Li, M.C. Hicks, J. Bae, Improving concrete performance with shrinkage-reducing admixtures, *Spec. Publ.* 217 (2003) 37–50.
- [96] V. Bílek, L. Kalina, R. Novotný, Polyethylene glycol molecular weight as an important parameter affecting drying shrinkage and hydration of alkali-activated slag mortars and pastes, *Constr. Build. Mater.* 166 (2018) 564–571. doi:<https://doi.org/10.1016/j.conbuildmat.2018.01.176>.
- [97] M. Palacios, F. Puertas, Effect of shrinkage-reducing admixtures on the properties of alkali-activated slag mortars and pastes, *Cem. Concr. Res.* 37 (2007) 691–702.
- [98] L. Kalina, E.B. Ková, J. Krouská, V.B. Jr., Polypropylene Glycols as Effective Shrinkage-Reducing Admixtures in Alkali-Activated Materials, *Mater. J.* 115 (n.d.). doi:[10.14359/51701099](https://doi.org/10.14359/51701099).
- [99] M. Criado, A. Palomo, A. Fernández-Jiménez, P.F.G. Banfill, Alkali activated fly ash: Effect of admixtures on paste rheology, *Rheol. Acta.* 48 (2009) 447–455. doi:[10.1007/s00397-008-0345-5](https://doi.org/10.1007/s00397-008-0345-5).
- [100] G. Habert, J.B. D’Espinose De Lacaillerie, N. Roussel, An environmental evaluation of geopolymer based concrete production: Reviewing current research trends, *J. Clean. Prod.* 19 (2011) 1229–1238. doi:[10.1016/j.jclepro.2011.03.012](https://doi.org/10.1016/j.jclepro.2011.03.012).
- [101] C.A. Rees, J.L. Provis, G.C. Lukey, J.S.J. van Deventer, The mechanism of geopolymer gel formation investigated through seeded nucleation, *Colloids Surfaces A Physicochem. Eng. Asp.* 318 (2008) 97–105. doi:[10.1016/j.colsurfa.2007.12.019](https://doi.org/10.1016/j.colsurfa.2007.12.019).
- [102] V. Bilek Jr, L. Kalina, O. Fojtík, Shrinkage-Reducing Admixture Efficiency in Alkali-Activated Slag across the Different Doses of Activator, in: *Key Eng. Mater.*, Trans Tech Publ, 2018: pp. 19–22.
- [103] F. Collins, J.G. Sanjayan, cracking tendency of alkali-activated slag concrete subjected to restrained shrinkage, *Cem. Concr. Res.* 30 (2000) 791–798. doi:[10.1016/S0008-8846\(00\)00243-X](https://doi.org/10.1016/S0008-8846(00)00243-X).
- [104] T. Bakharev, J.G. Sanjayan, Y.B. Cheng, Effect of admixtures on properties of alkali-activated slag concrete, *Cem. Concr. Res.* 30 (2000) 1367–1374. doi:[10.1016/S0008-8846\(00\)00349-5](https://doi.org/10.1016/S0008-8846(00)00349-5).
- [105] C. Li, H. Shi, W. Zhou, J. Cha, J. Huang, W. Shen, Influence of the Thermal Treatment Process of MgO on Alkali-activated Cement, *Bull. Chinese Ceram. Soc.* 35 (2016) 632–637.
- [106] Y. Yang, Z. Li, X. Zhang, J. Wei, Q. Yu, Reaction Mechanism of Compensating Shrinkage

- of Inorganic Polymer Pastes by Using Reactive MgO, *J. South China Univ. Technol. (Natural Sci. Ed.* 45 (2017) 102-109 (In Chinese).
- [107] Y. Gu, Y. Fang, Shrinkage, Cracking, Shrinkage-Reducing and Toughening of Alkali-Activated Slag Cement - A Short Review, *J. Chinese Ceram. Soc.* 40 (2012) 76–84.
- [108] X. Zhu, D. Tang, K. Yang, Z. Zhang, Q. Li, Q. Pan, C. Yang, Effect of Ca(OH)₂ on shrinkage characteristics and microstructures of alkali-activated slag concrete, *Constr. Build. Mater.* 175 (2018) 467–482. doi:10.1016/j.conbuildmat.2018.04.180.
- [109] B. Liu, J. Yang, D. Li, F. Xing, Y. Fang, Effect of a synthetic nano-CaO-Al₂O₃-SiO₂-H₂O gel on the early-stage shrinkage performance of alkali-activated slag mortars, *Materials (Basel)*. 11 (2018). doi:10.3390/ma11071128.
- [110] L.Y. Yang, Z.J. Jia, Y.M. Zhang, J.G. Dai, Effects of nano-TiO₂ on strength, shrinkage and microstructure of alkali activated slag pastes, *Cem. Concr. Compos.* 57 (2015) 1–7. doi:10.1016/j.cemconcomp.2014.11.009.
- [111] V. Mechtcherine, M. Gorges, C. Schroefl, A. Assmann, W. Brameshuber, A.B. Ribeiro, D. Cusson, J. Custódio, E.F. Da Silva, K. Ichimiya, S.I. Igarashi, A. Klemm, K. Kovler, A.N. De Mendonça Lopes, P. Lura, V.T. Nguyen, H.W. Reinhardt, R.D.T. Filho, J. Weiss, M. Wyrzykowski, G. Ye, S. Zhutovsky, Effect of internal curing by using superabsorbent polymers (SAP) on autogenous shrinkage and other properties of a high-performance fine-grained concrete: Results of a RILEM round-robin test, *Mater. Struct.* 47 (2014) 541–562. doi:10.1617/s11527-013-0078-5.
- [112] O.M. Jensen, P.F. Hansen, Water-entrained cement-based materials - I. Principles and theoretical background, *Cem. Concr. Res.* 31 (2001) 647–654. doi:10.1016/S0008-8846(01)00463-X.
- [113] P. Lura, F. Durand, O.M. Jensen, Autogenous strain of cement pastes with superabsorbent polymers, *Proc. International RILEM Conf. Vol. Chang. Hardening Concr. Test. Mitig. C* (2006) 57–66. doi:10.1617/2351580052.007.
- [114] J. Justs, M. Wyrzykowski, D. Bajare, P. Lura, Internal curing by superabsorbent polymers in ultra-high performance concrete, *Cem. Concr. Res.* 76 (2015) 82–90. doi:10.1016/j.cemconres.2015.05.005.
- [115] D. Snoeck, O.M. Jensen, N. De Belie, The influence of superabsorbent polymers on the autogenous shrinkage properties of cement pastes with supplementary cementitious materials, *Cem. Concr. Res.* 74 (2015) 59–67. doi:10.1016/j.cemconres.2015.03.020.
- [116] A.R. Sakulich, D.P. Bentz, Mitigation of autogenous shrinkage in alkali activated slag mortars by internal curing, *Mater. Struct.* 46 (2013) 1355–1367. doi:10.1617/s11527-012-9978-z.
- [117] N.K. Lee, S.Y. Abate, H.K. Kim, Use of recycled aggregates as internal curing agent for alkali-activated slag system, *Constr. Build. Mater.* 159 (2018) 286–296. doi:10.1016/j.conbuildmat.2017.10.110.
- [118] S. Oh, Y.C. Choi, Superabsorbent polymers as internal curing agents in alkali activated slag mortars, *Constr. Build. Mater.* 159 (2018) 1–8.

- doi:10.1016/j.conbuildmat.2017.10.121.
- [119] C. Song, Y.C. Choi, S. Choi, Effect of internal curing by superabsorbent polymers – Internal relative humidity and autogenous shrinkage of alkali-activated slag mortars, *Constr. Build. Mater.* 123 (2016) 198–206. doi:10.1016/j.conbuildmat.2016.07.007.
- [120] W. Tu, Y. Zhu, G. Fang, X. Wang, M. Zhang, Internal curing of alkali-activated fly ash-slag pastes using superabsorbent polymer, *Cem. Concr. Res.* 116 (2019) 179–190. doi:10.1016/j.cemconres.2018.11.018.
- [121] T. Bakharev, J.G. Sanjayan, Y. Cheng, Effect of elevated temperature curing on properties of alkali-activated slag concrete, *Cem. Concr. Res.* 29 (1999) 1619–1625.
- [122] J.J. Thomas, A.J. Allen, H.M. Jennings, Density and water content of nanoscale solid C-S-H formed in alkali-activated slag (AAS) paste and implications for chemical shrinkage, *Cem. Concr. Res.* 42 (2012) 377–383. doi:10.1016/j.cemconres.2011.11.003.
- [123] M. Chi, R. Huang, Binding mechanism and properties of alkali-activated fly ash/slag mortars, *Constr. Build. Mater.* 40 (2013) 291–298. doi:10.1016/j.conbuildmat.2012.11.003.
- [124] J.G. Jang, N.K. Lee, H.K. Lee, Fresh and hardened properties of alkali-activated fly ash/slag pastes with superplasticizers, *Constr. Build. Mater.* 50 (2014) 169–176. doi:10.1016/j.conbuildmat.2013.09.048.
- [125] F.H. WITTMANN, Interaction of Hardened Cement Paste and Water, *J. Am. Ceram. Soc.* 56 (1973) 409–415. doi:10.1111/j.1151-2916.1973.tb12711.x.
- [126] T.C. Powers, The thermodynamics of volume change and creep, *Matériaux Constr.* 1 (1968) 487–507.
- [127] ASTM C191-18a, Standard Test Methods for Time of Setting of Hydraulic Cement by Vicat Needle, (2019) 1–8. doi:10.1520/C0191-18A.2.
- [128] ASTM C1968, Standard Test Method for Autogenous Strain of Cement Paste and Mortar, (2013) 1–8. doi:10.1520/C1698-09.2.
- [129] Q. Tian, O.M. Jensen, Measurement with corrugated tubes of early-age autogenous shrinkage of cement-based materials, *J. Chinese Ceram. Soc.* 37 (2009) 39–45.
- [130] Z. Li, P. Gao, G. Ye, Experimental study on autogenous deformation of metakaolin based geopolymer, in: 2nd Int. RILEM/COST Conf. Early Age Crack. Serv. Cem. Mater. Struct., Brussels, 2017: pp. 209–214.
- [131] D. FENG, A. Mikuni, Y. HIRANO, R. KOMATSU, K. Ikeda, Preparation of Geopolymeric Materials from Fly Ash Filler by Steam Curing with Special Reference to Binder Products, *J. Ceram. Soc. Japan.* 113 (2005) 82–86. doi:10.2109/jcersj.113.82.
- [132] E.P. Barrett, L.G. Joyner, P.P. Halenda, The determination of pore volume and area distributions in porous substances. I. Computations from nitrogen isotherms, *J. Am. Chem. Soc.* 73 (1951) 373–380.
- [133] ASTM C 1608, Standard test method for chemical shrinkage of hydraulic cement paste, (2007) 667–670.

- [134] H. Huang, G. Ye, Examining the “time-zero” of autogenous shrinkage in high/ultra-high performance cement pastes, *Cem. Concr. Res.* 97 (2015) 107–114. doi:10.1016/j.cemconres.2017.03.010.
- [135] R.S. Barneyback, S. Diamond, W. Lafayette, Expression and analysis of pore fluids from hardened cement pastes and mortars, *Cem. Concr. Res.* 11 (1981) 279–285.
- [136] M. Azenha, R. Faria, F. Magalhães, L. Ramos, Á. Cunha, Measurement of the E-modulus of cement pastes and mortars since casting, using a vibration based technique, *Mater. Struct.* 45 (2012) 81–92. doi:10.1617/s11527-011-9750-9.
- [137] S. Uppalapati, Ö. Cizer, Assessing the autogenous shrinkage of alkali- activated slag/fly ash mortar blends, *Am. Concr. Institute, ACI Spec. Publ.* 2017-Janua (2017).
- [138] M.D. Cohen, Theories of expansion in sulfoaluminate-type expansive cements: schools of thought, *Cem. Concr. Res.* 13 (1983) 809–818.
- [139] W.K.W. Lee, J.S.J. van Deventer, Use of infrared spectroscopy to study geopolymerization of heterogeneous amorphous aluminosilicates, *Langmuir.* 19 (2003) 8726–8734. doi:Doi 10.1021/La026127e.
- [140] I. Garcia-Lodeiro, A. Palomo, A. Fernández-Jiménez, D.E. MacPhee, Compatibility studies between N-A-S-H and C-A-S-H gels. Study in the ternary diagram Na₂O-CaO-Al₂O₃-SiO₂-H₂O, *Cem. Concr. Res.* 41 (2011) 923–931. doi:10.1016/j.cemconres.2011.05.006.
- [141] S. Zhang, A. Keulen, K. Arbi, G. Ye, Waste glass as partial mineral precursor in alkali-activated slag/fly ash system, *Cem. Concr. Res.* 102 (2017) 29–40. doi:10.1016/j.cemconres.2017.08.012.
- [142] I. García Lodeiro, A. Fernández-Jimenez, A. Palomo, D.E. Macphee, Effect on fresh C-S-H gels of the simultaneous addition of alkali and aluminium, *Cem. Concr. Res.* 40 (2010) 27–32. doi:10.1016/j.cemconres.2009.08.004.
- [143] N.K. Lee, H.K. Lee, Reactivity and reaction products of alkali-activated, fly ash/slag paste, *Constr. Build. Mater.* 81 (2015) 303–312. doi:10.1016/j.conbuildmat.2015.02.022.
- [144] D. Ravikumar, N. Neithalath, Reaction kinetics in sodium silicate powder and liquid activated slag binders evaluated using isothermal calorimetry, *Thermochim. Acta.* 546 (2012) 32–43. doi:10.1016/j.tca.2012.07.010.
- [145] Z. Yu, *Microstructure Development and Transport Properties of Portland Cement-fly Ash Binary Systems*, Delft University of Technology, 2015.
- [146] J.L. Provis, P. Duxson, R.M. Harrex, J. van Deventer, Valorisation of Fly Ashes by Geopolymerisation, *Glob. NEST J.* 11 (2009) 147–154.
- [147] H. Dong, P. Gao, G. Ye, Characterization and comparison of capillary pore structures of digital cement pastes, *Mater. Struct.* 50 (2017). doi:10.1617/s11527-017-1023-9.
- [148] K. van Breugel, *Simulation of hydration and Formation of Structure in Hardening Cement-Based Materials*, (1991) 295.

- [149] Z. Zhang, L. Li, X. Ma, H. Wang, Compositional, microstructural and mechanical properties of ambient condition cured alkali-activated cement, *Constr. Build. Mater.* 113 (2016) 237–245. doi:10.1016/j.conbuildmat.2016.03.043.
- [150] O. Coussy, P. Dangla, T. Lassabatère, V. Baroghel-Bouny, The equivalent pore pressure and the swelling and shrinkage of cement-based materials, *Mater. Struct.* 37 (2004) 15–20. doi:10.1617/14080.
- [151] Y. Zuo, *Experimental Study and Numerical Simulation of the Reaction Process and Microstructure Formation of Alkali-Activated Materials*, Delft University of Technology, 2019.
- [152] S. Nagataki, H. Gomi, Expansive admixtures (mainly ettringite), *Cem. Concr. Compos.* 20 (1998) 163–170.
- [153] J.N. Israelachvili, *Intermolecular and surface forces*, Academic press, 2011.
- [154] X. Ouyang, D.A. Koleva, G. Ye, K. van Breugel, Understanding the adhesion mechanisms between C-S-H and fillers, *Cem. Concr. Res.* 100 (2017) 275–283. doi:10.1016/j.cemconres.2017.07.006.
- [155] K.C. Marshall, R. STOUT, R. Mitchell, Mechanism of the initial events in the sorption of marine bacteria to surfaces, *Microbiology.* 68 (1971) 337–348.
- [156] M. Hermansson, The DLVO theory in microbial adhesion, *Colloids Surfaces B Biointerfaces.* 14 (1999) 105–119.
- [157] N. V Churaev, B. V Derjaguin, V.M. Muller, *Surface forces*, Springer Science & Business Media, 2013.
- [158] E.J.W. Verwey, J.T.G. Overbeek, J.T.G. Overbeek, *Theory of the stability of lyophobic colloids*, Courier Corporation, 1999.
- [159] X. Ouyang, *Filler-hydrates Adhesion Properties in Cement Paste System: Development of Sustainable Building Materials*, Delft University of Technology, 2017.
- [160] A. Gmira, M. Zabat, R.-M. Pellenq, H. Van Damme, Microscopic physical basis of the poromechanical behavior of cement-based materials, *Mater. Struct.* 37 (2004) 3–14.
- [161] G. Peschel, P. Belouschek, M.M. Müller, M.R. Müller, R. König, The interaction of solid surfaces in aqueous systems, *Colloid Polym. Sci.* 260 (1982) 444–451. doi:10.1007/BF01448150.
- [162] J.N. Israelachvili, H. Wennerström, Entropic forces between amphiphilic surfaces in liquids, *J. Phys. Chem.* 96 (1992) 520–531. doi:10.1021/j100181a007.
- [163] Y. Zuo, M. Nedeljković, G. Ye, Pore solution composition of alkali-activated slag/fly ash pastes, *Cem. Concr. Res.* 115 (2019) 230–250. doi:10.1016/j.cemconres.2018.10.010.
- [164] J.A. Larbi, A.L.A. Fraay, J. Bijen, The chemistry of the pore fluid of silica fume-blended cement systems, *Cem. Concr. Res.* 20 (1990) 506–516.
- [165] H.J.H. Brouwers, others, Alkali concentrations of pore solution in hydrating OPC, *Cem. Concr. Res.* 33 (2003) 191–196.

- [166] C.J. Haecker, E.J. Garboczi, J.W. Bullard, R.B. Bohn, Z. Sun, S.P. Shah, T. Voigt, Modeling the linear elastic properties of Portland cement paste, *Cem. Concr. Res.* 35 (2005) 1948–1960. doi:10.1016/j.cemconres.2005.05.001.
- [167] A. Fernández-Jiménez, F. Puertas, others, Effect of activator mix on the hydration and strength behaviour of alkali-activated slag cements, *Adv. Cem. Res.* 15 (2003) 129–136.
- [168] Y. Ma, X. Yang, J. Hu, Z. Zhang, H. Wang, Accurate determination of the “time-zero” of autogenous shrinkage in alkali-activated fly ash/slag system, *Compos. Part B Eng.* (2019) 107367. doi:10.1016/J.COMPOSITESB.2019.107367.
- [169] S. Prinsse, Alkali-activated concrete: development of material properties (strength and stiffness) and flexural behaviour of reinforced beams over time, Master Thesis. (2017).
- [170] L.F. Nielsen, A research note on sorption, pore size distribution, and shrinkage of porous materials, Danmarks Tekniske Højskole. Laboratoriet for Bygningmaterialer, 1991.
- [171] K. Van Breugel, Relaxation of young concrete, (1980) 144.
- [172] H. van der Ham, E. Koenders, K. van Breugel, Creep model uncertainties in early-age concrete simulations, *Proc. Concreep.* 8 (2008) 431–436.
- [173] K.A. Riding, J.L. Poole, K.J. Folliard, M.C.G. Juenger, A.K. Schindler, Modeling hydration of cementitious systems, *ACI Mater. J.* 109 (2012) 225–234.
- [174] A.K. Schindler, K.J. Folliard, Heat of hydration models for cementitious materials, *ACI Mater. J.* 102 (2005) 24.
- [175] Z. Li, J. Liu, G. Ye, Drying shrinkage of alkali-activated slag and fly ash concrete. A comparative study with ordinary Portland cement concrete, in: *Proc. Work. Concr. Model. Mater. Behav. Honor Profr. Klaas van Breugel, Delft, 2018*: pp. 160–166.
- [176] A. Kostuchenko, Z. Li, G. Ye, Experimental study on creep behavior of alkali-activated concrete, in: *Int. Conf. Innov. Mater. Sustain. Civ. Eng., Nanjing, 2019*: p. 80.
- [177] M.R. Geiker, D.P. Bentz, O.M. Jensen, Mitigating autogenous shrinkage by internal curing, *ACI Spec. Publ.* (2004) 143–154.
- [178] G.R. de Sensale, A.F. Goncalves, Effects of fine LWA and SAP as internal water curing agents, *Int. J. Concr. Struct. Mater.* 8 (2014) 229–238.
- [179] O.M. Jensen, P. Lura, Techniques and materials for internal water curing of concrete, *Mater. Struct.* 39 (2006) 817–825. doi:10.1617/s11527-006-9136-6.
- [180] M. Wyrzykowski, P. Lura, Reduction of autogenous shrinkage in OPC and BFSC pastes with internal curing, in: *Proc. XIII Int. Conf. Durab. Build. Mater. Components, São Paulo, Brazil, 2014*: pp. 2–5.
- [181] V. Mechtcherine, D. Snoeck, C. Schröfl, N. De Belie, A.J. Klemm, K. Ichimiya, J. Moon, M. Wyrzykowski, P. Lura, N. Toropovs, A. Assmann, S. Ichi Igarashi, I. De La Varga, F.C.R. Almeida, K. Erk, A.B. Ribeiro, J. Custódio, H.W. Reinhardt, V. Falikman, Testing superabsorbent polymer (SAP) sorption properties prior to implementation in concrete: results of a RILEM Round-Robin Test, *Mater. Struct.* 51 (2018). doi:10.1617/s11527-018-1149-4.

- [182] D. Snoeck, C. Schröfl, V. Mechtcherine, Recommendation of RILEM TC 260-RSC: testing sorption by superabsorbent polymers (SAP) prior to implementation in cement-based materials, *Mater. Struct.* 51 (2018) 116. doi:10.1617/s11527-018-1242-8.
- [183] O.M. Jensen, Water absorption of superabsorbent polymers in a cementitious environment, *Int. RILEM Conf. Adv. Constr. Mater. Through Sci. Eng.* (2011) 22–35.
- [184] M. Wyrzykowski, S.-I. Igarashi, P. Lura, V. Mechtcherine, Recommendation of RILEM TC 260-RSC: using superabsorbent polymers (SAP) to mitigate autogenous shrinkage, *Mater. Struct.* 51 (2018) 135. doi:10.1617/s11527-018-1241-9.
- [185] NEN-EN 1097-7, Tests for mechanical and physical properties of aggregates - Part 7: Determination of the particle density of filler - Pycnometer method, (2008) 1–13.
- [186] NEN-EN 196-1, Methods of Testing Cement—Part 1: Determination of Strength, , 2005., *Eur. Comm. Stand.* (2005).
- [187] P. Zhong, M. Wyrzykowski, N. Toropovs, L. Li, J. Liu, P. Lura, Internal curing with superabsorbent polymers of different chemical structures, *Cem. Concr. Res.* 123 (2019) 105789. doi:10.1016/j.cemconres.2019.105789.
- [188] Q. Zhu, C.W. Barney, K.A. Erk, Effect of ionic crosslinking on the swelling and mechanical response of model superabsorbent polymer hydrogels for internally cured concrete, *Mater. Struct.* 48 (2015) 2261–2276. doi:10.1617/s11527-014-0308-5.
- [189] W. Siriawatwechakul, J. Siramont, W. Vichi-Vadakan, Superabsorbent Polymer Structures, *Int. RILEM Conf. Use Superabsorbent Polym. Other New Addit. Concr.* (2010) 253–262.
- [190] C. Schröfl, V. Mechtcherine, M. Gorges, Relation between the molecular structure and the efficiency of superabsorbent polymers (SAP) as concrete admixture to mitigate autogenous shrinkage, *Cem. Concr. Res.* 42 (2012) 865–873. doi:10.1016/j.cemconres.2012.03.011.
- [191] A. Favier, G. Habert, N. Roussel, J.-B. d’Espinoise de Lacaillerie, A multinuclear static NMR study of geopolymerisation, *Cem. Concr. Res.* 75 (2015) 104–109. doi:10.1016/j.cemconres.2015.03.003.
- [192] J.L. Bass, G. Turner, Anion distributions in sodium silicate solutions. Characterization by ²⁹Si NMR and infrared spectroscopies, and vapor phase osmometry, *J. Phys. Chem. B.* 101 (1997) 10638–10644. doi:10.1021/jp9715282.
- [193] H.X.D. Lee, H.S. Wong, N.R. Buenfeld, Effect of alkalinity and calcium concentration of pore solution on the swelling and ionic exchange of superabsorbent polymers in cement paste, *Cem. Concr. Compos.* 88 (2018) 150–164.
- [194] H. Lee, Potential of superabsorbent polymer for self-sealing cracks in concrete, *Adv. Appl. Ceram.* 109 (2009) 296–302. doi:10.1179/174367609x459559.
- [195] C. Shi, R.L. Day, A calorimetric study of early hydration of alkali-slag cements, *Cem. Concr. Res.* 25 (1995) 1333–1346.
- [196] J. Justs, M. Wyrzykowski, F. Winnefeld, D. Bajare, P. Lura, Influence of superabsorbent polymers on hydration of cement pastes with low water-to-binder ratio: A calorimetry

- study, *J. Therm. Anal. Calorim.* 115 (2014) 425–432. doi:10.1007/s10973-013-3359-x.
- [197] T. Zhang, Q. Yu, J. Wei, P. Gao, P. Zhang, Study on optimization of hydration process of blended cement, *J. Therm. Anal. Calorim.* 107 (2011) 489–498.
- [198] H. Huang, N. Van Tuan, G. Ye, The influence of the particle size of superabsorbent polymer on internal curing of high performance concrete: Haoliang Huang Nguyen Van Tuan, in: *Concr. Repair, Rehabil. Retrofit. III*, CRC Press, 2012: pp. 104–105.
- [199] M.T. Hasholt, O.M. Jensen, K. Kovler, S. Zhutovsky, Can superabsorbent polymers mitigate autogenous shrinkage of internally cured concrete without compromising the strength?, *Constr. Build. Mater.* 31 (2012) 226–230.
- [200] P. Lura, F. Durand, A. Loukili, K. Kovler, O.M. Jensen, Compressive strength of cement pastes and mortars with superabsorbent polymers, in: *Proc. Int. RILEM Conf. Vol. Chang. Hardening Concr. Test. Mitig.*, 2006: pp. 117–125.
- [201] F. Collins, J.G. Sanjayan, Microcracking and strength development of alkali activated slag concrete, *Cem. Concr. Compos.* 23 (2001) 345–352. doi:10.1016/S0958-9465(01)00003-8.
- [202] H. Ye, A. Radlińska, Effect of alkalis on cementitious materials: understanding the relationship between composition, structure, and volume change mechanism, *J. Adv. Concr. Technol.* 15 (2017) 165–177.
- [203] P. Lura, O.M. Jensen, J. Weiss, Cracking in cement paste induced by autogenous shrinkage, *Mater. Struct.* 42 (2009) 1089–1099. doi:10.1617/s11527-008-9445-z.
- [204] R. Loser, A. Leemann, An accelerated sulfate resistance test for concrete, *Mater. Struct.* 49 (2016) 3445–3457.
- [205] F.C.S. Carvalho, C.-N. Chen, J.F. Labuz, Measurements of effective elastic modulus and microcrack density, *Int. J. Rock Mech. Min. Sci.* 34 (1997) 43–e1.
- [206] J.L. Provis, J.S.J. Van Deventer, *Geopolymers: structures, processing, properties and industrial applications*, Woodhead, Cambridge, UK, 2009.
- [207] C.K. Yip, G.C. Lukey, J.S.J. Van Deventer, The coexistence of geopolymeric gel and calcium silicate hydrate at the early stage of alkaline activation, *Cem. Concr. Res.* 35 (2005) 1688–1697. doi:10.1016/j.cemconres.2004.10.042.
- [208] A. Buchwald, H. Hilbig, C. Kaps, Alkali-activated metakaolin-slag blends - Performance and structure in dependence of their composition, *J. Mater. Sci.* 42 (2007) 3024–3032. doi:10.1007/s10853-006-0525-6.
- [209] S.A. Bernal, E.D. Rodríguez, R. Mejía De Gutiérrez, M. Gordillo, J.L. Provis, Mechanical and thermal characterisation of geopolymers based on silicate-activated metakaolin/slag blends, *J. Mater. Sci.* 46 (2011) 5477–5486. doi:10.1007/s10853-011-5490-z.
- [210] A. Buchwald, R. Tatarin, D. Stephan, Reaction progress of alkaline-activated metakaolin-ground granulated blast furnace slag blends, *J. Mater. Sci.* 44 (2009) 5609–5617. doi:10.1007/s10853-009-3790-3.

- [211] S.A. Bernal, J.L. Provis, V. Rose, R.M. De Gutiérrez, High-resolution X-ray diffraction and fluorescence microscopy characterization of alkali-activated slag-metakaolin binders, *J. Am. Ceram. Soc.* 96 (2013) 1951–1957. doi:10.1111/jace.12247.
- [212] S.A. Bernal, J.L. Provis, V. Rose, R. Mejía De Gutierrez, Evolution of binder structure in sodium silicate-activated slag-metakaolin blends, *Cem. Concr. Compos.* 33 (2011) 46–54. doi:10.1016/j.cemconcomp.2010.09.004.
- [213] S.A. Bernal, R. Mejía De Gutiérrez, J.L. Provis, Engineering and durability properties of concretes based on alkali-activated granulated blast furnace slag/metakaolin blends, *Constr. Build. Mater.* 33 (2012) 99–108. doi:10.1016/j.conbuildmat.2012.01.017.
- [214] Z. Shi, C. Shi, J. Zhang, S. Wan, Z. Zhang, Z. Ou, Alkali-silica reaction in waterglass-activated slag mortars incorporating fly ash and metakaolin, *Cem. Concr. Res.* 108 (2018) 10–19. doi:10.1016/j.cemconres.2018.03.002.
- [215] S.A. Bernal, R.M. de Gutierrez, J.L. Provis, V. Rose, Effect of silicate modulus and metakaolin incorporation on the carbonation of alkali silicate-activated slags, *Cem. Concr. Res.* 40 (2010) 898–907. doi:10.1016/j.cemconres.2010.02.003.
- [216] O. Burciaga-Díaz, R.X. Magallanes-Rivera, J.I. Escalante-Garcia, Alkali-activated slag-metakaolin pastes: Strength, structural, and microstructural characterization, *J. Sustain. Cem. Mater.* 2 (2013) 111–127. doi:10.1080/21650373.2013.801799.
- [217] Z. Li, G. Ye, Experimental study of the chemical deformation of metakaolin based geopolymer, in: *SynerCrete'18 Int. Conf. Interdiscip. Approaches Cem. Mater. Struct. Concr.*, Funchal, 2018: pp. 443–448.
- [218] ASTM C191, Standard Test Methods for Time of Setting of Hydraulic Cement by Vicat Needle BT - Standard Test Methods for Time of Setting of Hydraulic Cement by Vicat Needle, (2013).
- [219] B. Delsaute, C. Boulay, J. Granja, J. Carette, M. Azenha, C. Dumoulin, G. Karaiskos, A. Deraemaeker, S. Staquet, Testing Concrete E-modulus at Very Early Ages Through Several Techniques: An Inter-laboratory Comparison, *Strain.* (2016) 91–109. doi:10.1111/str.12172.
- [220] I. García-Lodeiro, A. Fernández-Jiménez, M.T. Blanco, A. Palomo, FTIR study of the sol-gel synthesis of cementitious gels: C-S-H and N-A-S-H, *J. Sol-Gel Sci. Technol.* 45 (2008) 63–72. doi:10.1007/s10971-007-1643-6.
- [221] C. a Rees, J.L. Provis, G.C. Lukey, J.S.J. van Deventer, Attenuated total reflectance fourier transform infrared analysis of fly ash geopolymer gel aging., *Langmuir.* 23 (2007) 8170–8179. doi:10.1021/la700713g.
- [222] A.M. Neville, *Properties of Concrete*, London: Longman, 2011.
- [223] D. Krizan, B. Zivanovic, Effects of dosage and modulus of water glass on early hydration of alkali-slag cements, *Cem. Concr. Res.* 32 (2002) 1181–1188. doi:10.1016/S0008-8846(01)00717-7.
- [224] J. Davidovits, *Geopolymer Chemistry & Applications*, 4 th, Institut Géopolymère, Saint-Quentin, France, 2015.

- [225] B. Walkley, R. San Nicolas, M.A. Sani, G.J. Rees, J. V. Hanna, J.S.J. van Deventer, J.L. Provis, Phase evolution of C-(N)-A-S-H/N-A-S-H gel blends investigated via alkali-activation of synthetic calcium aluminosilicate precursors, *Cem. Concr. Res.* 89 (2016) 120–135. doi:10.1016/j.cemconres.2016.08.010.
- [226] O.M. Jensen, Autogenous deformation and RH-change—self-desiccation and self-desiccation shrinkage (in Danish), Phd Thesis, Build. Mater. Lab. Tech. Univ. Denmark, Lyngby, Denmark. 285 (1993).
- [227] Y. Zuo, M. Nedeljković, G. Ye, Coupled thermodynamic modelling and experimental study of sodium hydroxide activated slag, *Constr. Build. Mater.* 188 (2018) 262–279. doi:10.1016/J.CONBUILDMAT.2018.08.087.
- [228] X. Gao, Q.L. Yu, H.J.H. Brouwers, Reaction kinetics, gel character and strength of ambient temperature cured alkali activated slag-fly ash blends, *Constr. Build. Mater.* 80 (2015) 105–115. doi:10.1016/j.conbuildmat.2015.01.065.
- [229] I. Ismail, S.A. Bernal, J.L. Provis, R. San Nicolas, S. Hamdan, J.S.J. Van Deventer, Modification of phase evolution in alkali-activated blast furnace slag by the incorporation of fly ash, *Cem. Concr. Compos.* 45 (2014) 125–135. doi:10.1016/j.cemconcomp.2013.09.006.
- [230] M. Ben Haha, B. Lothenbach, G. Le Saout, F. Winnefeld, Influence of slag chemistry on the hydration of alkali-activated blast-furnace slag - Part II: Effect of Al₂O₃, *Cem. Concr. Res.* 42 (2012) 74–83. doi:10.1016/j.cemconres.2011.08.005.
- [231] T.-W. Cheng, J.P. Chiu, Fire-resistant geopolymer produced by granulated blast furnace slag, *Miner. Eng.* 16 (2003) 205–210.
- [232] J.L. Provis, Alkali-activated materials, *Cem. Concr. Res.* 114 (2018) 40–48. doi:10.1016/j.cemconres.2017.02.009.
- [233] M. Nedeljković, B. Ghiassi, S. van der Laan, Z. Li, G. Ye, Effect of curing conditions on the pore solution and carbonation resistance of alkali-activated fly ash and slag pastes, *Cem. Concr. Res. J.* 116 (2019) 146–158. doi:10.1016/j.conbuildmat.2017.12.005.
- [234] M.H. Hubler, J.J. Thomas, H.M. Jennings, Influence of nucleation seeding on the hydration kinetics and compressive strength of alkali activated slag paste, *Cem. Concr. Res.* 41 (2011) 842–846.
- [235] A. Wardhono, C. Gunasekara, D.W. Law, S. Setunge, Comparison of long term performance between alkali activated slag and fly ash geopolymer concretes, *Constr. Build. Mater.* 143 (2017) 272–279.
- [236] C. Duran Atış, C. Bilim, Ö. Çelik, O. Karahan, Influence of activator on the strength and drying shrinkage of alkali-activated slag mortar, *Constr. Build. Mater.* 23 (2009) 548–555. doi:10.1016/j.conbuildmat.2007.10.011.
- [237] G. Fang, W.K. Ho, W. Tu, M. Zhang, Workability and mechanical properties of alkali-activated fly ash-slag concrete cured at ambient temperature, *Constr. Build. Mater.* 172 (2018) 476–487.
- [238] ACI (American Concrete Institute), Building code requirements for structural concrete

- and commentary, (2011).
- [239] E. Tazawa, *Autogenous shrinkage of concrete*, CRC Press, 1998.
- [240] M.S. Sule, *Effect of reinforcement on early-age cracking in high strength concrete*, Delft University of Technology, 2003.
- [241] S.I. Igarashi, A. Bentur, K. Kovler, *Autogenous shrinkage and induced restraining stresses in high-strength concretes*, *Cem. Concr. Res.* 30 (2000) 1701–1707. doi:10.1016/S0008-8846(00)00399-9.
- [242] K. Arbi, M. Nedeljkovic, Y. Zuo, S. Grünewald, A. Keulen, G. Ye, *Experimental study on workability of alkali activated fly ash and slag-based geopolymer concretes*, *Geopolymers Route to Elimin. Waste Emiss. Ceram. Cem. Manuf.* ISBN 9781326377328. (2015) 75–78.
- [243] NEN-EN 12390-3, *Testing hardened concrete - Part 3: Compressive strength of test specimens*, (2009).
- [244] S.J. Lokhorst, *Deformational behaviour of concrete influenced by hydration related changes of the microstructure*, Delft University of Technology, 2001.
- [245] ASTM C 1581, *Standard Test Method for Determining Age at Cracking and Induced Tensile Stress Characteristics of Mortar and Concrete under Restrained Shrinkage*, *ASTM Int.* (2009) 1–7. doi:10.1520/C1581.
- [246] *Prediction of autogenous shrinkage in fly ash blended cement systems*, EPFL, 2017.
- [247] Z.P. BAZANT, *Prediction of concrete creep effects using age-adjusted effective modulus method*, *J. Am. Concr. Inst.* 69 (1972) 212–217.
- [248] NEN-EN 206-1, *Concrete - Part 1: Specification, performance, production and conformity*, *Eur. Comm. Stand.* (2001).
- [249] A. Fernández-Jiménez, J.G. Palomo, F. Puertas, *Alkali-activated slag mortars: mechanical strength behaviour*, *Cem. Concr. Res.* 29 (1999) 1313–1321.
- [250] F. Puertas, S. Martínez-Ramírez, S. Alonso, T. Vázquez, *Alkali-activated fly ash/slag cements. Strength behaviour and hydration products*, *Cem. Concr. Res.* 30 (2000) 1625–1632. doi:10.1016/S0008-8846(00)00298-2.
- [251] N. Arioglu, Z. Canan Girgin, E. Arioglu, *Evaluation of ratio between splitting tensile strength and compressive strength for concretes up to 120 MPa and its application in strength criterion*, *ACI Mater. J.* 103 (2006) 18–24. doi:10.14359/15123.
- [252] S. Prinsse, D.A. Hordijk, G. Ye, P. Lagendijk, M. Luković, *Time-dependent material properties and reinforced beams behavior of two alkali-activated types of concrete*, *Struct. Concr.* 21 (2020) 642–658. doi:10.1002/suco.201900235.
- [253] D.J. Cook, P. Chindaprasirt, *Influence of loading history upon the tensile properties of concrete*, *Mag. Concr. Res.* 33 (1981) 154–160. doi:10.1680/mac.1981.33.116.154.
- [254] A.D. Ross, *Creep of concrete under variable stress*, in: *J. Proc.*, 1958: pp. 739–758.
- [255] P. Lura, K. Van Breugel, I. Maruyama, *Effect of curing temperature and type of cement*

- on early-age shrinkage of high-performance concrete, *Cem. Concr. Res.* 31 (2001) 1867–1872. doi:10.1016/S0008-8846(01)00601-9.
- [256] A. Darquennes, S. Staquet, M.P. Delplancke-Ogletree, B. Espion, Effect of autogenous deformation on the cracking risk of slag cement concretes, *Cem. Concr. Compos.* 33 (2011) 368–379. doi:10.1016/j.cemconcomp.2010.12.003.
- [257] T.C. Hansen, Creep and stress relaxation of concrete: a theoretical and experimental investigation, Svenska forskningsinstitutet för cement och betong vid Kungl. Tekniska högskolan, 1960.
- [258] H.G. Heilmann, H. Hilsdorf, K. Finsterwalder, Strength and Deformation of Concrete Under Tensile Stress, *Bulletin.* (1969) 94.
- [259] J. Byfors, Plain concrete at early ages, *Cement-och betonginst.*, 1980.
- [260] NEN-EN 12350-8, Testing fresh concrete - Part 8: Self-compacting concrete - Slump-flow test, (2019).
- [261] R.J. Thomas, H. Ye, A. Radlinska, S. Peethamparan, Alkali-activated slag cement concrete, *Concr. Int.* 38 (2016) 33–38.
- [262] P. Duxson, J.L. Provis, G.C. Lukey, J.S.J. van Deventer, The role of inorganic polymer technology in the development of “green concrete,” *Cem. Concr. Res.* 37 (2007) 1590–1597. doi:10.1016/j.cemconres.2007.08.018.
- [263] A. Kostiuhenko, J. Liu, Z. Aldin, Mechanical properties and creep behavior of an alkali-activated concrete, *Mechanical properties and creep behavior of an alkali-activated concrete*, in: *Alkali Act. Mater. Geopolymers Versatile Mater. Offer. High Perform. Low Emiss.*, Tomar, 2018: p. 9.
- [264] S. Chithiraputhiran, N. Neithalath, Isothermal reaction kinetics and temperature dependence of alkali activation of slag, fly ash and their blends, *Constr. Build. Mater.* 45 (2013) 233–242. doi:10.1016/J.CONBUILDMAT.2013.03.061.
- [265] S. Zhang, Y. Zuo, Z. Li, G. Ye, Isothermal calorimetric study on heat evolution and apparent activation energy of alkali-activated slag/fly ash paste, in: *2nd Int. Conf. Sustain. Build. Mater.*, Eindhoven, 2019: pp. 1–8.

Propositions

1. High autogenous shrinkage does not necessarily mean high probability of cracking.
2. We cannot mitigate autogenous shrinkage in a proper way unless we know its mechanisms.
3. Our goal is clear: to make the shrinkage mechanisms clear; but we should be clear that nothing can be completely clear.
4. PhD = knowledge + skills + creativity. Unlike the former two, creativity can barely be obtained by training.
5. PhD research is challenging. However, challenge means not only difficulty, but also opportunity.
6. What determines the number of our publications? Is it thoroughness of thoughts or intensity of labour? - Both, but there is another factor: morality.
7. "If you do something, do it well; or don't do it". (Fred Schilperoort)
8. If you like doing something, it is more likely that you will be good at it, and vice versa.
9. Choice is more important than effort. For PhD candidates, the two most important choices are the choice of the supervisor and the choice of the PhD topic.
10. A good PhD supervisor must be a good researcher, but a good researcher may not be a good PhD supervisor.

These propositions are regarded as opposable and defendable, and have been approved as such by the promotors Prof. Klaas van Breugel and Dr. Guang Ye.

List of publications

Journal papers:

1. **Z. Li**, S. Zhang, Y. Zuo, W. Chen, G. Ye, Chemical deformation of metakaolin based geopolymer. *Cement and Concrete Research*. 120 (2019) 108–118.
2. **Z. Li**, M. Nedeljković, B. Chen, G. Ye, Mitigating the autogenous shrinkage of alkali-activated slag by metakaolin. *Cement and Concrete Research*. 122 (2019) 30–41.
3. **Z. Li**, T. Lu, X. Liang, H. Dong, J. Granja, M. Azenha, G. Ye, Mechanisms of autogenous shrinkage of alkali-activated slag and fly ash pastes. *Cement and Concrete Research*. 135 (2020) 106107.
4. **Z. Li**, M. Wyrzykowski, H. Dong, J. Granja, M. Azenha, P. Lura, G. Ye, Internal curing by superabsorbent polymers in alkali-activated slag. *Cement and Concrete Research*. 135 (2020) 106123.
5. **Z. Li**, J. Liu, G. Ye, Drying shrinkage of alkali-activated slag and fly ash concrete; A comparative study with ordinary Portland cement concrete. *Heron*. 64 (2019) 149.
6. **Z. Li**, S. Zhang, X. Liang, G. Ye, Cracking potential of alkali-activated slag and fly ash concrete subjected to restrained autogenous shrinkage. *Cement and Concrete Composites*. 114 (2020) 103767.
7. **Z. Li**, T. Lu, Y. Chen, B. Wu, G. Ye, Prediction of the autogenous shrinkage and microcracking of alkali-activated slag and fly ash concrete. *Cement and Concrete Composites*. 117 (2020) 103913.
8. **Z. Li**, S. Zhang, X. Liang, G. Ye, Internal curing of alkali-activated slag-fly ash paste with superabsorbent polymers. *Construction and Building Materials*. 263 (2020) 120985.
9. **Z. Li**, X. Liang, Y. Chen, G. Ye, Effect of metakaolin on the autogenous shrinkage of alkali-activated slag-fly ash paste. *Construction and Building Materials*. 278 (2020) 122397.
10. **Z. Li**, B. Delsaute, T. Lu, A. Kostuchenko, S. Staquet, G. Ye, A comparative study on the autogenous shrinkage-induced cracking of alkali-activated materials concrete and ordinary Portland cement concrete. *Construction and Building Materials*. (2020) (in revision).

11. **Z. Li**, I. Flores Beltran, Y. Chen, B. Šavija, G. Ye, Early-age properties of alkali-activated slag and glass wool paste. *Construction and Building Materials*. (2020) (in revision).
12. **Z. Li**, G. Ye, A low-autogenous-shrinkage alkali-activated slag and fly ash concrete. *Applied Science*. (2020). 6092.
13. M. Nedeljković, **Z. Li**, G. Ye, Setting, Strength, and Autogenous Shrinkage of Alkali-Activated Fly Ash and Slag Pastes: Effect of Slag Content. *Materials*. 11 (2018) 2121.
14. Y. Chen, **Z. Li**, S.C. Figueiredo, O. Copuroglu, F. Veer, E. Schlangen, Limestone and Calcined Clay-based Sustainable Cementitious Materials for 3D Concrete Printing: A Fundamental Study of Extrudability and Early-age Strength Development. *Applied Science*. 9 (2019) 1809.
15. T. Lu, **Z. Li**, K. van Breugel, Modelling of autogenous shrinkage of hardening cement paste. *Construction and Building Materials*. 264 (2020) 120708.
16. S. Zhang, **Z. Li**, B. Ghiassi, S. Yin, G. Ye, Fracture Properties and Microstructure Formation of Hardened Alkali-activated Slag/Fly ash Paste. *Cement and Concrete Research*. (2020) (in revision).
17. M. Nedeljković, B. Ghiassi, S. van der Laan, **Z. Li**, G. Ye, Effect of curing conditions on the pore solution and carbonation resistance of alkali-activated fly ash and slag pastes, *Cement and Concrete Research*. 116 (2019) 146–158.
18. Y. Chen, S. Chaves Figueiredo, **Z. Li**, Z. Chang, K. Jansen, O. Çopuroğlu, E. Schlangen, Improving printability of limestone-calcined clay-based cementitious materials by using viscosity-modifying admixture, *Cement and Concrete Research*. 132 (2020) 106040.
19. Y. Chen, C.R. Rodriguez, **Z. Li**, B. Chen, O. Copuroglu, E. Schlangen, Experimental Study on Fresh and Hardened Properties of Limestone and Calcined Clay-based Cementitious Materials for 3D Concrete Printing, *Cement and Concrete Composites*. 114 (2020) 103708.
20. X. Cao, L. Wu, **Z. Li**, Behaviour of steel-reinforced concrete columns under combined torsion based on ABAQUS FEA. *Engineering Structures*. 209 (2019) 109980.
21. X. Wang, S. Dong, **Z. Li**, B. Han, J. Ou. Nanomechanical signatures of interfacial transition zone in concrete with nanofillers. *Engineering*. (2020) (accepted).

Conference proceedings:

1. **Z. Li**, G. Ye, Autogenous shrinkage and mechanical properties of alkali activated slag blended with metakaolin. Prague, Czech Republic. (2019).
2. **Z. Li**, G. Ye, Do geopolymers also show chemical shrinkage? 73rd Rilem Week. International Conference on Innovative Materials for Sustainable Civil Engineering. Nanjing, China. (2019).
3. **Z. Li**, A Kostiuhenko, G. Ye, Autogenous shrinkage induced stress of alkali activated slag and fly ash concrete under restraint condition. International Conference on Alkali Activated Materials and Geopolymers: Versatile Materials Offering High Performance and Low Emissions. ECI Symposium Series. Tomar, Portugal. (2018).
4. **Z. Li**, G. Ye, Experimental Study of the Chemical Deformation of Metakaolin Based Geopolymer. SynerCrete'18: Interdisciplinary Approaches for Cement-based Materials and Structural Concrete. Madeira, Portugal. (2018).
5. **Z. Li**, P. Gao and G. Ye, Experimental study on autogenous deformation of metakaolin based geopolymer. 2nd International RILEM/COST Conference on Early Age Cracking and Serviceability in Cement-based Materials and Structures - EAC2. Brussels, Belgium. (2017).
6. **Z. Li**, M Nedeljkovic, Y Zuo, G. Ye, Autogenous shrinkage of alkali-activated slag-fly ash pastes. The 5th International Slag Valorisation Symposium. Leuven, Belgium. (2017).

Curriculum Vitae

Personal information

Name: Zhenming Li (李镇明)

Date of birth: October 1991

Place of birth: Cangzhou, Hebei Province, China

Email: z.li-2@tudelft.nl



Education background

01/2020 – present	Post-doc researcher Faculty of Civil Engineering and Geoscience Delft University of Technology
11/2015 – 11/2020	Phd candidate Faculty of Civil Engineering and Geoscience Delft University of Technology
01/2018-04/2018	Visiting researcher Concrete and Construction Chemistry Laboratory Empa, Switzerland
09/2013 – 10/2015	MSc student (supervisor: Prof. Jinping Ou) School of Civil Engineering Harbin Institute of Technology
02/2012 – 07/2012	Exchange study School of Civil Engineering National Central University (Taiwan)
07/2009 – 07/2013	BSc student (Outstanding Graduate in Heilongjiang Province) Honors School Harbin Institute of Technology

Acknowledgements

Time flies. Sometimes, it's really hard to realize how many years have passed and how it comes to this day. I become 5 years older now but it is not something to lament. By contrast, I do cherish the memory of these years, since I know that it will not never happen again in my life that I can fully devote myself for 4-5 years to one single scientific question, to clarify something that is unclear, to know something that is unknown and to try something that has not been tried before. I enjoyed this adventure and I am grateful to the people who helped me through.

I would like to begin by sincerely acknowledging my promoter Prof. Klaas van Breugel for giving me the chance to pursue my PhD degree in our section. The discussions with you are always helpful and inspiring. Your comments on materials, modeling and shrinkage related properties are very valuable. You taught me the significance to think critically and write logically. I really like the speeches you made on all kinds of activities.

My deep appreciation goes to my daily supervisor and promotor Dr. Guang Ye. First, I want to thank you for giving me this challenging but interesting PhD topic. I like it. The open and tolerant research environment you create is beneficial especially for me, who has all kinds of ideas flying around, although many of them do not really make sense. You provided me the freedom to do the research in my way and also valuable opportunities that I can get trained. You taught me to do good research and to be a responsible researcher. What's more, thanks for hiring me to do a postdoctoral project, when I finished the thesis writing but didn't really defend yet. Last but not least, I would like to give my gratitude to you and Ms. Lei Zhang for inviting me to your home for the New Year parties. The wine was so good that I drank more than I could.

I would also like to acknowledge my supervisor in my Master period, Prof. Jinping Ou, who wrote the letter of recommendation for me when I applied to study abroad and always supports and encourages me in my research career. Thank you for being a committee member of my defense.

I acknowledge also the other committee members of my defense, Prof. Jensen, Prof. Benboudjema, Dr. Cizer, Prof. Schlangen and Prof. Erkens. I am glad and honored to have you in the committee of my defense. Thanks for your time and efforts spent on my thesis.

I am very grateful to China Scholarship Council (CSC) and the Dutch Research Council (NWO) for funding me to do this project. Thanks also go to COST action TU1404, which covered my expenses for an international course, a conference and a three-month visit to Empa.

I want to thank my colleagues and friends for their help and support in work and life. You let me know that I can always count on you when I am helpless. In no particular order:

Dr. Marija Nedeljković helped me to get familiar with the lab when I just arrived. She has influenced me with her passion and energy. Time is never enough when I am chatting with you. Thanks also to Mr. Patrick Holthuisen, my friend, and little Lena, who was born in this special time. What do you think of 莉娜 to be her Chinese name? Special thanks to Patrick for translating the summary of this thesis into Dutch.

Dr. Peng Gao spent quite a bit of time discussing shrinkage related topics with me. I was always free to enter his office to ask questions. Your patience and knowledge speeded up my progress at the beginning of my PhD.

Dr. Tianshi Lu helped me a lot with modeling of shrinkage. I learned a lot from our collaboration. I wish you success in your new career in China, although I really miss your punch lines. I think you are a better crosstalk comedian than I am, at least in daily life.

Dr. Hua Dong, thanks very much for reviewing my whole PhD thesis. Without your critical comments and revision beforehand, the review by Dr. Ye and Prof. van Breugel would not be that smooth and quick. Your help in daily life is also very important to me.

Xuhui Liang helped a lot with my experiments, especially in my fourth year here. Without your contribution, I could never finish the experiments and thesis writing within four years. You are a good friend and a good neighbour. How are you bro?

Yun Chen, thanks very much for your friendship. It's a pleasant experience for me to share thoughts and ideas on work and life with you. I appreciate your help in delivering goods to me when I was busy ['leizi]. I also like the meals you cooked.

Xuliang Hou (and Dr. Ying Yang), thanks for your kind help and care like a big brother. Thanks also to my other office mates: Jiayi Chen (Dr. Wenqin Shi), Dr. Yun Huang, Amir and Bei Wu. It is an interesting coincidence that the room number of our office (6.06) is the same as that of my office in my Master period. I enjoy the atmosphere we create together and I appreciate the experiences you shared with me.

Hao Huang, thanks for teaching me to use many facilities and the discussions on shrinkage. Dr. Yong Zhang, thanks for sharing your thoughts and experience with me. Dr. Xiaowei Ouyang, thank you for giving me suggestions on shrinkage mechanisms. Dr. Zhuqing Yu, the chatting with you is interesting. By the way, I used your thesis as a template of mine. Albina Kostiuhenko, nice to work with you on the same project. Yu S. Chen, thanks for your good-eating meals and help in designing the cover of this thesis. I wish you success in the area of 3D printing. Xingliang Yao, let's meet more in China. Chen Liu, I am honoured to be your daily supervisor. Let's start the adventure together!

Maiko van Leeuwen, Paul Vermeulen, Fred Schilperoort, Kees van Beek, Ton Blom, John van den berg, Ron Penners and Arjan Thijssen, special thanks to you for help with my experimental work in Microlab and Stevin II lab. Many thanks to our secretaries, Nynke Verhulst, Jaap Meijer, Claire de Bruin, Jacqueline van Unen and Iris Batterham for their kind help with daily affairs.

I am thankful to other colleagues for creating the harmonious working environment. Prof. Erik Schlangen, Prof. Rob Polder, Dr. Ton van Beek, Dr. Henk Jonkers, Dr. Oguzhan Copuroglu, Dr. Dessi Koleva, Jeanette van den Bos, Dr. Zhiwei Qian, Dr. Branko Savija, Dr. Mladena Luković, Dr. Kamel Arbi, Dr. Bahman Ghiassi, Dr. Agus Susanto, Renée Mors, Dr. Xu Ma, Bart Hendrix, Zhipei Chen, Dr. Yibing Zuo, Stefan Chaves Figueiredo, Dr. Hongzhi Zhang, Dr. Wenjuan Lyu, Dr. Shi Xu, Shizhe Zhang, Claudia Romero Rodriguez, Yask Kulshreshtha, Fernando França de Mendonça Filho, Jakub Pawlowicz, Yidong Gan, Yading Xu, Boyu Chen, Ze Chang, Emanuele Rossi, Zainab Aldin, Zhiyuan Xu, Luiz Miranda de Lima Junior, Yu Zhang, Shan He, Zhi Wan, Irving Flores Beltran, Kohsuke Handa, Anne Linde van Overmeir, Deepanshu Mangla, Minfei Liang, etc. Thanks for your support and all the enjoyable time that we have shared.

Visiting researchers to the CMMB group. Dr. Yun Huang, working with you benefits me a lot. Prof. Jiangxiong Wei, thanks for your suggestions to me on doing research. Prof. Yingzi Yang, it's a happy time for me when you were here. Dr. Jiahua Liu, thanks for your care in life and help.

I am also grateful to external researchers and friends who helped me before. Prof. Pietro Lura and Dr. Mateusz Wyrzykowski, thanks for hosting and supervising me during my stay in Empa. Your insightful ideas and thoughts improved my understanding of shrinkage. Janis Justs, Nikolajs Toropovs, Peihua Zhong and Dr. Zhangli Hu are sincerely acknowledged for their help on my experiments performed in Empa and the discussions on the results. Dr. Barbara Lothenbach, your kindness and high working efficiency left a deep impression on me. Thanks also go to Dr. Zhenguo Shi, Dr. Biwan Xu and Yiru Yan, you made me feel at home when I was in Empa. I am sure our friendship will last for long. Thanks to Prof. Ole Mejlhede Jensen, you always feedback quickly and patiently on my questions on shrinkage, experimental methods and other research topics. Prof. Farid Benboudjema, I enjoyed talking and discussing with you. Thanks for your helpful information. Prof. Sybrand van der Zwaag, thanks for answering many of my questions. Your insights and sharp ideas impressed me. Dr. Henk Nugteren, thanks for the nice communication we have. Dr. Lin Chi, thanks for your concern when I was in Denmark for conference. Thanks to Dr. Yu Li for the discussion with me on chemical deformations. Prof. John Provis, thanks for your fast reply to my emails. Dr. Miguel Azenha (and also Dr. José Granja), thanks for helping me building the EMM-ARM facility. I learned a lot from the way you work and communicate. Dr. Brice Delsaute and Dr. Stéphanie Staquet, the collaboration with you benefits me much. Siva Uppalapati, thanks for the discussion on shrinkage related topics. I appreciate your open mind and friendliness.

I will not forget my good friends. Liangfu Wei and Hong Zhang, thanks for accompanying me at the beginning of my PhD career. Your friendship makes me feel warm in the Netherlands. Hong Zhang, my senior in HIT, who became Xiaohong ever since we fell into the same grade. I wish you a bright career. Liangfu, I am so lucky to have you, as a good roommate who shared the apartment with me for years, a good friend in life, a collaborator in research but also a perfect partner in comedies. I treasure our friendship very much. Liangyuan, you are such a screenwriter. Hope to have more chances to be your actor. Hongxiao, the time with you is a good memory of mine. Dr. Ruxin Jing, Dr. Nan Jiang and Dr. Xuedong Zhang, thanks for your support and suggestions. Weiyuan Zhang and Chengcheng, the talks with you are interesting and helpful.

I want to send the greatest gratitude to my parents. The brain I used to think, the hands I used to work and the voice I have to sing are all gifts from you. Thanks for your and my parents-in-law's hard work in taking care of my wife and my son. Without your help, my life would be much more difficult. My gratitude also goes to all other relatives in Li family. Thanks for your support from the hometown and for taking caring of many affairs which I should have been involved. Your love gives me power.

Now it's time to say thank you to Na Yu (Zhu), my beloved wife, for your understanding, support, encouragement, sacrifice and love in the past years. 8 years! Can you imagine that? I could never make it through without you. I know from my heart how much you have done for me and for our family. We have been apart for too long. It's time to reunite and live a normal life together.

Thanks also go to my son, Yichen (Guoguo). Thanks for coming into our life. Any of the videos of you easily made my day. For the time that I was not with you, I apologize; for the future that I am going to share with you, I appreciate. I hope you know how much your mom and I love you and that there is nothing I won't do for you.

Zhenming Li, in Delft. 2020. 12